On the Dynamics of Natural and Ventilated Cavitation Flows

An Experimental Investigation

Gawandalkar, U.U.

DOI
10.4233/uuid:7c9a4632-3352-4aee-9d47-4966059e352d

Publication date
2024

Document Version
Final published version

Citation (APA)
Gawandalkar, U. U. (2024). *On the Dynamics of Natural and Ventilated Cavitation Flows: An Experimental Investigation*. [Dissertation (TU Delft), Delft University of Technology].
https://doi.org/10.4233/uuid:7c9a4632-3352-4aee-9d47-4966059e352d

Important note
To cite this publication, please use the final published version (if applicable).
Please check the document version above.

ON THE DYNAMICS OF NATURAL AND VENTILATED CAVITATION FLOWS

AN EXPERIMENTAL INVESTIGATION

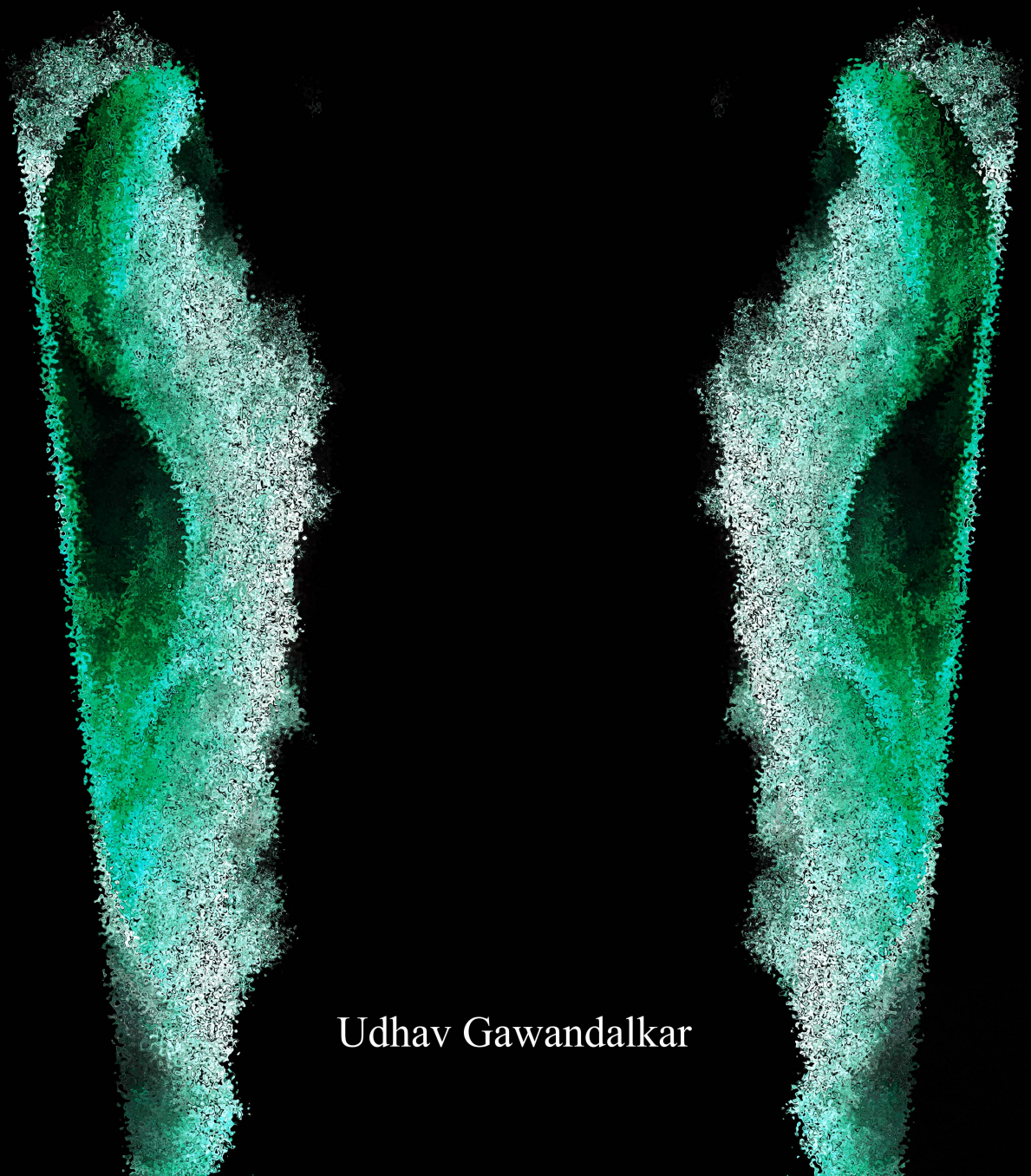

Udhav Gawandalkar

ON THE DYNAMICS OF NATURAL AND VENTILATED CAVITATION FLOWS

AN EXPERIMENTAL INVESTIGATION

ON THE DYNAMICS OF NATURAL AND VENTILATED CAVITATION FLOWS

AN EXPERIMENTAL INVESTIGATION

Dissertation

for the purpose of obtaining the degree of doctor
at Delft University of Technology
by the authority of the Rector Magnificus, prof. dr. ir. T.H.J.J. van der Hagen,
chair of the Board for Doctorates
to be defended publicly on
Wednesday 2 October 2024 at 10 o'clock

by

Udhav Ulhas GAWANDALKAR

Master of Science in Mechanical Engineering,
Delft University of Technology, The Netherlands
born in Mapusa, Goa-India.

This dissertation has been approved by the promotors.

Composition of the doctoral committee:

Rector Magnificus,	chairperson
Prof. dr. ir. C. Poelma,	Delft University of Technology, promotor
Prof. dr. ir. J. Westerweel,	Delft University of Technology, copromotor
Independent members:	
Prof. dr. S. L. Ceccio,	University of Michigan, USA
Prof. dr. ir. N. G. Deen,	Eindhoven University of Technology
Prof. dr. O. Supponen,	ETH Zürich, Switzerland
Prof. dr. ir. T. J. C. van Terwisga,	Delft University of Technology
Prof. dr. ir. W. S. J. Uijttewaal,	Delft University of Technology

This work is funded by the ERC Consolidator Grant No. 725183 “OpaqueFlows.”

Keywords: partial cavitation, cloud shedding, re-entrant flow, bubbly shock waves, ventilated cavities, ventilation hysteresis, X-ray densitometry, tomographic particle image velocimetry

Printed by: Gildeprint - Enschede

Front & Back: An attached partial cavity and shed cloud *re-imagined artistically* via pointillism, inspired by Paul Signac and ‘All Things Shining’, Pelagic Record (2024).

ISBN 978-94-6384-637-0

An electronic version of this dissertation is available at
http://repository.tudelft.nl/.

In loving memory of my beloved Maa, Lata,
who always encouraged my curiosity and shared my happiness...

CONTENTS

SUMMARY

Cavitation, a ubiquitous phenomenon responsible for the sound of knuckles cracking, the erosion-wear of ship propeller blades and targeted drug delivery permeates natural, industrial and biomedical realms. It presents both challenges and opportunities for various applications, hence, a fundamental understanding of cavitation flows is imperative. Cavitation can be broadly classified as *natural* or *ventilated*: Natural cavitation occurs when the pressure in the flow drops below the vapour pressure, leading to the formation of *vapour* bubbles/cavities. Alternately, ventilated cavities are formed by injecting non-condensable *gas* into the flow. Although fundamentally different, these flows share various underlying physical phenomena. In this dissertation, a commonly occurring, yet complex form of natural cavitation − *partial cavitation* is examined in combination with *ventilated cavities* to further our current understanding of cavitation flows.

In the first part of this dissertation, partial cavitation is examined in an axisymmetric venturi. Partial cavitation is an inherently unsteady form of cavitation where attached vapour cavities grow, get destabilised and detached, leading to periodic cloud shedding. The shed cloud then implodes giving rise to a pressure wave. It is widely accepted that two distinct destabilising mechanisms can cause cavity detachment, namely re-entrant jet below the cavity and bubbly shock wave emanating from the cloud implosion. However, *why the shedding mechanism switches from re-entrant jet to bubbly shock waves with decreasing cavitation number (σ)* remains unknown. This can be attributed to the difficulty in visualising and quantifying the underlying flow phenomenon mainly due to the optical opaqueness of such flows. In this dissertation, the re-entrant jet and bubbly shock waves are studied separately using various flow modalities to overcome the optical opacity to assess their role in cavity shedding for a range of cavitation numbers, $\sigma \sim$ 0.4-1.1 .

The axisymmetry and the periodicity of the re-entrant jet are utilised to visualise the near-wall *liquid* re-entrant film for a range of σ. The fluorescent tracer particles in the re-entrant flow are tomographically imaged with an appropriate optical filter. It is found that the re-entrant jet is a consequence of the impinging jet and a stagnation point formed at the cavity closure, driven by the pressure gradient near the cavity closure region. The re-entrant jet is seen to exist below the cavity at *all* cavitation numbers (σ). At a higher σ ($\approx$ 1.05), the strong interaction between the cavity and the re-entrant flow is suspected to cause cavity fragmentation. As σ decreases ($\approx$ 0.95), the interaction between the cavity and the re-entrant flow is minimal, initially. However, as the cavity grows, the re-entrant flow is seen to get thicker and faster, resulting in cavity pinch-off near the throat. The cloud implosion is suspected to be inconsequential for the cavity detachment at such σ. At a lower σ ($\approx$ 0.80), a sharp and discernible velocity discontinuity superimposed on the existing low-velocity re-entrant flow is seen to cause cavity detachment. This discontinuity is attributed to the bubbly shock wave due to the cloud implosion. It is observed that the re-entrant jet coexists with a bubbly shock wave and

vice versa in a shedding cycle.

Bubbly shock fronts are characterised in the same flow geometry using time-resolved X-ray densitometry, in combination with high-frequency pressure measurements. The densitometry circumvents the optical opacity of the cavitating flow to unveil the interaction of the pressure wave with the attached vapour cavity at different σ. At $\sigma \approx 0.47$, the upstream propagating pressure wavefront is found to be supersonic. Hence, after impinging on the cavity, it starts condensing the cavity due to the resulting condensation shock. As σ increases (≈ 0.78), the pressure wave created by the cloud collapse is weaker. Thus, the pressure wave impinging on the cavity is initially subsonic. However, as it propagates upstream, it accelerates and becomes supersonic, resulting in the onset of cavity condensation. This is accompanied by an increased pressure rise (Δp) across the shock front. The observed acceleration is attributed to the converging walls of the venturi seen by the shock front. With a further increase in σ ($\approx$ 0.84-0.90), the pressure discontinuity from the cloud implosion is even weaker and despite the acceleration of the shock front, the Mach number of the pressure wavefront remains subsonic. At such σ, a strong re-entrant jet existing between the cavity and venturi wall causes cavity detachment. All the shedding cycles are predominantly dictated by the re-entrant jet at higher σ (> 0.95). Thus, the emergence of re-entrant jet-triggered cavity shedding coincides with the pressure wavefront being subsonic.

The results show that the combination of low pressure and high vapour fraction leads to a low speed of sound (a few ms^{-1}) in the vapour cavity. Thus condensation shock fronts propagating at $0.55U_t$ assume a high Mach number, rendering compressibility effects significant. Although both the shedding mechanisms can coexist in a shedding cycle, the effect of compressibility appears to set the final cavity shedding mechanism, i.e. bubbly/condensation shock front for the high Mach number and re-entrant jets for the lower Mach number.

In the second part of this dissertation, ventilated cavities in the wake of a 2-D bluff body are investigated over a wide range of flow velocities (Froude Number, $Fr \approx 2-13.9$), and gas injection rates ($C_{qs} \approx 0.03-0.13$) using high-speed X-ray densitometry. The ventilated cavities were created using two different ventilation strategies, i.e. increasing ventilation ('L-H') and decreasing ventilation ('H-L') to answer the question: *why is the amount of gas required to maintain the cavity lesser than the amount of gas required to form the cavity?*

With the 'L-H' strategy, a regime map (Fr vs C_{qs}) was developed, where four different types of stable, fixed-length cavities are identified, each having a unique cavity closure. Foamy cavities (FC) were discerned without a well-developed closure region. Twin-branch cavity (TBC), re-entrant jet cavity (REJC), and long cavities (LC), on the other hand, have developed closures. TBC was observed at low Fr, having a 3-D closure and gas ejection via a wave-like travelling instability. For $Fr \geq 5.8$ and intermediate C_{qs}, REJ cavities are observed with a strong re-entrant flow entering inside the cavity. The gas was ejected out via spanwise vortex shedding and the re-entrant jet. Finally, at high Fr and C_{qs}, LC with a 2-D closure exists. The closure is characterised by travelling wave-type instability leading to gas pocket shedding. The cavity closure is seen to dictate the cavity length and pressure within it. The supercavities exhibit a maximum length (L_c) for a given Fr, meaning, a finite volume of gas ($\sim WHL_c$, where W, H are wedge width and

height, respectively) can be entrained to form a cavity. The excess injected gas is ejected out. The quantification of compressibility effects shows that it is insignificant and can be possibly omitted for numerical modelling of ventilated cavities.

The supercavity formation process is examined for the first time by quantifying the instantaneous gas ejection rate using void fraction fields. In particular, we focus on cavity closures formed during the transition process from one stable cavity regime to another. It is observed that cavities transitioning to TBC have much lower, but constant gas ejection rates than when REJC transitions to LC. This is due to the different cavity closures the cavity assumes during the transition process. A prominent re-entrant flow at the closure is seen to result in significantly higher gas leakage than vortex or wave-type closure. The transitional cavity closures and the resulting gas leakage during the cavity formation process provide us insights into the observed difference between the gas flux required to form and maintain the supercavity.

This dissertation demonstrates the capabilities of time-resolved X-ray densitometry in tandem with conventional flow modalities, such as high-speed photography, PIV and pressure measurements to generate distinctive insights into the dynamics of optically opaque multi-phase, multi-scale, and highly unsteady bubbly flows.

SAMENVATTING

Cavitatie, een alomtegenwoordig fenomeen verantwoordelijk voor het geluid van knakkende knokkels, de erosieslijtage van scheepsschroefbladen en gerichte medicijntoediening, doordringt natuurlijke, industriële en biomedische domeinen. Het biedt zowel uitdagingen als kansen voor verschillende toepassingen, waardoor een fundamenteel begrip van caviterende stromingen van cruciaal belang is. Cavitatie kan ruwweg worden ingedeeld als *natuurlijk* of *geventileerd*: Natuurlijke cavitatie treedt op wanneer de druk in de stroming onder de dampdruk daalt, wat leidt tot de vorming van *damp* bellen/cavitatie. Daarentegen wordt geventileerde cavitatie gevormd door het injecteren van niet-condenseerbaar *gas* in de stroming. Hoewel fundamenteel verschillend, delen deze stromingen verschillende onderliggende fysische verschijnselen. In dit proefschrift wordt een veelvoorkomende, maar complexe, vorm van natuurlijke cavitatie - *partiële cavitatie* - onderzocht in combinatie met *geventileerde cavitatie* om ons huidige begrip van caviterende stromingen verder te ontwikkelen.

In het eerste deel van dit proefschrift wordt partiële cavitatie onderzocht in een axisymmetrische venturi. Partiële cavitatie is een inherent instabiele vorm van cavitatie waarbij aangehechte dampbellen groeien, destabiliseren en loslaten, wat leidt tot periodieke wolkafschudding. De afgeschudde wolk implodeert vervolgens, resulterend in een drukgolf. Het is algemeen aanvaard dat twee verschillende destabiliserende mechanismen kunnen leiden tot loslating van de caviteit, namelijk een 're-entrant jet' onder de caviteit en een 'bubbly-shock wave' die voortkomt uit de wolkimplosie. Echter, *waarom het loslatingsmechanisme omschakelt van een re-entrant jet naar bubbly-shock waves bij een afnemend cavitatiegetal (σ)* is nog onbekend. Dit kan worden toegeschreven aan de moeilijkheid om de onderliggende stromingsfenomenen te visualiseren en kwantificeren, voornamelijk vanwege de optische ondoorzichtigheid van dergelijke stromingen. In dit proefschrift worden de re-entrant jet en bubbly-shock waves afzonderlijk bestudeerd met behulp van verschillende modaliteiten om de optische ondoorzichtigheid te ondervangen en hun rol in cavitatieloslating te beoordelen voor een reeks cavitatiegetallen, $\sigma \sim 0.4$-1.1.

De axisymmetrie en periodiciteit van de re-entrant jet worden benut om de nabijwandse *vloeibare* terugkerende film te visualiseren voor een reeks σ. De fluorescerende tracerdeeltjes in de stroming worden tomografisch afgebeeld met een passende optisch filter. Er wordt gevonden dat de re-entrant jet een gevolg is van de 'impinging jet' en een stagnatiepunt, wat is gevormd bij de afsluiting van de caviteit, gedreven door de drukgradiënt nabij de caviteitsafsluitingsregio. De re-entrant jet wordt gezien onder de caviteit bij *alle* cavitatiegetallen (σ). Bij een hogere σ (≈ 1.05) veroorzaakt de sterke interactie tussen de caviteit en de terugkerende stroming vermoedelijk caviteitsfragmentatie. Naarmate σ afneemt (≈ 0.95) is de interactie tussen de caviteit en de terugkerende stroming aanvankelijk minimaal. Echter, naarmate de caviteit groeit, wordt de terugkerende stroming breder en sneller, wat resulteert in afknijping van de caviteit nabij de keel. De

wolkimplosie wordt onbeduidend geacht voor de caviteitsloslating bij dergelijke σ. Bij een lagere σ (≈ 0.80), veroorzaakt een scherpe en duidelijke snelheidsdiscontinuïteit, bovenop de bestaande lage-snelheids terugkerende stroming, caviteitsloslating. Deze discontinuïteit wordt toegeschreven aan de bubbly-shock wave als gevolg van de wolkimplosie. Er wordt waargenomen dat de re-entrant jet samenvalt met een bubbly-shock wave en vice versa in een afschuddingscyclus.

Bubbly-shock fronts worden gekarakteriseerd in dezelfde stroomgeometrie met behulp van tijdgeresolveerde X-ray densitometrie, in combinatie met hoge frequentie drukmetingen. De densitometrie omzeilt de optische ondoorzichtigheid van de caviterende stroming om de interactie van de drukgolf met de aangehechte dampcaviteit bij verschillende σ te onthullen. Bij $\sigma \approx 0.47$ blijkt het stroomopwaarts voortbewegende drukgolffront supersonisch te zijn. Daarom begint het, na het inslaan, de caviteit te condenseren door de resulterende condensatieschok. Naarmate σ toeneemt (≈ 0.78), is de door het uiteenvallen van de wolk gecreëerde drukgolf zwakker. Daardoor is de drukgolf die op de caviteit stuit aanvankelijk subsonisch. Echter, naarmate deze stroomopwaarts voortbeweegt, versnelt hij en wordt hij supersonisch, wat resulteert in het begin van cavitatiecondensatie. Dit gaat gepaard met een verhoogde druk (Δp) over het schokfront. De waargenomen versnelling wordt toegeschreven aan de convergerende wanden van de venturi, gezien vanuit het schokfront. Bij een verdere toename van σ ($\approx$ 0.84-0.90), is de drukdiscontinuïteit van de wolkimplosie nog zwakker en ondanks de versnelling van het schokfront blijft het Mach-getal van het drukgolffront subsonisch. Bij dergelijke σ veroorzaakt een sterke re-entrant jet tussen de caviteit en de venturiwand loslating van de caviteit. Alle afschuddingscycli worden voornamelijk bepaald door de re-entrant jet bij hogere σ (> 0.95). Dus, het opkomen van de re-entrant jet geïnitieerde caviteitsloslating valt samen met het subsonisch zijn van het drukgolffront.

De resultaten tonen aan dat de combinatie van lage druk en een hoog dampfractie leidt tot een lage geluidssnelheid (een paar m/s) in de caviteit. Daardoor nemen condensatieschokfronten die zich voortbewegen bij $0.55U_t$ een hoog Mach-getal aan, waardoor de compressie-effecten significant zijn. Hoewel beide loslatingsmechanismen kunnen samenhangen in een afschuddingscyclus, lijkt het effect van compressibiliteit het uiteindelijke cavitatie-loslatingsmechanisme te bepalen, d.w.z. bubbly/condensatie schokfront voor het hoge Mach-getal en re-entrant jets voor het lagere Mach-getal.

In het tweede deel van dit proefschrift wordt geventileerde cavitatie in het kielzog van een 2-D stomp object onderzocht over een breed scala aan stromingssnelheden (Froude getal, $Fr \approx 2 - 13.9$) en gasinjectiesnelheden ($C_{qs} \approx 0.03 - 0.13$) met behulp van hogesnelheids X-ray densitometrie. De geventileerde cavitatie werd gecreëerd met twee verschillende ventilatiestrategieën, namelijk toenemende ventilatie ('L-H') en afnemende ventilatie ('H-L') om te vraag te beantwoorden: *waarom de hoeveelheid gas die nodig is om de caviteit te behouden minder is dan de hoeveelheid gas die nodig is om de caviteit te vormen?*

Met de 'L-H' strategie is een regimekaart (Fr vs C_{qs}) ontwikkeld, waar vier verschillende soorten stabiele, caviteiten worden geïdentificeerd, elk met een unieke cavitatie sluiting. 'Foamy cavities' (FC) werden onderscheiden zonder een goed ontwikkelde sluitingsregio. 'Twin-branch cavity' (TBC), 're-entrant jet cavity' (REJC) en 'long cavitities' (LC) hebben daarentegen ontwikkelde sluitingen. TBC werd waargenomen bij lage Fr,

met een 3-D sluiting en gasejectie via een golfachtige voortbewegende instabiliteit. Voor $Fr \geq 5.8$ en tussenliggende C_{qs} worden REJC waargenomen met een sterke terugkerende stroming die de caviteit binnendringt. Het gas werd uitgestoten via vortexloslating en de re-entrant jet. Uiteindelijk, bij hoge Fr en C_{qs}, bestaan LC met een 2-D sluiting. De sluiting wordt gekenmerkt door een voortlopende golfachtige instabiliteit die leidt tot gasafschudding. De cavitatiesluiting lijkt de cavitatielengte en druk erin te dicteren. De 'supercavities' vertonen een maximale lengte (L_c) voor een gegeven Fr, wat betekent dat een eindige hoeveelheid gas ($\sim WHL_c$, waar W, H respectievelijk de breedte en hoogte van de wig zijn) kan worden ingesloten om een caviteit te vormen. Het overtollige geinjecteerde gas wordt uitgestoten. De kwantificering van compressie-effecten toont aan dat deze verwaarloosbaar zijn en mogelijk kunnen worden weggelaten voor numerieke modellering van geventileerde cavitatie.

Het proces van supercavitatievorming wordt voor het eerst onderzocht door de instantane gasuitstootsnelheid te kwantificeren met behulp van gasfractievelden. In het bijzonder richten we ons op cavitatiesluitingen gevormd tijdens het transitieproces van het ene stabiele cavitatieregime naar het andere. Er wordt waargenomen dat cavitatie die overgaat naar TBC veel lagere, maar constante gasafgiftesnelheid heeft dan wanneer REJC overgaat naar LC. Dit komt door de verschillende cavitatiesluitingen die de caviteit aanneemt tijdens het transitieproces. Een prominente terugkerende stroming bij de sluiting zorgt voor aanzienlijk hoger gasverlies dan bij een vortex- of golfachtige sluiting. De overgangscavitatiesluitingen en het resulterende gasverlies tijdens het cavitatievormingsproces bieden inzichten in het waargenomen verschil tussen de gasflux die nodig is om de supercavity te vormen en te behouden.

Dit proefschrift toont de mogelijkheden aan van tijdgeresolveerde X-ray densitometrie in combinatie met conventionele stroommodaliteiten, zoals hogesnelheidsfotografie, PIV en drukmetingen om onderscheidende inzichten te genereren in de dynamiek van optisch ondoorzichtige multi-fase, multi-schaal en zeer onstabiele bubbelsstromen.

1

INTRODUCTION

We must only begin. Believe me and you will see.

–Epictetus, Discourses

This chapter provides a brief background to cavitation flows and its engineering relevance. Two types of cavitation flows – natural and ventilated – are introduced separately. The motivation for studying these flows is made clear by identifying open questions in the literature. The challenges involved are discussed and the measurement approach adapted to overcome these challenges is concisely explained. Based on this, the research objectives are formulated. The chapter concludes with the structure of this dissertation.

1.1. CAVITATION: A UBIQUITOUS PHENOMENON

Cavitation can be broadly classified as either *natural* or *ventilated*. Natural cavitation is defined as the rupture of the liquid phase when subjected to regions of strongly reduced pressure. When the liquid ruptures, voids called 'cavitation bubbles' are formed (Brennen, 1995). These bubbles can implode violently when they reach a region where the pressure has recovered, giving rise to pressure/shock waves. Thus, benign-looking bubbles can deform and even destroy metal surfaces. Ventilated cavitation, on the other hand, refers to the gas cavity formed by injecting non-condensable gas in the region where the flow has separated (Silberman and Song, 1961). Natural cavities occur at low pressure, i.e. pressure close to the vapour pressure, and are filled with vapour. In contrast, ventilated cavities are composed of air (in most applications) and can be formed at a much higher pressure. Regardless of this fundamental difference, both natural and ventilated cavitation flows share several similarities, and are ubiquitous in nature and engineering.

In nature, cavitation can occur in a wide variety of flows, such as in river beds (Whipple et al., 2000), waves breaking (Allen, 1985), and embolisms in trees (Tyree and Sperry,

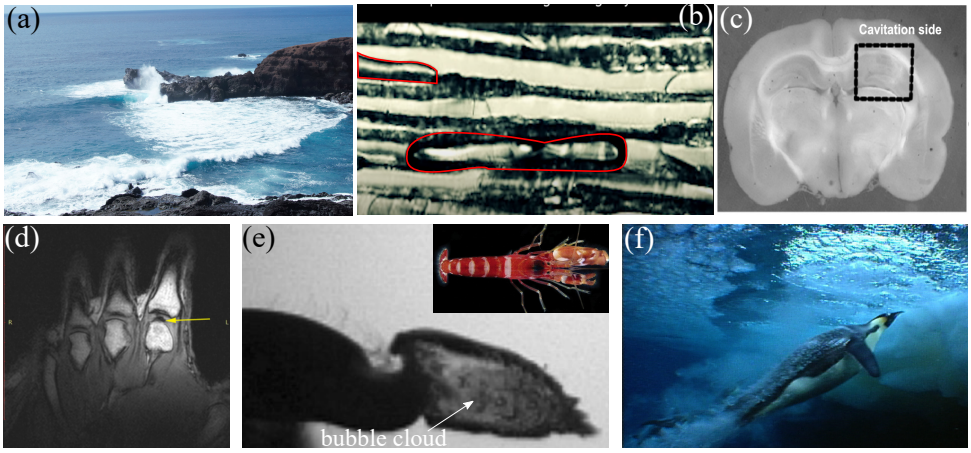

Figure 1.1: Cavitation in nature: (a) waves breaking at the beach, (b) embolism in the xylem (cavities are marked in red) (Hochberg et al., 2016), (c) traumatic head injury (Canchi et al., 2017), (d) cavitation due to knuckle cracking (air cavity is marked by yellow arrow) (Kawchuk et al., 2015), (e) pistol shrimp punch (Versluis, 2013), (f) emperor penguin moments before launching itself to the water surface (taken from: Blue Planet, BBC).

1989). Cavitation is also responsible for the violent punch of pistol shrimps (Versluis et al., 2000), the sound of knuckles cracking (Kawchuk et al., 2015), and even lethal traumatic injuries in the brain (Adhikari et al., 2016). Further, ventilated cavities are known to enable emperor penguins to leap in the air by wrapping their bodies in the cloak of air bubbles to reduce the friction drag (Davenport et al., 2011). Some of the examples of cavitation in nature are illustrated in figure 1.1.

Apart from nature, cavitation occurs widely in engineering realms. Natural cavitation is commonplace in engineering applications, such as in ship propellers (Van Terwisga et al., 2007), pump impellers (Kuiper, 1997), and even in dam spillways (Chanson, 2010). The violent bubble collapse is an important feature of natural cavitation, which is usually associated with detrimental effects such as wear, erosion and vibrations. However, natural cavitation also finds multiple useful applications in process industries; it is favourable for mixing of fuel in diesel injectors (Blake and Gibson, 1987), biomass pretreatment (Nakashima et al., 2016), and water disinfection (Jyoti and Pandit, 2004). The violent bubble collapses have also been leveraged for industrial deep-cleaning (Johnson et al., 1982) and in biomedical applications such as shock wave lithotripsy for kidney stone destruction (Xu et al., 2003), and ultrasound drug delivery to targeted tumour sites (Graham et al., 2014).

Alternatively, ventilated cavitation has the potential to minimise the deleterious effects of natural cavitation. For instance, 'aeration' in dam spillways and ship propellers is known to reduce the cavitation wear on the concrete walls and impeller blades (Pfister et al., 2011). Further, large ventilated cavities, a.k.a. supercavities have also found application in drag reduction in maritime transportation (Arndt et al., 2009, Ceccio, 2010). Thus, a fundamental understanding of natural and ventilated cavitation flows is imperative to maximise their favourable effects and/or minimise their detrimental effects.

1.2. PARTIAL NATURAL CAVITATION

Partial cavitation is a commonly occurring form of natural cavitation omnipresent in various engineering applications. The strong accelerations and shear experienced by such flows rupture the liquid, forming bubbles when the local pressure drops below the vapour pressure at a nearly constant temperature. Initially, cavitation bubbles are formed, which are convected with the flow and implode in the region where pressure has recovered. When cavitation bubbles coalesce, they form quasi-stable, attached vapour cavities. This is referred to as 'sheet cavitation'. However, as the cavities grow longer, they get *destabilised* and detached leading to periodic cavity shedding. The detachment and shedding of the cavity is termed as 'cloud cavitation' (Knapp, 1958). The shed cavity convects and implodes in a high-pressure region, emanating pressure waves (Reisman et al., 1998). This inherently unstable form of cavitation is commonly called *partial cavitation*. The violent cloud collapse is an important feature of partial cavitation, which can often lead to deleterious effects such as noise, erosion-wear and even failures. For instance, it can cause severe pitting erosion-wear on the surface of the ship propeller, pump impeller, and dam spillways affecting their performance and reliability (see figure 1.2).

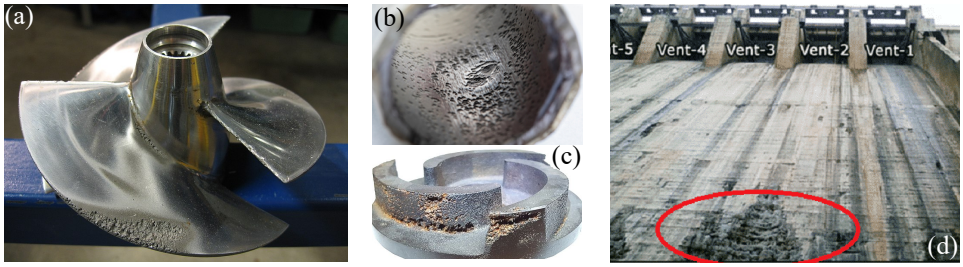

Figure 1.2: Pitting erosion-wear effects of cavitation due to the violent cloud collapse: (a) ship propeller (Asnaghi, 2015), (b) throttle valve (taken from tameson.com, the image is made available by Scott Louis Simonson), (c) pump impeller (Pokharel et al., 2022), (d) dam-spillway erosion encircled in red (Mittapalli, 2015).

The intensity of cavitation is usually described by the cavitation number (σ, defined in equation 4.1), where P and U are flow pressure and velocity, ρ is the mass density, and P_v is the vapour pressure. Physically, this parameter indicates the proximity of the flow pressure to the vapour pressure. Hence, a lower cavitation number denotes more intense cavitation and vice versa. Typically $\sigma \gg 1$ represents a non-cavitating flow. The onset of cavitation bubbles occurs as σ is reduced to unity.

$$\sigma = \frac{P - P_v}{\frac{1}{2}\rho U^2} \tag{1.1}$$

Partial cavitation has been studied in various canonical flow geometries: external flows include flow over wedges (Ganesh et al., 2016, Laberteaux and Ceccio, 2001b) and hydrofoils (De Lange and De Bruin, 1997, Foeth et al., 2006, Dular et al., 2005), while internal flows include 2-D nozzles and venturis (Gopalan and Katz, 2000, Jahangir et al., 2018) and orifices (Stanley et al., 2014). However, the exact physics underlying the cavity destabilisation/detachment process remains unclear. Furthermore, the influence of flow ge-

ometry on the cavity destabilisation phenomenon is unexplored, which precludes translating results across the different flow geometries. This know-how is crucial for understanding partial cavitation and controlling its effects.

1.2.1. SHEET TO CLOUD CAVITATION

The detachment of attached cavities to form cavitation clouds is at the heart of partial cavitation and is referred to as *sheet-to-cloud cavitation* as shown in figure 1.3. To understand this phenomenon, it is critical to understand the underlying cavity destabilising mechanisms. Classically, a periodic *re-entrant jet* travelling below the vapour cavity was considered solely responsible for periodic cloud shedding (Callenaere et al., 2001; Kawanami et al., 1997; Knapp, 1958). However, recent experimental studies (Ganesh et al., 2016) and supporting numerical studies (Bhatt and Mahesh, 2020; Budich et al., 2018) have unveiled that a periodic *bubbly shock front* emanating from the periodic cloud collapse can also cause periodic cloud shedding. Since then, bubbly shock waves characterised by a sharp vapour fraction discontinuity have been identified in various other experimental studies (Jahangir et al., 2018, Wu, Ganesh, and Ceccio, 2019). Further, it has been established that the re-entrant jets exist at (relatively) high σ, while the condensation shock fronts exist at low σ (Ganesh et al., 2016; Jahangir et al., 2018). More recently, Gawandalkar and Poelma (2022) and Bhatt et al. (2023) showed that both mechanisms could coexist in both regimes, i.e. a re-entrant jet is present at lower σ and a pressure wave due to the cloud implosion exists at higher σ. However, one mechanism prevails over the other, setting the cloud shedding frequency. The main question *'Why does the shedding mechanism change from one to another?'* remains unresolved. Although these two mechanisms are fundamentally very distinct, they operate at a similar (but distinct) shedding frequency. Thus, it is important to study the dynamics of these two shedding mechanisms in detail apart from mere global parameters, such as shedding frequencies.

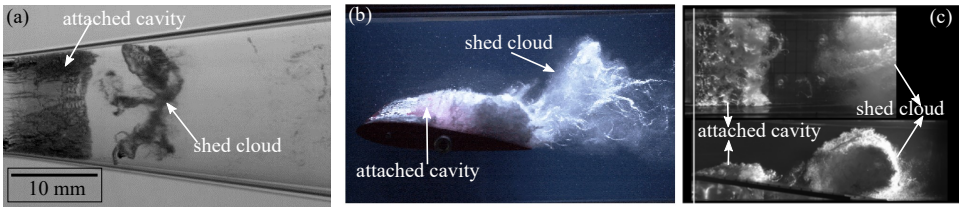

Figure 1.3: (a) High-speed images of the sheet to cloud cavitation in an axisymmetric venturi (black shows vapour, while light grey shows the liquid). The images have been taken during the study of Gawandalkar and Poelma, 2022. (b) Partial cavitation over a hydrofoil (Arndt et al., 2000, the vapour is shown in white colour). (c) Partial cavitation over a 2-D wedge (Ganesh et al., 2016), black shows the liquid, while white shows vapour). The bulk flow is from left to right in all the cases.

The origin of the bubbly shock fronts also remains disputed: The numerical simulations of Budich et al. (2018) suggested that cloud collapse is not a necessary condition for a bubbly shock front. Rather, it was suggested that the adverse pressure gradient is a sufficient condition for shock formation. Alluding to this, Large Eddy Simulations (LES) of Trummler et al. (2020) proposed that the re-entrant jet gets converted into the bubbly/condensation shock front. Zhang et al. (2022) asserted that pressure waves can

detach the growing cavity without an *obvious* vapour fraction discontinuity. Therefore, the interaction of the pressure wave emanating from the cloud implosion with the attached vapour cavity needs further investigation. The above conflicting hypotheses also suggest that there is a lack of consensus on the phenomenological description of the cavity detachment processes. This exemplifies our incomplete understanding of partial cavitation.

1.2.2. CHALLENGES

The gap in the knowledge can majorly be attributed to the difficulty in getting quantitative insights into the dynamics of such flows occurring at various length and time scales. Bubbly flows, in general, are optically inaccessible due to the strong glaring and occlusion brought about by opaque and reflecting vapour cavities, respectively (Poelma, 2020). Due to the complex multiphase dynamics, quantifying various flow quantities such as velocity fields, density fields (vapour/void fraction), and pressure is essential to decipher the exact flow physics.

Furthermore, the underlying mechanisms are cumbersome to resolve experimentally: The re-entrant jet has a complicated geometry, i.e. it exists as a thin liquid film close to the wall (Dular et al., 2005; Foeth et al., 2006). The strongly reflecting nature of the vapour cavity (intense glaring) impedes simple light-based measurements of the re-entrant jet. The bubbly shock wave renders measurement of density fields and compressibility effects (static pressure, Mach number) crucial, which is experimentally challenging. The existing optical imaging and whole-field flow measurement techniques like particle image velocimetry (PIV), and laser-induced fluorescence (LIF) are insufficient to probe the dynamics of such flows. Further, single-point measurement techniques such as electrical impedance and optical probes (Barre et al., 2009; Pham et al., 1999) provide limited information about the cavitation flow.

Numerical studies, on the other hand, are unable to resolve the fundamental flow phenomenon (re-entrant jets and condensation shocks) robustly due to the extent of scales (both spatial and temporal) involved in the flow (Ghahramani et al., 2019; Mahesh, 2022). Further, the complexity of the flow, i.e. accounting for the presence of vapour cavity, phase transitions, turbulence, and even shock waves is a challenging task (Madabhushi and Mahesh, 2023). This, along with high computational cost makes high-fidelity numerical simulations, like large eddy simulations (LES) and direct numerical simulations (DNS) of such flows scarce.

1.2.3. SCOPE OF THIS STUDY

In chapters 2 and 3 of the present study, partial cavitation is studied in a canonical flow geometry; an *axisymmetric venturi* (see figure 1.4). This flow geometry allows us to build on the qualitative insights from the previous studies of Jahangir et al. (2018). Further, it allows us to study cavitation dynamics for a large range of cavitation numbers ($\sigma = \frac{P-P_v}{\frac{1}{2}\rho U_t^2}$, see figure 1.4 for the definition of symbols) to probe into the cavity destabilisation/detachment phenomenon.

We study the underlying shedding mechanisms in detail: the re-entrant jet and the bubbly shock fronts using measurement techniques that can circumvent/overcome the optical opaqueness of the bubbly cavitating flow (explained in section 1.4). The velocity

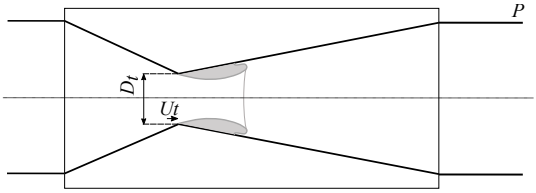

Figure 1.4: A schematic of partial cavitation in an axisymmetric venturi used in Gawandalkar and Poelma (2022). P is measured at the wall far downstream of venturi, U_t is the throat velocity and D_t is the throat diameter.

field of the re-entrant jet is measured directly using tomographic PIV. The density fields, measured using X-ray densitometry, in combination with pressure measurements, allow us to characterise the bubbly shock waves. The insights gained help us to address the research objectives listed in section 1.5.

1.3. VENTILATED CAVITIES

The entertainment of gas into the liquid flow to form an *artificial* gas cavity is referred to as ventilation (Semenenko, 2001). The ventilated cavities are generally formed by injecting non-condensable gas behind a flow separating bodies, a.k.a. 'cavitators'. Despite the fundamental difference between the ventilated cavities (*air-filled*) and natural cavities (*vapour-filled*) described in section 1.2, these flows share multiple similarities, such as the entrainment and shedding/ejection of vapour/gas, the existence of re-entrant jets and multiphase effects. Thus, studying ventilated cavities alongside natural cavities can be mutually beneficial for the understanding of both flows.

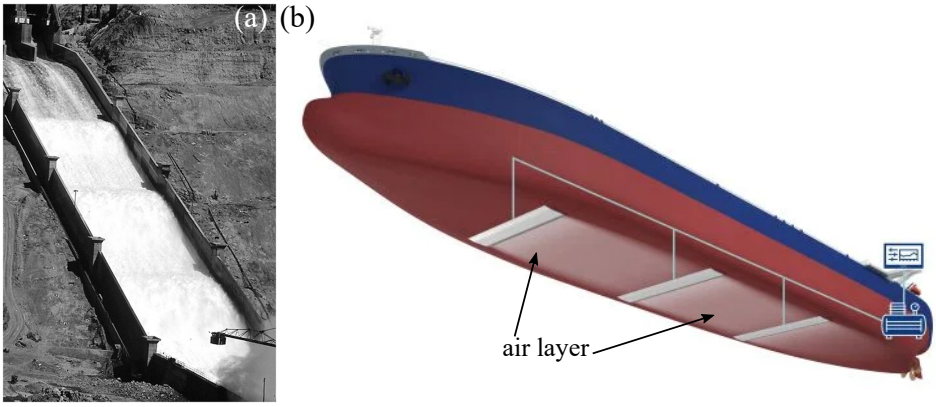

Figure 1.5: (a) Aerated dam spill-ways in operation (Pfister et al., 2011), (b) air layer drag reduction on a ship hull developed by Alfa Laval (image taken from alfalaval.com).

Further, ventilation has the potential to minimise the deleterious effects of partial (cloud) cavitation (Young et al., 2017). As mentioned earlier, aeration in dam spillways and ship propellers can reduce the cavitation wear on the concrete walls and propeller

blades, respectively (see figure 1.5). The gas injection in partial cavities (Tomov et al., 2016, Mäkiharju et al., 2017a) has shown that the cavitation behaviour can be modified significantly. Mäkiharju et al. (2017b) reported that vapour formation and bubbly shock characteristics can be altered by ventilation. Ventilation can make the bubbly mixture less susceptible to condensation shocks by elevating pressure in the cavities, making them 'less compressible' than pure vapour cavities. Further, ventilation can arrest cloud shedding and the associated harmful effects.

Most importantly, large ventilated cavities, a.k.a. supercavities have also found application in drag reduction in maritime transportation (Arndt et al., 2009, Ceccio, 2010). For instance, air can be injected on the ship hull to reduce skin friction drag for energy-efficient transportation (Nikolaidou et al., 2022; Zverkhovskyi, 2014) (see figure 1.5b). The air injection can achieve 95% drag reduction with 20% net energy saving (Mäkiharju, Perlin, and Ceccio, 2013). However, how to keep the gas locked in to form a stable ventilated cavity is an overarching engineering question for such applications. This requires a fundamental understanding of ventilated cavity dynamics, especially the cavity formation and gas ejection dynamics at the cavity closure region (see figure 1.6).

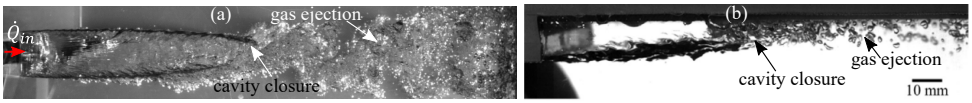

Figure 1.6: (a) High-speed image of a ventilated cavity in the wake of 2-D wedge showing cavity closure, taken from chapter 4 in this dissertation. The bulk flow and ventilation direction are shown by red arrows. (b) Ventilated cavity behind a backward-facing step in Qin et al. (2019).

1.3.1. GAS ENTRAINMENT AND EJECTION

The injected gas is entrained to form a ventilated cavity, while some gas is ejected out of the cavity. Typical examples of ventilated cavities are shown in figure 1.6. The dynamics of gas entrainment and ejection are seen to occur at the *cavity closure region* (Semenenko, 2001). The characteristics of the closure govern the rate of gas ejection out of the cavity, which in turn dictates the stability and the geometry of the cavity. Therefore, it is important to study the types of cavity closures and the flow conditions at which each type of closure exists.

Distinct cavity closures are observed for different cavitator geometries. Most of the previous studies deal with a 3-D cavitator (Arndt et al., 2009, Lee and Arndt, 2013, Karn et al., 2016), or wall-bounded cavitator (Barbaca et al., 2017; Mäkiharju, Elbing, et al., 2013; Qin et al., 2019), with less attention to 2-D bluff body cavitators. For instance, cavitators employed for bubble-drag-reduction systems in ships are quasi-2D. Thus, it is important to study 2-D ventilated cavities. The quantification of gas ejection rates is essential in formulating empirical models to predict the ventilation demands for different flow conditions and closures. However, the quantification of gas ejection out of the cavity remains unexplored due to various reasons, such as the lack of accurate void (gas) fraction distribution data in the flow. Further, existing studies are dedicated to studying and characterising the closure of stable (fixed-length) cavities. Examining the gas ejection during the formation of a cavity could provide much better estimates of ventilation

demands.

Furthermore, due to the complex multiphase flow interaction (gas-liquid), a gap also exists between model trials (large scale) and laboratory experiments (relatively small scales) in the drag reduction and energy savings achieved. It is observed that there is a discrepancy between the amount of gas required to *establish* a cavity and *maintain* a cavity (Kawakami and Arndt, 2011; Mäkiharju, Elbing, et al., 2013). However, the physics underlying this observation remains unexplained. A thorough understanding of the cavity closure region during its formation and in its stable state can help us address the question: *Why is the amount of gas required to maintain a cavity less than the amount of gas required to form a cavity?*.

1.3.2. CHALLENGES

The cavity closure region is extremely complex, i.e. turbulent, frothy, and optically opaque as shown in figure 1.6. Thus, conventional laser-based measurement techniques cannot provide quantitative insights, especially at the liquid-gas-liquid interface and cavity closure, critical for understanding entrainment-leakage physics (Wosnik and Arndt, 2013; Yoon et al., 2020). Digital inline holography (Shao et al., 2022) can provide information on instantaneous gas leakage, albeit the internal flow in the cavity remains inaccessible. The void fraction (density) fields are necessary to visualise the gas-liquid dynamics and estimate the gas entrainment/leakage rates. However, such density measurements are rarely available. Furthermore, numerical simulations can predict the cavity geometry with fair accuracy, yet the gas-liquid interface and cavity closure can not be well resolved. High-fidelity numerical simulations like DNS suffer due to large density ratios (in the phases) and turbulent motions with a wide range of scales in such flows. For instance, the only DNS study of ventilated cavities is limited to a low Reynolds number (Liu et al., 2023). Thus, a non-invasive whole-field measurement technique capable of seeing through the optical opaqueness and distinguishing the gas-liquid phase is indispensable.

1.3.3. SCOPE OF THIS STUDY

In chapter 4 of this dissertation, we will focus on ventilated cavities in the wake of a 2-D wedge (see figure 1.7). The cavities are governed by a few non-dimensional parameters

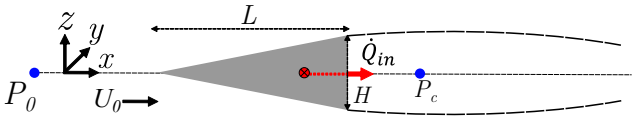

Figure 1.7: A schematic of the ventilated cavity behind a 2-D wedge used in chapter 4 of this dissertation. P_0, U_0 are the incoming pressure and velocity, P_c is the cavity pressure, $\dot{Q}_{in}$ is the gas injection rate, and L, W, H are wedge dimensions.

given by the Froude number (Fr), ventilation coefficient (C_{qs}), cavitation number (σ_c), and Reynolds number (Re_H), as defined by equation 1.2 (see figure 1.7 for definitions). The ratio of Fr to Re_H is fixed by the virtue of flow geometry and working fluid. Fr refers to the importance to flow inertia over the buoyancy of the entrained gas (gas cavity), C_{qs} refers to the gas injection volume flux with respect to volumetric liquid flux, while

σ_c is the non-dimensional pressure inside the cavity. It is important to note that σ_c is synonymous with σ (see equation 4.1) defined for natural cavitation flows.

$$Fr = \frac{U_0}{\sqrt{gH}} \quad C_{qs} = \frac{\dot{Q}}{U_0 HW} \quad \sigma_c = \frac{P_0 - P_c}{\frac{1}{2}\rho U_0^2} \quad Re_H \approx 8200 Fr \tag{1.2}$$

The ventilated cavities are created by systematically varying Fr and C_{qs}. The cavity dynamics are investigated with X-ray densitometry (elaborated in subsection 1.4) that can circumvent the issues of flow opacity. The density fields allow us to distinguish between gas and liquid phases with excellent spatial and temporal resolution. The cavity formation dynamics are observed and gas ejection rates are quantified. The acumen gained helps us address the research objectives listed in section 1.5.

1.4. FLOW DIAGNOSTIC TECHNIQUES

Based on the challenges identified in subsections 1.2.2, 1.3.2, it is clear that we need a non-invasive whole-field measurement technique capable of seeing through the optical opaqueness manifested by the liquid-vapour and liquid-gas bubbly mixture in natural and ventilated cavities respectively. Due to the extent of scales involved, sufficient spatial and temporal resolution is desirable. This dissertation is a part of the ERC-COG 'OpaqueFlows' project, which relies on non-conventional measurement modalities to (i) gain insights into the dynamics of optically-opaque flows, and (ii) generate a quality dataset for modelling such complex flows. The following section briefly describes the flow measurement modalities employed in this dissertation.

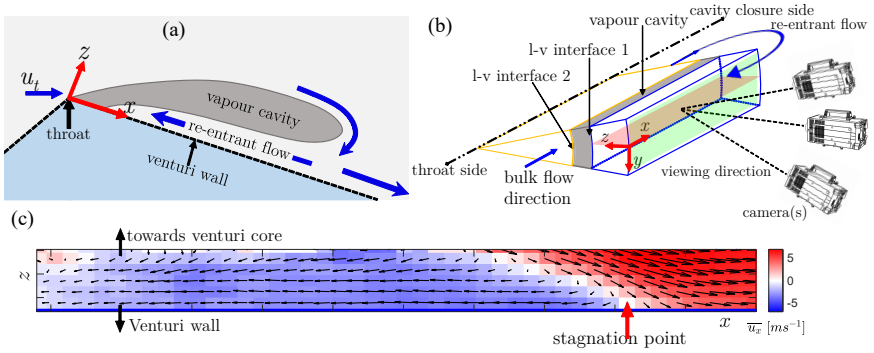

Figure 1.8: A schematic of (a) near wall re-entrant flow (only the half of venturi is shown), (b) tomographic imaging approach used to image the re-entrant flow (not to scale), (c) a sample re-entrant flow velocity field (reproduced from Gawandalkar and Poelma (2022)).

1.4.1. TOMO-IMAGING AND VELOCIMETRY WITH FLUORESCENT TRACERS

The topology of the re-entrant flow in a cavitating venturi makes the whole-field optical measurement challenging. The optical access to the re-entrant flow is achieved from the front side (see viewing direction in figure 1.8b). This is facilitated by the axisymmetry of the venturi. Hence, a slender measurement volume is chosen, extending in the

x-direction and relatively short in the y and z-direction. The extent of the z-direction is dictated by the re-entrant flow thickness. The flow is seeded with fluorescent tracer particles and illuminated with green laser light (Deen et al., 2002). These particles absorb green light and reflect orange light. The optical filter on the camera eliminates spurious reflections/glare arising from green light. Thus, tracer particles in the re-entrant jet are imaged against the backdrop of the vapour cavity in three different views as shown in figure 1.8b. These views are used to tomographically reconstruct the particle image intensities in the liquid re-entrant jet in 3-D. Thus, the re-entrant jet is resolved spatially and temporally in chapter 2, as shown in figure 1.8c.

1.4.2. X-RAY DENSITOMETRY

X-ray densitometry is a non-invasive, radiation-based flow modality that can overcome the flow visualisation challenges encountered in bubbly flows, i.e. occlusion, glaring and optical opaqueness. It is absorption-based, i.e. attenuation of the X-ray intensity is a function of the mass density of the matter it passes through, governed by Beer-Lambert's principle (Aliseda and Heindel, 2021). Further X-rays do not refract significantly as the refractive index is very close to 1. This makes it an ideal tool to probe into two-phase flows where the densities are separated by orders of magnitude, such as natural (liquid/vapour) and ventilated cavity (liquid/gas) flows. Further, it provides time-resolved whole-field vapour/void fraction (density) fields necessary to resolve flow dynamics at different spatial and temporal scales. This is demonstrated in figure 1.9. For instance, 1.9a and c show how X-ray densitometry can overcome the opacity of bubbly flows to reveal unique flow features like the re-entrant jets in the ventilated cavity (indicated by a yellow arrow in figure 1.9a) and condensation shock fronts (indicated by a red arrow in figure 1.9c) during periodic cloud shedding in partial cavitation. Moreover, the unique density dataset is valuable for validating and tuning numerical models for such flows. However, X-ray densitometry systems remain accessible to a few research groups (Stutz and Reboud, 1997, Mäkiharju, Gabillet, et al., 2013, Mitroglou et al., 2016, Zhang, Khlifa, and Coutier-Delgosha, 2020, Jahangir et al., 2019) due to stringent safety protocols and costs involved.

In this dissertation (chapters 3 and 4), 2-D void fraction fields of bubbly flows are measured with X-ray-based densitometry systems. Although it measures a span-averaged void fraction, the essential dynamics are well visualised and resolved. Some unique insights into the dynamics of cavitating flows are generated with time-resolved density (void/vapour fraction) measurements, which remain inaccessible to conventional flow measurement techniques. This helps deepen our understanding of partial cavitation and ventilated cavity flows.

1.5. RESEARCH OBJECTIVES

This dissertation aims to generate a fundamental understanding of *optically opaque flows*. Two canonical flow cases were selected: partial cavitation in an axisymmetric venturi and ventilated cavity flows in the wake of a 2-D bluff body.

One of the main objectives of this research is to further our current understanding of the partial cavitation phenomenon by generating *quantitative* insights into the shed-

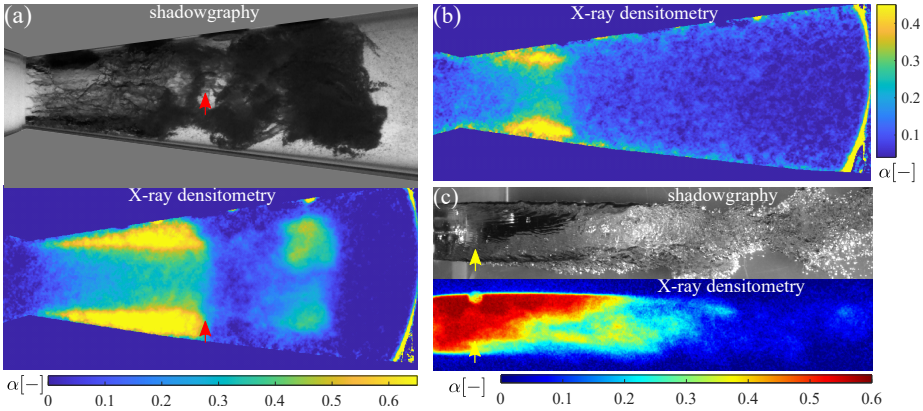

Figure 1.9: High-speed optical visualisation vs densitometry: (a) Comparison of high-speed flow visualisation with X-ray imaging for a case of a condensation shock front marked by a red arrow, (b) X-ray image of a cloud roll-up due to re-entrant jet pinching the cavity, (c) comparison of high-speed visualisation with X-ray imaging for a case of a ventilated cavity with re-entrant jet (yellow arrow shows the re-entrant jet front).

ding mechanisms responsible for cavity detachment, namely (i) re-entrant jet, and (ii) bubbly shock wave. The acumen gained from these two studies is used to answer the overarching question:

Why does the shedding mechanism change from re-entrant jet to condensation shock and vice-versa?

To answer this question, we pose a few sub-questions:

- How can we overcome optical opaqueness to perform a whole-field velocity measurement of the re-entrant jet in partial cavitation?
- What are the characteristics and the role of the re-entrant jet in cavity shedding at different σ?
- What are the characteristics of the pressure wave and shock fronts at different σ?
- How does the pressure wave interact with the attached vapour cavity at different σ?

The dynamics of the re-entrant jet and bubbly shock waves will be visualised at different flow conditions (cavitation numbers, σ, see table 3.1). Various flow parameters: velocity, pressure, vapour fractions are measured using different measurement techniques. This helps us to characterise the strength of the re-entrant jet and bubbly shock waves. With this and a simple model, we propose a modified phenomenological description of cavitation dynamics. This helps to explain the transition of the shedding mechanism from a re-entrant jet to bubbly shock waves.

The second objective of this dissertation is to investigate ventilated cavities. Ventilated cavities are fundamentally different from natural cavities. However, they share similar underlying physics, such as the existence of re-entrant jets due to multiphase

Table 1.1: Experimental parameters (see figure 1.4 for the definitions)

Parameter	Definition	Value
throat diameter	D_t	16.67 mm
cavitation number	$\sigma = (P - P_v)/\frac{1}{2}\rho U_t^2$	0.39-1.1
Reynolds number	$Re_t = U_t D_t/\nu$	1.86-2.3 × 10^5

interaction, entrainment and shedding/ejection of vapour/gas. Hence, ventilated cavities are examined alongside natural cavities in this dissertation. The ventilated cavities will be studied in the wake of the 2-D wedge with emphasis on the cavity closure region. Various aspects of the cavities such as geometry, pressure, gas ejection mechanism, and cavity closure formation hysteresis will be characterised. The formation of cavities will be studied at different flow conditions and gas ejection rates will be estimated using a simple control volume approach via measured void fraction distribution. The insight gained will be used to address the open question:

Why is the amount of gas required to maintain the cavity less than the amount of gas required to form the cavity?

To answer this question, a few sub-questions are posed:

- What are the types of cavity closures exhibited by the ventilated cavities and at what flow conditions?
- Does the cavity closure exhibit hysteresis with respect to gas injection?
- What are the gas ejection mechanisms gas ejection rate for different closures?
- What are the characteristics of cavity closures during its formation?

The cavities are established by two different methodologies: (i) increasing the ventilation to achieve a given C_{qs}, (ii) decreasing ventilation to achieve a given C_{qs}. A large number of experiments are performed by independently varying flow inertia (Fr) and ventilation (C_{qs}) (see table 1.2) to create flow regime maps based on the closures. The dynamics of cavity formation are quantitatively studied with time-resolved X-ray densitometry to estimate gas leakage rates.

Table 1.2: Experimental Parameters (see figure 1.7 for the definitions)

Parameter	Definition	Value
Wedge dimensions	$L \times W \times H$	72×76×19 mm^3
Froude Number	$Fr = U_0/\sqrt{gH}$	2 - 13.9
Ventilation coefficient	$C_{qs} = \dot{Q}/U_0 HW$	0.03-0.13
Cavity under-pressure (cavitation number)	$\sigma_c = (P_0 - P_c)/\frac{1}{2}\rho U_0^2$	0.8-3.5
Reynolds number	$Re_H = U_0 H/\nu$	15960-115900

Finally, this dissertation also intends to generate quantitative datasets. Most importantly, the unique time-resolved vapour/void fraction dataset in the context of (i) partial cavitation in the venturi, and (ii) ventilated cavitation in the wake of a 2-D wedge is made

available for future use. Such experimental datasets can be valuable for validating and constructing new numerical models aimed at simulating complex, multi-scale bubbly flows. Further, it can also be useful for the development of measurement techniques, such as Magnetic Resonance imaging, applied to bubbly flows.

1.6. STRUCTURE OF THIS DISSERTATION

Chapter 2 exploits the flow geometry of the re-entrant jet to tomographically quantify its velocity and thickness. The re-entrant jet dynamics at high and low σ are observed to assess its contribution to cloud shedding. It is observed that the re-entrant jet is present at all considered σ, however, it can cause cavity detachment only at higher σ. At a lower σ, a propagating velocity discontinuity is seen to travel towards the throat. This bubbly shock front signature is responsible for cavity detachment at lower σ.

Chapter 3 focuses on the bubbly shock-driven cloud cavitation. The condensation shock waves are characterised with time-resolved X-ray densitometry in combination with high-frequency dynamic pressure and static pressure measurements. The X-ray densitometry overcomes the optical opaqueness of the flow to reveal the interaction of the pressure wave with the attached vapour cavity, while also enabling quantification of the vapour fraction and shock speed for a range of σ. The Mach number of the pressure wave travelling through the bubbly mixture is seen to dictate whether the pressure wave changes to a condensation shock front as it propagates upstream for a range of σ. It is seen that the converging geometry of the venturi can strengthen the pressure wave, favouring cavity condensation. If the cavity condensation is not favoured, the re-entrant jet is seen to cause the cavity detachment. Chapters 2 and 3 collectively show that the re-entrant jet takes over as a shedding mechanism when the pressure wave is too weak to change to the condensation shock front. With this, we address the first research question *'Why does the shedding mechanism change from re-entrant jet to condensation shock wave?'*.

In Chapter 4, ventilated cavities are studied in the wake of a 2-D bluff body via high-speed X-ray densitometry. A regime map based on four different cavity closure types is established based on more than fifty independent experiments. The flow conditions and topology for each type of cavity are discussed. This is followed by a thorough analysis of gas ejection mechanisms, including the quantification of gas ejection rates. Broadly, the cavity assumes two types of closures, i.e. with wave-type instability, and with a re-entrant jet. The presence of a re-entrant jet at the closure is seen to result in a significant gas ejection which is responsible for hysteresis in cavity closure formation. With this, we address the second research question *'Why is the amount of gas required to maintain the cavity lesser than the amount of gas required to form the cavity?'*.

The conclusions from this study are presented in chapter 5. This is followed by an outlook on future perspectives and open questions.

2

THE STRUCTURE OF NEAR-WALL RE-ENTRANT FLOW

The so-called 're-entrant jet' is fundamental to periodic cloud shedding in partial cavitation. However, the exact physical mechanism governing this phenomenon remains ambiguous. The complicated topology of the re-entrant flow renders whole-field, detailed measurement of the re-entrant flow cumbersome. Hence, most studies in the past have derived a physical understanding of this phenomenon from qualitative analyses of the re-entrant jet. In this chapter, we present a methodology to experimentally measure the re-entrant flow below the vapour cavity in an axisymmetric venturi. The axisymmetry of the flow geometry is exploited to image tracer particles in the near-wall re-entrant flow. The main objective of employing tomographic particle image velocimetry is to resolve the thickness and the velocity of the re-entrant flow. Additionally, phase-averaging conditioned on cavity length sheds light on the temporal evolution of re-entrant flow in a shedding cycle. The measured re-entrant film is as thick as ~ 1.2 *mm for a maximum cavity length of* $\sim 0.9D_t$*, where* D_t *is the venturi throat diameter. However, the re-entrant film thickness at a higher cavitation number is measured to be about 0.5 mm. Further, the re-entrant flow is seen to attain a maximum velocity up to half the throat velocity as the vapour cavity grows in time and the re-entrant flow thickens. We observe that the thickness of the re-entrant liquid film w.r.t. the cavity thickness can influence the cavity shedding behaviour. Further, a complex spatio-temporal evolution of re-entrant flow is involved in cavity detachment and periodic cloud shedding. Finally, we apply the demonstrated methodology to study the evolution of the near-wall liquid flow, below the vapour cavity in three different cavity shedding flow regimes. The role of two main mechanisms responsible for cloud shedding, i.e. (i) the adverse-pressure gradient driven re-entrant jet, and (ii) the bubbly shock wave emanating from the cloud collapse are quantitatively assessed. Further, we show that both the mechanisms could be operating at a given flow condition, with one of them dominating to dictate the cloud shedding behaviour.*

This chapter is based on: Gawandalkar, U.U., Poelma, C. (2022). *The structure of near-wall re-entrant flow and its influence on cloud cavitation instability,* Experiments in Fluids **63**(5), 1-19.

2.1. INTRODUCTION

Hydrodynamic cavitation is a phase change from liquid to vapour when the local pressure in the flow drops below the vapour pressure. Cavitation often occurs in turbomachinery and hydraulic equipment, such as ship propellers, pump impellers (Kuiper, 1997), and even in diesel injectors (Giannadakis et al., 2008). Partial cavitation is a common form of cavitation that is characterised by unstable vapour cavities, which are intermittently shed. The larger vapour cavities are often shed periodically, resulting in cloud cavitation. This cloud cavitation is known to cause detrimental effects like erosion wear, material fatigue, noise and vibration due to unsteady loads, which can all affect reliability and the lifetime of the equipment (Brennen, 1995). On the other hand, cavitation also finds beneficial applications in the pre-treatment of biomass (Nakashima et al., 2016), water disinfection (Jyoti and Pandit, 2004) and other chemical processes. Hence, understanding the fundamentals of cloud cavitation is imperative to manipulate its effects.

The 're-entrant jet' travelling beneath the vapour cavity is crucial for understanding periodic cloud shedding (Knapp, 1958). The topology of the re-entrant flow is such that it exists as a thin liquid film wedged between the solid boundary and vapour cavity (see figure 2.1). Classically, it is assumed to be periodically generated at the cavity closure region when the vapour cavity has assumed its maximum length in a shedding cycle (Furness and Hutton, 1975). It then travels upstream, i.e. opposite to the bulk flow direction, with a velocity of similar magnitude as the bulk velocity until it triggers cavity detachment. This detached cloud travels downstream and collapses in the region where pressure has recovered. At the same time, a new vapour cavity starts growing. Several experimental and numerical studies have explored the role of the re-entrant jet in cloud cavitation in a variety of cavitating flows. The external flows include flow over wedges (Lush and Skipp, 1986, Ganesh et al., 2016, Stutz and Reboud, 1997, Laberteaux and Ceccio, 2001b, Gnanaskandan and Mahesh, 2016a), hydrofoils (De Lange and De Bruin, 1997, Saito et al., 2007, Kubota et al., 1989, Foeth et al., 2006, Dular et al., 2005, Pham et al., 1999, Kawanami et al., 1997), divergent steps (Callenaere et al., 2001, Trummler et al., 2020), while internal flows include 2D nozzles (Furness and Hutton, 1975, Pelz et al., 2017), venturis (Gopalan and Katz, 2000, Barre et al., 2009, Jahangir et al., 2018), and orifices (Stanley et al., 2014). However, the exact physical mechanism responsible for the formation of a jet and its role in cloud cavitation instability remains unclear.

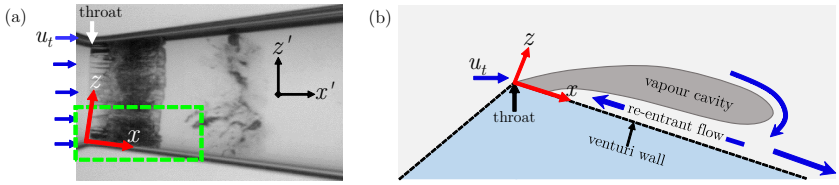

Figure 2.1: (a) A shadowgraph of a cavitating venturi, dark and light regions indicate vapour and liquid phase, respectively; (b) Schematic zoomed-in view of the vapour cavity and the re-entrant flow corresponding to the mid-plane in the green dashed box. The bulk flow is from left to right. Note the different coordinate systems: $x-z$ is aligned with the venturi wall, while $x'-z'$ is the laboratory reference frame.

Several studies highlight the conditions necessary for the generation of the re-entrant jet and the cloud cavitation instability. Callenaere et al. (2001) systematically varied

the adverse pressure gradient to establish that a pressure gradient in the cavity closure region is necessary for the cavitation instability to occur, i.e. transition from stable sheet cavity to periodic cloud cavitation. Franc (2001), Gopalan and Katz (2000), and Laberteaux and Ceccio (2001b) also asserted that the pressure gradient below the vapour cavity was a function of the cavity closure position, i.e. cavity length. Hence, the presence of a re-entrant jet was seen to be dependent on the cavity length. Further, Coutier-Delgosha et al. (2007) found that the delay between the inception of the re-entrant jet and cavity break-off is nearly constant, suggesting that cloud detachment depends only on the jet velocity, without any influence of cloud collapse. Hence, the correlation between adverse pressure gradient and the re-entrant jet development was established. Furthermore, Le (1993), using dye injection and high-speed visualisations, observed that dye injected near the cavity closure made its way to the leading edge of the hydrofoil in a cyclic manner. Kawanami et al. (1997) also performed experiments with a hydrofoil where an obstacle was placed to block the re-entrant jet. It was observed that blocking the re-entrant jet stopped cloud shedding, resulting in a frothy vapour mixture. Thus, the periodic nature of the re-entrant jet and its role in periodic cloud shedding was hypothesised (Pham et al., 1999, De Lange and De Bruin, 1997).

On the other hand, Leroux et al. (2004) performed wall pressure measurements on a hydrofoil and observed intense pressure pulse near the cavity closure region. This was attributed to the shockwave produced by the collapse of the previously shed cloud. Thus, it was speculated that cavity destabilisation and shedding were perhaps due to the interaction of the re-entrant jet and the shock wave. Further, Stanley et al. (2014) proposed that the flow re-attachment in the cavity closure region provides a transient pulse of momentum that drives the re-entrant liquid flow. In addition, a pressure pulse created by cloud collapse creates a reverse flow of larger velocity. Both effects combine to produce a periodic travelling wave of constant velocity, leading to cloud cavitation. This was corroborated by Large Eddy Simulations of Trummler et al. (2020), who also proposed that flow reversal is correlated to the pressure peaks observed in the downstream region of the step nozzle. Consequently, there is no consensus on the physical mechanism driving the re-entrant jet initiated cloud shedding.

It can be argued that the lack of consensus is due to the dearth of experimental data for near-wall liquid flow, below the vapour cavity. There have been previous attempts to measure the velocity of the re-entrant flow to understand the re-entrant flow driven cloud shedding. However, the flow geometry of re-entrant flow poses a major challenge in studying it experimentally and numerically. It occurs as a thin film close to the wall. Hence, most of the numerical models aimed at understanding global cavitation behaviour likely do not resolve it in sufficient detail (Brunhart et al., 2020). At the same time, whole-field laser-based optical measurement techniques such as particle image velocimetry (PIV), laser-induced fluorescence (LIF) are limited by strong reflections, occlusion of laser illumination and opacity due to the cavitation cloud (Poelma, 2020). Moreover, optical access below the vapour cavity in canonical 2D geometries such as 2-D wedges and venturis, hydrofoil is limited. Single point measurement techniques have been employed in the past to measure the velocity and thickness of the re-entrant jet beneath the cavity. Callenaere et al. (2001) measured the re-entrant flow thickness at a fixed point using an ultrasound probe for different cavitation conditions and reported that the

ratio of re-entrant flow thickness to vapour cavity thickness is an important parameter that governs the cavity shedding dynamics. Pham et al. (1999), using surface electrical impedance probes, measured the velocity of the re-entrant jet at various axial positions below the vapour cavity. They reported that the re-entrant flow velocity was of the same order as that of the free stream velocity. Further, Stutz and Reboud (1997) and Barre et al. (2009), using a double optical probe, reported a similar finding. They also asserted that the velocity of the jet was not constant.

Foeth et al. (2006) and Laberteaux and Ceccio (2001b) performed PIV measurements of the cavitating flow over a wedge and hydrofoil, respectively. However, near-wall velocity fields could not be measured beneath the vapour cavity and consequently in the re-entrant flow, due to strong reflections by the vapour cloud and the lack of optical access. Dular et al. (2005) also performed PIV-LIF measurements to study cavitation flow structures and found only a handful of vectors pointing in the reverse direction at the interface of the vapour cavity. The majority of studies rely on high-speed shadowgraphy to track bubbles in the re-entrant flow (Stanley et al., 2014), or they track the cavity deformations by the re-entrant flow (chaotic interface) to qualitatively infer the velocity of the re-entrant jet (Barbaca et al., 2019; Callenaere et al., 2001; Jahangir et al., 2018; Sakoda et al., 2001). Thus, direct and complete measurements of re-entrant flow have not been reported in the available literature.

In this chapter, we aim to provide quantitative information of re-entrant flow in a cavitation flow, to examine its role in periodic cloud shedding. Three modalities are used to unveil the re-entrant flow dynamics: high-speed shadowgraphy, tomographic imaging and planar PIV. Shadowgraphy, being qualitative, is ideal to study large-scale phenomena such as cavity front growth and cloud shedding. However, the underlying physics, such as the re-entrant jet dynamics, are quantitatively studied using velocimetry. We show that the axisymmetry of the venturi can be used to achieve direct optical access below the vapour cavity. The flow topology of the re-entrant flow is further exploited to implement tomographic imaging to evaluate the re-entrant flow thickness and velocity fields. This allows us to capture the spatio-temporal evolution of the re-entrant flow. Furthermore, it is demonstrated that the flow velocity of the thin liquid flow beneath the vapour cavity can also be reliably measured using planar PIV, if the flow thickness information is not needed. This not only helps in deepening our understanding of re-entrant jet initiated cloud shedding, but also provides acumen into the physics of other shedding behaviours such as re-entrant flow initiated aft cavity shedding and bubbly shock-driven cloud cavitation occurring in a cavitating venturi. The velocity data generated can further be used to validate numerical models aimed at capturing cavitation dynamics.

2.2. EXPERIMENTAL METHODOLOGY

2.2.1. FLOW FACILITY

The experiments are performed in the cavitation loop at the Laboratory for Aero and Hydrodynamics in Delft with water as a working fluid. The flow facility shown schematically in figure 2.2 has been described in detail in the previous work of Jahangir et al. (2018). Partial cavitation is realised at the throat of a venturi with a divergence angle of 8° and a throat diameter (D_t) of 16.67 mm. The cavitation behaviour in the venturi is governed

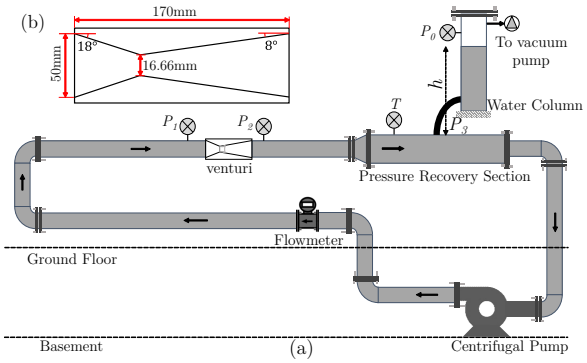

Figure 2.2: (a) A schematic of the cavitation loop in the Laboratory for Aero and Hydrodynamics, Delft. (b) The convergent-divergent axisymmetric venturi with geometric dimensions.

by the cavitation number, $\sigma = (P_3 - P_v)/(\frac{1}{2}\rho U_t^2)$, with P_v the vapour pressure and U_t the throat velocity. A lower σ corresponds to more aggressive cavitation and vice versa. The vacuum pump in the flow loop allows independent control of the global static pressure (P_0) aside from the flow velocity (U_t), thus providing a wider range of σ. Further, the shedding frequency (f) is expressed as a Strouhal number, $St_t = fD_t/U_t$. A study of global cavitation behaviour revealed that re-entrant jet-dominated cloud shedding occurs for: $0.95 \leq \sigma < 1$ (Jahangir et al., 2018). Hence, the experiments are performed for $\sigma \simeq 0.97$, a Reynolds number defined at the venturi throat $Re_t \sim 170{,}000$, and $St_t \simeq 0.22$ (shedding frequency of 133 Hz). The large-scale cavity shedding dynamics are visualised using high-speed shadowgraphy. The field of view (FOV) is centred along the venturi axis and spans 33 × 57 mm^2 in the $x' - z'$ plane. It is back-illuminated with a continuous white LED source. A high-speed CMOS camera (Photron Fastcam APX RS) equipped with an objective lens of 105 mm and aperture ($f^\#$) of 5.6 captures the contrast between the liquid (light) and vapour (dark) phase (see figure 2.1a). The images are acquired at a rate of 12,000 Hz with an exposure time of 1/12,000 seconds.

2.2.2. IMAGING APPROACH

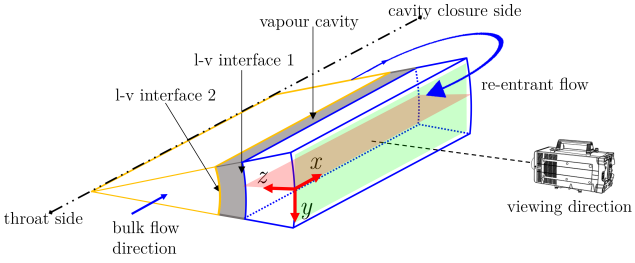

Figure 2.3: A schematic (not to scale) showing the measurement volume of the re-entrant liquid film, highlighted by the blue edges (the $x - z$ plane is shown in red). The grey volume is the vapour cavity, bound by the bulk flow (liquid) shown in yellow edges and the re-entrant jet. The respective liquid-vapour (l-v) interfaces are also indicated. The venturi wall is not shown but bounds the re-entrant jet on the camera side.

The topology of the re-entrant flow in a cavitating venturi makes its whole-field optical measurement challenging. Ideally, the re-entrant flow is measured in the mid-plane of the venturi (see figure 2.1a). However, the proximity of the flow close to the wall and the strongly reflecting nature of the vapour cavity results in particle image contamination due to intense glaring and reflections (Dular et al., 2005; Laberteaux and Ceccio, 2001a). Additionally, the opaque vapour cavity restricts optical access to the re-entrant flow (Foeth et al., 2006; Gopalan and Katz, 2000). To circumvent these issues, optical access to the re-entrant flow is achieved from the front side (see viewing direction in figure 2.3). This is facilitated by the axisymmetry of the venturi and time-averaged re-entrant flow attributes, such as the flow velocity and the thickness. Hence, a slender measurement volume is chosen, extending in the x-direction and relatively short in the y and z-direction. The extent of the z-direction is dictated by the re-entrant flow thickness, while the extent of y-direction is < 6% of the local circumference of the venturi. Thus, the choice of the FOV minimises the effect of the curvature of the venturi and optimises the image acquisition frequency to resolve essential flow dynamics.

Broadly, two imaging approaches are employed: Firstly, tomographic imaging of tracer particles is performed with multiple views followed by reconstruction of particles in the measurement volume (see volume indicated by blue boundaries in figure 2.3). We do not expect variation in the y-direction for the averaged behaviour, hence the y-direction is used as averaging direction. To achieve this, the reconstructed particle image intensities are projected on the $x-z$ plane. The velocity vector fields are also evaluated in this $x-z$ plane, shown in red. Thus, the re-entrant flow in front of the vapour cavity can be resolved. Secondly, in separate experiments, planar PIV is also performed on particle images in the $x-y$ plane. Here, the evaluated velocity fields are (inherently) averaged in z-direction, i.e. along the thickness of re-entrant flow.

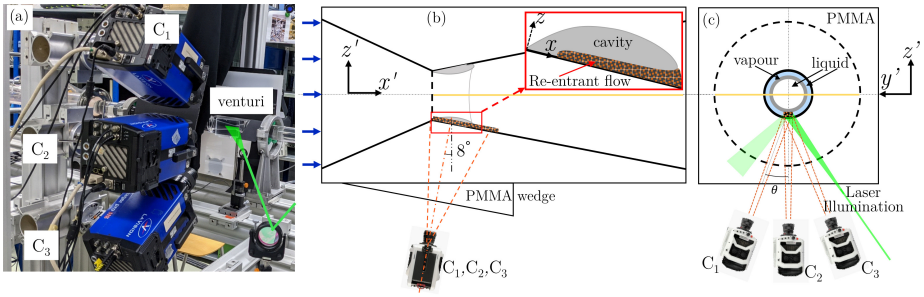

Figure 2.4: (a) Experimental setup for tomographic imaging. (b) Schematics of tomographic imaging setup in $x'-z'$ plane. The inset shows a zoomed-in view of re-entrant liquid film and vapour cavity in $x-z$ plane.The bulk flow is from left to right (c) $y'-z'$ plane shows the laser illumination.

2.2.3. TOMOGRAPHIC IMAGING

Tomographic imaging is performed with the objective of measuring the thickness and the velocity of the re-entrant flow. The axisymmetry of vapour cavity and re-entrant flow is exploited to gain optical access to the re-entrant jet, as shown in figure 2.3, and figure 2.4b,c. Three high-speed cameras (LaVision Imager HS 4M) equipped with an objec-

tive lens of 105 mm ($f^{\#}$ = 5.6) and high-pass optical filter (λ >590 nm) provide multiple imaging views. The spatial resolution of the image corresponds to approximately 0.038 mm per pixel. The cameras are arranged in a linear configuration ($\theta \simeq 27°$,0°, −27°) in the $y'-z'$ plane as shown in figure 2.4a,c. Such a configuration is chosen due to the elongated measurement volume. The cameras are mounted such that they make an angle of 8° in the $x'-z'$ plane to account for the divergence angle of venturi. This is complemented by a polymethylmethacrylate (PMMA) wedge of the same angle to reduce image distortion due to refraction at the outer surface of the venturi. Furthermore, scheimpflug adapters are used to align mid-planes of the illuminated area with the focal planes of the cameras.

The liquid flow is seeded with fluorescent tracer particles ('FLUOSTAR', acrylate resin particles coated with Rhodamine B, 13μm diameter) which absorb green light and emit orange light. The use of these orange fluorescent particles, in combination with a high-pass optical filter to block the green light of lower wavelength, eliminates the spurious reflections and glare arising from the vapour cavity. The volume illumination of particles is achieved by a Nd:YLF laser (25 mJ per pulse at 1 kHz and 527 nm wavelength, Litron Lasers) introduced from the front side of the venturi and diverged using a plano-concave lens as shown in figure 2.4a,c. Interestingly, the re-entrant flow is enclosed by the venturi wall and the vapour cavity. Hence, the measurement volume is naturally formed by venturi wall on one side and vapour cavity on the other (see inset in figure 2.4b). Thus, knife-edge filters are not required. The effective measurement volume spans ~ 24×3.2×2.8 mm^3. For each measurement, 20,000 images are acquired, at a rate of 17.9kHz to achieve the required particle image displacement (< 6 pixels). The geometric calibration approach is outlined in Appendix 2.A. Tap water is used as working fluid, which is expected to be saturated with cavitation nuclei. This implies that there are sufficient sites for cavitation to occur if the local hydrodynamics condition demands it, and adding (tracer) particles beyond this saturation level has no influence on the cavitation dynamics. To ensure this, St_t as a function of σ is examined before and after adding tracer particles at several global static pressures. The comparison showed good agreement (within the scatter of the data), hence the measurements are adjudged to be non-intrusive.

2.2.4. DATA PROCESSING

All data handling and processing are performed using DaVis 8.4 (LaVision GmbH). First, the acquired particle images are pre-processed to remove the background intensity by subtracting the temporal sliding minimum. Further, particle image intensities are normalised using min-max filtering (Westerweel, 1997). Volume self-calibration (Wieneke, 2008) is performed to reduce the calibration error to ~ 0.03 pixel. This further aids in minimising particle intensity reconstruction errors. The particle intensities are then reconstructed in the measurement volume using an iterative MART (multiplicative algebraic reconstruction technique) algorithm with 6 iterations and a relaxation parameter of 1. Further, the projections of the particle image intensity in the $x-z$ plane are computed to visualise the re-entrant flow. The global particle seeding density is maintained low (~ 0.03 g/L, $\mathcal{O}(20)$ particles per mm^3) to not influence global cavitation dynamics. Note that the mentioned seeding density does not account for the unavoidable settling

of particles in the flow loop. Therefore, the effective particle density is increased by phase-averaging, conditioned on the cavity length in a shedding cycle (explained later in subsection 2.2.6). If this averaging approach had not been pursued, unfeasible levels[1] of seeding would be required for the current magnification. Further, it is expected that the time-averaged velocity variation in the y-direction is negligible. Hence, the velocity fields in the $x-z$ plane are evaluated from the particle image projections, with a multi-pass interrogation approach such that the final interrogation window size is 12×12 pixels with 50% overlap. This is followed by spurious vector elimination via universal outlier detection (Westerweel and Scarano, 2005). Removed outliers are not replaced by interpolation, since only phase-averaged velocity fields are of interest. It is ensured that after vector elimination, each velocity vector is averaged over at least 90% of the samples at a given location.

2.2.5. PLANAR PARTICLE IMAGE VELOCIMETRY

The planar PIV setup is identical to the one used for tomographic imaging, yet now using a single camera (C_2, see figure 2.5). In principle, the tomographic images could have been processed to obtain similar velocity data, by averaging in the z-direction (see figure 2.3). The main reason for these additional planar PIV experiments is to verify if they can provide similar information in future studies while being considerably easier to implement. The flow conditions (σ and U_t) are the same as for the tomographic measure-

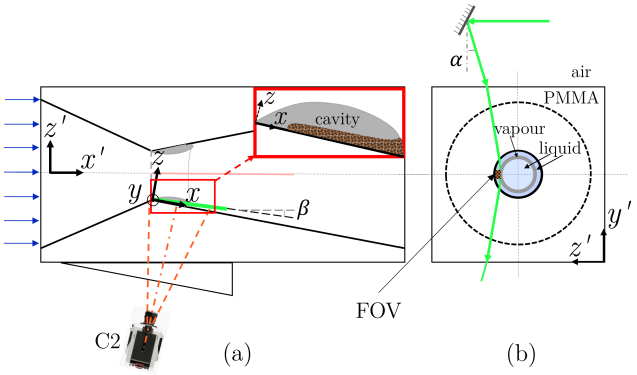

Figure 2.5: A schematic of the experimental setup for planar PIV: (a) in the $x'-z'$ plane, (b) in the $y'-z'$ plane, with light sheet path. The bulk flow is from left to right.

ments. The significant difference in the planar PIV measurement is the light sheet illumination. Exploiting the flow topology, i.e. the axisymmetry of the re-entrant flow and the thin nature of the liquid film, the light sheet is introduced in the re-entrant flow at an angle α with respect to the y' axis. Further, the light sheet is oriented at an angle of β with respect to the x-axis to account for the varying path length in water due to the diverging geometry of venturi (see ray diagram in figure 2.5). Such an arrangement ensures that the light-sheet is refracted as shown in figure 2.5b, illuminating the liquid film enclosed by the vapour cloud and the venturi wall. The flow is seeded with the same fluorescent

[1] in terms of cost, opacity, 'non-invasiveness'

tracers as mentioned previously (subsection 2.2.3). The camera is equipped with an objective lens of 200 mm ($f^{\#} = 4$) and a high-pass orange optical filter. It is placed normal to the x-axis such that images are recorded in the $x-y$ plane. The FOV is centred at y-axis, spanning 22×3.4 mm^2. A total of 15,000 images are acquired at 18,000 Hz with an exposure of 1/18,000 seconds. To evaluate the velocity vector fields, a multi-pass interrogation approach is followed with a final interrogation window size of 32×32 pixels (50% overlap). The vector fields are post-processed by vector validation using universal outlier detection (Westerweel and Scarano, 2005). It is possible that the thin laser sheet is scattered by the vapour cloud, illuminating the entire liquid film in z-direction. However, due to the small thickness of the re-entrant film and low velocity gradients in z-direction (shown later), the velocity fields in $x-y$ plane can be deemed accurate.

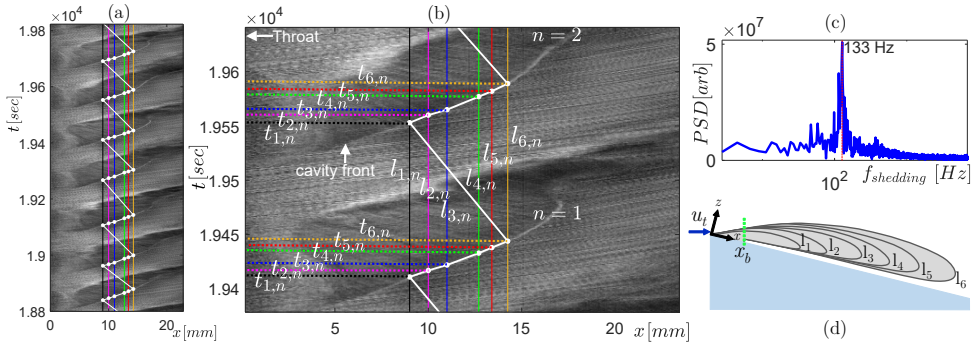

Figure 2.6: (a) A space-time ($x'-t$) plot showing the cavity front growth. Only 7 shedding cycles are shown for clarity. (b) Detail of the $x'-t$ plot showing five different cavity lengths: 9 mm, 10 mm, 11 mm, 12.7 mm, 13.4 mm, and 14.3 mm, corresponding to $t/T = 0.3, 0.34, 0.38, 0.48, 0.54$, and 0.58 over which data (tracer particle distribution and velocity) is phase-averaged. (c) Power spectral density showing periodicity in the cloud shedding process. (d) A schematic showing the cavity growth, x_b corresponds to the length of streak type bubble.

2.2.6. CONDITIONAL PHASE AVERAGING

The cloud shedding phenomenon is periodic in nature (see figure 2.6c for the dominant peak in the power spectral density (PSD) of the image intensity time series). Therefore, we study the dynamics of the re-entrant jet, and its role in periodic cloud shedding in a phase-averaged sense. The phase-averaging also helps in augmenting the signal-to-noise ratio of the data (velocity, projections) to discern the temporal evolution of the re-entrant jet. We employ a conditional phase-averaging approach, where the velocity fields and particle image projections are averaged conditioned on the cavity length. This is justified since the attached cavity front grows with a constant velocity. To determine the phase, the space-time ($x-t$) diagram of the vapour cavity front is constructed from the time-resolved raw PIV particle images (frontal view, C_2, see figure 2.4). Note that we choose a rectangular window centred about the x axis in each image. Further, we average the image intensity along the y-direction (see figure 2.3 for the coordinate system) such that for every time instance, we have the axial (x) extent of the vapour cavity. These are then stacked along a vertical time (t) axis, resulting in an $x-t$ plot shown in figure 2.6a. The bright cavity front can be discerned in the $x-t$ diagrams, indicating the

length of the vapour cavity in a shedding cycle. Six cavity lengths in each cycle ($l_1 ... l_6$) are selected: 9 mm, 10 mm, 11 mm, 12.7 mm, 13.4 mm, and 14.3 mm, corresponding to $t/T = 0.3, 0.34, 0.38, 0.48, 0.54$, and 0.58 (see schematic in figure 2.6d). Here, T corresponds to the time period of the shedding process derived from the PSD (see figure 2.6c). Further, vertical lines corresponding to the above lengths ($l_1 ... l_6$) are plotted on the $x-t$ diagram and its time of occurrence is noted on the ordinate ($t_{1,n} ... t_{6,n}$), where n corresponds to the number of the shedding cycle (see figure 2.6b). Further, two samples on either side of each ordinate ($t_{1,n}, ... t_{6,n}$) are included for averaging to augment the signal-to-noise ratio. Finally, the velocity fields and projections for each cavity length ($l_1 ... l_6$) are averaged over 75 independent shedding cycles. This approach assumes that cycle-to-cycle variation is negligible in the cavity growth stage that is of interest ($t/T = 0.3 - 0.58$, see figure 2.6). The cycle-to-cycle variation was quantified by the variation in the maximum cavity length and the cavity front growth rate per shedding cycle. The cavity front growth velocity in each cycle was estimated from the upward-sloping cavity front in the $x-t$ plot, as shown in figure 2.6b. The vapour cavity growth rate was estimated to be 3 $\pm$ 0.22 ms^{-1} (variation of < 7.5 %), while the maximum vapour cavity length (l_c) had a variation of < 9%. Further, variation in the phase-averaged axial velocity ($\overline{u_x}$) for multiple time instances is within 10%. Moreover, a convergence study of the phase-averaged velocity shows that the relative change in velocity is less than 1.5 % (data not shown here) for the number of samples considered.

2.3. RESULTS

2.3.1. GLOBAL SHEDDING DYNAMICS: A QUALITATIVE ANALYSIS

Firstly, we analyse the global shedding dynamics of re-entrant jet initiated cloud cavitation. This will allow us to identify a region of interest in a cavity shedding cycle to probe the re-entrant jet dynamics. Since the vapour cavity evolves both in space (x) and time (t), the $x-t$ diagram is an ideal tool to study large-scale shedding dynamics in a qualitative sense. Additionally, the inverse of the slope of a line in the $x-t$ diagram can be used to get a rough estimate of the cavity front growth rate.

A single shedding cycle for the case of re-entrant jet-driven cloud cavitation (σ = 0.97, $U_t = 13.56\ ms^{-1}$) is considered for in-depth analysis (see figure 2.7). It is observed that the vapour cavity typically grows in three stages. S-1 corresponds to the growth of streak type bubbles near the throat, which are seen for $0 < t/T \leq 0.2$ in a cycle (see the yellow vertical line at $x = x_b$ in figure 2.7). Such attached bubbles have been widely reported in the literature in other cavitating flow geometries, such as Pelz et al. (2017). In the next stage, $0.2 < t/T \leq 0.6$, the cavity grows at a nearly constant velocity, as evident from the linear cavity front in the S-2 stage (see the second blue line in figure 2.7). During this stage, re-entrant jets are seen developing from the cavity closure region, travelling upstream towards the attached bubbles. These are visualised by the green solid lines in figure 2.7, observed also by De Lange and De Bruin (1997) and Sakoda et al. (2001). Further, during the S-3 stage, the vapour cavity is seen to develop a discontinuity or a tear-up at about $x \sim x_b$ and the cavity growth rate is reduced. This is evident from the steeper cavity front shown by the blue line in the S-3 stage. Moreover, the vapour cavity breaks away from the streak bubbles and the remaining streak bubbles retract, as repre-

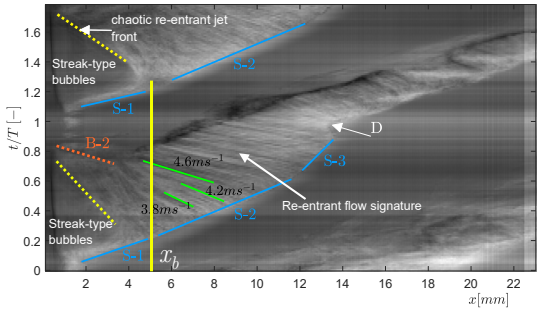

Figure 2.7: A space-time ($x-t$) diagram of a single shedding cycle for $\sigma = 0.97, U_t = 13.56\ ms^{-1}$. The bulk flow is from left to right.

sented by B-2 (orange dotted line in figure 2.7). However, this retraction of streak bubbles is quite abrupt in some shedding cycles. Furthermore, D marks the end of bubble retraction, indicating the complete detachment of the cavity. Post this, the shed cloud is convected downstream with considerable swirl into the high-pressure region, where it eventually collapses. The latter event is outside the domain shown in figure 2.7. In the meantime, a new vapour cavity starts growing at the throat. This marks a complete shedding cycle for the current cavitation regime.

It is possible to estimate the velocity of the re-entrant flow from the $x-t$ diagrams: when re-entrant flow travels upstream, it imparts deformations on the cavity surface, giving rise to upstream travelling flow structures. These are visualised by sloping green lines in the S-2 and S-3 regions (see figure 2.7) of cavity growth. The inverse of the slope of these lines roughly indicates the velocity of re-entrant flow, i.e. the steeper the streak, the lesser is the velocity. Typical values range from 3.8 to 4.6 ms^{-1} in this cycle (see figure 2.7). Several studies in the past have relied on such an approach to estimate re-entrant jet velocity (Callenaere et al., 2001; Sakoda et al., 2001; Stanley et al., 2014). However, this approach measures the deformation on the cavity interface rather than the actual re-entrant flow velocity.

2.3.2. RE-ENTRANT JET FLOW VISUALISATION

The temporal evolution of the re-entrant jet below the vapour cavity is visualised with phase-averaged particle image projections in the $x-z$ plane. See the inset in the left panel of figure 2.8 for the FOV and the coordinate system. Five time instances in a shedding cycle are considered, i.e. $t/T = 0.1$, 0.34, 0.48, 0.58, and 0.85, (see left panel of figure 2.8). The colour in the contour plots indicates the phase-averaged intensity, $\langle I \rangle$. Yellow colours indicate high intensity, i.e. the presence of tracer particles. Conversely, blue indicates lower intensity, i.e. the absence of particles. By virtue of the measurement technique and flow topology, tracer particles carried by the liquid phase are imaged in front of the vapour cavity. However, specular reflection on the cavity interface prevents the imaging of tracer particles inside the vapour cavity. Thus, tracer particles in the vapour cavity are not imaged and hence are not reconstructed. This results in two sharp interfaces; liquid-vapour (between the re-entrant jet and vapour cavity) and liquid-solid (at

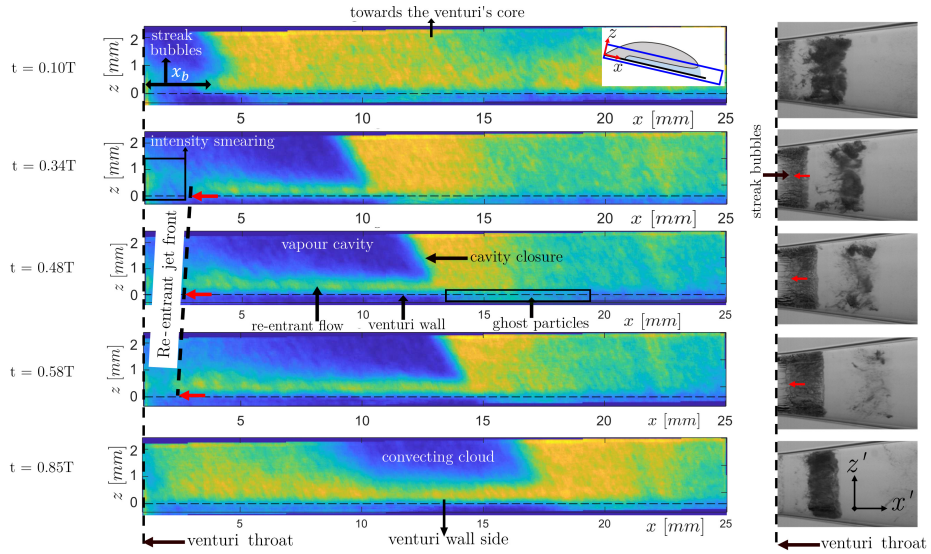

Figure 2.8: Left panel: phase-averaged re-entrant flow in the $x-z$ plane (colour indicates averaged concentration of tracer particle: dark blue patches indicates no particles in the vapour cavity, while green/yellow indicates liquid flow) for five different time instances ($t/T = 0.10, 0.34, 0.48, 0.58$, and 0.85) in a shedding cycle. The horizontal black dashed line indicates the venturi wall. The inset in the top right corner indicates the FOV. Right panel: corresponding instantaneous shadowgraphs in the $x'-z'$ plane at the equivalent time instance in a shedding cycle. The red arrow marks the re-entrant jet front. See figure 2.1 for the coordinate systems. The bulk flow is from left to right.

the venturi wall). However, near the throat, smearing of $\langle I \rangle$ is observed. It is brought about by a different axial extent of the streak-type bubbles across different cycles (see figure 2.8). Note that the venturi wall is shown via a black dotted line. Further, no ghost intensities (Elsinga et al., 2006) are reconstructed in the vapour cavity. However, minimal ghost intensities can be seen outside the expected region, i.e. outside the venturi wall (see figure 2.8).

A comparison of the time-series of re-entrant jet dynamics is made with the cavity front growth and shedding using instantaneous high-speed shadowgraphs at equivalent time instances (see right panel of figure 2.8). Note that these are not recorded simultaneously. The cavitation number is identical for both cases ($\sigma \sim 0.97$). The dark and bright regions indicate vapour and liquid phase, respectively. Note that the coordinates systems are different in the left and the right panel, i.e. the orientation of the venturi in the left panel is such that it is rotated by an angle ($8\,^\circ$) in an anti-clockwise direction. The comparison shows that liquid-vapour phase separation is captured accurately throughout the shedding cycle, confirming the robustness of the phase-averaging methodology, despite minor intensity smearing due to cycle-to-cycle variation in cavity shedding. As the cavity front grows beyond the attached streak type bubbles (x_b), re-entrant liquid flow is seen to exist below the vapour cavity, in line with our shadowgraphy observations. During this time ($t/T = 0.1 - 0.58$), the re-entrant flow front travels upstream towards the throat, as shown in figure 2.8. Thus, the re-entrant jet is not periodically generated,

rather it seems to be continually present below the vapour cavity for the most part of the shedding cycle. This is in contradiction to the classical description of the re-entrant flow, which suggests that re-entrant flow is periodically generated when the vapour cavity has assumed the maximum length (Knapp, 1958). Finally, the re-entrant jet front can be seen in the phase-averaged flow visualisations (see black dotted line in the left panel of figure 2.8) moving upstream with velocity $\sim 0.12U_t$. This chaotic front is also seen in the high-speed shadowgraph (although less clearly). Similar observations were reported by Barbaca et al. (2019), De Lange and De Bruin (1997), and Jahangir et al. (2018), who interpreted it as the re-entrant jet velocity.

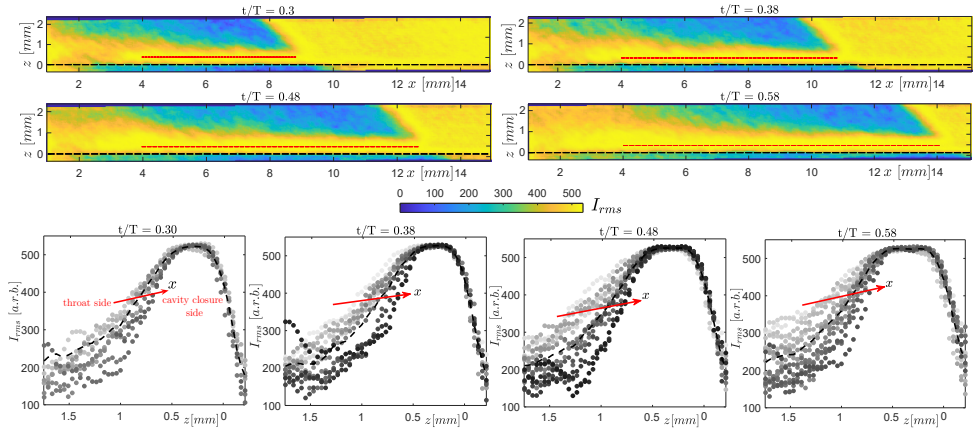

Figure 2.9: Re-entrant flow thickness evolution at t/T=0.3, 0.38, 0.48, 0.58. The black dotted line indicates the venturi wall. The bottom panel shows I_{rms} profiles in the z-direction perpendicular to the red line in the axial direction (x). The black dashed lines show the average of all profiles for reference.

2.3.3. RE-ENTRANT FLOW THICKNESS

Callenaere et al. (2001) reported that the thickness of re-entrant flow with respect to the vapour cavity thickness is an important parameter that governs the cavity shedding dynamics. Hence, one of the major objectives of performing tomographic imaging of re-entrant flow was to quantify its thickness and its spatio-temporal evolution. This requires accurate identification of two interfaces that enclose the re-entrant flow: (i) the liquid-vapour interface at the free cavity surface, and (ii) the liquid-solid interface at the venturi wall. For this, we utilise the standard deviation in the particle image intensity, I_{rms}, akin to Reuther and Kähler (2018), who used a similar approach to identify the turbulent-non turbulent interface in a turbulent mixing layer. The standard deviation at a given time instance (t/T = 0.3-0.58) is computed with respect to the phase-average intensity field $\langle I \rangle$ for that given phase.

The absence of tracer particles in the vapour region and outside the venturi results in a lower standard deviation in these regions (see figure 2.9). Conversely, tracer particles in the re-entrant film result in significant I_{rms}. This results in a large step change in the standard deviation of the intensity values across the liquid film. This approach allows us to resolve the re-entrant film with a higher resolution, i.e. $\sim \mathcal{O}$(particle image

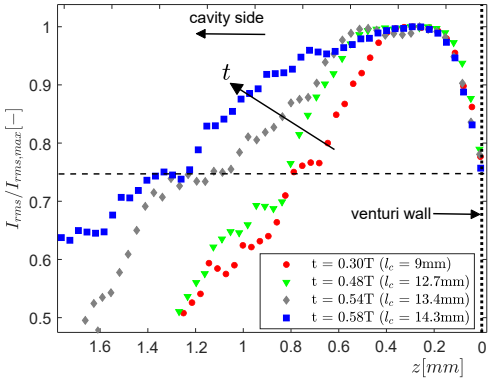

Figure 2.10: RMS of phase averaged particle image intensity profiles showing re-entrant flow thickness at different time-instances in a shedding cycle at a fixed axial location ($x/D_t = 0.36$). The I_{rms} profile is normalised with the maximum value for comparison. The black dashed line shows the chosen threshold value of 0.75, while the black dotted line shows the position of the venturi wall.

size), rather than the velocity vector spacing, which is larger. It is imperative to consider the particle image size in the reconstruction, as it forms the basis of the re-entrant jet film thickness estimation. It is observed that due to the shallow viewing angles of the cameras (see figure 2.4c), dictated by the thin nature of the re-entrant flow, the particle intensities in the depth direction (z) are reconstructed at an angle and are slightly elongated (~ 7-8 pixels). This can be explained by an increased in-plane uncertainty in the 3D particle triangulation (δ) defined as $\delta = d_\tau/\tan(\theta/2)$, where d_τ and θ are the particle image diameter and angle between the optical axes of the cameras, respectively (Kim et al., 2013). For instance, for a particle image diameter of 2 pixels, δ could be almost 8 pixels. However, the estimated thickness of the re-entrant flow spans over 35-50 pixels. In our estimates, re-entrant flow thickness can be overestimated by ~ 4-5 pixels. Closer to the throat ($x < 4$ mm), the I_{rms} values are inflated by the aforementioned cycle-to-cycle variation in the phase averages, and hence the thickness data are deemed unreliable in this region (see top panel of figure 2.9). I_{rms} profiles in the z direction are plotted perpendicular to the red dashed line in figure 2.9, such that re-entrant flow thickness as a function of axial distance (x) can be studied. The profiles with a lighter shade indicate x positions closer to the throat, while darker shades are further away from the throat, respectively.

It is observed that re-entrant flow gets thicker as it progresses upstream, further away from the cavity closure region. This is evident from the I_{rms} profiles, which get wider (compare the profiles in lighter shades with the darker shades in the bottom panel of figure 2.9). Moreover, as the cavity grows longer in time, re-entrant flow beneath it gets thicker, as clear from the flatter and wider averaged intensity profiles (see the lower panel of figure 2.9). This is further illustrated by I_{rms} profiles at a fixed axial location ($x/D_t = 0.36$) for different time instances (see figure 2.10). The RMS intensity is normalised with the maximum of the profile, while a threshold of 0.75 is chosen to quantify the thickness. For the considered time instances in a cycle, the re-entrant film thickness is seen to increase from 0.9 mm to 1.2 mm. The maximum re-entrant flow thickness in a cy-

cle is estimated to be approximately 1.2 mm for a maximum cavity length of $0.9D_t$. At this cavity length, the maximum cavity thickness is estimated to be $0.27D_t$ (~ 4.5 mm) based on the X-ray measurements of Jahangir et al. (2019), for similar flow conditions. Thus, the re-entrant film thickness is estimated to be 26% of the vapour cavity thickness. This is in line with the ultrasound measurement of Callenaere et al. (2001), who reported this value to be in the range of 15% to 35%. The described spatio-temporal variation of re-entrant flow thickness suggests that as the cavity grows in time and re-entrant flow travels further upstream near the throat, the re-entrant flow gets thick enough with respect to the vapour cavity thickness. This allows interaction of re-entrant flow with the vapour cavity, initiating the cavity pinch-off at $x \sim x_b$. This agrees well with the discontinuity observed in the vapour cavity at a similar axial position ($x \sim x_b$) in the S-3 stage of the shedding cycle (see figure 2.7).

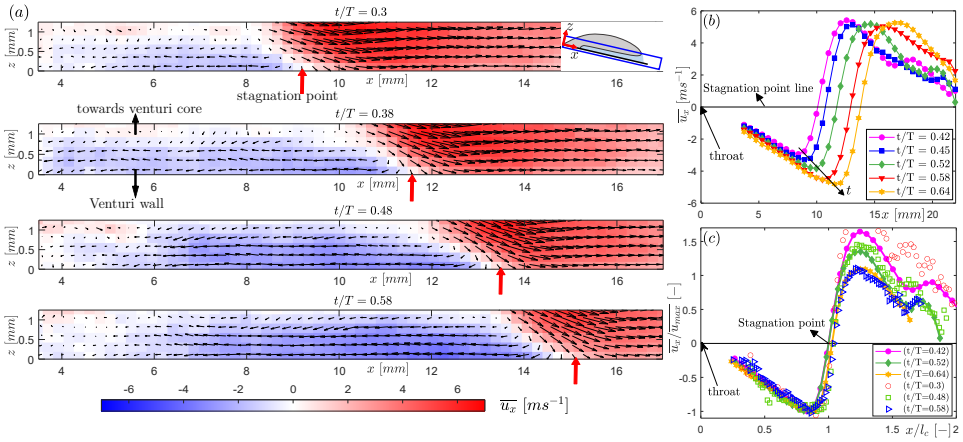

Figure 2.11: (a) Phase-averaged re-entrant flow velocity fields at t/T = 0.3, 0.38, 0.48, 0.58, (b) Phase-averaged axial velocity variation evaluated with planar PIV along the x-direction during cavity front growth (t/T = 0.42, 0.45, 0.52, 0.58, 0.63), (c) Comparison of normalised depth-averaged axial velocity variation with planar PIV at various time instances.

2.3.4. RE-ENTRANT FLOW VELOCITY

The liquid-vapour phase determination methodology described in the previous subsection does not make a distinction between a stagnant liquid film and a re-entrant jet below the vapour cavity. Hence, quantifying the flow velocity corresponding to the re-entrant flow thickness is imperative. The velocity evaluation method from raw particle images has been explained in detail in subsection 2.2.4, while the phase-averaging methodology is detailed in 2.2.6. The phase-averaged velocity field of re-entrant flow ($\overline{u_x}$) in the $x-z$ plane in the laboratory frame of reference at several time instances in a cycle (t/T = 0.3, 0.38, 0.48, 0.58) are shown in figure 2.11. The bulk flow ('red') is from left to right, while the re-entrant flow ('blue' false colours) is from right to left. The velocity field shows that re-entrant flow is a consequence of an impinging jet and a stagnation point formed at the cavity closure region (see red arrows in figure 2.11a). It is seen that as the vapour cavity grows beyond the streak bubbles, the flow encounters a stagnation

point near the cavity closure region and the re-entrant flow is swept below the vapour cavity. The stagnation point moves further away as the vapour cavity grows in time (t/T = 0.3-0.58). Supplementary movie S1 shows a visualisation based on all reconstructed phases. During this time, the re-entrant flow is continuously fed by the bulk flow below the cavity, while the fluid on the other side of the stagnation point moves away from the throat. This is evident from the change of velocity direction past the stagnation point in figure 2.11a and b. The spatial variation of the re-entrant jet velocity shows that as the jet begins from the stagnation point, it starts accelerating towards the throat to achieve a maximum velocity ($\overline{u_{max}}$). However, at about $x/l_c \sim 0.85$, it starts slowing down (see figure 2.11c). Here, l_c indicates the vapour cavity length. This is because the re-entrant jet is blocked by the streak type attached bubbles, as seen from the raw particle images and high-speed shadowgraphs (see figure 2.5). Such a decrease of velocity in the axial direction has also been reported by Pham et al. (1999) and Sakoda et al. (2001) in other cavitation flows. As the vapour cavity grows in time, a jet with higher velocity is generated from the cavity closure point further away from the throat, as evident from figure 2.11. This is inline with the earlier observations of Franc (2001), Gopalan and Katz (2000), and Laberteaux and Ceccio (2001b), suggesting that re-entrant flow is adverse pressure gradient driven.

We observe that the maximum re-entrant flow velocity increases substantially from 2.5 ms^{-1} to 5 ms^{-1} for the throat velocity of 10.2 ms^{-1} (see figure 2.11b). This is consistent with our velocity estimates from the $x-t$ plots (see figure 2.7). This is also in close agreement with Callenaere et al. (2001) and Pham et al. (1999), who reported re-entrant jet velocity to be about half of the mean flow velocity (U_∞) for a diverging step and hydrofoil, respectively. The width (z-direction) of reverse flow region indicates that the re-entrant flow gets thicker in time, as also stated in the earlier subsection. Moreover, the momentum of the re-entrant flow approaching the throat increases monotonically in time until the vapour cavity develops a discontinuity (also see figure 2.8). This corroborates the hypothesis that as the cavity grows in time, the re-entrant flow gets thicker. At the same time, a stronger re-entrant flow is pushed below the cavity. The combination of these effects are involved in causing a cavity pinching off and discontinuity in the vapour at $x \sim x_b$. Consequently, this leads to cloud shedding. We report that the maximum velocity of re-entrant flow is less than the bulk velocity (U_t). This is in contrast to potential flow theory, which predicts the re-entrant flow velocity to be *higher* than the bulk velocity (u_t): $u_{jet} = u_t(\sqrt{1+\sigma})$ (Furness and Hutton, 1975). Interestingly, the averaged velocity ($\overline{u_x}$) normalised with the peak velocity ($\overline{u_{max}}$) and axial distance (x) normalised with the cavity length (l_c), collapse on top of each other, showing self-similarity for the re-entrant jet beneath attached cavities (see figure 2.11c).

2.3.5. DATA VALIDATION

While the re-entrant jet velocity and its spatio-temporal variation is resolved accurately in the axial direction (x) (see figure 2.11b), its spatial resolution in the depth (z) direction is limited to 4-5 vectors. This is mostly brought about by the thin film topology of the re-entrant flow. The measurement technique is also limited by: (i) the diffraction-limited particle images wherein particle images appear bigger than their actual size, (ii) the finite resolution of PIV dictated by the interrogation window size. Furthermore, there is

a limitation on tracer particle concentration to preserve non-intrusiveness of the measurements, since a large concentration of impurities (such as tracer particles) can alter the cavitation dynamics and also induce opacity to the flow.

In order to assess the quality of the measured velocity data, the development of the axial velocity ($\overline{u_x}$) profile along the x direction is considered. A qualitative comparison of re-entrant flow is made with a submerged impinging jet flow (Fitzgerald and Garimella, 1997), as the re-entrant jet flow field resembles it closely (see figure 2.11). The phase-averaged axial velocity profile ($\overline{u_x}$) at a time instance, $t/T = 0.48$ ($l_c = 12.7$mm), is treated for the sake of clarity at various axial positions (see figure 2.12a and the inset). It is seen

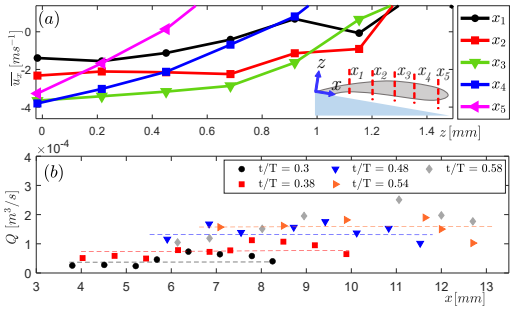

Figure 2.12: (a) Axial velocity profile development of the re-entrant flow at $t/T = 0.48$ at various axial positions. (b) Volume flux variation of re-entrant flow along the axial direction for t/T=0.3-0.58.

that the gradient of the velocity profile is higher near the cavity closure region, yet the profiles progressively get flatter as the jet approaches the throat due to the deceleration it experiences. Such evolution of the axial velocity profile agrees well with the observations of Fitzgerald and Garimella (1997). Further, due to the limited spatial resolution of PIV, the thin high-shear region close to the venturi wall could not be resolved (see velocity profile in figure 2.12a). Assuming that re-entrant flow is axisymmetric in a phase-averaged sense, the velocity profiles in the z-direction can be integrated along its thickness over the entire circumference of the venturi. This is done to verify mass conservation, i.e. the volumetric flow rate in the jet (Q) is constant for various x-positions (see equation 2.1). Here, $R_i(x)$ and $R_o(x)$ are the inner and outer radii of the annulus, formed by the re-entrant flow, which are both also a function of the axial position due to the diverging geometry of the venturi.

$$Q(x) = \int_{R_i(x)}^{R_o(x)} 2\pi \overline{u}(r,x)\, r(r,x)\, \mathrm{d}r \tag{2.1}$$

The volume flux of the re-entrant flow at different axial positions at various time instances ($t/T = 0.3, ..., 0.58$) in a shedding cycle are shown in figure 2.12b. It is observed that at every time instance, the re-entrant flow flux remains nearly constant (see figure 2.12b) except for $t/T = 0.58$, where cavity detachment is suspected to have an influence. This also confirms that the loss of velocity data in the high-shear region is perhaps small. Further, as expected, the volume flux of the re-entrant jet increases monotonically with time as a stronger re-entrant flow is fed by the bulk flow (see figure 2.11a).

2.3.6. COMPARISON OF TOMOGRAPHIC IMAGING AND PLANAR PIV

The planar PIV inherently yields depth (z)-averaged velocity fields in the $x-y$ plane, due to the finite light sheet thickness. Further, the velocity fields are phase-averaged conditioned on cavity length. The variation of the axial velocity component ($\overline{u_x}$) in the y-direction appears to be negligible. Hence, the vector field is further averaged in the y-direction to get the axial (x) variation of $\overline{u_x}$, as shown in figure 2.11b. In an independent experiment, the velocity fields are computed from y-averaged tomographic particle image projections, in the $x-z$ plane. These are also averaged along the re-entrant flow thickness (z-direction) such that the axial (x) variation of $\overline{u_x}$ is obtained.

When non-dimensionalised with the corresponding $\overline{u_{max}}$, and l_c, the one-dimensional variation of $\overline{u_x}$ shows a good agreement (see again figure 2.11c). Here, the $\overline{u_x}$ evaluated from planar PIV is shown by filled symbols while the $\overline{u_x}$ evaluated from tomographic image projections are shown by open symbols. The maximum velocities at a given time instance are also comparable. Thus, it is observed that the velocity variation of the re-entrant flow is small along its thickness. This is also confirmed by the velocity profiles in figure 2.12. Hence, the re-entrant flow velocity beneath attached vapour cavities is seen to have a unidirectional variation. Consequently, planar PIV is expected to provide robust estimates of axial velocity variation in an axial direction.

2.4. APPLICATION OF THE TECHNIQUE AND DISCUSSION

A thorough understanding of cavitation physics is strongly driven by the quantification of flow characteristics, such as the velocity field, pressure, and void fractions. Hence, the discussed methodology can now be applied to evaluate the velocity field of re-entrant flow below the vapour cavity in different cavity shedding flow regimes that exist in the axisymmetric venturi.

Firstly, the global cavitation behaviour is studied by systematically varying the σ to identify various flow regimes. The vapour cavity dynamics is characterised by the vapour shedding frequency (f) expressed as Strouhal number ($St_t = fD_t/U_t$) and the pressure drop across the venturi expressed as pressure loss coefficient, $K = (p_1 - p_2)/(\frac{1}{2}\rho U_t^2)$, see figure 2.2 for definitions. St_t and K are plotted for various σ at different global static pressures in the flow loop as shown in figure 2.13. It is seen that the variation of the

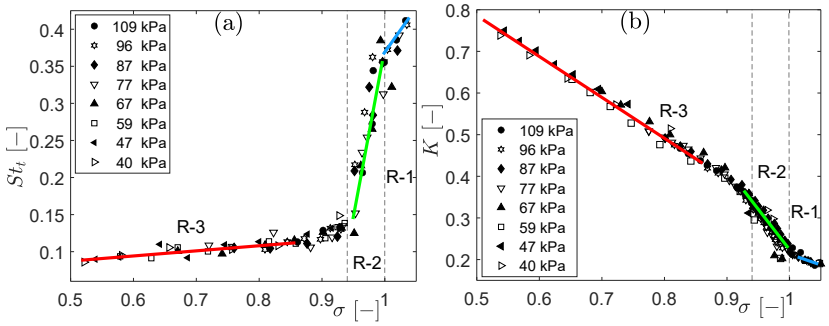

Figure 2.13: Cavitation flow regimes (R1, R2, R3): (a) Strouhal number (St_t), (b) Pressure loss coefficient (K) as a function of cavitation number (σ) at different global static pressures.

Table 2.1: Flow parameters for the studied flow cases

Flow regime	P_3 [kPa]	U_t [ms^{-1}]	σ[−]
R1	57	10.2	1.03
R2	55	10.4	0.97
R3	43	9.9	0.82

Strouhal number with σ exhibits a change in slope at $\sigma \sim 1$ and 0.95 (see figure 2.13a). This change in slope is well reproduced in the variation of the pressure loss coefficient as a function of σ (see also figure 2.13b). This forms the basis of three distinct cavity shedding behaviours that will be discussed. As the intensity of cavitation is increased gradually, i.e. σ is decreased, the following shedding behaviours are observed: (i) re-entrant flow initiated aft cavity shedding (R1: $\sigma \geq 1$), (ii) re-entrant jet initiated periodic cloud shedding (R2: $0.95 \leq \sigma < 1$), and (iii) bubbly shock driven periodic cloud shedding (R3: $\sigma \leq 0.85$) (see again figure 2.13). The R2 and R3 flow regimes have been discussed qualitatively by Jahangir et al. (2018). However, R1 has not been explored in the cavitating axisymmetric venturi, mainly because of its less severe effects when compared to periodic cloud cavitation.

A typical case of each flow regime is now examined with the velocity fields below the vapour cavity. The global static pressure in the system is varied while maintaining comparable bulk flow velocity at the throat in all three flow cases. As a result, three different cavitation numbers, covering the three regimes, are achieved (see table 2.1). Due to the ease of implementation and demonstrated robustness, planar PIV is used. The velocity vector fields below the vapour cavity are evaluated in the $x-y$ plane, as discussed in subsection 2.2.5. The axial velocity (u_x) is averaged along the y-direction to yield $\overline{u_x}$ as a function of x. The axial variation of $\overline{u_x}$ is then stacked on a time-axis to generate an $x-t$ evolution of axial velocity. These $x-t$ diagrams resemble those commonly used in cavitation research but are now encoded with the local velocity. Despite averaging of the velocity (u_x) in the y-direction, the instantaneous flow structures are well-preserved in the space-time evolution of $\overline{u_x}$. A few representative shedding cycles for each flow regime are shown in figure 2.14 for clarity. Here, red and blue indicate bulk (positive) and re-entrant flow velocity (negative), normalised with the throat velocity (U_t).

At the highest cavitation number considered, the vapour cavities are the thinnest and the shortest, as also reported by Ganesh et al. (2016). We observe that the vapour cavity grows, rolls up, and gets fragmented into multiple smaller vapour cavities (R1, figure 2.14a). The cavity appears to be continually attached to the throat for spatial extent (x) < 2 mm. For x > 2mm, there is a continuous presence of re-entrant liquid flow below the cavity. This is evident from the patchy reverse flow structures in the space-time plot of velocity. These reverse flow structures can extend longer in the axial direction in some shedding cycles (see long blue patches). This is because the reverse flow further away from the throat appears to be induced by the fragmented, smaller vapour structures. They carry significant swirl and consequently low pressure in their cores. Thus, they can sustain for a longer time, i.e. their collapse is delayed as they approach the high-pressure region of the venturi. The time-averaged thickness of re-entrant flow film

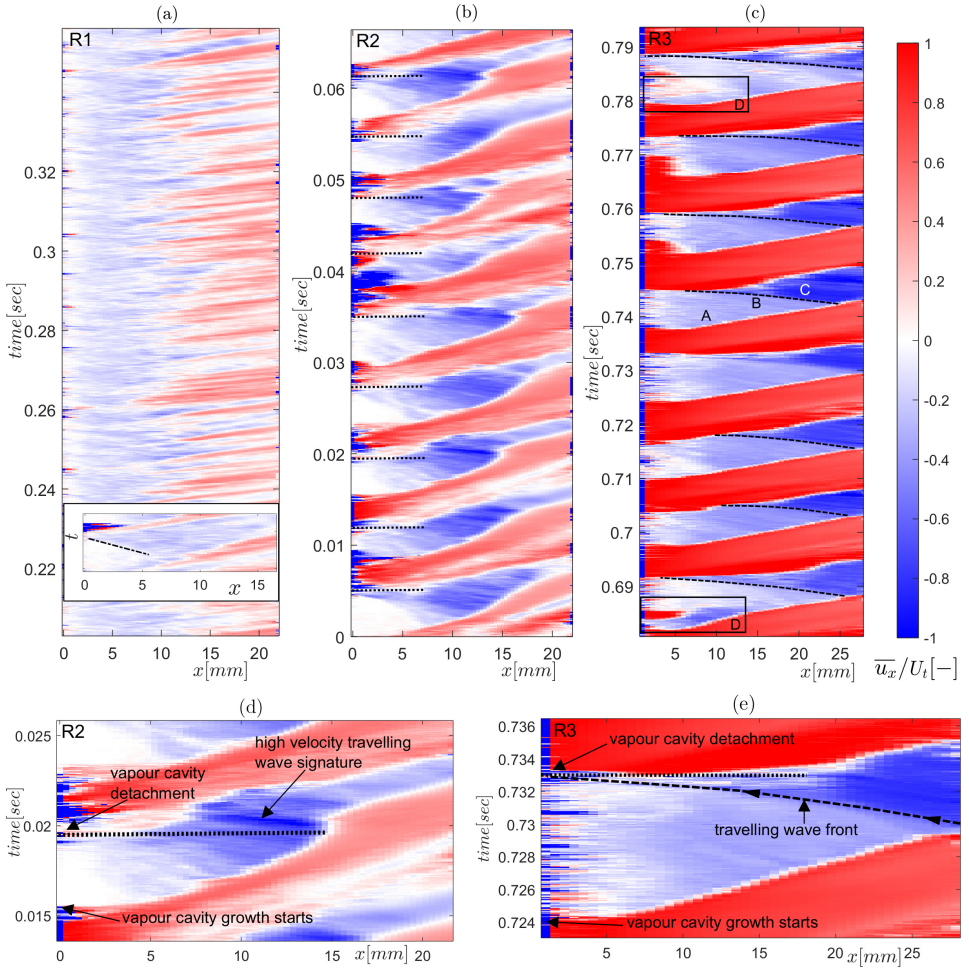

Figure 2.14: Flow regimes of partial cavitation in an axisymmetric venturi shown by space-time plots (a) R1: re-entrant jet initiated aft cavity shedding ($\sigma = 1.03$, $U_t = 10.2ms^{-1}$) (b) R2: re-entrant jet initiated cloud shedding ($\sigma = 0.97$, $U_t = 10.4ms^{-1}$), (c) R3: Bubbly shock driven cloud shedding ($\sigma = 0.82$, $U_t = 9.9ms^{-1}$). (black dashed profile indicates the front of bubbly shock wave), (d) zoom-in of a single shedding cycle in R2, (e) zoom-in of a single shedding cycle in R3. The bulk flow is from left to right. (R3 in bold)

in R1 is estimated to be about 0.5 mm from the tomographic imaging. Since the vapour cavities are thin with respect to the re-entrant flow thickness, the re-entrant flow is suspected to interact with the vapour cavity strongly. This interaction is involved in the fragmentation of the vapour cavity at multiple points along the axial direction, giving rise to the observed patchy flow structures. Thus, the vapour cavity is destabilised by the re-entrant flow, while re-entrant flow may not reach all the way upstream up to the throat. Consequently, it appears that the cavity is being shed from its aft side (closure region of the cavity) for the majority of instances. However, it also appears that the cavity is shed from the throat in some shedding cycles. This can be seen from the re-entrant jet

front approaching the throat (see black dash-dotted profile in the inset of figure 2.14a). This intermittency is responsible for disturbing the periodicity in the cavity shedding process. Such behaviour is also evident from a weaker peak in the Power spectral density of the axial velocity time series (not shown here). Thus, vapour cavities appear to undergo shedding in a quasi-periodic manner. Such 'quasi-stable sheet cavities' or 'oscillating thin cavities' have been mentioned in the past by Callenaere et al. (2001) and De Lange and De Bruin (1997) on a diverging step and hydrofoil, respectively. More recently, Barbaca et al. (2019) reported such a flow regime using x-ray densitometry over a wall-mounted fence. It was reported by Gopalan and Katz (2000), Leroux et al. (2004) that no re-entrant flow exists beneath the vapour cavity in this flow regime, besides a weak re-entrant flow at the cavity closure region. However, instantaneous velocity fields show that a reverse flow does exist ($\overline{u_{max}} \sim -0.25U_t$) below the majority of the length of the vapour cavity. Further, it is responsible for the shedding of the vapour cavity at multiple points along the cavity length.

As σ is decreased ($0.95 \leq \sigma < 1$), vapour cavities get longer and thicker. As the shedding cycle begins, the re-entrant liquid film is thin with respect to the vapour cavity. However, it evolves into a thicker film (as thick as ~ 1.2 mm) as the vapour cavity grows in time. Hence, it can be argued that the interaction between the re-entrant flow and the vapour cavity is delayed until the re-entrant flow is thick enough with respect to the vapour cavity. Consequently, a coherent re-entrant liquid flow is seen to exist below the vapour cavity for the majority of the cycle, in comparison to the more patchy reverse flow structures in R1. This can be seen from the $x-t$ diagram in figure 2.14b and flow visualisations in figure 2.8. The axial velocity variation in the $x-t$ diagram for R2 shows that as the vapour cavity grows, a stronger re-entrant flow is pushed below the vapour cavity. This is then followed by the cavity detachment. The cloud detachment instance for each cycle is shown by a black dotted line in figure 2.14b. The detached cloud then convects downstream with a significant swirl velocity. A maximum reverse velocity in the laboratory frame of reference ($\sim -0.90U_t$) below the vapour cavity is occasionally observed after the cavity has detached. This can be explained by the travelling wave generated by the collapse of the cavitation cloud, which then gets superimposed on the existing re-entrant flow. The signature of this wave can be seen in figure 2.14d: the dark blue (high velocity) structure travelling upstream. However, it appears that cavity detachment triggered by the interaction of the re-entrant flow and the vapour cavity *precedes* the arrival of the travelling wave at the throat, as illustrated by figure 2.14d. In the current study, sharp pressure peaks were picked up by a high-speed dynamics pressure probe in the cavity collapse region (not shown here). This corroborates the presence of bubbly shock waves. In summary, we report the presence of high-velocity upstream travelling waves of nearly constant velocity in the re-entrant jet dominated cavity shedding regime (R2). However, it is not a necessary condition for cavity detachment. Consequently, adverse pressure gradient-driven re-entrant jet dynamics is here identified as a sufficient condition for the cavity detachment.

Further reduction of σ leads to the largest vapour cavities (Jahangir et al., 2018). This results in a prominent bubbly shock wave emanating from the collapse of the large cavitation cloud. The signature of bubbly shock waves is registered by a high-speed dynamic pressure sensor in the downstream region of the venturi. The distinct and high-pressure

peaks are recorded periodically with a frequency identical to the cloud shedding frequency. These are further seen to trigger the cavity detachment and dictate the periodic cloud cavitation, as shown in figure 2.14c, figure 2.14e. For the majority of shedding cycles, the bubbly shock wave gives rise to an upstream travelling wave-like flow structure. This seems to be superimposed on the existing adverse pressure gradient-driven re-entrant flow. A similar observation has also been reported by Stanley et al. (2014) as a phenomenological description of re-entrant jet-initiated cloud shedding in a cylindrical orifice. However, the velocimetry confirms that this is an alternate mechanism for cloud cavitation instability, inline with Budich et al. (2018), Ganesh et al. (2016), and Jahangir et al. (2018). The wavefront is visualised by a sharp jump in the axial velocity magnitude in the $x-t$ plot (see the black dashed curved profiles in figure 2.14c, e.g. near label B). It demarcates low velocity re-entrant flow region (A in figure 2.14c) and high velocity region (C).

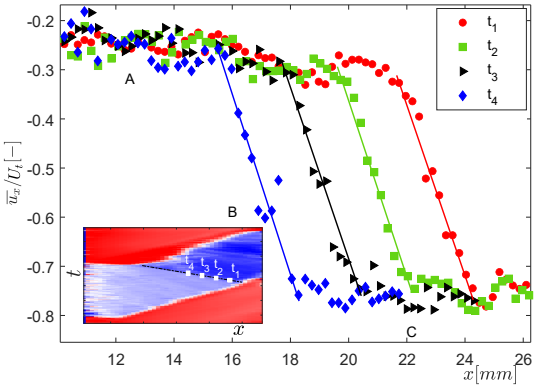

Figure 2.15: The instantaneous variation of $\overline{u_x}$ along the axial direction to show the propagation of velocity discontinuity towards the throat in time. A: reverse flow region due to the re-entrant flow, B: shock front, C: bubbly shock wave velocity.

This is further illustrated by an $x-t$ diagram for a single shedding cycle in figure 2.14e. The dashed profile indicating the shock front travels upstream until the vapour cavity detachment point is shown by a black dotted line. Further, the shock front is seen to travel at a near-constant velocity, however it seems to accelerate closer to the throat. This is evident from the changing slope of the black dashed profiles. It is suspected that the varying cross-section of the venturi could be responsible for the observed acceleration. Across this travelling discontinuity, the velocity in the laboratory frame of reference can jump from 2.5ms^{-1} to 7.5 ms^{-1} over the nominal shock-front thickness of $\sim$ 2.5 mm, for the given flow conditions (see figure 2.15). The shock front spans over 4 PIV interrogation windows. The finite thickness of the shock front could be related to the fact that the vapour cavity is a collection of cavitation bubbles. Hence, the shock front thickness should depend on the length scale of collapsing bubbles in the vapour cavity (Brennen, 1995). The velocity of the wave-front can also be approximated from the slope of the linear part of the discontinuity ($x \sim$ 12 mm - 27 mm), in the $x-t$ diagram (see black dashed line in figure 2.14e). It is estimated to be about -0.57U_t, which is lower than the

maximum reverse flow velocity of -0.78U_t as shown in figure 2.15.

Further, we observe that in a few shedding cycles (see cycles marked D in figure 2.14c), although a strong re-entrant flow exists below the cavity, the rate of vaporisation at such flow conditions is high. This allows the vapour cavity to continue growing, despite the presence of the re-entrant flow. Therefore, the re-entrant jet cannot dictate the cloud shedding. Instead, we can observe a typical re-entrant jet initiated shedding cycle 'within' a bubbly shock initiated cavity shedding cycle (see again region marked D in figure 2.14c). Further, the vapour cavity continues to grow beyond an axial position (x), where the adverse pressure gradient is not strong enough to drive the liquid flow upstream. Hence, a nearly stagnant pool of liquid is seen below the cavity. Ultimately, an upstream travelling wave of higher velocity ($-\overline{u_x} \sim 0.64U_t - 0.75U_t$) arrests the growth of the vapour cavity, resulting in cavity detachment and subsequent shedding. As the focus of this study was on the re-entrant jet regime, no tomographic imaging was performed in this regime, hence we do not have an estimate for its thickness.

2.5. CONCLUSIONS

The 're-entrant jet' is known to play a key role in cloud cavitation instability. However, the exact physical mechanism governing this phenomenon remains obscure. One of the main aims of this work was thus to delve into the re-entrant jet dynamics and assess its role in the periodic cloud shedding in an axisymmetric venturi. This is realised via multiple flow measurement modalities, i.e. high-speed shadowgraphy, tomographic imaging and planar PIV. The shadowgraphs help us to identify the upstream travelling flow structures due to the re-entrant jet in the S-2 and S-3 stages of cavity growth in a shedding cycle. Thus, we probed into these stages to unveil the underlying re-entrant jet dynamics.

We employ tomographic imaging with the primary aim of measuring the spatio-temporal variation of the thickness and the velocity of the re-entrant liquid film in the R2 flow regime. The axisymmetry of the venturi and the re-entrant flow is exploited to gain optical access to the flow from the front side. Further, fluorescent tracer particles are used to circumvent the issue of strong reflections and opacity arising from vapour cavity and frothy mixture. Moreover, a conditional phase-averaging methodology is adopted to study the temporal evolution of re-entrant flow in a shedding cycle. The phase-averaged reconstructed particle intensity projections are used to visualise the re-entrant flow, while the standard deviation corresponding to the phase-averaged particle image intensity is used to quantify the thickness of the re-entrant jet. It appears that as the vapour cavity grows, the re-entrant flow is continuously fed below the vapour cavity, contrary to the previous understanding that it is periodically generated. Further, it is estimated that the maximum re-entrant flow thickness is about 1.2 mm for the given flow condition, i.e. 26% of the vapour cavity thickness.

The velocity vector fields reveal that the re-entrant jet is a consequence of an impinging jet and a stagnation point formed at the cavity closure region. Moreover, the velocity of the jet starting further away from the throat is higher. This suggests that the reverse flow involved in cavity detachment is driven by an adverse pressure gradient at the cavity closure region and not correlated to the pressure peaks due to the cloud collapse. The maximum velocity of the re-entrant flow below an attached cavity is found to be 0.5U_t.

Further, the validity of the velocity measurements has been evaluated by checking the conservation of mass, which was deemed to be within acceptable limits. Nevertheless, the gradients close the venturi wall and air cavity cannot be resolved due to the limited particle seeding and relatively large particle size.

It is hypothesised that the thickness of re-entrant flow with respect to the vapour cavity is an important parameter, in line with Callenaere et al. (2001). At the highest cavitation number (R1), we suspect that the vapour cavities are thin enough with respect to the re-entrant flow to interact strongly with it. This prevents the re-entrant flow from reaching the throat, leading to the fragmentation of the cavity at multiple points from the cavity closure region. Hence, the upstream part of the cavity remains attached to the throat despite the continuous re-entrant flow below the cavity. As the cavitation number is decreased (R2), longer and thicker vapour cavities are formed. This limits the interaction of the re-entrant flow with the cavity. Hence, a coherent liquid flow can sustain below the vapour cavity for a large part of the shedding cycle. The re-entrant flow evolves in time, i.e. it gets thicker with respect to the vapour cavity. This allows the re-entrant flow to interact with the vapour cavity, resulting in its pinch-off at $x \sim x_b$. This is corroborated by an increase in the maximum re-entrant jet velocity from $0.25U_t$ to $0.5U_t$ as the vapour cavity grows in time. Thus, simultaneous measurement of the re-entrant flow thickness and the velocity reveal that a complex spatio-temporal evolution of near-wall re-entrant flow is involved in cavity detachment. Further, the imploding cavitation cloud gives rise to a high-velocity travelling wave that appears to be superimposed on the existing re-entrant flow. However, this travelling wave is deemed not necessary for the cavity detachment process in R2. Lastly, a sharp and distinct upstream travelling discontinuity is observed in the axial velocity at the lowest cavitation number (R3 regime). This is attributed to a bubbly shock wave emanating from the cloud collapse. This bubbly shockwave is superimposed on the existing pressure gradient driven re-entrant flow, creating a periodic travelling wave of a higher velocity, $0.64U_t - 0.75U_t$. Moreover, this discontinuity is seen to dictate the periodic cloud detachment and shedding.

Thus, tomographic imaging followed by velocimetry of near-wall 're-entrant flow' has helped to further uncover the complex interaction between the near-wall flow and the vapour cavity. This deepens our understanding of the observed vapour cavity shedding behaviour, omnipresent in various industrial and maritime applications.

APPENDIX 2.A: CALIBRATION

The calibration for planar PIV measurement is performed using a calibration target attached to a 3-D printed venturi negative. The markers ('+') with known spacing are shown in figure 2.16a. The markers are closely spaced (i.e. next to each other). Hence, it appears as a grid. The target is carefully slid inside the venturi, which is held in place by a set of O-rings on either ends. This part of the flow loop, with venturi, is then filled with water. A sample calibration image is shown in figure 2.16b. The LED panel is used to illuminate the markers from the backside.

The positions of detected markers (in pixels) are plotted in horizontal and vertical directions, shown by blue and red symbols respectively (see figure 2.16c). It is seen that the magnification in vertical and horizontal directions is identical. Moreover, there is no image warping as evident by a linear fit to the detected markers, where the residual error

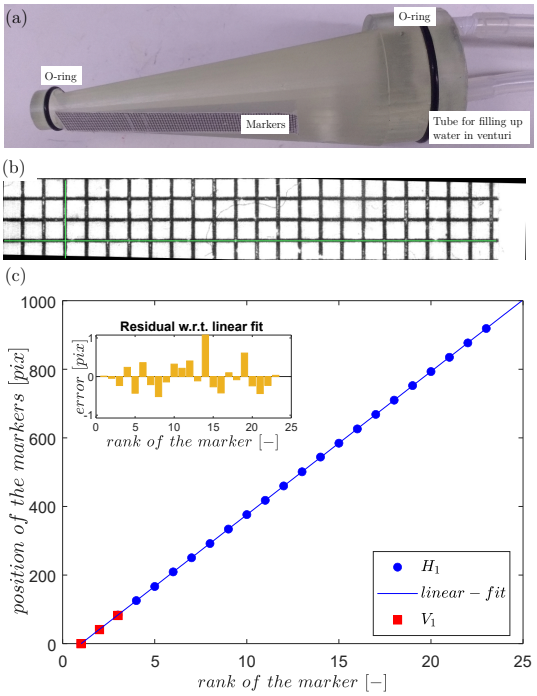

Figure 2.16: (a) 3-D printed venturi negative with a calibration target. (b) A sample calibration image of marker ('+'). (c) Positions of markers detected by a 3-point Gaussian fit to the intensity in the horizontal direction (H_1) and vertical direction (V_1). The least-square linear fit is applied to H_1 data points and residual errors are shown in the inset.

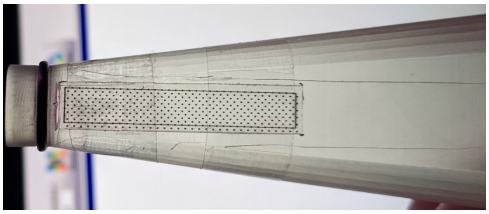

Figure 2.17: 3-D printed venturi negative with calibration target for tomographic PIV

is within 1.5 pixels (illustrated in the inset of figure 2.16c). This is expected as the camera plane is parallel to the calibration target (see the experimental setup in figure 2.4 and 2.5).

A similar approach is employed for the calibration of tomographic imaging. Due to the restricted access to the FOV, traversing the calibration target inside the venturi in the z-direction was impractical. Hence, 3-D calibration was performed using two available z-planes. The calibration markers ('•') were laser-printed on each side of a glass slide to provide two calibration planes. Further, the markers were staggered to identify the appropriate plane in the calibration image (see figure 2.17). This calibration target is

then attached to the 3-D printed venturi negative such that the markers can be placed at the desired location of measurement. The calibration is further improved by using self-calibration, as discussed in the manuscript.

SUPPLEMENTAL MATERIAL

Movie S1 shows the phase-averaged time evolution of the vapour cavity and the re-entrant flow beneath it, in the 'S-2' stage of the cavity growth.

3

THE CHARACTERISTICS OF BUBBLY SHOCK WAVES

The bubbly shock-driven partial cavitation in an axisymmetric venturi is examined with time-resolved 2-D X-ray densitometry in this chapter. The bubbly shock waves are characterised using the vapour fraction and pressure changes across it, propagation velocity, and Mach number. The sharp changes in vapour fraction measured with X-ray densitometry, combined with high-frequency dynamic pressure measurements, reveal that the interaction of the pressure wave with the vapour cavity dictates the shedding dynamics. At the lowest cavitation number ($\sigma \sim 0.47$), the condensation shock front is the predominant shedding mechanism. However, as σ increases ($\sigma \sim 0.78$), we observe an upstream travelling pressure discontinuity that changes into a condensation shock as it approaches the venturi throat. This coincides with the increasing strength of the bubbly shock wave as it propagates upstream, manifested by the increasing velocity of the shock front and the pressure rise across it. Consequently, the Mach number of the shock front increases and surpasses the critical value of 1, favouring condensation shocks. Further, at higher σ ($\sim 0.84 - 0.9$), both the re-entrant jet and pressure wave can cause cavity detachment. However, at such σ, the pressure wave likely remains subsonic. Hence, cavity condensation is not favoured readily. This leads to the re-entrant jet causing the cavity detachment at higher σ. The shock front is accelerated as it propagates upstream through the variable cross-section of the venturi. This enhances its strength, favouring cavity condensation and eventual shedding. These observations explain the existence of shock fronts in an axisymmetric venturi for a large range of σ.

This chapter is based on: Gawandalkar, U.U., Poelma, C. (2024). *The characteristics of bubbly shock waves in a cavitating axisymmetric venturi via time-resolved X-ray densitometry*, Journal of Fluid Mechanics 988 (A34), 1-33.

3.1. INTRODUCTION

Hydrodynamic cavitation can occur in a wide variety of flows, such as flow near ship propeller blades, throttle valves, and fuel injectors (Blake and Gibson, 1987). Partial cavitation is a commonly occurring form of cavitation, where attached vapour cavities are formed in the low-pressure regions. They get destabilised and are shed periodically or quasi-periodically, depending on the flow condition. The shed vapour then gets convected to a relatively high-pressure region, where it implodes (Brennen, 1995). This inherent unsteadiness can lead to unwanted and detrimental effects such as noise, vibration, erosion-wear, or even a catastrophic failure of the flow equipment. Hence, understanding the fundamental physics of such flows is crucial. Specifically, it becomes imperative to understand the underlying vapour cavity destabilising mechanisms.

Classically, it was believed that the periodically generated re-entrant jet travelling below the vapour cavity is the sole mechanism responsible for cavity destabilisation and cloud cavitation (Callenaere et al., 2001; Kawanami et al., 1997; Knapp, 1958). On the other hand, the watershed study of Reisman et al. (1998) and the subsequent studies of Arndt et al. (2000) and Leroux et al. (2004) hypothesised an alternate cavity destabilising/shedding mechanism: it was proposed that a bubbly shock wave emanating from the *coherent* cloud collapse can dictate the cavity shedding dynamics. The recent experimental study of Ganesh et al. (2016) and the supporting numerical studies Gnanaskandan and Mahesh (2016a) demonstrated that indeed bubbly shock waves emanating from the collapse of a relatively large cavitation cloud play a crucial, if not dominant, role in the dynamics of cloud cavitation. Since then, this alternate shedding mechanism has been identified in various flow geometries (Brandao et al., 2019; Jahangir et al., 2018; Trummler et al., 2020). Further, the shedding mechanism is seen to change gradually from re-entrant jet to bubbly shock as cavitation number (σ) decreases with a transition region, where both shedding mechanisms are seen to operate. The cavitation number expresses the intensity of the cavitation, as defined later. Using particle image velocimetry (PIV) applied to the near-wall flow, Gawandalkar and Poelma (2022) showed that re-entrant flow is present at the cavity closure region even at low σ. Further, it weakens severely at lower σ as the vapour cavity grows long enough such that it experiences a low adverse pressure gradient that drives the re-entrant jet. Interestingly, the numerical study of Budich et al. (2018) proposed that cloud collapse is not a necessary condition for shock front formation. Rather, it was suggested that an adverse pressure gradient is a sufficient condition for shock formation. Alluding to this, Trummler et al. (2020) used Large Eddy Simulations and proposed that the re-entrant jet gets converted into a condensation shock as it travels upstream. Recently, Zhang et al. (2022) proposed a third cavity destabilising mechanism due to the collapse-induced pressure wave. Zhang et al. (2022) observed that a collapse-induced pressure wave does not result in a vapour fraction discontinuity when it propagates through the vapour cavity, although it can arrest its growth. Hence, there is no consensus on the phenomenological description of cavity destabilisation, especially the role of cloud collapse on the overall cavity dynamics. Additionally, the flow conditions favouring the respective shedding mechanism and the cause of the transition of the shedding mechanism from re-entrant jet to bubbly shock wave still remain open questions. It is worthwhile to note that the disparate shedding mechanisms give rise to different cavitation dynamics, such as shedding frequency and

maximum pressure pulse, which can influence the degree of unsteadiness and wear.

Cavitating flows are generally a highly turbulent, bubbly mixture. Further, the morphology of the vapour cavity is such that it is a nearly homogeneous mixture of liquid and vapour. Even a modest vapour fraction (~ 0.05) can significantly reduce the speed of sound in the bubbly mixture, making the fluid locally supersonic at a velocity of the order of the bulk flow velocity (Bhatt and Mahesh, 2020; Ganesh et al., 2016). As cavitation develops with decreasing σ, the vapour fraction of the flow is expected to be significantly higher. This makes bubbly flows highly compressible and susceptible to condensation shocks (Brennen, 1995; Prosperetti, 2015). It has been demonstrated that the local Mach number (Ma) of the propagating bubbly shock-front in a developed cavitation flow could be as high as 4 (Brandao et al., 2019). In order to assess the effect of compressibility in cavitating flows, the quantification of vapour fraction and the pressure of the bubbly mixture becomes vital. Moreover, cloud cavitation, i.e. the implosion of the shed cloud, will inevitably give rise to a pressure wave. The strength of this pressure wave and its interaction with the attached vapour cavity dictate the cavity-shedding dynamics. In order to observe and study this interaction, it is also necessary to quantify the strength of the pressure wave. More importantly, it is imperative to see through the occluding vapour cavity. However, the bubbly-frothy nature of the flow presents a significant challenge to make a meaningful experimental observation. Naturally, the efficacy of light-based measurement techniques (such as shadowgraphy, and particle image velocimetry) is limited due to the lack of optical access induced by the opacity of the vapour cavity. Thus, non-optical measurement techniques such as X-ray densitometry or Magnetic Resonance imaging are favoured (Poelma, 2020). Furthermore, the cloud shedding and collapse dynamics occur at small time scales. Thus, whole-field, time-resolved measurements of vapour fractions are essential to gain insights into cavitating flow physics.

To this end, X-ray densitometry is emerging as a promising qualitative and quantitative measurement technique for studying cavitation dynamics. The ability of X-rays to penetrate through the liquid-vapour interface can circumvent the issues of optical artefacts manifested by refraction, diffraction and multiple scatterings (Aliseda and Heindel, 2021). Further, absorption-based X-ray imaging can provide quantitative information on the composition of two-phase mixtures. Stutz and Legoupil (2003) and Coutier-Delgosha et al. (2006) carried out vapour fraction measurements, with X-ray densitometry in a 2-D venturi and 2-D hydrofoil respectively, to investigate the two-phase morphology and the vapour fraction within the cavity. Further, Jahangir et al. (2019) studied cavitation in an axisymmetric venturi using time-averaged X-ray densitometry followed by computed tomography (CT) akin to Mitroglou et al. (2016). Similarly, Zhang, Khlifa, Fezzaa, et al. (2020) and Karathanassis et al. (2021) used synchrotron X-ray densitometry to study time-averaged vapour fractions to generate insights into cloud cavitation in a micro-venturi and a cylindrical orifice, respectively. These time-averaged measurements provide only a limited insight into the highly unsteady partial cavitation phenomena. The copious amount of literature originating from the group at the University of Michigan (Ann Arbor, USA) with high-speed X-ray densitometry (Mäkiharju, Gabillet, et al., 2013) has generated invaluable acumen into the physics of partial cavitation. Although their measurement system has a sufficiently high spatial resolution, the temporal resolution is insufficient to capture the entire shedding dynamics.

Furthermore, it has been shown that cavitation dynamics can be unique for each canonical flow geometry, such as wedges (Ganesh et al., 2016), hydrofoils (Wu, Ganesh, and Ceccio, 2019), backwards-facing steps (Bhatt et al., 2021), and bluff bodies (Wu et al., 2021). It should be noted that these studies are limited to external flows. The axisymmetric venturi, on the other hand, has a significant pressure gradient induced by the virtue of geometric confinement, i.e. walls (blockage). For instance, the area-based blockage (contraction ratio) in the previous is limited to 3 (Ganesh et al., 2016) and 1.15 (Bhatt et al., 2021). However, for the current geometry, the area-based blockage is ~ 9, which is substantially higher. Evidently, less attention is dedicated in the literature to characterising the dynamics and kinematics of the condensation shock front that dictates the cavity shedding in internal flows, despite the significant industrial relevance, such as venturis and throttle valves. Moreover, Jahangir et al. (2018) reported that the bubbly shock front underwent severe acceleration as it approached the throat. Therefore, the kinematics of the condensation shock front and its influence on the shedding dynamics are worth exploring.

In this chapter, we aim to clarify the role of the pressure wave emanating from the cloud implosion in periodic cloud cavitation at different flow conditions (σ). We employ an axisymmetric venturi as the flow geometry, as it remains less explored in the literature. Further, it allows us to build upon the insights gained from previous studies of Jahangir et al. (2018) and Gawandalkar and Poelma (2022). Time-resolved (3.6-6 kHz) X-ray densitometry is employed in conjunction with time-synchronised, high-frequency (100 kHz) dynamic pressure measurements and high-speed shadowgraphy to (i) track the propagating pressure discontinuity for the first time, (ii) visualise the interaction of the bubbly shock waves with the growing vapour cavity, and (iii) decipher the role of this interaction on the cavitation dynamics. This is done by quantifying characteristics of the pressure wave propagating in the low vapour fraction liquid and the bubbly shock front that is formed upon the impingement of the pressure wave on the growing cavity. The bubbly shock fronts are characterised by the vapour fraction and the pressure rise across the shock front along with the shock front velocity. The pressure rise across the front and its Mach number are used as proxies for the strength of the condensation front. The decreasing strength of the bubbly shock front (with increasing σ) is used to corroborate the observed cavitation dynamics at different σ. Our investigation shows that the kinematics, i.e. the acceleration of the condensation shock front, can play a significant role in dictating the cavity shedding dynamics in a high-blockage axisymmetric venturi. Based on this, we propose a modified phenomenological description of cavity shedding dynamics. A simple model can be constructed, which agrees with our experimental observations. Supersonic shock fronts are hypothesised to be readily favoured in such converging geometries, resulting in the destabilisation of vapour cavities via condensation.

This chapter is organised as follows; a description of the experimental setup, measurement technique and data processing approach is detailed in § 3.2. The results are reported in § 3.3: The vapour cavity topology, such as shape and vapour fractions are presented. Additionally, we discuss the time-resolved cavity dynamics at different cavitation numbers. The observed shedding dynamics are corroborated by quantifying the characteristics of the bubbly shock waves. Moreover, we shed light on the kinematics of

#	$P_d[kPa]$	$P_v[kPa]$	$U_t[ms^{-1}]$	$Re_t[-]$	$\sigma[-]$
1	59.9	3.83	11.15	1.86×10^5	0.90
2	56.36	3.42	11.22	1.87×10^5	0.84
3	56.17	3.59	11.59	1.93×10^5	0.78
4	59.33	4.01	12.91	2.15×10^5	0.67
5	59.39	4.22	13.49	2.25×10^5	0.61
6	56.38	3.86	13.54	2.25×10^5	0.57
7	44.95	3.67	13.38	2.23×10^5	0.47
8	36.26	4.56	12.80	2.13×10^5	0.39

Table 3.1: The flow parameters at different cavitation numbers (σ)

the condensation shock front and its interplay with the shedding dynamics, supported by a simple model. Finally, the phenomenological description of cavity shedding dynamics in an axisymmetric venturi is summarised in § 3.4.

3.2. EXPERIMENTAL SETUP AND METHODOLOGY

3.2.1. FLOW FACILITY

The experiments were performed in a cavitation loop, described in detail in Jahangir et al. (2018). Tap water is used as a working fluid, which was deionised, filtered and de-gassified for several hours before performing experiments. The flow is driven by a centrifugal pump, while the volumetric flow rate is measured with a magnetic inductive flow meter (KROHNE). The flow loop consists of plexiglass pipe sections with an inner diameter (D) of 50 mm. Cavitation is realised at the throat of the axisymmetric venturi, having a divergence angle of 8°, and which is installed $50D$ downstream of the last elbow. This acts as a flow development length, such that the incoming flow is fully developed turbulent pipe flow. The venturi has a throat diameter (D_t) of 16.67 mm, leading to an area-based contraction ratio of 9. The flow loop allows independent control of the flow rate and the global static pressure via a vacuum pump. The intensity of cavitation is dictated by the cavitation number (σ), defined as $\sigma = (P_d - P_v)/(\frac{1}{2}\rho {U_t}^2)$. Here, P_d is the far-downstream pressure, P_v is the vapour pressure and U_t is the throat velocity. P_v and the kinematic viscosity of the working fluid are determined using the measured temperature of the liquid during each run. In the current work, σ was varied between 0.39-0.90 by varying the global static pressure and U_t independently (see table 3.1 for detailed flow conditions). For consistency and comparison, the reproducibility of the flow was established by comparing global cavitation dynamics ($St_t = fD_t/U_t$ as a function of σ, where, $f = 1/T$ is the cavity shedding frequency and T is the shedding time period) with the previous studies.

3.2.2. X-RAY DENSITOMETRY

The time-resolved X-ray densitometry measurements were performed at the High-Speed X-ray (HSX) facility of TNO Ypenburg-The Hague, The Netherlands, shown in figure 3.1(*a*). The X-ray imaging facility consists of a Varian Medical Systems tube X-ray source

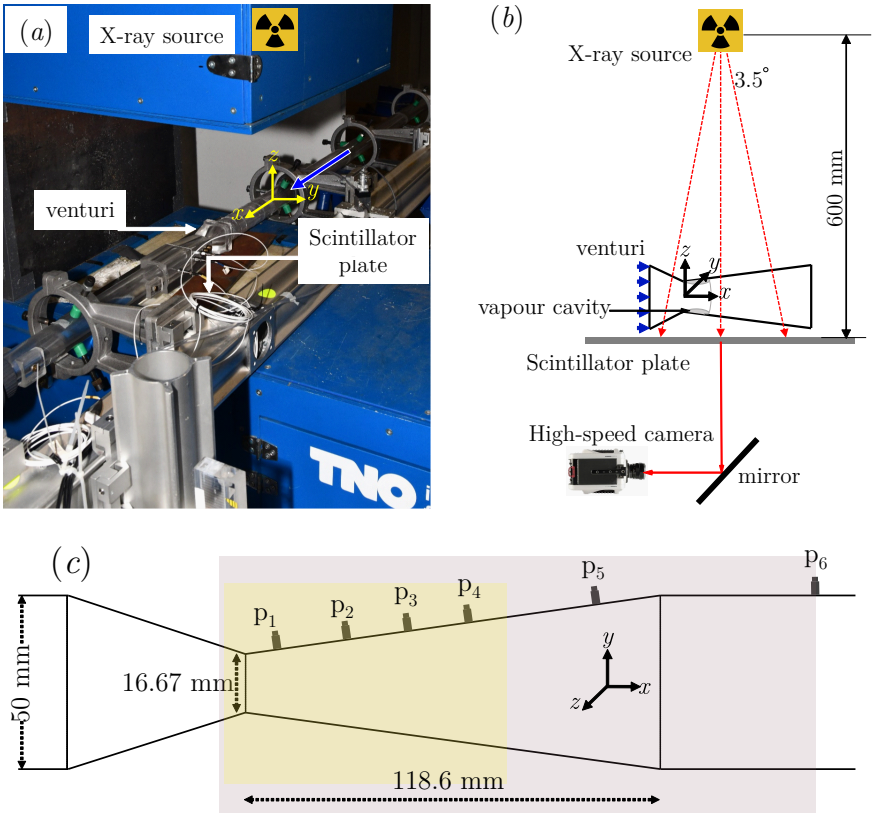

Figure 3.1: (*a*) High-speed X-ray (HSX) measurement imaging system at TNO-Ypenburg with the cavitation loop, the blue arrow shows the direction of bulk flow, (*b*) a schematic of the measurement system, (*c*) schematic showing the dimensions of the venturi, the position of the pressure ports, and the field of view of the X-ray densitometry (yellow) and high-speed imaging (grey).

capable of producing 150kV at 80kW. The anode insert is made of rhenium-tungsten molybdenum and produces a fan-beam of a maximum 12° cone angle. The source is coupled with a scintillator plate and image intensifier, wherein the attenuated X-ray (electrons) are converted into visible light. This is then imaged with a high-speed camera (Photron, FASTCAM NOVA S-12, 12,000 fps at 1 Megapixel) placed perpendicular to the scintillator plate as shown in figure 3.1(*b*). The scintillator plate and the image intensifier are made of the fastest Phosphor (P46), which has a decay time of about 20 μs. This ensures minimum 'ghosting' in the time series of X-ray images, allowing higher temporal resolution. It is crucial to note that the obtained X-ray images (radiographs) are z-averaged, i.e. along the X-ray beam direction. The density measurements via X-ray are based on the attenuation of the X-ray intensity by different materials through which it passes, governed by Beer-Lambert's law. Thus, by recording the incident intensity (I_0) and the intensity after passing through the bubbly flow (I), the mass density of fluid in-

tegrated along the X-ray beam path can be obtained, as per equation 4.1.

$$\frac{I}{I_0} = e^{-\sum_{i=1}^{N} \mu_i \rho_i x_i} \tag{3.1}$$

Here, I is the received intensity, I_0 the incident intensity, μ_i the medium attenuation coefficient, ρ_i the medium mass density, and x_i the path length through a medium. The summation accounts for multiple mediums such as plexiglass, liquid, and vapour. The X-ray source is at a distance of approximately 590 mm from the test section. The beam is incident on the test section in the $x-z$ plane. The axisymmetric venturi test section is modified such that the amount of plexiglass that is encountered by the X-ray beam is minimal while maintaining structural integrity. This ensures low X-ray baseline attenuation to augment the signal-to-noise ratio in the radiographs. The field of view (FOV) spans 70×50 mm^2 wherein the centre of the beam approximately coincides with the centre of the FOV (see the yellow region in figure 3.1*c*). Hence, the maximum angles subtended by the beam in x-direction and y-direction are 3.4° and 2.4°, respectively (see figure 3.1(*b*)). Thus, it can be assumed that the X-ray beam is nearly parallel as it passes through the region of interest. In the current experimental campaign, the X-ray source is operated at an amperage of 710 mA and voltage of 40 kV. This allowed enough separation in the X-ray image counts (contrast) to quantify the expected densities (0.8-1000 kg/m^3) in this geometry. With these settings, the X-ray source had a maximum run time of 0.63 seconds to avoid overheating of the anode. This enabled us to capture at least 32 shedding cycles for the slowest cavity shedding. The images are acquired at a frequency of 18,000 Hz.

3.2.3. HIGH-SPEED IMAGING

The cavity shedding dynamics are also visualised using conventional high-speed shadowgraphy to supplement the time-resolved X-ray densitometry. The FOV is centred along the venturi axis and spans 189×64 mm^2 in the $x-z$ plane, which is orthogonal to and larger than the FOV used in X-ray imaging (see the grey region in figure 3.1*c*). It is back-illuminated with a continuous white LED source. A high-speed CMOS camera (Photron Fastcam APX RS) equipped with an objective lens of 105 mm and aperture (f/7.2) ensures sufficient contrast between the liquid and vapour phase. The images are acquired at a rate of 18,000 Hz with an exposure time of 1/18,000 seconds.

3.2.4. PRESSURE MEASUREMENTS

The high-speed X-ray densitometry and shadowgraphy are complemented with high-frequency dynamic pressure measurements at various axial locations (p_1 to p_6; see figure 3.1(*c*)). The pressure port locations (p_1 to p_6) measured from the venturi throat are 0.6, 1.45, 2.5, 3.6, 5.9, 10.2D_t respectively. We employ several flush-mounted PCB102 sensors with a sensitivity of 0.15 mV/kPa and a rise time of <1 μs to pick up the fluctuations in local pressures at the specified axial locations (see again figure 3.1(*c*)). The pressure transducer has a nearly flat transfer function up to the sampling frequency of 300 kHz. Thus, pressure signals are reliably acquired at 100 kHz. The dynamic pressure acquisition is time-synchronised with the X-ray imaging using an external signal generator (KEYSIGHT 33210A). This is done with the aim of quantifying the pressure peak

brought about by the cavitation cloud implosion and pressure rise due to the propagating bubbly shock, both through the liquid and the attached vapour cavity. The pressure rise brought about by the condensation shock front in the attached cavity is measured at locations p_1 to p_3. The pressure peak due to the cloud implosion is measured at p_4 to p_6. Pressure transducers at multiple locations are used because (i) the expected cloud collapse region is a function of σ, and (ii) the high-frequency response of multiple pressure sensors at a fixed distance allows us to track the propagating pressure wave and thus estimate its propagation velocity in the low vapour fraction liquid. The unsteady *static* pressure in the cavity is measured at a fixed axial location (p_1) in a separate set of experiments using a flush-mounted IPSL series piezo-resistive silicon sensor with an accuracy of 0.25% of its full-scale (0-100 kPa) and response time of ~ 1.5 ms. The static pressure data is time-synchronised with high-speed imaging to omit the pressure data segments where the cavity does not cover the static pressure transducer.

3.2.5. PROJECTED VAPOUR FRACTION ESTIMATION

The raw X-ray images are enhanced to eliminate vertical stripes due to the electronic noise of the camera sensor. This is done using Fourier-based stripe filtering (Münch et al., 2009), followed by a median filtering with a kernel size of 5×5 pixels. This resulted in a maximum loss of 1 % in the energy (I^2) in the image. Further, a spatial mean filter of the same kernel size is applied to eliminate high-frequency noise. The image intensity of the bubbly mixture (I_m) is converted to vapour fraction (α) using a two-point calibration approach as per equation 3.2.

$$\alpha = \frac{\log \frac{I_m}{I_w}}{\log \frac{I_a}{I_w}} \tag{3.2}$$

This is based on assumptions that; (i) the flow is strictly two-phase (water and vapour), i.e. the mixture density (ρ_m) can be expressed as $\rho_m = \alpha\rho_a + (1-\alpha)\rho_w$, where w and a are subscripts for water and air respectively, (ii) the X-ray source is monochromatic (single energy), and (iii) the X-rays are nearly parallel. Further, a two-point calibration approach is deemed sufficient as also shown by Jahangir et al. (2019). The X-ray image of the venturi fully filled with water (I_w) and venturi fully empty/full air (I_a) were used for the calibration process. Note that air is used as a proxy for water vapour as their densities are comparable and almost three orders of magnitude lower than that of water. Further, a metal calibration grid is used for geometric calibration. Thus, the projected vapour fractions are resolved with a spatial resolution of 0.45 mm ($0.027D_t$) and a temporal resolution of 1/3600 seconds (averaging over five frames) to 1/6000 seconds (averaging over three frames), depending on the cavitation number (σ). The cavitation dynamics are faster at higher σ, hence for these cases, we evaluate vapour fractions at a higher temporal resolution to capture essential flow dynamics. Furthermore, the signal-to-noise ratio (SNR) in X-ray radiographs reduced for higher σ due to low vapour fractions in the flow. Hence, the vapour fraction could not be measured reliably for $\sigma > 0.90$. This also precludes pressure wave characterisation at such σ. In order to make a rough estimate of the uncertainty level in vapour fraction measured via the current X-ray densitometry system, we examined the measured vapour fraction *upstream* of the venturi throat. This region contains pure liquid for which the vapour fraction ought to be 0. The measured

instantaneous vapour fraction upstream is < 0.05.

3.2.6. PLANAR VAPOUR FRACTION ESTIMATION

In the axisymmetric venturi, the vapour formation is localised in the near-wall region due to the pressure field. Consequently, the z-projected X-ray images estimate vapour fraction close to the wall with good accuracy, however, they will overestimate vapour fractions in the core of the venturi. Thus, the time-averaged ($\overline{\alpha(x,y)}$) and the phase-averaged ($\langle\alpha(x,y,t/T)\rangle$) projected vapour fractions are back-projected using Filtered Back Projection (FBP) via the ASTRA toolbox (van Aarle et al., 2016) to yield planar vapour fractions. This is commonly referred to as computed tomography (CT). A similar approach was used by Jahangir et al. (2019) and Mitroglou et al. (2016) to estimate time-averaged void fractions. However, due to the high temporal resolution in this study, we extend their approach to phase averages to resolve vapour fractions in a shedding cycle. The demonstrated periodicity in the cavitation dynamics allows us to perform phase-averaging similar to Gawandalkar and Poelma (2022). It is however imperative to realise that CT does not provide any additional information in the present study as the imaging is limited to a single camera view. The aim of CT is thus to estimate the planar ($x-y$) vapour fraction fields (β) to provide experimental data for the validation of numerical models. This approach is subject to assumptions, i.e. (i) the X-rays passing through the attached cavity are near-parallel, and (ii) the attached cavity is axisymmetric in an averaged sense (time and phase). CT reconstructions are performed on the z-projected averaged X-ray images (time and phase), which serve as an input to the FBP algorithm, while attenuation coefficients (μ_m) are generated as an output. Further, μ_m values are converted into β using the two-point calibration (see equation 3.3).

$$\beta = \frac{\mu^m - \mu^w}{\mu^a - \mu^w} \tag{3.3}$$

The two reference points are the attenuation due to pure liquid (μ^w for $\beta = 0$), and pure vapour (μ^a for $\beta = 1$). This yields vapour fractions in a $y-z$ plane, as detailed extensively in Jahangir et al. (2019). Further, this process is repeated for each axial location (x) and reconstructed $y-z$ planes are stacked along the central axis of the venturi (x-axis). Finally, planar vapour fraction fields, $\overline{\beta(x,y)}$, are extracted from the reconstructed 3-D vapour fraction fields at the centre plane. Similarly, phase-averaged planar void fractions ($\langle\beta(x,y,t/T)\rangle$) are also obtained.

3.3. RESULTS

3.3.1. VAPOUR FRACTIONS FIELDS

The time-averaged planar vapour fraction field ($\overline{\beta(x,y)}$) along with the radial profiles of $\overline{\beta(x,y)}$ for the lowest cavitation number (σ = 0.47), are shown in figure 3.2(*a*) and (*b*), respectively. It can be seen that $\overline{\beta(x,y)}$ achieves a maximum value of 0.43 near the wall (close to the throat), while the vapour fraction is 0.05 in the core of the venturi, a value comparable to the measurement uncertainty. The time-averaged vapour fraction gradually reduces away from the throat as the vapour cloud is convected downstream. This is consistent with the previous observations of Jahangir et al. (2019), who measured time-

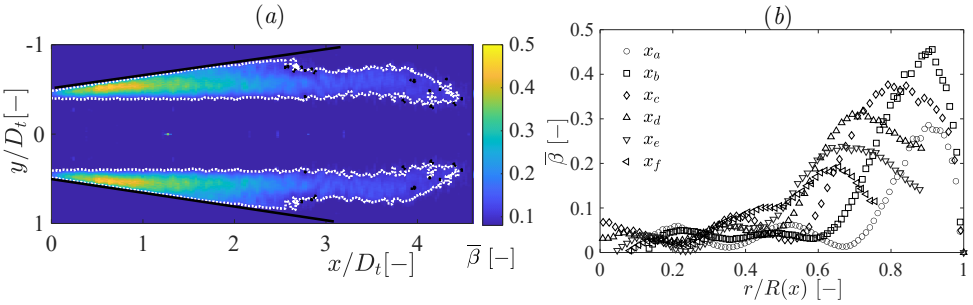

Figure 3.2: (*a*) Time-averaged back-projected planar vapour fraction field ($\overline{\beta}$). The white dotted outline indicates the vapour-liquid interface ($\overline{\beta}$=0.1), while the black solid lines indicate the venturi wall, (*b*) profiles of $\overline{\beta}$ at different axial locations (x_a to x_f: 0.12, 0.55, 1.1, 1.7, 2.2, 2.8 D_t) in the venturi for σ = 0.47, where $R(x)$ is the local venturi radius.

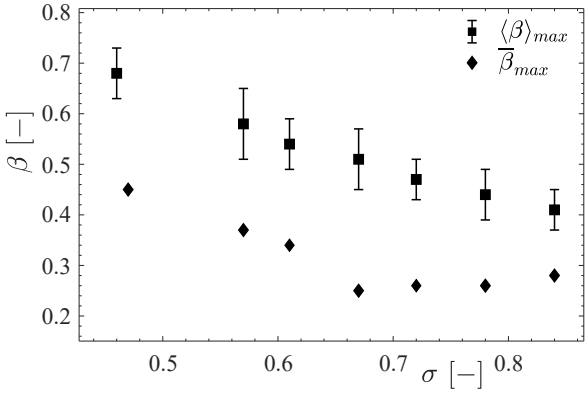

Figure 3.3: The phase-averaged maximum vapour fraction in a shedding cycle ($\langle\beta\rangle_{max}$) and maximum time-averaged vapour fraction ($\overline{\beta}_{max}$) at different cavitation numbers (σ).

averaged vapour fractions at σ = 0.40. Further, the instantaneous vapour fraction in a cycle (or a phase) can be as high as 0.68 at the same flow conditions, see figure 3.3. In the same figure, it can be seen that the maximum vapour fraction in a cycle is significantly higher than the maximum time-averaged vapour fraction. This is attributed to the temporal averaging of vapour fractions due to the periodic growth and collapse of the cavity. Further, the maximum vapour fraction decreases with σ. This shows the necessity of time-resolved vapour fraction fields in such flows.

3.3.2. VAPOUR CAVITY TOPOLOGY

The phase-averaged planar vapour fractions, $\langle\beta(x, y, t/T)\rangle$, also allow us to quantify the shape and size of the attached vapour cavity in a venturi. The Froude number ($Fr_{L_c} = U_t/\sqrt{gL_c}$) defined on the cavity length is $\gtrsim 20$. Hence, the effect of gravity on the cavity shape can be expected to be negligible. Further, the Weber number ($We_{L_c} = \rho U_t^2 L_c/\gamma$) is $\mathcal{O}(10^4)$, so the effects of inertia dominate the surface tension (γ) effects. The iso-contour

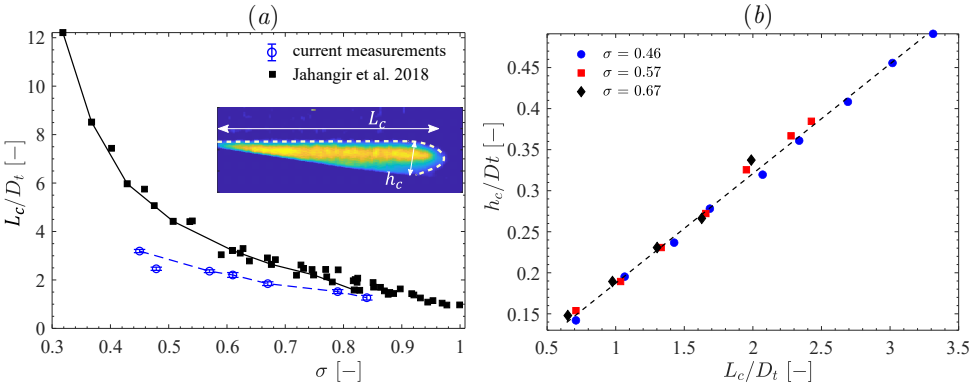

Figure 3.4: (*a*) Maximum cavity length (L_c) normalised with the throat diameter (D_t) as a function of cavitation number (σ). Square markers show shadowgraphy measurements of Jahangir et al. (2018), while circles show current X-ray densitometry measurements. The white dotted outline in the inset shows the isocontour of β = 0.1, demarcating the cavity interface. (*b*) Maximum cavity thickness (h_c) normalised with D_t for different cavity lengths and σ.

of $\beta = 0.1$ is used to demarcate the boundary of the cavity, see inset in figure 3.4(*a*). Since the attached vapour cavity grows in a shedding cycle, the maximum cavity length (L_c) and maximum cavity height (h_c) are used to describe the topology of the attached cavity. The maximum cavity length for different σ is shown in figure 3.4(*a*). It can be seen that L_c/D_t measured by X-ray densitometry is systematically shorter than the results from shadowgraphy (Jahangir et al., 2018), with a deviation up to 50% at $\sigma = 0.47$. This observation is not sensitive to our chosen threshold of $\beta = 0.1$ to demarcate the cavity: L_c estimated with a threshold of $\beta = 0.05$ is about 4 pixels ($0.02D_t$) higher than with a threshold of $\beta = 0.1$. L_c remains unaltered with an increase of threshold β from 0.1 to 0.15. The observed deviation could be attributed to the difficulty in defining the vapour content (vapour fractions) and thus cavity in shadowgraphs (Dash et al., 2018). The vapour bubbles detached from the cavity may appear to be a part of it in shadowgraphs, overestimating cavity lengths. The maximum thickness of the attached cavity (h_c) is also quantified (see figure 3.4(*b*)). It is observed that h_c increases monotonically with the cavity length. Further, cavity height scales directly with the cavity length, irrespective of the cavitation number.

3.3.3. VAPOUR SHEDDING DYNAMICS

The time-synchronised X-ray imaging with dynamic pressure (dp) measurements allows us to visualise the shedding dynamics and ascertain the role of a pressure wave in the shedding cycle at different cavitation numbers (σ). The instantaneous projected vapour fractions (α) are used to visualise the cavity dynamics. The colour indicates the vapour fraction: blue being a completely liquid phase, while yellow being a higher vapour content. Further, the cavity front evolution in a shedding cycle is studied with a space-time ($x-t$) plot of α. The fixed axial locations of the pressure transducers make dp measurement at the *exact* location of each cloud collapse cumbersome. Thus, the dp measurement closest to each cloud collapse location is used to measure the cloud implosion

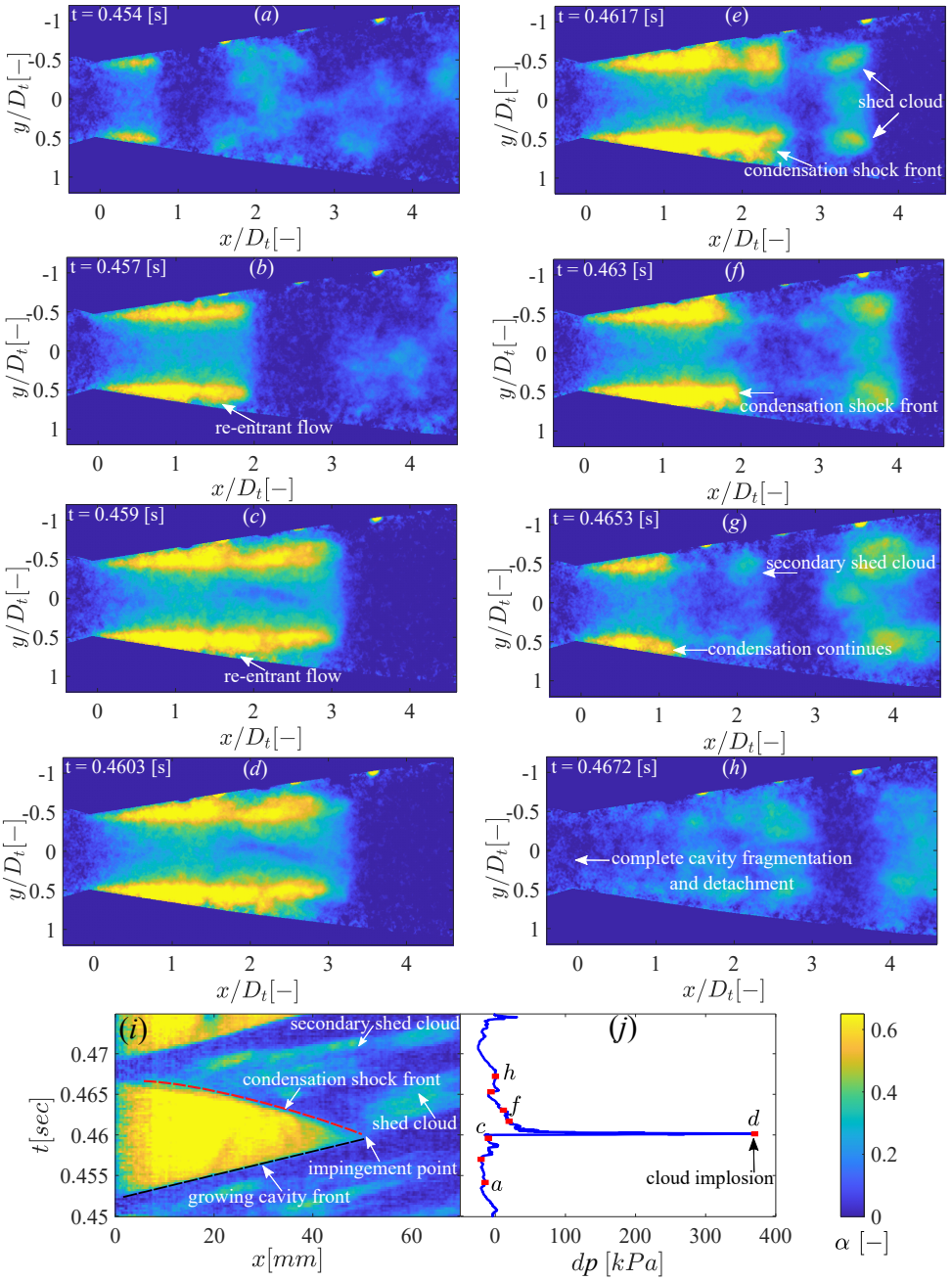

Figure 3.5: (*a-h*) A single shedding cycle at $\sigma = 0.47$, (*i*) the $x-t$ evolution of the vapour fraction for this shedding cycle, (*j*) the time-trace of the dynamic pressure recorded simultaneously at p_6. The bulk flow is from left to right. The colour indicates the z-projected vapour fractions.

pressure peak. This peak arrives at the transducer with a minor delay, as discussed in the next paragraph. A single representative shedding cycle will be shown for σ = 0.47, 0.78 and 0.84 in the following discussion.

The cavity dynamics at $\sigma = 0.47$ is illustrated in figure 3.5. The cavity is seen to grow from (*a*) to (*c*). As the cavity grows, there is a continuous re-entrant flow beneath the cavity at the closure region, as shown in figure 3.5(*b*) and (*c*). This is inferred from a fairly low vapour fraction close to the venturi wall ($\alpha \sim 0.2$) in comparison to the vapour cavity ($\alpha = 0.7$). The presence of a re-entrant jet for the considered range of σ was also directly observed by Gawandalkar and Poelma (2022) with near-wall velocimetry in the same flow geometry. At the instance marked by '*d*' (see figure 3.5(*j*)), the imploding cavitation cloud from the *previous* shedding cycle gives rise to a pressure wave, evident from a strong pressure peak in dp at p_6. The cloud collapse appears to have been coherent, as evident from a single sharp peak of 340 kPa for a very short duration. The cloud collapse itself could not be visualised in the X-ray images at this σ, as the collapse is expected to occur at $x \sim 9D_t$, as observed in previous high-speed shadowgraphy (Jahangir et al., 2018). Note that the structure labelled 'shed cloud' in figure 3.5(*e*) will result in a pressure peak in the *next* cycle. The pressure wave emanating from the collapse propagates through the low-vapour-fraction liquid: The high-frequency pressure transducers at p_5 and p_6 pick up the pressure wave propagating at a velocity (u_{pw}) of ~ 450 ms^{-1}. This is estimated using the time delay between the peaks and the distance between the transducers. There is a small time delay between the cloud implosion and the pressure wave reaching the pressure transducer (~ 0.04 ms, estimated using u_{pw} and transducer locations). Additionally, there is a time delay (~ 0.24 ms) between the cloud collapse and the impingement (see next paragraph) on the cavity due to the finite distance between the cloud implosion and the impingement point. However, these time delays are negligible in comparison to the cavity shedding time period (T) of 17.4 ms. For all intents and purposes, the $x-t$ diagram and pressure signals can thus be considered to be synchronous, with no time delay between cloud collapse and impingement.

The upstream travelling pressure wave impinges on the attached cavity and arrests the cavity growth. Here, impingement is defined as the first point of interaction between the pressure wave and the attached cavity. The impingement leads to a maximum cavity length, referred to as L_c. The 'impingement point' can be seen in the $x-t$ evolution of the cavity front in figure 3.5(*i*), where the growing cavity front is shown by a black dashed line, while the retracting cavity front is shown by a red dashed curve. Due to this impingement, a large part of the cavity gets shed (see figure 3.5(*e*)) and is then convected downstream with the bulk flow, where it will implode. After impinging, the upstream-travelling pressure wave *immediately* starts condensing the attached cavity. The condensation shock front is seen to travel upstream through the cavity, destabilising the attached cavity. This process is more clear in the supplementary movie S1. The shock front is also evident in the $x-t$ diagram as shown in figure 3.5(*i*): it is shown by a red dashed curve and is characterised by a sharp decrease in vapour fraction across it. The inverse of the slope of the condensation shock front in the $x-t$ plot is the shock front velocity.

It can be observed that the shock front accelerates significantly as it approaches the throat, as evident from the changing slope of the shock front. This will be addressed

in subsection 3.3.7. Further, some amount of vapour remains after the shock front has passed over the cavity and condensed it. This leads to low vapour-fraction streaks in the $x-t$ plot and is also indicated by the 'secondary shed cloud' in figure 3.5(*g*). This is suspected to be a result of the interaction of the bubbly shock wave with the attached cavity, which is essentially composed of coalesced vapour bubbles. The condensation shock front travels upstream and reaches the throat, resulting in complete cavity fragmentation and destabilisation. This is in line with the previous observations of Ganesh et al. (2016) and Jahangir et al. (2018), and Budich et al. (2018) at low σ. This is followed by a brief period where the venturi throat is left 'cavitation-less'. Meanwhile, the shed cloud is convecting downstream. This completes a shedding cycle until a new cavity starts growing at the throat as described above.

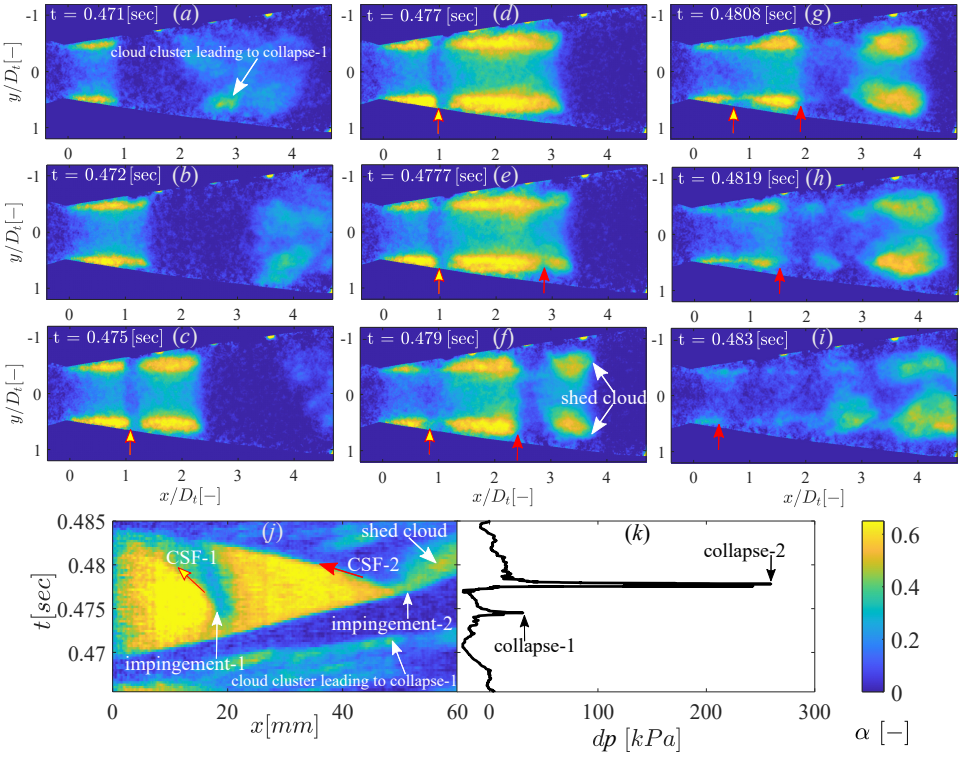

Figure 3.6: (*a*)-(*i*) A shedding cycle at σ=0.47, showing multiple condensation shock fronts (CSF) in one cycle. (*j*) shows the $x-t$ evolution of the cavity front, while (*k*) shows the dp time-trace recorded simultaneously at station p_6. The arrows show propagating condensation shock fronts: CSF-1 is marked by a yellow arrow with a red outline, while CSF-2 is marked by a full red arrow.

It is worthwhile to note that in a few (three in forty) shedding cycles at $\sigma = 0.47$, multiple bubbly shock waves are seen to travel through the growing cavity (see figure 3.6), exhibiting multi-step cavity shedding modes. Interestingly, the implosion of the secondary shed cloud (from the previous cycle, shown in figure 3.6(*a*)) produces a weaker pressure wave ($dp \sim 30$ kPa, 'collapse-1' in figure 3.6(*k*)). This gives rise to an *upstream*-travelling

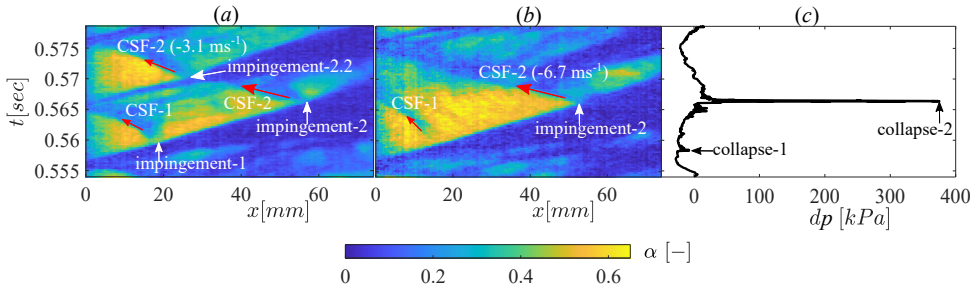

Figure 3.7: A shedding cycle at σ=0.47, showing multiple condensation shock fronts (CSF), (*a*) shows the *upper* part of the vapour cavity, while (*b*) shows the *lower* part of the cavity. (*c*) The dp time-trace is recorded simultaneously at station p_6.

bubbly shock wave as indicated by 'CSF-1' (see the yellow arrow in figure 3.6). This is inferred from collapse-1 coinciding in time with the emergence of CSF-1 in figure 3.6(*j*). However, the rate of vaporisation at the throat is expected to be high, dictated by the pressure at the throat. Thus, the cavity continues to grow to assume its maximum length (L_c). During this time, the bubbly shock wave (CSF-1) appears frozen for a while before it moves upstream very slowly, as shown by the yellow arrow in figure 3.6(*c*)-(*e*). The rate of vapour production near the throat is likely sufficiently high to oppose the shock front propagation. This is followed by a stronger cloud implosion ($dp \sim 260$ kPa, 'collapse-2') producing a 'CSF-2' (see the red arrow in figure 3.6) that ultimately destabilises the cavity similar to the shedding cycle shown in figure 3.5. Furthermore, it is clear from the $x-t$ plot (figure 3.6(*j*)) that the initial velocity of 'CSF-1' (-2.2 ms^{-1}) is substantially lower than 'CSF-2' (-6.4 ms^{-1}). Consequently, an earlier smaller cloud implosion does not have any consequence on the global shedding dynamics. Instead, the larger cloud implosion dictates the cloud shedding frequency.

Similarly, in a limited number of shedding cycles (two in forty), it is observed that the cavity undergoes asymmetric cavity detachment. It is seen that the upper (figure 3.7(*a*)) and the lower part (figure 3.7(*b*)) of the cavity show different growth and shedding behaviour. It is seen that the cavity starts condensing due to CSF-1 emanating from collapse-1 (see 'impingement-1' in figure 3.7(*a*) and 'collapse-1' in figure 3.7(*c*)). The upper part of the cavity gets completely condensed, while the lower part is partially condensed. To this end, the vapour production rate is high enough for the cavity to keep growing near the throat. However, the pressure wave due to the implosion of the cloud from the previous cycle ('collapse 2' in figure 3.7(*c*)) is already travelling upstream. The propagating shock-front (CSF-2) impinges on the cavity at impingement-2 and *condenses* the vapour it comes across (see figure 3.7(*a*) and (*b*)). Further, it encounters a growing cavity front leading to impingement 2.2 as shown in figure 3.7(*a*). Consequently, the propagating velocity of the shock front reduces significantly from -6.7 ms^{-1} to -3.1 ms^{-1}. This leads to the condensation shock fronts experiencing two distinct velocities, as evident from the two different slopes of the fronts (CSF-2) shown in figure 3.7(*a*). This suggests that the condensation shock front, after impingement 2.2 (see figure 3.7(*a*)) has to overcome the strong vaporisation (cavitation) brought about by the low pressure at the throat. The above anomalous shedding cycles may cause cycle-to-cycle variations,

however, the condensation shock front due to the larger pressure pulse is seen to enforce a strong periodicity in the cavity shedding dynamics. This was confirmed by a matching sharp peak in the Fast Fourier Transform (FFT) of pressure and vapour fraction time series(s) at such σ (see figure 3.19 in appendix 3.A).

As the cavitation number increases ($\sigma = 0.78$), we observe slightly different cavitation dynamics with respect to the bubbly shock front. The vapour cavity grows linearly as shown in figure 3.8(*a*)-(*c*). The cavitation cloud shed from the previous cycle, shown in figure 3.8(*b*), will implode in the downstream region. However, the cloud collapse appears less coherent as evident from multiple small peaks around the main peak, giving rise to a low-pressure rise ($dp \sim 120$ kPa) recorded at p_5 location (see figure 3.8(*j*)). The cloud implosion gives rise to the upstream travelling pressure wave that impinges on the growing attached cavity, arresting the cavity growth. The impingement is evident from the change in the slope of the cavity front at the impingement point, as shown by the two black dotted lines in figure 3.8(*i*). The 'bubbly shock wave' is seen to propagate through the cavity without significant condensation, as shown by snapshots in figure 3.8(*d*)-(*e*) and a white dotted line in $x-t$ plot (see figure 3.8(*i*)). The pressure wave can propagate through the cavity if the shock front is subsonic (Brandao et al., 2019). As it travels further upstream, it begins to condense the cavity (see again red arrow in figure 3.8(*f*)-(*g*)). See also supplementary movie S2. The shock front can be seen more clearly by the emergence of a sharp change in the vapour fraction across the travelling front, as shown by the red dashed curve in figure 3.8(*i*). This coincides with the observed acceleration of the shock front as it approaches the venturi throat, inferred from the changing slope of this red dashed curve. The condensation front then reaches the throat, resulting in complete cavity condensation and eventual shedding.

At higher cavitation numbers ($\sigma = 0.84$), two different *types* of shedding cycles are seen. In a few cycles, a pressure wave transformed into a condensation shock front is seen to cause cavity destabilisation, similar to $\sigma = 0.78$ (see figure 3.9). In other cycles, the cavity dynamics differ, as shown in figure 3.10. The vapour cavity grows linearly in time (figure 3.10(*a*)-(*d*)). At the instance marked '*e*' in figure 3.10(*j*), the cloud implosion from the previous cycle gives rise to an incoherent and a lower pressure rise ($dp \sim 60$ kPa). The dynamic pressure time trace is recorded at location p_4. The upstream travelling pressure wave cannot be seen impinging on the growing cavity in the $x-t$ diagram in figure 3.10(*i*). Moreover, the slope change of the cavity front growth is smoother and not abrupt as in the previously considered cases of $\sigma = 0.47$ and 0.78. This is shown by a black dashed curve in figure 3.10(*i*). There is no sharp upstream travelling vapour fraction discontinuity in the $x-t$ evolution of the cavity following the cloud implosion, as clear from figure 3.10(*i*). It can be hypothesised that the pressure wave propagates upstream through the attached cavity *without* condensing it. Thus, there is no significant effect of the cloud implosion on cavity growth and detachment. Instead, we observe that the cavity gets pinched off near the venturi throat (see figure 3.10(*h*)) and rolls up to form a convecting cloud, similar to shedding brought about by the re-entrant jet travelling beneath the cavity. This can be seen in the supplementary movie S3. With a further increase in σ (~ 0.9), most shedding cycles are seen to be destabilised by the re-entrant jet. It was also previously shown by Gawandalkar and Poelma (2022) that there is a strong upstream-travelling re-entrant jet below the cavity in the same flow geometry at these

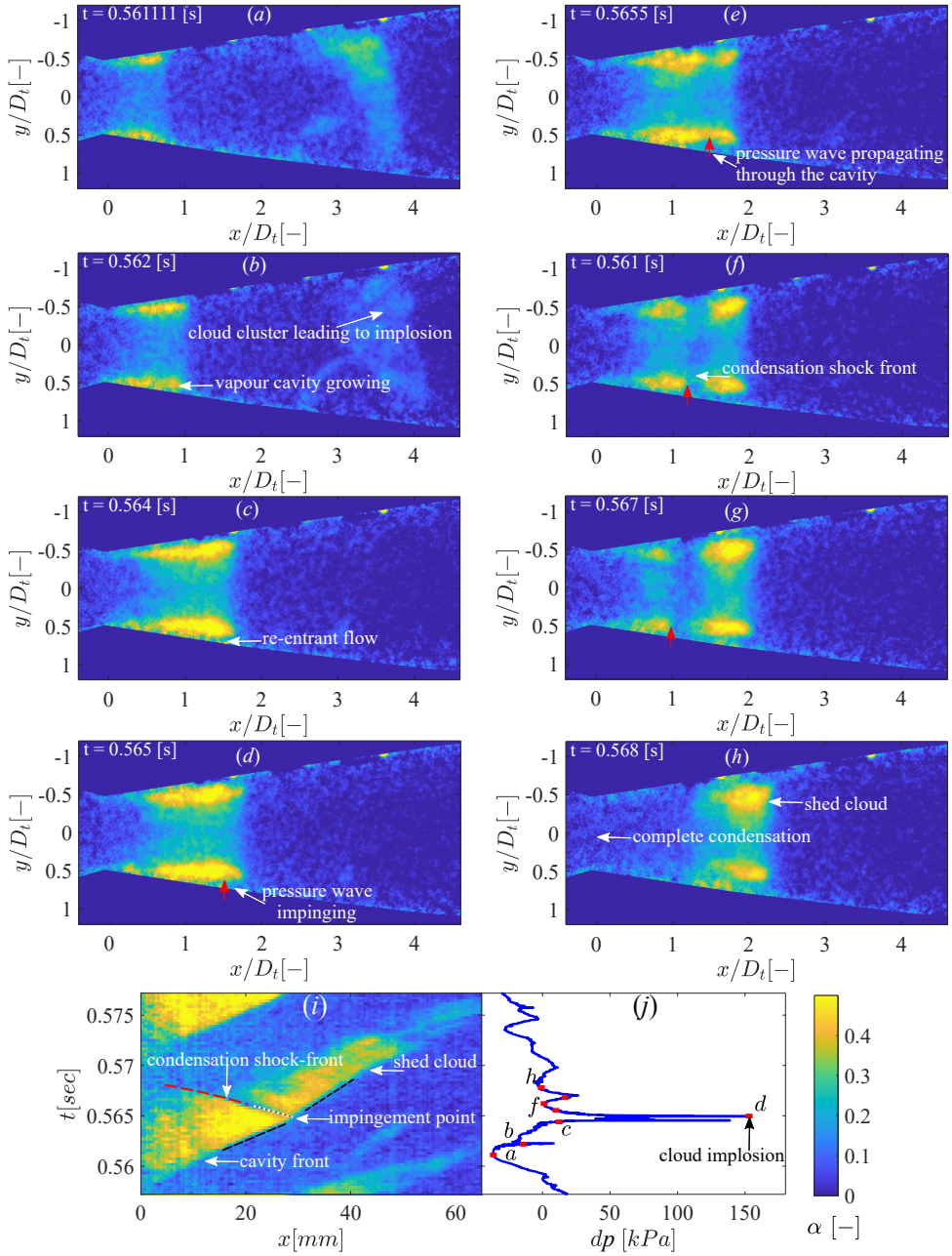

Figure 3.8: (*a*)-(*h*) A single shedding cycle for the case of $\sigma = 0.78$, (*i*) shows the $x-t$ evolution of the vapour fraction of the cavity, (*j*) shows the dynamic pressure corresponding to the above cycle recorded simultaneously at station p_5.

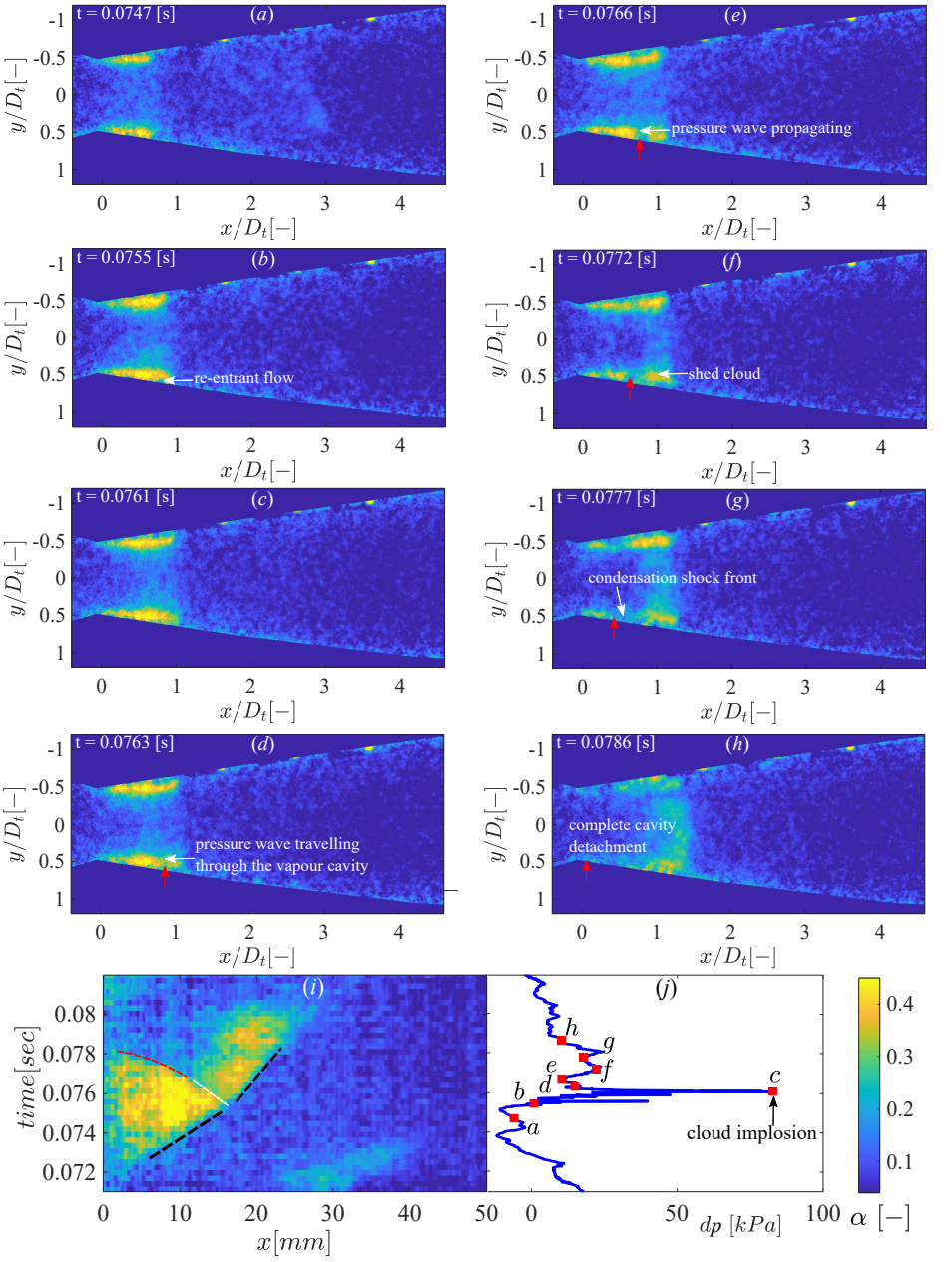

Figure 3.9: (*a*)-(*h*) A single shedding cycle for a case of $\sigma = 0.84$, (*i*) shows the $x-t$ evolution of the vapour fraction of the cavity, (*j*) shows the dynamic pressure corresponding to the above cycle recorded simultaneously at station p_5.

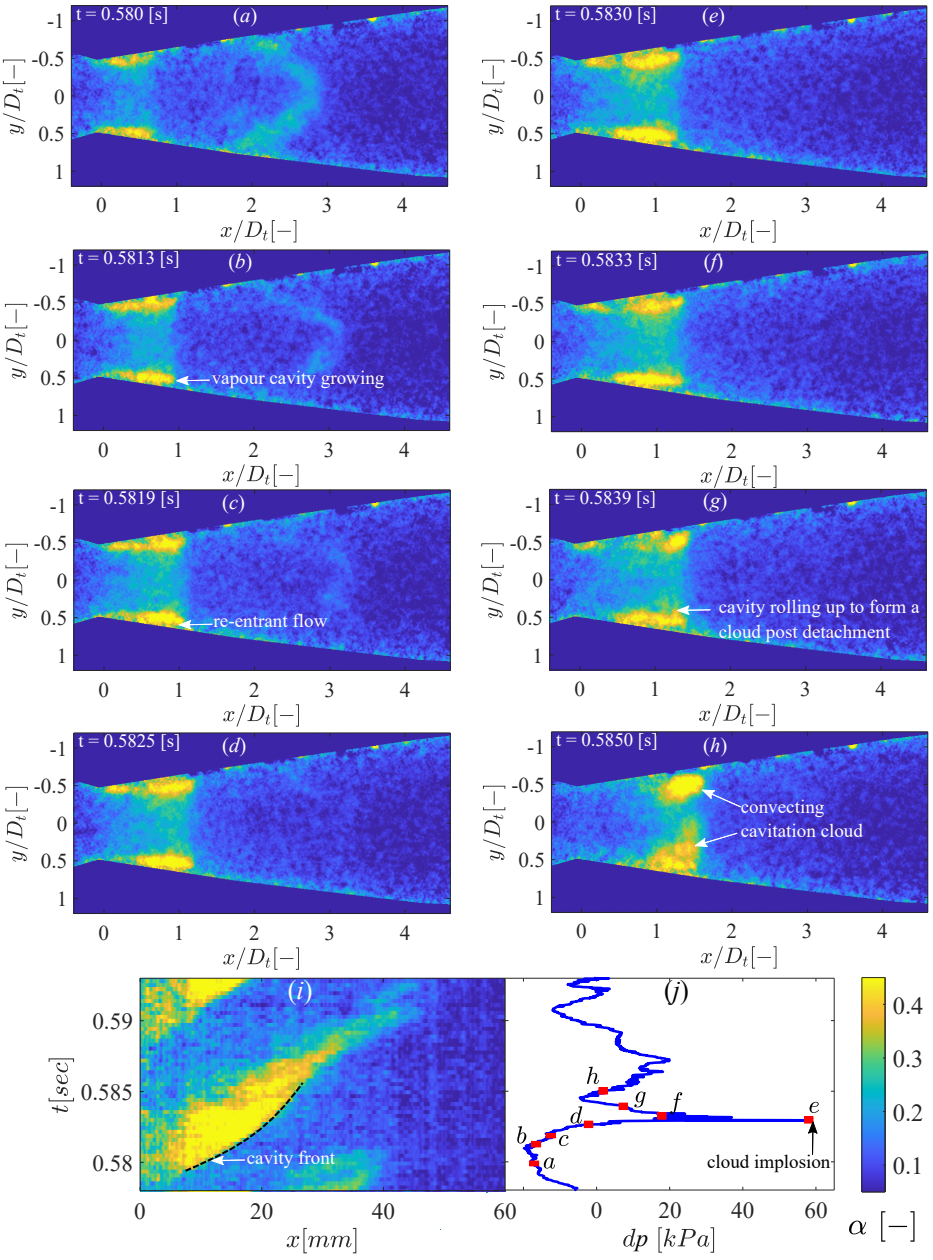

Figure 3.10: (*a*)-(*h*) A single shedding cycle for a case of $\sigma = 0.84$. The figure layout is the same as the previous figure. The dynamic pressure is recorded at station *p*4.

higher σ.

It is important to stress that these two types of cavity shedding mechanisms are fundamentally different: at low σ, the cavity gets condensed and fragmented by the condensation front before the new cavity starts growing. However, at high σ, a strong re-entrant jet below the vapour cavity pinches the cavity before the new cavity starts growing. It is confirmed in our study that the likelihood of the re-entrant jet causing cavity shedding increases with the increase in σ as also shown recently by Bhatt et al. (2023). Pressure waves due to cloud implosions are present at *all* σ (Gawandalkar and Poelma, 2022). These observations suggest that both pressure waves emanating from the cloud implosion and re-entrant jets are present to destabilise the attached cavity for a given σ. However, the way in which the pressure wave interacts with the attached cavity dictates the dominant shedding mechanism. At low σ ($\lesssim 0.78$), the pressure wave gets transformed into a condensation shock front in nearly every shedding cycle, condensing and fragmenting an attached cavity. However, at $\sigma \sim 0.84$, the pressure wave cannot transform into a condensation shock in all the shedding cycles. In these cycles, the attached cavity is destabilised by a re-entrant jet. With an even further increase in σ (~ 0.97), the attached cavity is destabilised solely by the re-entrant jet as shown previously by Gawandalkar and Poelma (2022). The correlation between the pressure peaks due to cloud collapse and cavity detachment is further established by computing the dominant frequency of the α and dp time signals for a range of σ, as discussed in Appendix 3.A. Further, the time scale of the condensation shock front is in agreement with the global shedding frequencies at low to moderate σ, as presented in Appendix 3.B.

3.3.4. CHARACTERISTICS OF BUBBLY SHOCK WAVES

In order to understand the above-mentioned shedding behaviour(s), it is imperative to understand the interaction of pressure waves with the attached vapour cavity. Thus, we characterise bubbly shock waves travelling through the cavity. In particular, we use the vapour fraction pre-shock front (α_1), post-shock front (α_2), pressure rise across the shock front (Δp), the velocity of the condensation shock front (u_{sf}), and Mach number (Ma_{sf}) to characterise the bubbly shock waves. Further, all the quantities are phase-averaged using the approach detailed in Gawandalkar and Poelma (2022). The standard deviation of the phase average is expressed as error bars. The error bars can be attributed mainly to the cycle-to-cycle variation in shedding dynamics along with random noise in the measurement.

The pressure wave emanates from cloud collapse/implosion in the downstream region of the venturi. This is inferred from the sharp peak in the dynamic pressure (dp) signal during the shedding process (see panel (*j*) in figure 3.5, 3.8, and 3.10). The pressure peak brought about by the cloud implosion is recorded by the transducer closest to the collapse location (p_4, p_5 or p_6, see figure 3.1 for a schematic). It can be seen that the phase-averaged pressure peak ($\overline{dp}$) decreases significantly with increasing σ, as shown in figure 3.11(*a*). The pressure wave propagating through the low vapour fraction region is detected as a pressure discontinuity by transducers at p_4 to p_6 locations. The availability of multiple transducers allows us to track this pressure discontinuity in time. The time delay between the peaks and the distance between the transducers are used to estimate its velocity of propagation ($\overline{u_{pw}}$). The pressure wave is seen to prop-

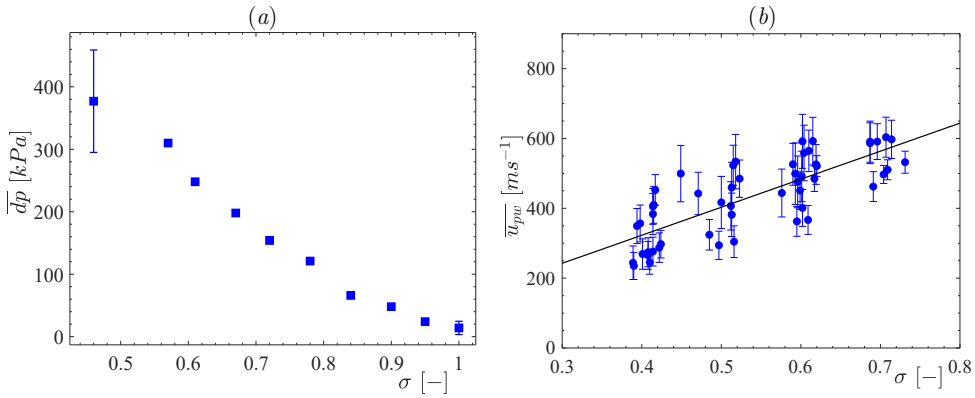

Figure 3.11: (*a*) The phase-averaged pressure rise due to the cloud implosion recorded in the pressure recovery section (p_4, p_5 or p_6, whichever is closest to the location of the cloud implosion). (*b*) The phase-averaged velocity of the pressure wave travelling through the liquid, measured using dynamic pressure transducers at p_4 to p_6.

agate at a velocity which is an order of magnitude higher than the bulk velocity (U_t), as shown in figure 3.11(*b*). This pressure wave, after impinging on the cavity, interacts with it, i.e. condenses it. The pressure rise (Δp) associated with this bubbly shock wave was recorded using multiple pressure transducers, located at p_1, p_2, and p_3 (see again figure 3.1 for a schematic). The pressure rise magnitude is measured as the shock front propagates through the attached cavity.

An example of the pressure wave dynamics and its interaction with the growing cavity is shown for $\sigma = 0.67$, in figure 3.12. The collapsing cloud is shown in figure 3.12(*a*) and (*b*). Note that the collapse takes place to the right side of the p_3 location, which in this case falls within our FOV. The pressure wave emanating from this implosion propagates upstream through the liquid and is first picked up by the pressure transducer at p_3: See the sharp peak (marked as *b*) in the red dp signal in figure 3.12(*g*). Further, this discontinuity is seen to propagate through the cavity as a condensation shock front (marked by red arrows) as identified near p_2 in figure 3.12(*d*) and p_1 in figure 3.12(*e*). This coincides with the pressure rise at p_2 (marked '*d*' in green time signal) and p_1 (marked '*e*' in blue time signal), as shown in figure 3.12(*g*). It is important to note that the condensation shock front appears somewhat obscure in these high-speed images, necessitating vapour fraction measurements like in this study. The pressure rise (Δp) at p_1 appears to be higher than the pressure rise at p_2. This will be addressed in subsection 3.3.7. It is observed that the pressure discontinuity (Δp) across the condensation front is weaker, i.e. the pressure rise is almost one order of magnitude lower than the pressure peak (dp) due to the cloud implosion. The phase-averaged Δp across the condensation front decreases with increasing σ as shown in figure 3.13(*a*). Thus, the pressure rise caused by the condensation shock front at higher σ is lower, indicating that the strength of the condensation shock front is decreasing with increasing σ. This then coincides with the condensation shock front becoming a less dominant shedding mechanism, as illustrated by the observed shedding dynamics.

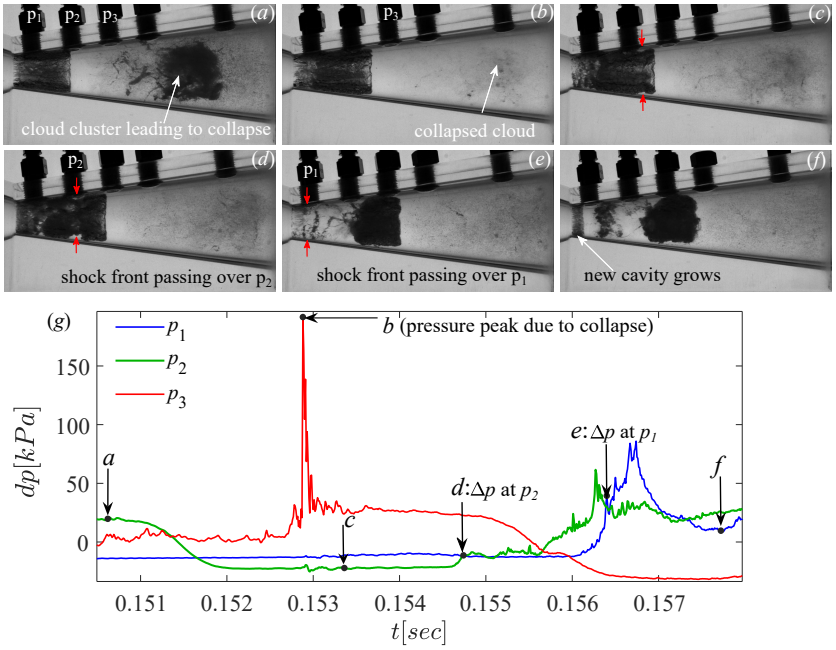

Figure 3.12: (*a*)-(*f*) High-speed shadowgraphs show the propagation of the condensation shock front through the vapour cavity at σ=0.67 (red arrows show the bubbly shock wave signature), (*g*) the corresponding dynamic pressure time-series at three axial locations (p_1, p_2, p_3) exhibits the pressure rise brought by it.

The vapour fraction is quantified using time-resolved X-ray densitometry, as mentioned with an uncertainty of less than 5%. The vapour fractions on either side of the condensation shock front (red dashed curve in figures 3.5(*i*), 3.8(*i*), and 3.9(*i*)) are expressed as α_1 and α_2 (see also inset in figure 3.13(*c*). The vapour fraction ahead of the condensation shock front (α_1) varies from 0.83 to 0.45 with a variation of σ from 0.39 to 0.84. α_1 decreases monotonically with σ. However, the post-shock vapour fraction is almost constant at $\alpha_2 \sim 0.1$ as shown in figure 3.13(*b*). Thus, there is a strong gradient of vapour fraction across the shock front, suggesting rapid condensation of the vapour cavity by the propagating condensation shock front. Further, the measured vapour fraction values are in agreement with the vapour fractions reported by Ganesh et al. (2016). The velocity of the shock front in the laboratory frame of reference is estimated by computing the inverse of the gradient to the *linear part* of the shock front identified in the $x-t$ plot (see red markers in figure 3.13(*c*)). The linear fit to the shock front follows the previous studies of Ganesh et al. (2016) and Budich et al. (2018). Alternatively, the shock front velocity ($\sim L_c/t_{ret}$) is also determined using the length of the vapour cavity through which it travels (L_c) and the time it spends in the cavity (t_{rec}, see Appendix 3.B). These are shown by *star* markers in figure 3.13(*c*). They are consistently somewhat higher than the previous velocity estimates, suggesting that the condensation shock front velocity is not constant, rather it accelerates as it approaches the throat. This is in agreement with direct PIV measurements by Gawandalkar and Poelma (2022). The acceleration

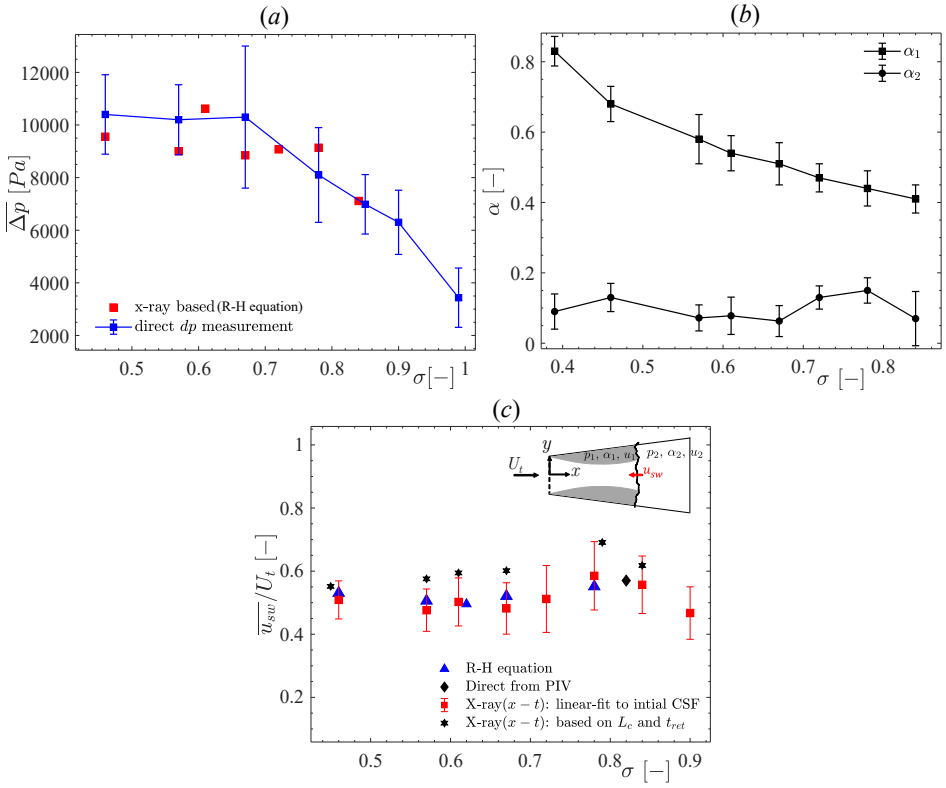

Figure 3.13: Characteristics of the bubbly shock waves; (*a*) The phase-averaged pressure rise recorded across the condensation shock front travelling through the attached vapour cavity (P_1-P_3). The red markers show the pressure rise predicted using measured shock front velocity and vapour fractions with equation 3.4. (*b*) Phase-averaged vapour fraction: pre (α_1) and post (α_2) shock front. (*c*) Phase-averaged condensation shock front velocity (u_{sw}) normalised with the throat velocity (U_t): blue markers indicate velocity predicted with R-H equation (u_{rh}), red markers indicate the velocity computed by fitting a straight line to the condensation shock-front in the $x-t$ evolution of α, star markers indicate the shock front velocity obtained by L_c/t_{rec}, and the diamond marker indicates the velocity of the shock front measured directly using PIV by Gawandalkar and Poelma (2022).

will be addressed in detail in subsections 3.3.7. Despite a relatively large variation in α_1, the shock front velocity at different σ is almost constant when normalised by U_t, i.e. $\sim 0.55U_t$. Interestingly, it is close to the maximum velocity of the re-entrant jet in a shedding cycle reported by Gawandalkar and Poelma (2022). Further, u_{sw} is almost two orders of magnitude lower than u_{pw} as shown in figure 3.11(*b*) and 3.13(*c*).

Δp and vapour fraction (α_1, α_2) measurements are validated with each other using a one-dimensional Rankine-Hugoniot (R-H) equation, given by 3.4 (Brennen, 1995).

$$u_{rh}^2 = \frac{\Delta p}{\rho_l}\left[\frac{(1-\alpha_2)}{(1-\alpha_1)(\alpha_1-\alpha_2)}\right] \tag{3.4}$$

Here, all the symbols have previously defined meanings. The R-H equation is derived

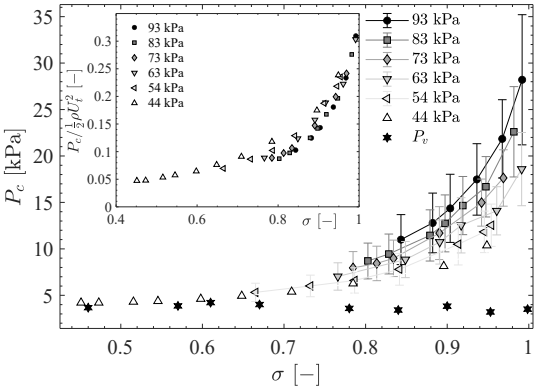

Figure 3.14: Conditionally phase-averaged static pressure inside the cavity (P_c) measured at location p_1 as a function of cavitation number (σ) for different global static system pressures. P_v refers to the vapour pressure. The inset shows the pressure normalised with the incoming dynamic pressure.

using mass, and momentum conservation along with the binary mixture model for density. The shock-front velocities predicted using measured α_1, α_2, Δp using R-H equation (blue markers in figure 3.13(*c*)) show an excellent agreement with the estimated values from $x-t$ plots (red markers in figure 3.13(*c*)). Further, Δp predicted using measured α_1, α_2 and u_{sw} using equation 3.4 (red markers in figure 3.13(*a*)) agrees with direct Δp measurement.

3.3.5. CAVITY PRESSURE

The absolute pressure inside the vapour cavity is cumbersome to measure experimentally. Thus, to get a ballpark estimate of the pressure inside the cavity, we measure the pressure at the venturi wall, at a location p_1 (see figure 3.1). This pressure at a single point is used as a proxy for the whole cavity pressure. The unsteady total pressure measurement is time-synchronised with high-speed imaging. This is done to discount the pressure time signal where the pressure transducer is not covered by the cavity. Further, the periodic, sharp pressure peaks caused by the cloud implosion downstream are filtered out using a low-pass filter. This is followed by time-averaging the pressure signal for 10 seconds to yield the cavity pressure (P_c). It is seen that P_c can be higher than the vapour pressure (P_v). However, at a lower cavitation number (σ), the pressure is seen to approach the P_v (see figure 3.14). This can be attributed to the bubbly nature of the cavity, where the vapour fraction increases with the decrease in cavitation number. For a given static pressure in the system, the pressure is seen to be decreasing monotonically with the increase in the free-stream velocity. Naturally, with the decrease in the global static pressure, the absolute pressure inside the cavity decreases. The absolute pressure when normalised by the dynamic pressure at the throat collapses on a curve, suggesting that σ and U_t are sufficient to estimate the pressure inside the cavity (see the inset in figure 3.14). The pressure of the bubbly cavity mixture will be used to estimate the speed of sound in such a mixture.

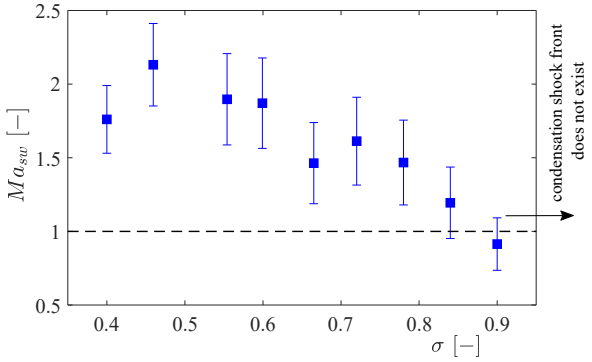

Figure 3.15: Mach number of the condensation shock front (Ma_{sw}) as a function of cavitation number (σ). The black dotted line shows $Ma_{sw} = 1$.

3.3.6. MACH NUMBER OF CONDENSATION SHOCK FRONT

It is well known that the speed of sound is significantly lower in a bubbly mixture than in pure liquid or vapour (Prosperetti, 2015; Shamsborhan et al., 2010). The cavity having substantial vapour fractions (0.4-0.8, see figure 3.13(*b*)) can reduce the speed of sound, rendering the medium compressibility important. Thus, with the measured vapour fraction (α_1) and the pressure of the bubbly mixture of the cavity (P_c), we can now make a rough estimate of the speed of sound in the cavity (c_m) with equation 3.5 (Brennen, 1995).

$$c_m = \left\{ \left[\frac{\alpha_1}{kP_c} + \frac{1-\alpha_1}{\rho_l c_l^2} \right] [\alpha_1 \rho_v + (1-\alpha_1)\rho_l] \right\}^{-\frac{1}{2}} \tag{3.5}$$

It is assumed that the cavity is a homogeneous bubbly mixture and water vapour behaves as a perfect gas with the polytropic gas constant k. Further, the bubble dynamics in the cavity such as coalescence and surface tension are omitted for simplicity. ρ is the mass density and c is the speed of sound in the medium; subscript v and l are used for vapour and liquid, respectively. The mixture pressure (P_c) is estimated in the previous subsection. The Mach number of the shock front (Ma_{sw}) can now be estimated with the speed of sound (c_m) and u_{sw}, as per equation 3.6.

$$Ma_{sw} = \frac{u_{sw}}{c_m} \tag{3.6}$$

Since we are interested in the interaction of the pressure wave with the bubbly cavity when it impinges on it, the phase-averaged condensation shock front velocity estimated in figure 3.13(*c*) is used to estimate the Mach number (Ma_{sw}). Figure 3.15 shows that the Ma_{sw} decreases with increasing σ, further corroborating that the strength of the condensation shock travelling through the cavity is decreasing with increasing σ. Such behaviour of the condensation shock front was also reported by Bhatt and Mahesh (2020) and Ganesh et al. (2016) for a 2-D wedge and backward facing step geometry, respectively. We see that Ma_{sw} is greater than unity, i.e. it is supersonic for lower σ. However, it falls below or hovers close to unity for higher σ (~ 0.90). At even higher σ, the condensation shock fronts were not observed in our study. Thus, $Ma_{sw} \sim 1$ coincides with the

disappearance of condensation shock fronts. This suggests that the pressure and vapour fraction fields at higher σ render the pressure wave weaker and likely subsonic. This weakening of the shock front is likely to mitigate the complete condensation of the cavity at higher σ, as opposed to lower σ, where the pressure wave completely condenses the cavity. This is in line with observed cavity dynamics at $\sigma \sim 0.84$ and 0.90 where, most shedding cycles begin to show re-entrant jet-driven shedding. With further increase in σ (~ 0.97), all the shedding cycles were destabilised by the re-entrant jet, as shown previously by Gawandalkar and Poelma (2022) and Jahangir et al. (2018). Thus, the shedding mechanism switches from a condensation shock front to a re-entrant jet as the pressure wave emanating from the cloud implosion becomes weaker.

In summary, it is evident that the Mach number of bubbly shock front (Ma_{sw}) decreases as σ increases, suggesting that the pressure wave travelling through the vapour cavity appears to get weaker with increasing σ. This is corroborated by the observed cavity shedding dynamics, i.e. at $\sigma = 0.47$: the impinged pressure wave starts immediately condensing the cavity. At intermediate $\sigma = 0.78$, a condensation shock front emerges as the pressure wave propagates upstream. However, at $\sigma = 0.84$, the pressure wave appears to be too weak to condense the cavity readily. Thus, the pressure wave is expected to propagate through the cavity without condensing it for the majority of the cycles. At this σ, a strong re-entrant jet is also present below the cavity, as shown by Gawandalkar and Poelma (2022). Therefore, the re-entrant jet takes over as the dominant cavity detachment mechanism for higher σ. The velocity of the condensation shock front and re-entrant jet is of the same order of magnitude. If the pressure and the vapour fraction of the bubbly cavity allows the condensation of the cavity, the phase change from vapour to liquid will dictate the cavity destabilisation. Alternately, the cavity pinch-off by the re-entrant jet is favoured. Therefore, it is seen that the pressure field and the shock wave characteristics have a strong influence on the prevalence of the dominant shedding mechanism.

3.3.7. KINEMATICS OF CONDENSATION SHOCK FRONT

As stated in the previous subsection, the condensation shock-front is seen to accelerate as it travels upstream towards the venturi throat. This can also be seen in previous studies: For instance, in the $x-t$ diagram showing the cavity dynamics in the experiments of Wu, Ganesh, and Ceccio (2019) and the large eddy simulations of Bhatt and Mahesh (2020). However, due to the low flow blockage in those studies, the acceleration is suspected to be not severe. As a result, it has not received much attention. In the current flow geometry, the flow blockage ratio is ~ 9, which is significantly higher. Further, it is seen that at intermediate cavitation numbers ($\sigma \sim 0.78$-0.85), the emergence of a sharp condensation shock front coincides with the observed acceleration of the shock front. Thus, it is imperative to account for the effect of acceleration of the condensation shock front in the present context. The velocity of the condensation shock front as a function of axial distance (x) is evaluated by computing the phase-averaged gradient to the measured condensation shock front in the $x-t$ diagram (see figure 3.16). The phase averaging of $u_{sw}(x)$ is performed over so-called 'clean cycles' ($\sim 80\%$), omitting shedding cycles with local variations such as sudden acceleration, multiple condensation shock fronts, etc. The error bars indicate the cycle-to-cycle variation in the velocity. The ac-

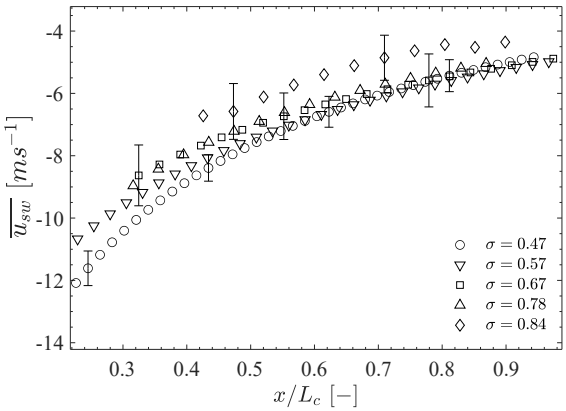

Figure 3.16: The axial (x) variation of the shock wave velocity (u_{sw}) plotted against x normalised by maximum cavity length (L_c).

celeration appears significant: the velocity doubles in half the cavity length. The acceleration experienced by the shock front while travelling upstream could be attributed to the axial variation of vapour fraction across the shock front ($\alpha_1(x)$), the change in the cross-section of the venturi as seen by the shock front, or the change in pressure of the cavity. Due to the difficulty in experimentally measuring the pressure inside the cavity, the pressure is assumed to be constant.

The axial variation of the vapour fraction ($\alpha_1(x)$) encountered by the travelling shock front is shown for three σ (see figure 3.17(a)). The axial variation is negligible ($\lesssim 0.07$) and within the measurement uncertainly. Further, we check if the shock front is accelerating due to the converging walls of the venturi (from the shock front frame of reference, given that it is travelling upstream). In that case, the measured shock wave velocity must vary to obey the mass conservation imposed by the geometry. This can be used to construct a simple model based on 1-D mass conservation and the initial shock front velocity to predict the velocity variation. The measured phase averaged shock front velocity ($\overline{u_{sw}(x)}$) variation with x is shown by markers in figure 3.17(b). It is observed that the agreement with predictions (dashed lines in figure 3.17(b)) is good. However, closer to the throat, the agreement appears worse. This can be attributed to assumptions made in the model such as constant pressure, density, and the difficulty in defining the condensation shock front close to the throat. Considering this, we can safely attribute the acceleration to the converging walls of the venturi as seen by the shock front.

Further, we examine if this increasing velocity of the shock front has an effect on the dynamics of the condensation shock wave. We measure Δp brought about by the condensation shock front as it travels upstream. Δp measurements are done at multiple axial locations, p_1, p_2, p_3 (see figure 3.1 for the locations). Interestingly, at $\sigma = 0.47$, the pressure rise of the shock front at p_2 location is 10.38 kPa which increases to 17.01 kPa at p_1. Similarly, at $\sigma = 0.67$, the pressure rise increases from $\Delta p_2 = 10.32$ kPa to $\Delta p_1 = 13.60$ kPa. Thus, the pressure rise across the bubbly shock front is seen to increase as it propagates upstream. Finally, we estimate the Mach number of the accelerating condensation

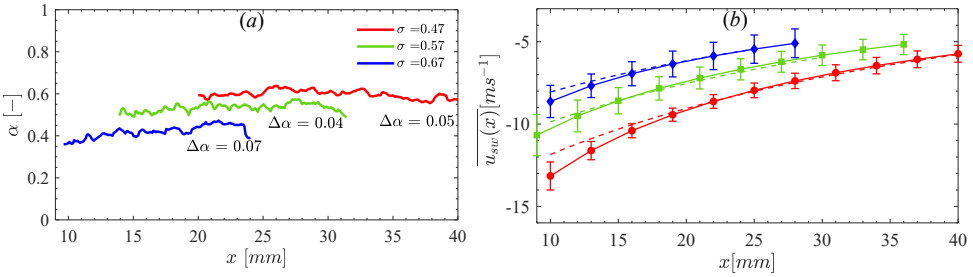

Figure 3.17: (*a*) The axial (x) variation of pre-shock vapour fraction (α_1), (*b*) The axial variation of phase-averaged shock wave velocity ($\overline{u_{sw}}$) (markers) compared with velocity predictions by mass conservation (dashed lines) at different σ (same colour coding as in left panel). Every third data point is shown for clarity.

front, $M_{sw}(x)$, as it travels upstream through the bubbly vapour cavity (see figure 3.18). It is assumed that the pressure of the bubbly mixture through which the condensation front travels is constant. Further, the vapour fraction it encounters is nearly constant as shown in figure 3.17(*a*). Thus the speed of sound is also assumed to be constant in accordance with equation 3.5. It is seen that at the lowest cavitation number ($\sigma \sim 0.47$), the bubbly shock front is supersonic as it impinges on the cavity and remains supersonic as it travels through the cavity. This results in complete condensation of the cavity, as also observed in the time series shown in figure 3.5. The complete condensation is evident from the sharp jump in the vapour fraction over the entire shock front, as shown in figure 3.5(*i*). As the cavitation number increases (σ = 0.78), the bubbly shock wave is initially subsonic as it impinges on the cavity, until $x/L_c \sim 0.89$, as shown in figure 3.18. This is also seen in the vapour fraction time series, where the pressure wave front is seen to travel through the cavity without condensing it (see figure 3.8). However, as it accelerates while travelling upstream, it becomes supersonic at $x/L_c \sim 0.84$ (corresponding to x = 21.2 mm in the $x-t$ diagram shown in figure 3.8(*i*)) and starts complete condensation of the vapour cavity. Thus, the axial location where the pressure wave becomes subsonic agrees well within the measurement uncertainty. At even higher σ ($\sim$ 0.84-0.90), the pressure wave cannot become supersonic readily (see figure 3.18). This can also be seen in shedding dynamics shown in figure 3.9(*i*): the shock front inferred from a sharp change in α appears further upstream. At such a flow condition, the pressure wave after impinging on the vapour cavity is less likely to condense it, allowing the re-entrant jet below the cavity to pinch it off. This shows the effect of the kinematics of the shock front on the cavity shedding dynamics.

The phenomenological description of the vapour cavity shedding in an axisymmetric venturi for *intermediate* σ can be given as follows: The pressure wave emanating from the previous cloud implosion impinges on the growing cavity. However, the velocity of the pressure wavefront (u_{sw}) and the pressure rise across it (Δp) is not enough to condense the cavity, i.e. it is likely subsonic. As the pressure wave travels upstream, its velocity increases due to the converging geometry of the venturi (blockage). Consequently, the pressure rise across it also increases. This makes the shock front stronger or even supersonic, favouring condensation. At lower σ, the impinging pressure discontinuity is

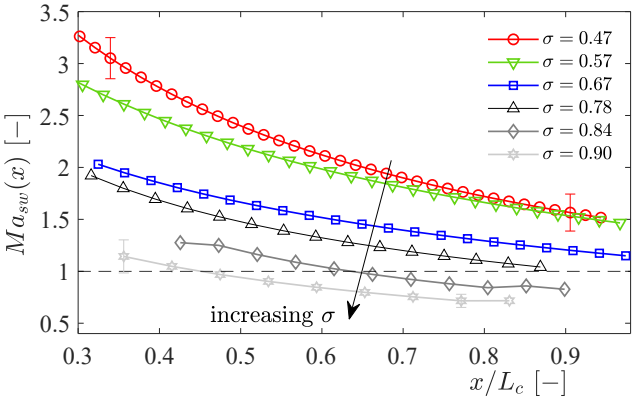

Figure 3.18: Mach number (Ma_{sw}) variation of the bubbly shock front with the axial distance (x) normalised by cavity length (L_c) for different cavitation number (σ). The direction of propagation of the shock front is upstream, i.e. to the left in this figure.

supersonic. Hence, the condensation shock front is seen to exist over the entire cavity length. However, at high σ, the pressure discontinuity is weak and remains subsonic, despite the acceleration. Thus, it appears that the effect of such a flow geometry with a large blockage is to accelerate the pressure wave, increasing its strength as it travels upstream. This, in turn, explains the large range of cavitation numbers ($\sigma \simeq 0.3$-0.84) for which the condensation shock front is the cavity destabilising mechanism, as opposed to the re-entrant jet, which is seen to occur only for $\sigma \simeq 0.95$-1.1.

3.4. SUMMARY AND CONCLUSIONS

Partial cavitation in an axisymmetric venturi has been studied with time-resolved X-ray densitometry, in combination with high-frequency pressure transducers. The densitometry allows us to circumvent the opacity of the cavitating flow, enabling robust estimations of vapour cavity topology such as cavity length, height and vapour fractions (instantaneous, time-averaged, and phase-averaged) at different cavitation numbers (σ). On the other hand, the pressure transducers allow us to detect the pressure discontinuity arising from the cloud collapse and track the pressure wave as it propagates through the attached cavity. The measured static pressure in the cavity in combination with vapour fractions enable us to estimate the speed of sound in a bubbly cavity. This allows us to quantify the Mach number of the shock front.

The primary aim of this study is to examine the interaction of the pressure wave emanating from the cloud implosion with the attached cavity at different flow conditions (σ). This helps us to probe the physics underlying the transition of the cavity destabilising mechanism from re-entrant jet to condensation shock wave in an axisymmetric venturi. This is realised by characterising the pressure wave travelling *upstream* through the attached cavity at different σ, i.e. vapour fraction (pre-front (α_1), post-front (α_2)), pressure rise (Δp) across the shock front. Further, the velocity of the shock front propagation (u_{sw}) and its Mach number (Ma_{sw}) shed light on the importance of compressibility in

such bubbly flows of substantial vapour fraction. Moreover, the pressure pulse propagating in the bubbly liquid (low vapour fraction region) is also characterised. The periodicity in the cavity shedding is leveraged to undertake phase-averaging on the quantities. It is seen that the pressure peak (dp) and propagation velocity (u_{pw}) of the pressure wave propagating through a low vapour fraction bubbly mixture are two orders of magnitude higher in comparison to when it propagates through the attached cavity. The upstream propagating pressure wave, when impinging on the cavity, starts condensing it. The pressure rise across the condensation shock front (Δp) is of the order of magnitude $\sim$ 10 kPa. The vapour fraction of the cavity is in the range of (0.4-0.8). Further, the condensation shock front is seen to travel at about $\sim 0.55U_t$, which is interestingly of the same order of magnitude as that of the re-entrant jet velocity reported earlier by Gawandalkar and Poelma (2022) in the same flow geometry. This also means that the timescale of shedding associated with the two shedding mechanisms is similar, however, the shedding mechanisms are fundamentally different.

The cavitation dynamics visualised by the time-series of vapour fraction reveal that the interaction of the pressure wave with the attached cavity at a low cavitation number can be explained as: the pressure wave impinges on the cavity, the pressure wavefront is supersonic as the bubbly mixture through which it propagates has a high vapour fraction ($\alpha_1 \sim 0.7$) and low mixture pressure (P_c). The combination of this makes the shock front supersonic ($Ma_{sw} > 1$), which completely condenses the vapour cavity, resulting in its fragmentation and destabilisation. It is also observed that the condensation shock enforces a strong periodicity in shedding, despite local instantaneous events in the shedding process. As the cavitation number increases, the pressure wave impinging on the cavity is weaker and likely subsonic ($Ma_{sw} < 1$). However, as it propagates upstream, it becomes stronger, i.e. supersonic ($Ma_{sw} > 1$), resulting in the onset of cavity condensation. This is evident from the emergence of a sharp gradient in the vapour fraction as the bubbly shock wave propagates upstream. This coincides with an increase in shock front velocity ($u_{sw}(x)$) as it propagates upstream, leading to an increased pressure rise (Δp) across it according to equation 3.4. The observed acceleration is attributed to the converging walls of the venturi as seen by the shock front. A simple model based on mass conservation is found to predict the acceleration of the shock front fairly well. Thus, the kinematics of bubbly shock waves can have a significant influence on their dynamics, which in turn influences the shedding dynamics.

With a further increase in the cavitation number, the pressure discontinuity from the cloud implosion gets even weaker and despite the acceleration of the shock front, the Mach number of the pressure wavefront seems to remain low or subsonic, i.e. $Ma_{sw} \lesssim 1$. Thus, condensation is not favoured readily in the majority of the cycles. This coincides with a strong re-entrant jet existing beneath the cavity in such cycles. They exhibit cavity pinching, cloud detachment and roll-up, typical of cavity shedding triggered by a strong re-entrant jet below the vapour cavity. With an even further increase in cavitation number ($\sigma > 0.95$), all the shedding cycles will be predominantly shed by the re-entrant jet as shown previously by Jahangir et al. (2018) and Gawandalkar and Poelma (2022).

Thus, pressure and density/vapour fraction fields in such a bubbly flow have a significant influence on the interaction of the pressure waves with a cavity. This interaction determines if the shock front remains subsonic or becomes supersonic which in turn in-

fluences if the cavity shedding is caused by the bubbly shock wave or the re-entrant jet. Moreover, the effect of a high-blockage flow geometry, such as the axisymmetric venturi, is to strengthen the shock front by accelerating it. This helps to explain the dominance of bubbly shock waves over re-entrant jets as a mechanism driving the periodic cloud shedding in an axisymmetric venturi.

APPENDIX 3.A: CORRELATION BETWEEN PRESSURE PEAKS AND SHEDDING

The correlation between vapour cavity shedding and pressure peaks arising from the cloud collapse is shown by computing the FFT of the dp and the α time signals at different σ. For the $x-t$ diagram, several x positions are averaged to estimate the spectral density. Note that dp and α are measured independently but in the same experiment. It is seen that for $\sigma \leq 0.78$ (see top two panels in figure 3.19), dominant frequencies match accurately, suggesting a good correlation between pressure pulse and cloud shedding via condensation. However, at $\sigma \geq 0.84$, there is a mismatch between peaks (see bottom two panels in figure 3.19). This is attributed to the pressure peaks not being strong enough to condense and cause cavity detachment in most cycles. Thus, the correlation between pressure peaks and cavity detachment appears weaker.

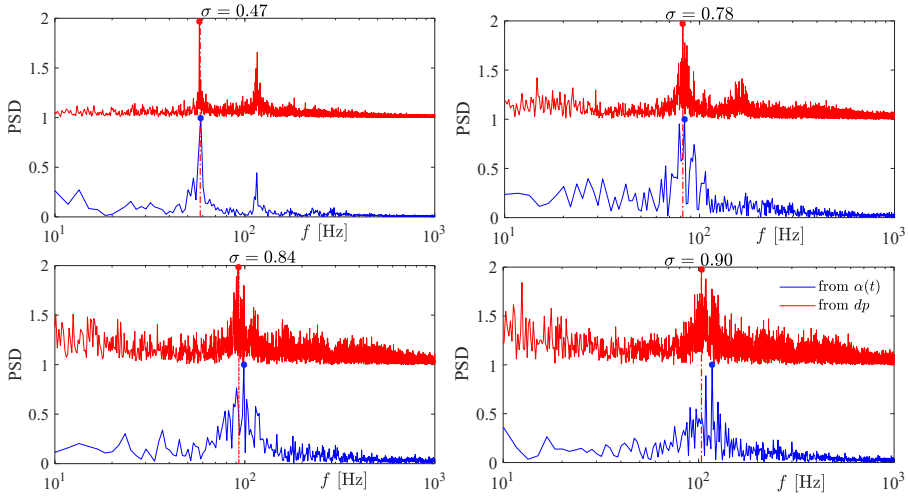

Figure 3.19: FFT showing the dominant frequency of vapour fraction $\alpha(t)$ and pressure pulse due to cloud implosion $dp(t)$ for σ=0.47, 0.78, 0.84, and 0.90.

APPENDIX 3.B: TIME SCALES OF SHOCK FRONT

A typical vapour cavity shedding cycle can be thought of as composed of three parts: (i) cavity growth, (ii) cavity retraction by the condensation shock front, and (iii) no cavitation near the throat. An $x-t$ plot of the cavity evolution is an ideal tool to examine the time scales of the shedding process (see figure 3.20(a)). Here, t_{cg} denotes the time

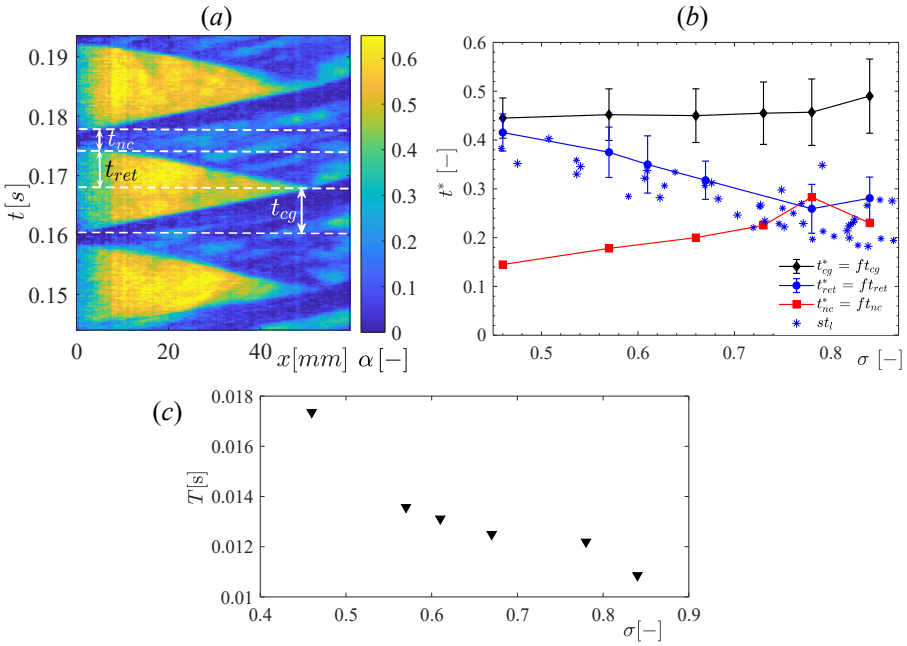

Figure 3.20: Time-scales (t^*) involved in the cavity destabilisation; (*a*) $x-t$ diagram for $\sigma = 0.47$ explaining $t \in (t_{cg}, t_{ret}, t_{nc})$, (*b*) normalised time-scales (t^*) at different σ. The star markers show the global cloud shedding frequency expressed as Strouhal number ($St_l = fL_c/U_t$) measured by Jahangir et al. (2018), (c) the shedding time period ($T = 1/f$) as a function of σ.

scale for which the cavity grows to its maximum length (L_c), while t_{ret} shows the time taken by the cavity to retract. This is also the time scale of the condensation shock front propagation if the condensation shock front is responsible for cavity destabilisation and shedding. Further, t_{nc} is the time for which the cavity is completely detached at the venturi throat. All these time scales (t_{cg}, t_{ret}, t_{nc}) are phase-averaged over a number of shedding cycles and normalised with the respective shedding time period (T) to yield the corresponding dimensionless time t^*. Here, T is estimated from the dominant peak in the power spectral density in the FFT of the α signals (see figure 3.20(*c*)). The error bars are attributed to the cycle-to-cycle variations in shedding. It is observed that the cavity for all σ reaches the maximum length (L_c) in about $0.45T$. Consequently, the time scale of cavity destabilisation is constant at $\sim 0.55T$. The time scale of cavity destabilisation includes the cavity detachment time (t^*_{ret}) and no-cavitation time (t^*_{nc}). It is observed that the time scale of the condensation shock front causing cavity detachment (t^*_{ret}) is a strong function of σ, i.e. at lower σ, the shock front requires more time (fraction of a cycle) to retract the cavity completely. Further, this trend agrees well with the variation of Strouhal number ($St_l = fL_c/U_t$) with σ, reported by Jahangir et al. (2018) (see star markers in figure 3.20(*b*)). Hence, the time scale of condensation shock front through the cavity is in agreement with the global shedding frequency. In tandem with this, t_{nc} increases with σ, meaning the time for which the vapour throat is left cavitation-less increases with σ. This has also been observed in the numerical simulations of cavitating

flow over a circular cylinder Gnanaskandan and Mahesh (2016b).

SUPPLEMENTARY MOVIES

Supplementary movies are available here

4

VENTILATED CAVITIES

In this chapter ventilated cavities in the wake of a 2-D bluff body are studied experimentally via time-resolved X-ray densitometry and high-speed imaging. With a systematic variation of flow velocity and gas injection rate, expressed as Froude number (Fr) and ventilation coefficient (C_{qs}) respectively, four stable cavities with different closures are observed. A regime map governed by Fr and C_{qs} to estimate flow conditions associated with these cavity closures is constructed. Each closure exhibits a different gas ejection mechanism, which in turn dictates the geometry and the pressure inside the cavity expressed as cavitation number (σ_c). Two types of cavity closures are seen: (i) with a wave-type instability, and (ii) with a re-entrant jet depending on Fr and C_{qs}. Three-dimensional cavity closure is seen to exist for supercavities at low Fr. However, closure is nominally 2-D for supercavities at higher Fr. Apart from stable cavities, re-entrant flow closure is also seen to exist for transitional cavities during the supercavity formation. The strength of this liquid re-entrant flow depends on the flow inertia and cavity interface curvature. With the measured gas fraction of these unsteady ventilated cavities, a simple gas balance analysis is performed to quantify gas leakage at the cavity closure. Gas ejection due to re-entrant flow at high Fr is found to be substantially higher than gas ejection due to vortex shedding and wave-type instability at low Fr. The strength of the re-entrant jet is seen to dictate the rate of gas transport within the cavity at higher Fr. The supercavity exhibits hysteresis with respect to gas injection due to the unique closure formation and the resulting gas ejection. Consequently, the ventilation required to maintain the supercavity is significantly less than the ventilation required to establish the cavity.

This chapter is based on: Gawandalkar, U. U., Lucido, N. A., Jain, P., Poelma, C., Ceccio, S. L., Ganesh, H. (2024). *Examination of ventilated cavities in the wake of a two-dimensional bluff body using X-ray densitometry*, under review at the Journal of Fluid Mechanics, arXiv preprint.

4.1. INTRODUCTION

Ventilated partial- and super-cavitation[1] (VPC and VSC, respectively) are characterised by gas cavities formed by injecting non-condensable gas behind a flow separating body called a 'cavitator' (Logvinovich, 1969). This technique has gained significant attention due to its potential application for drag reduction on ship hulls by forming an air layer and reducing the near-wall density (Ceccio, 2010). Ventilated cavities (VC) have also found applications in hydraulic engineering (Chanson, 2010) and process industries (Rigby et al., 1997) to mitigate deleterious effects of natural cavitation, such as wear, erosion, and failure, all resulting from violent cloud collapse (Brennen, 1995). Insufficient ventilation may lead to cavity collapse, while excessive ventilation could result in cavity oscillation, both undesired and often detrimental (Ceccio, 2010). The stability of ventilated cavities is important as unstable ventilated cavities can get detached abruptly, leading to a sudden increase in drag forces. Hence, it is necessary to understand the exact flow conditions that govern stable ventilated cavities. Ventilated cavities are generally governed by the incoming flow pressure (P_0) and velocity (U_0), input gas injection rate ($\dot{Q}_{in}$), cavity pressure (P_c), and cavitator geometry (cross-sectional area$-A$ and cavitator length scale$-H$). See figure 4.1 for the definition of these parameters. They can be expressed as the cavitation number (σ_c), Froude number (Fr), and ventilation coefficient (C_{qs}) as defined below.

$$\sigma_c = \frac{P_0 - P_c}{\frac{1}{2}\rho U_0^2} \qquad Fr = \frac{U_0}{\sqrt{gH}} \qquad C_{qs} = \frac{\dot{Q}_{in}}{U_0 A}.$$

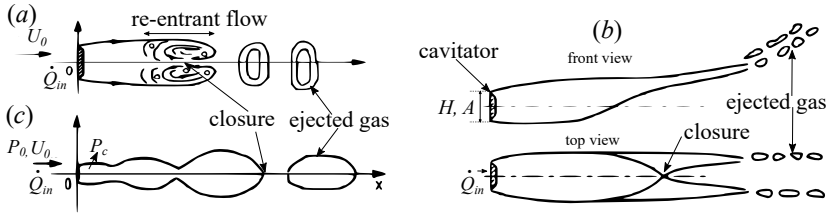

Figure 4.1: A schematic representation of different types of ventilated cavities (and closures) observed behind an axisymmetric cavitator, adapted from Semenenko (2001): (*a*) with re-entrant flow, (*b*) frontal and top view of a twin-vortex type cavity, (*c*) a pulsating type cavity with inplane oscillation. The bulk flow is from left to right, U_0, P_0 are the incoming flow condition, and H, A are dimensions of the cavitator.

Ventilated cavities are formed when a part of the injected gas ($\dot{Q}_{in}$) gets entrained in the separated flow behind the cavitator, while the remainder of the gas is ejected from the cavity closure region ($\dot{Q}_{out}$). This is shown schematically in figure 4.1. The entrained gas, i.e. the gas that is dragged *into* the cavity results in the growth of the cavity. The closure refers to the way the cavity closes itself and dictates the amount of gas ejected out of the cavity. Further, cavity closure influences the cavity geometry (length, thickness and gas distribution) and, most importantly, the stability of the cavity. Hence, a thorough understanding of the cavity closure is imperative.

[1] supercavities refer to cavities which are relatively longer than the length scale of the flow

Various closure modes have been observed in the past, especially 3-D axisymmetric cavitators have been investigated widely. It was shown that at a high Fr, the cavity closure is characterised by a weak re-entrant jet (Epshteyn, 1961; Karn et al., 2016; Logvinovich, 1969), see also figure 4.1(*a*). However, at low Fr, buoyancy effects result in lift generation and the formation of two vortex tubes at the closure (Semenenko, 2001), see figure 4.1(*b*). Karn et al. (2016) explained these observations based on the pressure difference across the cavity closure ($\Delta\tilde{P}$): a higher $\Delta\tilde{P}$ gave rise to a re-entrant jet similar to natural partial cavities (Callenaere et al., 2001; Knapp, 1958), while a lower $\Delta\tilde{P}$ resulted in vortex tube closure. At significantly high ventilation inputs, oscillating cavities called pulsating cavities (PC) were identified (Silberman & Song, 1961; Skidmore, 2016), see figure 4.1(*c*). For the 3-D fence-type cavitator[2], similar observations were made: cavities with re-entrant flow were seen at higher Fr, while at lower Fr the cavity was seen to split into two separate branches with re-entrant flow on each branch (Barbaca et al., 2017). All the cavities had a re-entrant flow closure, possibly due to the high Fr in that study. Ventilated cavities behind a 2-D cavitator have received less attention in the literature despite their wide application for partial cavity drag reduction on ships (Mäkiharju, Elbing, et al., 2013). In a wall-bounded 2-D cavitator, Qin et al. (2019) observed a twin-branch cavity (TBC), analogous to vortex tube closure. Qin et al. (2019) also reported supercavities with dispersed bubbles at the closure, and cavities with re-entrant jet closure were not observed, likely due to the low Froude number ($Fr < 6$) considered in their study. In summary, distinct closure regions are seen for different cavitator geometries.

The cavity closure influences the gas entrainment/ejection rate into/out of the cavity. Understanding the gas entrainment and ejection mechanisms is important to establish and maintain VCs efficiently. Spurk (2002) postulated that the injected gas is carried to the closure by a growing internal boundary layer (IBL) at the gas-liquid interface, where it is ejected out in the form of toroidal vortices. For wall-bounded cavitators, Qin et al. (2019) proposed that the re-circulation region interface is responsible for entraining the gas bubbles into the separated shear layer, which are then carried away downstream. This was verified experimentally by Wu, Liu, et al. (2019) in a study on the gas flow *inside* the ventilated cavity using particle image velocimetry (PIV). Although the gas entrainment mechanisms were found to be identical for different cavity closures, the gas leakage mechanisms were seen to be different. Various gas ejection mechanisms are identified in ventilated cavities; (i) gas ejection due to a re-entrant jet (Barbaca et al., 2017; Kinzel & Maughmer, 2010; Spurk, 2002), (ii) vortex tube gas leakage (Cox & Clayden, 1955; Semenenko, 2001), (iii) pulsation of cavities (Karn et al., 2016; Michel, 1984; Skidmore, 2016), and (iv) surface waves pinching the cavity (Zverkhovskyi, 2014). Furthermore, Qin et al. (2019) clarified the role of capillary wave pinch-off in gas ejection in twin-branch cavities (TBC).

Studies dedicated to the quantification of gas leakage out of cavities ($\dot{Q}_{out}$) for different cavity closures are scarce. Yet, quantifying gas ejection rates is essential in formulating empirical models, validating numerical models, and furthering our understanding of the underlying flow physics at closure. This enables better prediction of gas ventilation demands under different flow conditions (Fr and C_{qs}). Recently, Shao et al. (2022)

[2] 2-D fence refers to the fence that spans the complete span of the test section width, while 3-D fence spans only a part of the test section width

used digital inline holography (DIH) to quantify the instantaneous $\dot{Q}_{out}$ for stable cavity closure modes. While stable cavity modes have received adequate attention in the literature, unsteady cavity closure modes during the formation of a supercavity remain unexplored. The ventilation demands to establish and maintain VCs can be more accurately estimated by studying the gas ejection of these unsteady VCs. Furthermore, hysteresis in ventilated cavity formation plays a significant role in determining the accurate ventilation demands, i.e. for a given ventilation (C_{qs}), a ventilated cavity can assume a different length and closure depending upon how the ventilation condition was reached (Karn et al., 2016; Kawakami & Arndt, 2011; Mäkiharju, Elbing, et al., 2013). Ventilation hysteresis is widely reported in ventilated cavities, albeit the exact physical mechanism responsible for it remains unclear. The characterisation and implication of ventilation hysteresis are essential to devise control strategies for efficient drag-reduction and aeration systems.

The lack of quantitative insights in ventilated cavities can be attributed to the challenges brought about by turbulence, frothiness, and optical opaqueness of the flow. Thus, conventional optical-based measurement techniques are untenable, especially at the liquid-gas-liquid interface and cavity closure. Wosnik and Arndt (2013) attempted to estimate the void fraction and velocity fields in the frothy mixture of the VCs with laser-illuminated bubble images, however, the uncertainty in the measurements was high. Holography is limited to the far-field, where individual ejected gas bubbles can be imaged (Shao et al., 2022). High-fidelity numerical simulations like DNS are limited to low Reynolds numbers due to the large density ratios and turbulent motions, with a wide range of scales in the flow (Liu et al., 2023). These shortcomings can be overcome by whole-field radiation-based measurement techniques such as time-resolved X-ray densitometry, wherein gas-liquid interfaces and the cavity closure region can be resolved reliably (Aliseda and Heindel, 2021). Such time-resolved void fraction measurements can provide quantitative information in gas entrainment and leakage dynamics apart from time-averaged gas distribution in ventilated cavities. The void fraction fields are indispensable for quantifying the compressibility effects in ventilated cavity flows, deemed crucial in *natural* cavitation flows (Budich et al., 2018; Ganesh et al., 2016). Further, void fraction profiles in ventilated cavities can be useful for validating numerical models aimed at simulating ventilated cavity flow.

In this chapter, we study the entrainment of gas in the wake of a 2-D wedge by systematically varying the flow inertia (Fr) and gas injection rate (C_{qs}). We identify different types of stable ventilated cavities and determine the associated flow conditions that result in a regime map. The main objective of this study is to examine the types of cavity closure and the corresponding gas ejection mechanisms. The effect of Fr and C_{qs} on the cavity closure is studied in detail using 2-D time-resolved X-ray densitometry and high-speed videography. The dynamics of cavity formation are studied and gas leakage out of the cavity is quantified during the formation using a simple gas balance based on a control volume. The re-entrant jet in the ventilated cavity is thoroughly characterised and a simple empirical model based on experimental data is constructed to estimate the gas ejection rate. The hysteresis in the formation of a fully developed supercavity was also studied. Finally, we link the observed hysteresis to the cavity closure formation and the ensuing gas ejection rates. The rest of the chapter is organised into five additional sections. The experimental methodology is described in §4.2. The stable and unstable

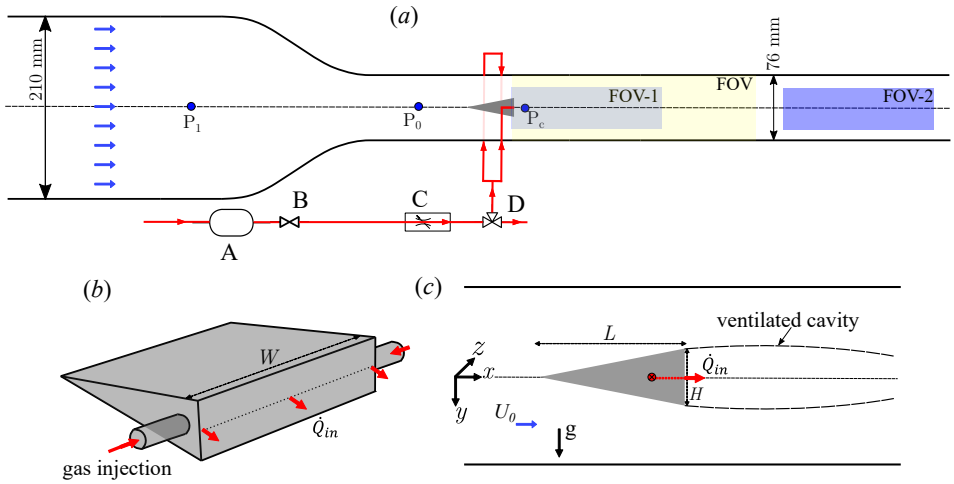

Figure 4.2: (*a*) A schematic of the experimental flow facility with ventilation line shown in red, A: pressure vessel, B: valve, C: voltage regulated mass flow controller, D: three-way valve. The yellow region indicates the field of view (FOV) for high-speed optical imaging, while the grey (FOV-1) and blue regions (FOV-2) indicate the field of view of X-ray imaging. The pressure is measured at P_0, P_1, and P_c. (*b*) A schematic of the 2-D wedge with ventilation holes. (*c*) A schematic of the partial ventilated cavity. Note that the red arrows show the direction of the gas flow, while the blue arrow shows the direction of the bulk flow.

ventilated cavities are treated separately; the characteristics of stable ventilated cavities are described in detail in §4.3, while unstable cavities during the formation of super-cavities are examined in §4.4. Ventilation hysteresis is discussed in §4.5, followed by conclusions summarised in §4.6.

4.2. EXPERIMENTAL METHODOLOGY

4.2.1. FLOW FACILITY

The experiments were performed at the University of Michigan in the 9-inch (~ 210 mm) recirculating water tunnel with a reduced square test-section of cross-section 76×76 mm^2, as discussed by Ganesh et al. (2016). The inflow velocity in the test section (U_0) was measured based on the pressure drop across the contraction ($\Delta P = P_1 - P_0$, see figure 4.2(*a*)) using a differential pressure transducer (Omega Engineering PX20-030A5V). Inflow static pressure (P_0) was measured using an Omega Engineering PX409030DWU10V, 0 to 208 kPa transducer. The experiments were performed at ambient system pressure, i.e. without any vacuum. Dissolved gas content was controlled using a deaeration system. The flow velocity (U_0) is varied from 0.84 ms^{-1} to 6.2 ms^{-1}, corresponding to Fr of 2 to 14 (see table 4.1 for definition).

The ventilated partial cavity was generated behind a 2-D bluff body cavitator (wedge), by injecting non-condensable gas in its wake as shown in figure 4.2(*c*). The wedge had a height (H) of 19 mm and an angle of 15°, and was seal-secured tightly by the test-section windows, resulting in a blockage (ξ) of 25%. The wedge has an internal bore-hole leading to multiple ventilation ports of 1 mm diameter each on the wedge base, as detailed

Parameter	Definition	Units	Value
wedge dimensions	$L \times W \times H$ (see figure 4.2)	[mm]	72×76×19
incoming bulk velocity	U_0	[ms^{-1}]	0.84 - 6.2
gas mass flow rate	$\dot{Q}$	[SLPM]	0.1 - 50
Froude Number	$Fr = U_0/\sqrt{gH}$	–	2 - 13.9
ventilation coefficient	$C_{qs} = \dot{Q}/U_0 HW$	–	0.02-0.12
cavitation number	$\sigma_c = (P_0 - P_c)/\frac{1}{2}\rho U_0^2$	–	0.8-3.5
Reynolds number	$Re_H = U_0 H/\nu$	–	1.60-11.6 × 10^4

Table 4.1: Experimental parameters, ρ, ν, and g refers to the mass density, the kinematic viscosity of the liquid, and gravitational acceleration constant.

in Wu et al. (2021). The bore-hole is connected to the external compressed air supply via pneumatic fittings as shown in figure 4.2(*b*). The gas ventilation line is schematically illustrated in figure 4.2(*a*). The non-condensable gas was fed through a pressure vessel to maintain the required stagnation pressure (~ 400 kPa) to mitigate choking in the ventilation lines. The mass flow rate ($\dot{Q}_{in}$) was controlled using two flow controllers: Omega FMA series 0-15 and 0-50 standard litres per minute (SLPM). The injected gas flow rate was expressed as a non-dimensional ventilation coefficient C_{qs} (see table 4.1 for definition) and was varied from 0.02 to 0.12 over more than 100 values for a given base pressure. The pressure inside the cavity (P_c) was measured from the side window of the test-section at $x \approx 1H$, along the wedge centreline, using an Omega Engineering PX409030DWU10V, 0 to 208 kPa transducer (see again 4.2(*a*)). The measured cavity pressure (P_c), incoming pressure (P_0) and dynamic pressure of the incoming flow ($\frac{1}{2}\rho U_0^2$) were used to define the cavitation number expressed as σ_c (see table 4.1 for definition). Note that the cavitation number is used extensively in natural cavitating flows to indicate the closeness of cavity pressure to the vapour pressure, such as in chapters 2 and 3 of this dissertation.

4.2.2. FLOW VISUALISATION

Visual observation and qualitative analyses of ventilated cavities are performed via front-illuminated high-speed cinematography using a single Phantom Cinemag 2 v710 camera placed perpendicular to the field-of-view (FOV). The FOV is centered along the tunnel axis and spans $13.6H \times 8.4H$ in the $x-y$ plane with the origin (x, y, $z = 0$) defined at the centre of the wedge base. See the yellow region in figure 4.2(*a*) for the FOV. The camera was equipped with a 105 mm Nikkor lens set to $f^{\#} = 5.6$ to allow sufficient contrast in images. The images were acquired at 500–2000 Hz for ~ 11–44 seconds, depending on the nature of the experiment. Time-resolved, spanwise-averaged void fraction fields of ventilated cavities were measured using a high-speed 2-D X-ray densitometry system described in detail in Mäkiharju, Gabillet, et al. (2013). The current and the voltage of the X-ray source were set to 140 mA and 60 kV respectively, resulting in a measurement time of 1.6 seconds. The FOV-1, corresponding to X-ray densitometry, spans $8.2H \times 4H$ in the $x-y$ plane (see grey region figure 4.2(*a*)). An obstruction in the line of sight of X-rays resulted in a small circular, nonphysical artefact in the void fraction fields, located

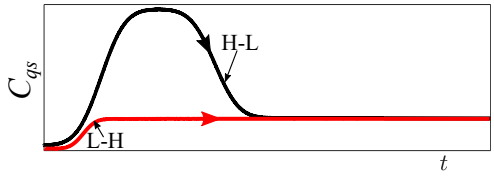

Figure 4.3: Gas injection profiles in time: red indicates a typical L-H profile, while black indicates a typical H-L profile.

at $x/H \approx 0.78$, $y/H \approx$ -0.52: see for instance black circle in figure 4.5(*c*). The instantaneous void fractions are estimated with a spatial resolution of 0.16 mm ($0.0084H$) and a temporal resolution of 0.001 seconds. For long cavities with closure in the region beyond the X-ray measurement (FOV-1), only qualitative X-ray visualisation (i.e. no *quantitative* void fraction field measurements) could be performed from $x = 14H$ to $22H$. This alternate FOV is shown by the blue region marked 'FOV-2' in figure 4.2(*a*). The thicker and denser PVC walls of the test facility led to a substantial reduction in signal-to-noise ratio precluding quantification of void fractions. The image acquisition (high-speed photography and X-ray radiography) was time-synchronised with gas ventilation input ($\dot{Q}$) and pressure transducers (P_1, P_0, P_c) using a digital pulse generator (DG535, Stanford Research Systems).

4.2.3. EXPERIMENTAL PROCEDURE

The ventilation experiments were performed for a range of U_0 (Fr) and over 100 different ventilation inputs (C_{qs}). Since the aim of this study was also to study the formation of a ventilated gas cavity, we performed two different types of experiments: In the first set of experiments, the gas was injected from $C_{qs} \sim 0$ to the desired C_{qs} with a known error function, i.e. ($dC_{qs}/dt > 0$ or $\dot{C}_{qs} > 0$). This ventilation strategy is referred to as 'L-H', as the ventilation is increased from zero to a given C_{qs} (see red profile in figure 4.3) typically in about 5 seconds and kept constant for at least 10 seconds depending on the nature of the experiment. In the second set of experiments, a fully-developed supercavity was used as an initial condition, and the gas injection rate was reduced with a known error function to achieve the desired C_{qs}, i.e. $\dot{C}_{qs} < 0$ (see black profile in figure 4.3). This ventilation strategy will be referred to as 'H-L' as the ventilation rate is reduced. The high C_{qs} is maintained for at least 5 seconds to ensure that the cavity closure is fully developed before reducing it to the final low C_{qs}, which is kept constant for at least 15 seconds. Thus, upon establishing a cavity, measurements were performed after waiting for sufficient time to ensure that the cavity length did not change. Note that the effect of the rate of increases of C_{qs} is beyond the scope of the current study. The ventilation is increased/decreased smoothly with an error function to mitigate the sharp overshoot in $\dot{Q}_{in}$ inherent to the first-order step response of the mass flow controller. This allows precise control of the volume of gas injected into the cavity. After each measurement, the flow loop is carefully de-aerated to ensure that there is no incoming free gas. The flow parameters of the experimental campaign are listed in table 4.1.

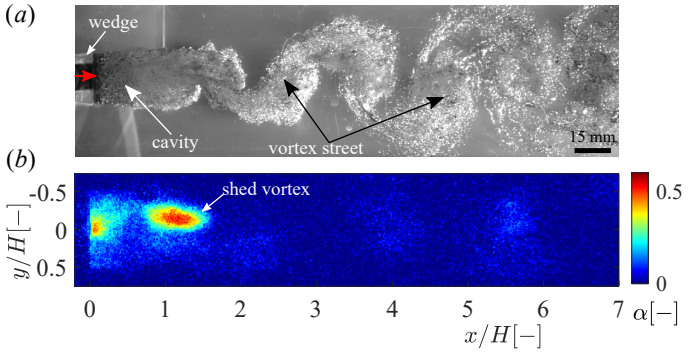

Figure 4.4: A side view ($x-y$) of a foamy cavity (FC); (*a*) A snapshot from high-speed optical imaging, (*b*) A snapshot from high-speed X-ray imaging. The red arrow shows the direction of the ventilation and the bulk flow. The bottom panel shows an instantaneous void fraction field.

4.3. STABLE VENTILATED CAVITIES

The defining characteristics of stable, fixed-length ventilated cavities are discussed in this section along with their occurrence on a regime map. Unsteady cavities observed during the transition from one stable cavity closure mode to another are discussed in section 4.4.

4.3.1. CAVITY CLASSIFICATION

Four types of stable ventilated cavities are identified based on the cavity closure region for the range of C_{qs} and Fr considered. They are classified as foamy cavities (FC), twin-branch cavities (TBC), re-entrant jet cavities (REJC), and long cavities (LC) as per the visual interpretation of optical and X-ray snapshots.

Foamy cavities (FC): These cavities were observed for $C_{qs} < 0.043$ and all the considered Fr (2-13.9). Figure 4.4(*a*) shows a snapshot from high-speed optical imaging of a foamy cavity observed at $Fr = 13.9$ and $C_{qs} = 0.0205$. Figure 4.4(*b*) shows the corresponding instantaneous void fraction field measured using time-resolved X-ray densitometry in a separate experiment. Densitometry is indispensable as it allows us to visualise void fractions inaccessible to conventional high-speed imaging. The cavity is characterised by the presence of injected gas as dispersed gas bubbles in the near-wake of the wedge. Foamy cavities do not have a well-defined closure region and are characterised by the shedding of injected gas due to vortex shedding in the wake of the wedge (Gnanaskandan & Mahesh, 2016b; Wu et al., 2021). Visual observation reveals that cavities are nominally 2-D in the near wake region, similar to natural cavities reported by Wu et al. (2021) in the same geometry. Foamy cavities have also been observed in other cavitator geometries like backward-facing steps (Qin et al., 2019), disc cavitators (Karn et al., 2016) and 3-D fences (Barbaca et al., 2017).

Twin-branched cavities (TBC): For $2.08 \leq Fr \leq 4.17$ and $C_{qs} > 0.043$, an attached cavity with a *weak* re-entrant flow near its closure (see flow structure near region marked 'closure' in figure 4.5(*b*) along with supplementary movie S3) and two prominent branches (legs) alongside the walls is observed as shown in figure 4.5. A prominent travelling wave-

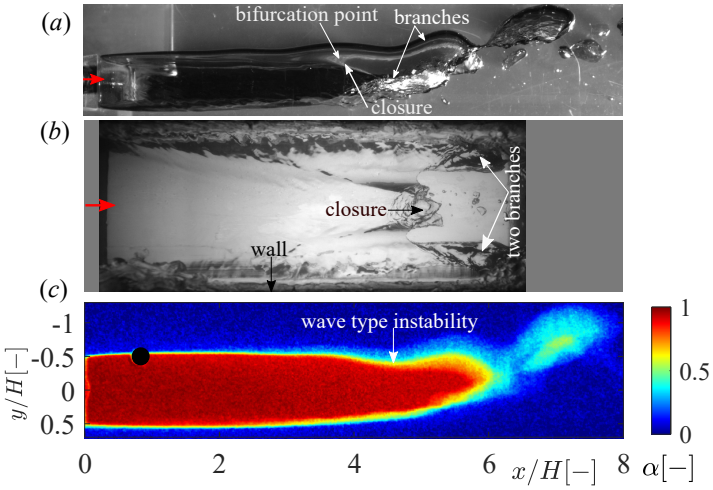

Figure 4.5: Twin-branched cavity (TBC); (*a*) shows a snapshot from high-speed optical imaging in the $x-y$ plane, (*b*) shows the top view ($x-z$ plane), (*c*) shows the instantaneous void fractions field of a TBC in $x-y$ plane. The black circle is a measurement artefact. The red arrow shows the direction of ventilation and bulk flow

type instability is seen on the upper cavity interface (see figure 4.5(*c*)). TBC cavities are clear (filled with gas) and exhibit a prominent camber due to buoyancy effects. The resulting upward curvature of the upper cavity interface leads to lift generation and formation of trailing vortices, observed as two branches (see figure 4.5). Similar cavities were observed for a 2-D cavitator by Qin et al. (2019) and Barbaca et al. (2017). These cavities show a close resemblance to the *twin vortex tube* type ventilated cavities reported in 3-D axisymmetric cavitators (Karn et al., 2016; Kawakami & Arndt, 2011; Semenenko, 2001). With an increase in Fr, the upward camber of the cavity decreases due to the increased effect of fluid inertia relative to gravity. TBCs are nominally 2-D along their axis until the bifurcation point slightly upstream of the closure where the cavity is divided into two branches, resulting in 3-D cavity closure, as shown in figure 4.5.

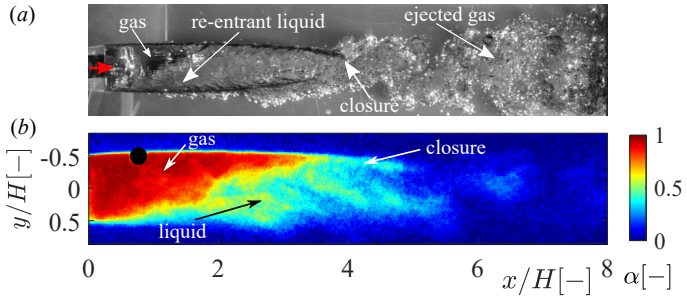

Figure 4.6: A side view ($x-y$) of a re-entrant jet cavity (REJC). The red arrow shows the direction of ventilation and bulk flow.

Re-entrant Jet Cavities (REJC): A third type of cavity, characterised by a *strong* re-entrant flow at the cavity closure, was observed at higher flow velocity ($5.79 \leq Fr \leq 13.9$) and intermediate ventilation rate ($0.045 \leq C_{qs} \leq 0.065$). These are termed re-entrant jet cavities (REJC) and an example is shown in figure 4.6. The gas in the cavity can be identified by a relatively clear part (see also the labelled region 'gas' in figure 4.6(*a*)), while the re-entrant flow is seen by the frothy liquid inside the cavity (see region labelled 're-entrant liquid' in figure 4.6(*a*)). REJ cavities are nominally 2-D except for the highly frothy and turbulent cavity closure, and slightly asymmetric about the wedge centreline ($z = 0$). Despite this asymmetry, REJ cavity shapes do not have a strong dependence on buoyancy (Fr). Re-entering liquid is confined to the lower half of the cavity, while the gas accumulates in the upper half (see figure 4.6(*b*)). Such ventilated cavities have not been observed before, although they resemble those reported by Barbaca et al. (2017) for a 3-D fence.

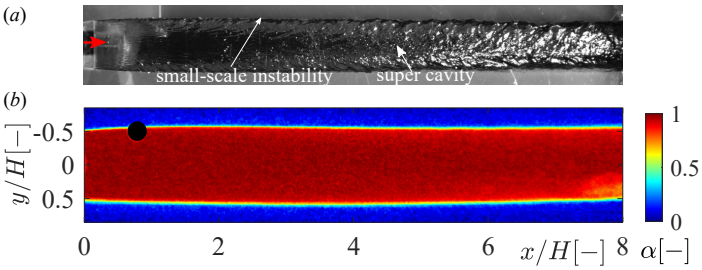

Figure 4.7: The side view ($x-y$) of a long cavity (LC). The red arrow shows the direction of ventilation and bulk flow.

Long Cavities (LC): Long cavities form for $5.79 \leq Fr \leq 13.9$ and $C_{qs} \geq 0.07$. LCs span beyond the optical FOV (see figure 4.7). Thus, the complete cavity could not be visualised with high-speed imaging and the cavity closure could not be measured quantitatively using X-ray densitometry. However, qualitative X-ray-based visualisation was performed to study cavity closure dynamics. Typically, the length of such cavities is more than $12H$. The observable portion of these cavities was 2-D, filled with gas as evident from instantaneous void fraction distribution, and with no observable effect of gravity on their shape (see figure 4.7(*b*)). These cavities exhibited small-scale instability/waves on the cavity interface, as indicated in figure 4.7(*a*). LCs exhibit oscillation in the $x-y$ plane similar to pulsating/vibrating cavities reported by Silberman and Song (1961), Michel (1984), and Skidmore (2016).

4.3.2. CAVITY REGIME MAP

The observed cavity types and transition regions in between them are identified on a regime map defined by the Froude number (Fr) and ventilation coefficient C_{qs} (see figure 4.8). Note that this regime map is specific to the cavitator geometry under consideration. The regime map was generated by fixing U_0 (Fr), followed by increasing the gas injection to achieve a C_{qs} following the L-H ventilation strategy explained in subsection 4.2.3 (see red profile in figure 4.3). Note that every data point is an independent experiment, i.e. ventilation profile starts from $C_{qs} = 0$. For $Fr \gtrsim 5$, the effect of gas buoy-

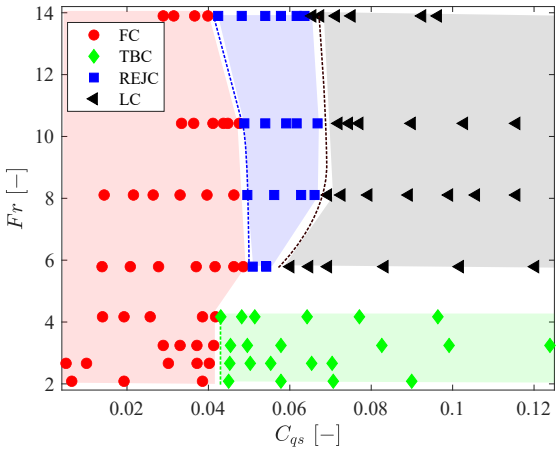

Figure 4.8: The regime map ($Fr - C_{qs}$) shows different types of observed ventilated partial/supercavities indicated by different colors. The dashed lines show the demarcation from one regime to another, i.e. green dashed line: $C_{qs,tr,fc-tbc}$, blue dashed line: $C_{qs,tr,fc-rejc}$, black dashed line: $C_{qs,tr,rejc-lc}$

ancy was observed to be less pronounced, and thus cavity types observed for $Fr \lesssim 5$ and $Fr \gtrsim 5$ were different. FCs (red region) and TBCs (green region) were observed only for $Fr \lesssim 5$, meaning TBC is the only supercavity observed at low Fr. FC (red region), REJC (blue region), and LC (grey region) were observed for $Fr \gtrsim 5$. Thus two types of supercavities were observed at high Fr, namely REJC and LC. The transition between the regimes occurs at a critical Froude number of ~ 5 and near the dashed lines shown in figure 4.8.

4.3.3. CAVITY PRESSURE

The pressure in the ventilated cavity is measured on the wedge centreline near the base, marked P_c in figure 4.2(*a*). The measured pressure is used to calculate the cavitation number (σ_c) as defined in table 4.1. Figure 4.9(*a*) shows the variation of σ_c with C_{qs} for a range of Fr considered in this study: the low Fr cases are shown by red markers, while the high Fr cases are shown by blue markers. This demarcation in low vs high Fr reflects the observations in the regime map (figure 4.8), which show a change in cavity closure type near $Fr = 5$. At low Fr (~ 2.08 – 4.17), the cavity pressure could only be measured for twin-branch cavities, as foamy cavities at low Fr were short barring reliable reliable measurement at the P_c location. Cavity pressure is seen to be the highest (high σ_c) at the lowest Fr. At lower Fr, once TBCs are formed, σ_c does not change significantly for increasing C_{qs}.

For foamy cavities, the cavity pressure oscillates about a mean due to the periodic vortex street, but for twin-branch cavities and re-entrant jet cavities the cavity pressure remains fairly constant. For long cavities, pressure oscillations are the largest due to the cavity pulsation in the $x - y$ plane. These pressure pulsations are evident from the large standard deviations in σ_c for long cavities as shown in figure 4.9(*a,b*). Figure 4.9(*b*) shows the variation of σ_c with C_{qs} along with flow visualisation for a fixed Froude number (Fr ~ 13.89): σ_c decreases with an increase in ventilation (C_{qs}) in the

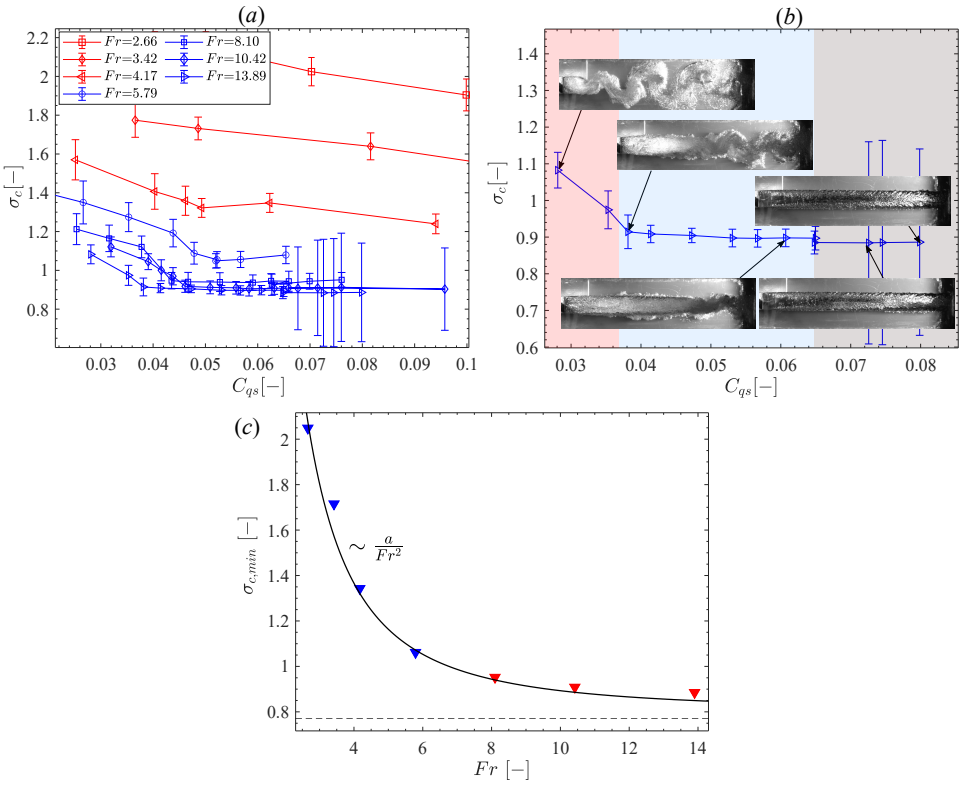

Figure 4.9: (*a*) Cavitation number (σ_c) based on measured cavity pressure as a function of ventilation coefficient (C_{qs}) at different Fr (red markers show low Fr cases, while blue markers show high Fr cases), (*b*) σ_c at Fr = 13.89 showing different ventilated cavity regimes. The red, blue and grey regions correspond to FC, REJC and LC closures respectively, (*c*) minimum σ_c as a function of Fr. The black curve shows aFr^{-2} curve fit, where a is a constant. The black dashed line shows σ_c = 0.77 computed with the Bernoulli equation.

FC regime. With a further increase in C_{qs}, σ_c decreases minimally in the REJC regime until it reaches the asymptotic minimum ($\sigma_{c,min}$) when the formation of LCs occurs. In the LC regime, σ_c stays constant at $\sigma_{c,min}$. Figure 4.9(*c*) shows the minimum cavitation number, $\sigma_{c,min}$, attained at a given Fr. For LC (high Fr and C_{qs}), the streamlines near the wedge base tend to straighten towards being parallel to the incoming flow (see figure 4.7(*b*)) and the pressure in the cavity approaches a minimum. With streamlines parallel to the tunnel walls, the liquid pressure outside of the air-cavity, P_ℓ, can be estimated from the Bernoulli equation using the wedge's solid blockage percentage, ξ. The pressure is given as $P_\ell = P_0 + 1/2\rho_\ell U_0^2\left[1-(1-\xi)^{-2}\right]$. Here, $\xi = 0.25$, and the pressure coefficient $C_p = (P_0 - P_\ell)/(1/2\rho U_0^2) \approx 0.77$. This value is indicated by the black dashed line in figure 4.9(*c*). As the cavity interface becomes *straighter*, P_c approaches the theoretical P_ℓ.

4.3.4. CAVITY GEOMETRY

The void fraction fields (instantaneous and time-averaged) of the cavity, along with high-speed visualisations, are used to study various geometrical aspects of the cavity, such as length, thickness, and shape.

CAVITY LENGTH

The cavity length is defined by the distance of the closure region to the wedge base for FC, REJC, and LC. For TBC, the cavity length is defined from the wedge base to the bifurcation point along the mid-span of the cavity. Non-dimensional cavity length (L_c/H) variation with C_{qs} for $Fr \leq 4.17$ and $Fr \geq 5.8$ is shown in figure 4.10(*a*) and (*b*) respectively. Figure 4.10(*c*) shows the variation of (L_c/H) with cavitation number (σ_c) for supercavities.

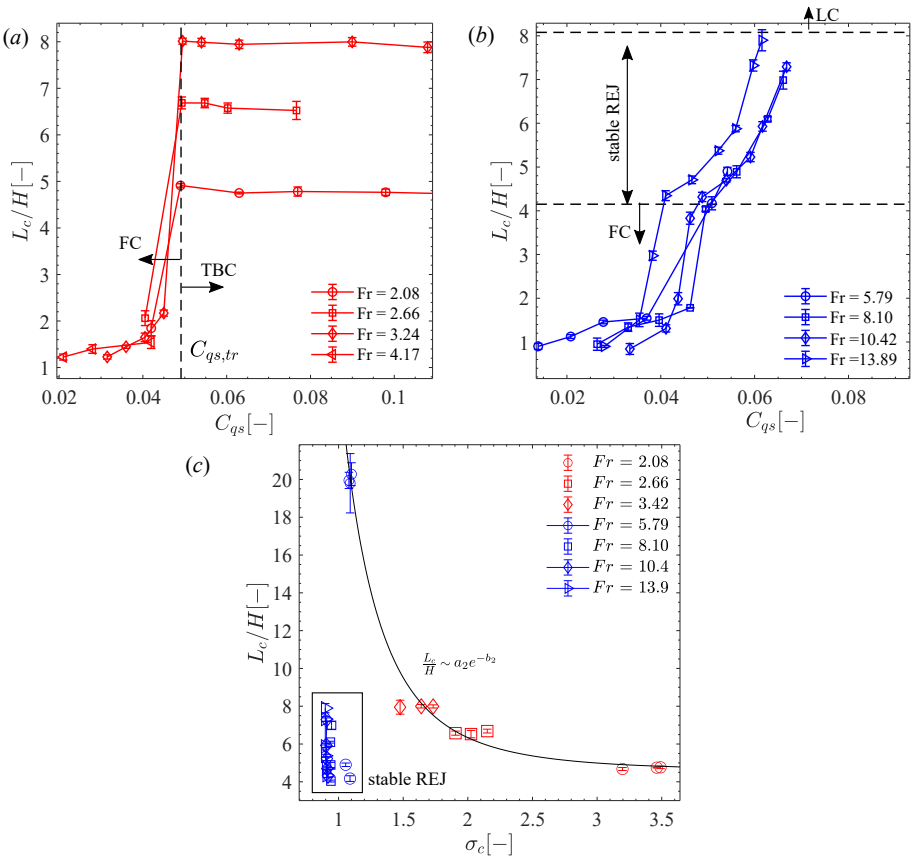

Figure 4.10: The length (L_c) of the partial ventilated cavities, normalised by wedge height (H) at different Fr as a function of ventilation coefficient (C_{qs}): (*a*) shows cavities at low Fr (< 5), while (*b*) shows cavities at higher Fr (> 5). (*c*) Cavity length (supercavity) variation with cavitation number (σ_c) (the low Fr cases are shown by red markers, while the high Fr cases are shown by blue markers). The solid black curve shows the exponential fit to the data points, with constants a_2 and b_2.

For $Fr \leq 4.17$, the length of foamy cavities increases monotonically with C_{qs}. The absence of a well-defined closure leads to a modest increase in L_c/H with increasing C_{qs}. L_c/H increases abruptly when FC transitions to TBC, and with a further increase in C_{qs} at a fixed Fr, L_c/H remains unchanged (see figure 4.10(*a*)). The observed trend is accompanied by the thickening of the two branches and a higher gas ejection rate needed to maintain the same cavity length. At $Fr \geq 5.8$, foamy cavities increase in length monotonically with C_{qs} similar to the low Fr case (figure 4.10(*b*)). A sharp change in cavity length, from $L_c/H \approx 2$ to 4, with an increase in C_{qs} is observed as the cavity regime changes from the foamy cavity to the re-entrant jet cavity. As C_{qs} is increased further, REJ cavities (figure 4.10(*b*)) increase in length, and are seen to span over $4H$ to $8H$ for all Fr considered. With further increase in C_{qs} ($\gtrsim 0.07$), abrupt growth of REJ cavities results in the formation of long cavities that grow out of the field of view. It was not possible to quantitatively study the closure region of LC due to limited optical and X-ray densitometry access. However, qualitative visualisation of closure using X-ray imaging allowed the estimation of cavity length for long cavities for $Fr \approx 5.79$.

The measured maximum cavity length (for a fixed Fr) appears to have a power law relationship with the cavitation number, σ_c, as shown in figure 4.10(*c*). Such a trend in cavity lengths has been reported previously in Franc and Michel (2005) and Terentiev et al. (2011). Interestingly, REJ cavities appear *stunted* as they do not fall on the power law, suggesting a different scaling law governing their lengths. This will be addressed in subsection 4.4.3. The maximum *thickness* of cavities shows a minor dependence on C_{qs}: it varies from $1-1.1H$ for FC, while it is close to $1.18H$ for all other supercavities observed in this study. This is in agreement with Wu et al. (2021) who reported the geometric features of natural cavities in the same geometry.

AVERAGE VOID FRACTION DISTRIBUTION

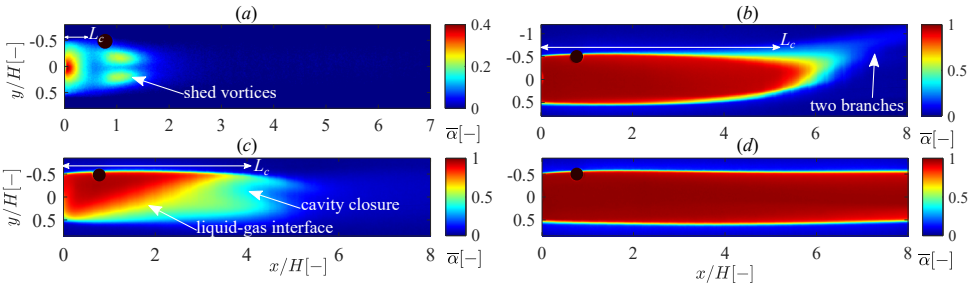

Figure 4.11: Time-averaged void fractions fields of cavities in the four regimes; (*a*) FC: Fr = 13.9, C_{qs} = 0.0205, (*b*) TBC: Fr = 2.08, C_{qs} = 0.058, (*c*) REJC: Fr = 5.79, C_{qs} = 0.054, (*d*) LC: Fr = 10.42, C_{qs} = 0.090. The black disc is a measurement artefact.

Figure 4.11 shows the time-averaged and spanwise integrated void fraction, $\overline{\alpha}$, for ventilated cavities considered. The black dot located at about (x/H=0.78, y/H= -0.52) in the void fraction fields is a measurement artefact as mentioned before. For foamy cavities, the maximum of time-averaged void fractions is ~ 0.4 as cavities are composed of dispersed bubbles in the near wake, as shown in figure 4.11(*a*). The gas-filled vortex streets appear as lobes with an average void fraction of ~ 0.2 and the time-averaged void

fraction is symmetric about the x-axis for foamy cavities. TBC, REJC, and LC are composed predominantly of air, resulting in $\alpha = 1$ as shown in figure 4.11(*b-d*). For TBCs, the void fraction distribution is asymmetric about the x-axis due to the upward camber as a result of buoyancy (see figure 4.11(*b*)). $\overline{\alpha}$ in the closure region ranges from approximately $0.1-0.6$ and this variation is due to the averaging of the three-dimensional, time-varying cavity geometry as shown in figure 4.5. Figure 4.11(*c*) shows the void fraction distribution of REJ cavities. There is a clear separation of gas and liquid phases inside the cavity due to the buoyancy effects as seen by a sharp gas-liquid interface. The cavity shape exhibits asymmetry about x-axis, with a downward curvature of the upper cavity interface. The downward curvature of the cavity interface relaxes as cavity length increases to form long cavities. The streamlines of long cavities are straighter, with the shape of the cavity almost symmetric about x-axis, as shown in figure 4.11(*d*). The void fractions at the closure of Long cavities could not be measured due to the limitations imposed by the FOV. Nevertheless, qualitative gas distribution is discussed in subsection 4.3.5.

4.3.5. DYNAMICS AT CAVITY CLOSURE AND GAS EJECTION MECHANISMS

Foamy Cavities (FC): Foamy cavities do not have a well-defined closure, akin to natural

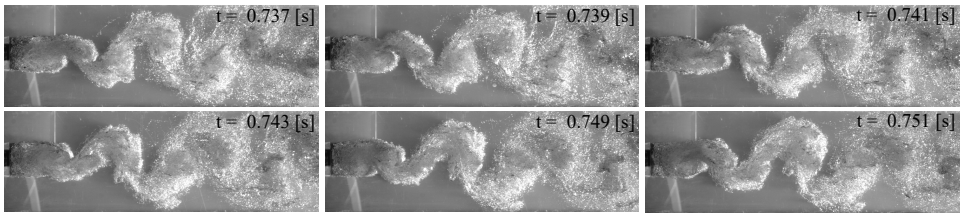

Figure 4.12: High-speed flow visualisation of gas ejection for FC at $Fr = 13.9$, $C_{qs} = 0.0290$, showing periodic gas ejection via a Von Kármán vortex street.

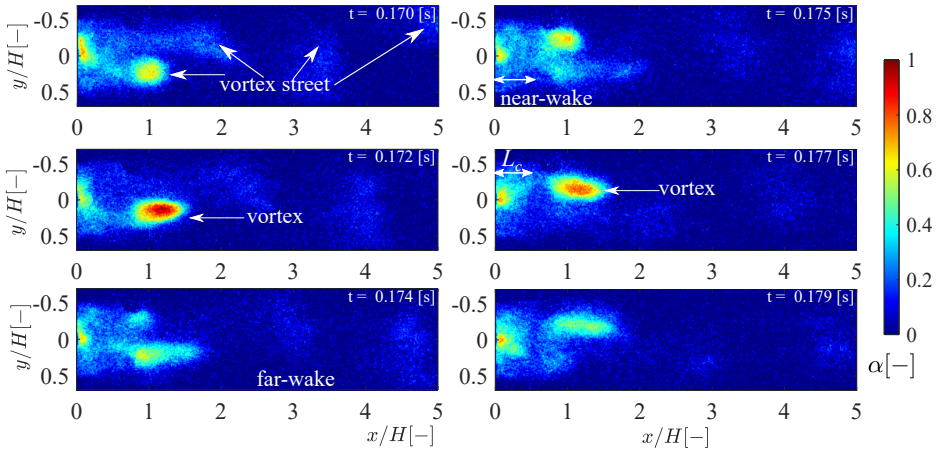

Figure 4.13: Instantaneous void fraction fields for FC at $Fr = 13.9$, $C_{qs} = 0.0205$, showing periodic gas ejection via a Von Kármán vortex street.

open cavities defined by Laberteaux and Ceccio (2001a). In FCs, the entrained gas is

ejected out periodically via an alternating Von Kármán vortex street, as shown by high-speed snapshots in figure 4.12 and void fraction time series in figure 4.13 (acquired in a separate set of experiments). See supplementary movies S1 and S2. The gas ejection frequency, expressed as Strouhal number (St_H), is estimated to be ~ 0.31, which is in close agreement with values reported for other bluff bodies (Brandao et al., 2019; Wu et al., 2021).

Twin-Branch Cavities (TBC): TBCs are nominally 2-D until their bifurcation point but have a well-defined 3-D closure. The closure of these cavities is characterised by two branches along the walls as shown in figure 4.14 and 4.5. The cavity closure is marked by a weak re-entrant flow along the centreline of the cavity in the $x-z$ plane shown in figure 4.5(*b*).

Based on high-speed videos, two gas ejection mechanisms can be identified. Firstly, the gas ejection appears to be due to a re-entrant flow in the narrow mid-tail region where gas is ejected in small parcels as shown in the region marked by 'closure' in figure 4.5(*a,b*). This is shown more clearly in the supplementary movie S3. Secondly, gas ejection is observed at the downstream tips of the two branches via a wave-like instability shown in figure 4.14. Figure 4.15 (*a-f*) shows X-ray-based visualisation of the wave-induced gas ejection in twin-branch cavities. The convecting wavefront on the upper cavity interface is marked and shown by white arrows. As the travelling wave disturbance propagates downstream along the cavity (*a-e*), it pinches the cavity at the twin branches leading to a gas ejection (see supplementary movie S4 and S5). Since the length of the cavity does not change with increasing C_{qs} for a given Fr (see figure 4.10(*a*)), larger gas ejection must occur at higher C_{qs}. The larger gas ejection appears as larger slugs as shown in figure 4.14(*f-j*) and supplementary movie S6. It is observed that the amplitude of the waves is higher for larger ventilation (C_{qs}) for a given Fr, suggesting larger pulsation at higher C_{qs} as illustrated in figure 4.14. The convecting wavefront is marked by a white dashed line in figure 4.14 for C_{qs} = 0.058 (*a–e*) and 0.128 (*f–j*). The slope of the white dashed lines can be used to approximate the propagation speed of the wave and appears to be the same, despite a significant difference in C_{qs}. For a given Fr, the wave propagation velocity is close to the velocity of the upper cavity interface ($\mathcal{O}(U_0)$) for the considered range of C_{qs} (~ 0.058–0.128). This suggests that it is an inertial wave possibly triggered by a Kelvin-Helmholtz instability due to the density difference at the upper cavity interface. The wave speed at the upper interface ($c_{r,tbc}$) in this case can be expressed by equation 4.1 (Drazin, 2002), where subscripts l, g correspond to liquid and gas phases respectively. $c_{r,tbc}$ reduces to U_l due to the large density difference across the cavity interface ($\rho_g \ll \rho_l$) as per equation 4.1. This is consistent with our experimental observations.

$$c_{r,tbc} = \frac{\rho_g U_g + \rho_l U_l}{\rho_g + \rho_l} \approx U_l \approx U_0 \tag{4.1}$$

Re-entrant Jet Cavities (REJC): A time series obtained from high-speed videography of a REJ cavity is shown in figure 4.16. In the optical measurements, gas-liquid interfaces result in reflections (bright, white regions) which obfuscate the internal cavity flow. However, the large field of view allows for the wedge base, cavity, and wake to be simultaneously visualised. A re-entrant flow, visualised by a frothy mixture along with the

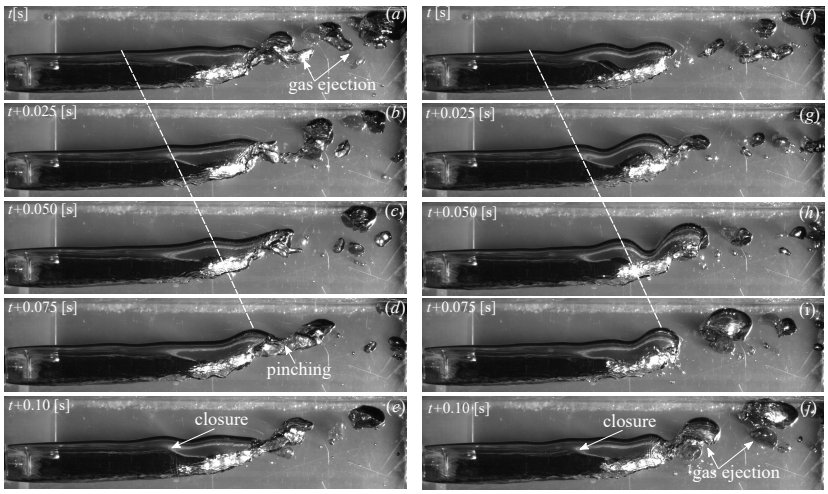

Figure 4.14: TBC cavity closure for Fr = 2.08 for two different cases of ventilation; left (*a-e*): C_{qs} = 0.058, right (*f-j*) : C_{qs} = 0.128. The white dashed line shows a convecting wave-type instability on the upper cavity interface responsible for cavity pinching.

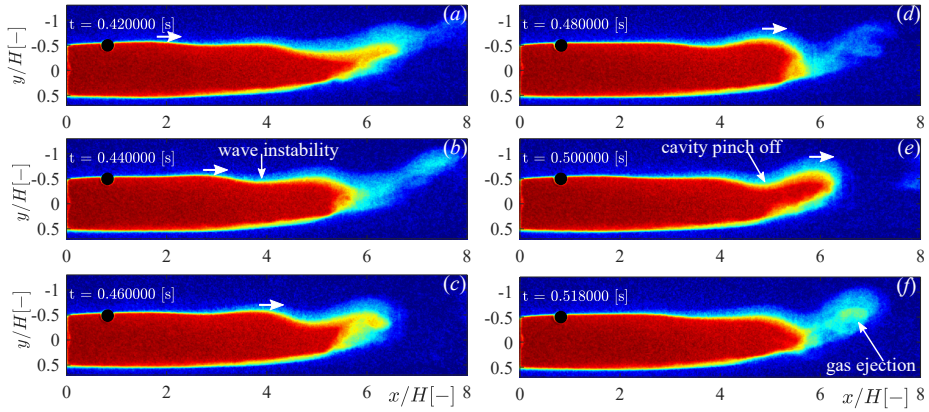

Figure 4.15: Instantaneous gas ejection at TBC cavity closure for Fr = 2.08, C_{qs} = 0.058. The white arrows show the travelling wavefront. The colorbar of the jet colormap showing void fractions span from 0 to 1.

flow-front indicated by a red arrow can be seen propagating upstream in figure 4.16(*a-e*). As the re-entrant liquid flow reaches the base of the wedge it seems to be redirected to the cavity interfaces (figure 4.16(*e*)). This is illustrated in the supplementary movie S7. A clearly defined Von Kármán vortex street can be seen in the cavity wake (figure 4.16(*d,e*)), suggesting vortex shedding and gas ejection are coupled. As the re-entrant jet front propagates upstream, it displaces gas at the bottom of the cavity as seen in figure 4.16(*c,e*). While the gas can be seen advecting away from the cavity, the gas volume cannot be quantified from the high-speed imaging.

Time-resolved void fraction measurements of a REJ cavity for the same condition show the internal cavity behaviour in figure 4.17. Note that the X-ray densitometry mea-

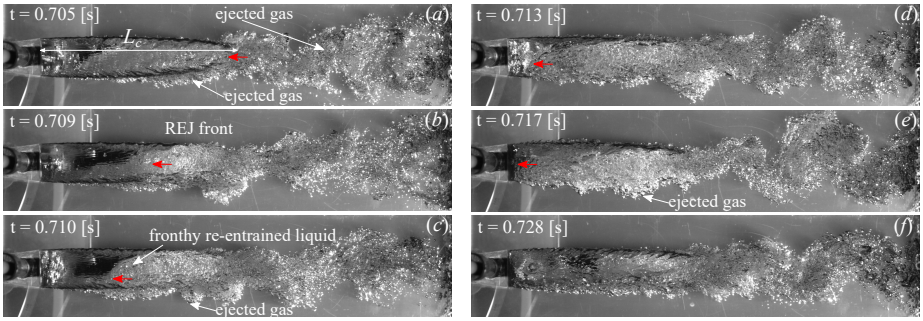

Figure 4.16: High-speed visualisation of REJC dynamics for $Fr = 5.79$, $C_{qs} = 0.054$ (time increases from top to bottom, left to right). The red arrows in (*a-e*) indicate the re-entrant flow front. The Von Kármán vortex street can be clearly seen in (*e, f*).

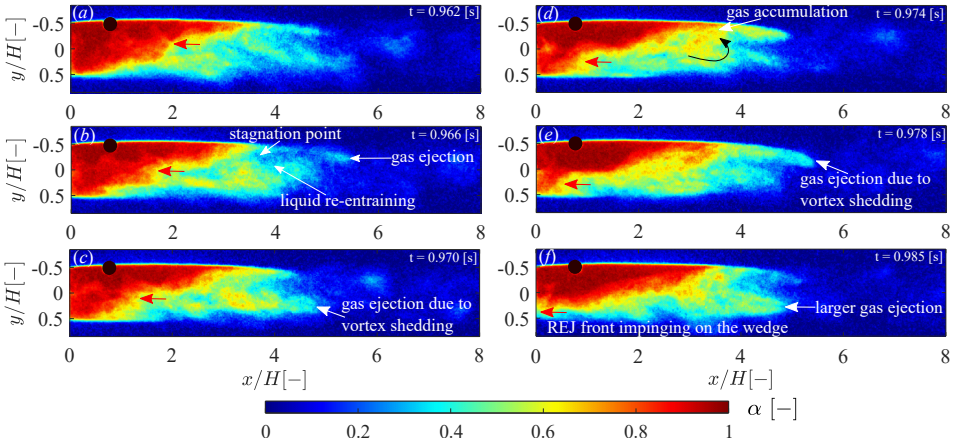

Figure 4.17: Instantaneous void fraction fields for a REJ cavity; $Fr = 5.79$, $C_{qs} = 0.054$ showing gas accumulation and ejection. Red arrows indicate the re-entrant flow front propagating upstream.

surements are separate experimental trials from the high-speed videography measurements. The gas accumulation in the upper half of the cavity is evident from the red (high-void fraction) regions in figure 4.17. Supplementary movie S8 shows that the injected gas reaches the closure and gets accumulated in the upper part of the cavity, as also indicated by figure 4.17(*d*). The liquid re-entrant flow is visualised by a low void fraction (~ 0.5) region in the lower part of the cavity. A stagnation point is formed near the closure (indicated in figure 4.17(*b*)) and liquid re-entrant flow is pushed inside the cavity. The front propagates towards the wedge base and eventually becomes confined to the bottom part of the cavity due to the effects of gravity (see figure 4.17) Here the red arrows indicate the liquid re-entrant jet front. Figure 4.17(*f*) shows that the propagating re-entrant liquid flow displaces the gas, resulting in a gas ejection. Additionally, gas is also ejected from the cavity via the spanwise vortices of the wake flow downstream as shown in figure 4.17(*b, e, f*). This re-entrant flow cycle continues to sustain a stable REJ cavity.

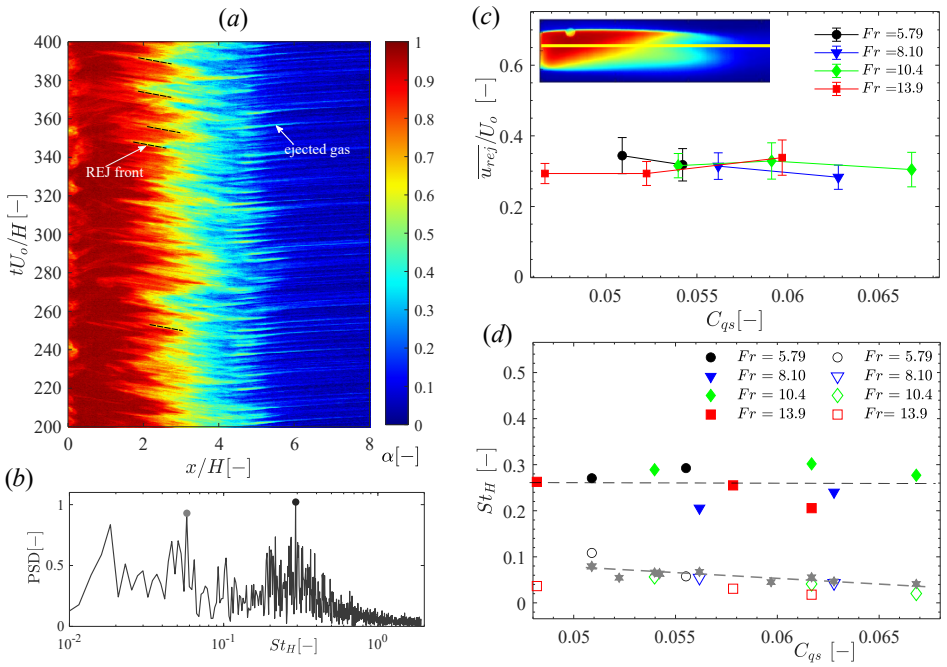

Figure 4.18: (*a*) A sample $x-t$ diagram showing the evolution of the void fraction for a REJ cavity at $Fr = 5.79$, $C_{qs} = 0.054$. Examples of the re-entrant flow front are indicated by black dashed lines. (*b*) Power spectral density of the void fraction computed from the $x-t$ plot at $X/H \approx 5$, showing two *distinct* peaks. (*c*) Re-entrant jet velocity measured from the space-time diagram. (*d*) Non-dimensional shedding frequency (St_H) for a range of Fr and C_{qs}: Solid markers show the gas ejection frequency due to vortex shedding. Open markers show the gas ejection frequency due to the re-entrant jet impingement. Grey markers ($*$) show St based on measured kinematics of the re-entrant jet (L_c and $\overline{u_{rej}}$). The grey dashed line fit to grey markers is given as $St_{H,rej} = 0.2 - 2.375 C_{qs,in}$.

The characteristics of the liquid re-entrant flow can be estimated from a space-time ($x-t$) diagram of time-resolved void fraction fields. The $x-t$ plot in figure 4.18(*a*) shows the void fraction time evolution along the yellow line ($y/H \sim$ -0.27) shown in the inset of figure 4.18(*c*). The black dotted lines visualise the REJ front *inside* the cavity, and the ejected gas is indicated by the white arrow in the $x-t$ plot. The velocity of the re-entrant jet front and the convection of the ejected gas are estimated from such $x-t$ diagrams. The measured REJ front velocity u_{rej}, when normalised with the inlet velocity, is constant ($\overline{u_{rej}}/U_0 \approx 0.3$) irrespective of C_{qs} and Fr as shown in figure 4.18(*c*). Strouhal number ($St_H = fH/U_0$) of the gas ejection is estimated by computing shedding frequency (f), where f is computed via an FFT of the time signal extracted from the $x-t$ plot in figure 4.18(*d*). The FFT was performed on the time signal of the void fraction at a probing point in the wake ($X/H \approx 5$). Two distinct peaks were observed in the spectral density (see figure 4.18(*b*)), corresponding to two distinct gas ejection mechanisms. Gas ejection due to vortex shedding occurs at a roughly constant non-dimensional frequency ($St_{H,v} \approx 0.27$). The gas ejection associated with the re-entrant jet displacing the gas occurs at a lower frequency ($St_{H,rej} \lesssim 0.1$). St based on the time taken by the re-entrant jet

to impinge on the wedge base (using $1/t = \overline{u}_{rej}/L_c$) matches the shedding frequency estimated from the FFT of re-entrant flow-induced gas ejection reasonably well as shown in figure 4.18(*d*). This suggests a correlation between the re-entrant jet and gas ejection. Additionally, it is observed that $St_{H,rej}$ decreases linearly: $St_{H,rej} = 0.2 - 2.375C_{qs,in}$ as C_{qs} increases as shown by a grey dashed line in figure 4.18(*d*). This empirical relation will be invoked for constructing a model in subsection 4.4.3.

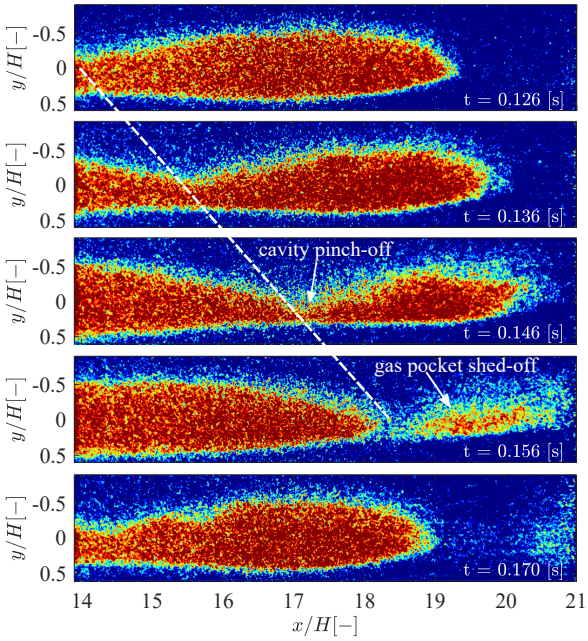

Figure 4.19: X-ray flow visualisation of cavity closure corresponding to the LC regime at $Fr = 5.79$, $C_{qs} = 0.069$. X-ray images were taken through the thicker and denser PVC walls of the test section leading to greatly reduced contrast. As such, the void fraction cannot be accurately estimated. However, the shape of the cavity can be visualised. The white dashed line shows the travelling wavefront leading to the gas pocket shed-off.

Long Cavities (LC): Closure of long cavities was not observed using high-speed images as it spanned beyond the FOV. Nevertheless, X-ray-based flow *visualisation* was performed through the thicker and denser PVC walls of the test facility at FOV-2, as shown in figure 4.2. This led to low signal-to-noise ratio in void fractions allowing only qualitative visualisation. From these qualitative visualisations, the following observations were made: Long cavities do not exhibit a re-entrant flow-like closure. The gas appears to be ejected out of the cavity closure via inertial wave-type instability, as shown in figure 4.19. The wave is seen to be convecting on the upper cavity interface with a velocity close to free-stream velocity (U_0) as evident in the supplementary movie S9. This leads to cavity pinch-off and a gas pocket shed-off with a non-dimensional frequency (St_H) of about 0.19. This is in close agreement with Shao et al. (2022), who reported an average St of 0.20 for oscillatory cavities behind a 3-D axisymmetric cavitator. With an even further increase in C_{qs}, the cavity lengths do not increase substantially, rather, the amplitude of oscillation is seen to increase. The size of the gas pocket shed-off is expected to increase

to allow higher gas ejection. The similarity of the observed closure mechanism of a long cavity with a twin-branch cavity is an open question and will be investigated in a future investigation.

4.3.6. COMPRESSIBILITY EFFECTS

In natural cavitating flows, the compressibility of the medium plays a significant role in dictating cavity dynamics (Ganesh et al., 2016; Wu et al., 2021). Moderate vapour fractions (~ 0.4-0.7) in combination with low pressure in the vapour cavity (of the order of vapour pressure) reduces the speed of sound in this bubbly mixture to $\mathcal{O}(1)$ ms^{-1} (Shamsborhan et al., 2010). This can result in high cavity Mach numbers, giving rise to the propagating bubbly/condensation shock fronts as observed experimentally by Ganesh et al. (2016) and Jahangir et al. (2018), and numerically by Budich et al. (2018). In ventilated cavities, the void fractions (α) can attain values close to 0.5, especially in REJ cavities due to the entertainment of liquid inside the cavity (see figure 4.17), leading to minima in the speed of sound as per equation 4.20. Hence, the effects of compressibility need to be examined for such cavities. The direct void fraction (α) and pressure measurements (P_c) allow us to make a ballpark estimate of the speed of sound in the binary mixture within the cavity (c_m) using equation 4.2 (Brennen, 1995), where k is the polytropic constant of the mixture. In equation 4.2 it is assumed that the cavity is composed of liquid (subscript l) and gas (subscript g) with negligible surface tension effects, bubble dynamics, and mass transfer between phases. The Mach number is then estimated with equation 4.3, where the velocity scale u is either the incoming free stream velocity (U_0) or the velocity of the re-entrant jet front ($\overline{u_{rej}}$).

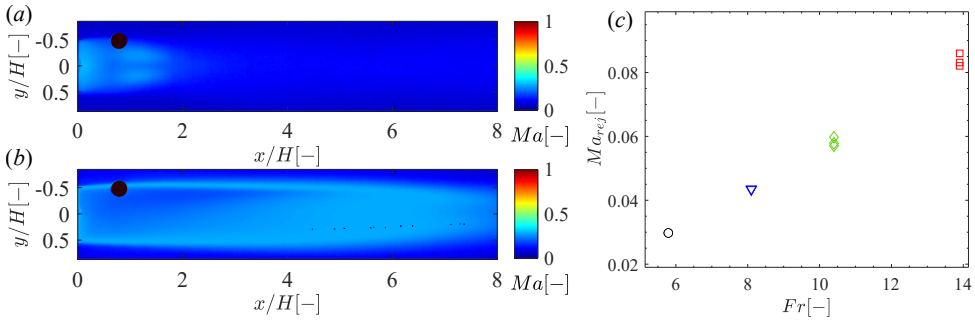

Figure 4.20: Mach number based on averaged void fraction fields ($\overline{\alpha}$) and incoming velocity (U_0) for (a) Fr=13.89 C_{qs}= 0.029, (b) Fr=13.89 C_{qs}= 0.0617, (c) Mach number of the re-entrant jet front at different Fr.

$$c_m = \left\{ \frac{\alpha}{kP_c} [\alpha \rho_g + (1-\alpha)\rho_l] \right\}^{-\frac{1}{2}} \tag{4.2}$$

$$Ma = \frac{u}{c_m} \tag{4.3}$$

TBCs and LCs are filled with air ($\alpha \sim 1$) as seen by the void fraction distribution shown in figures 4.11(*b,d*). Hence, the speed of sound is expected to be high (~ 300 ms^{-1}) in

these cavities, resulting in a low Ma. These cavities are omitted from the analyses. Note that for a given cavity (fixed P_c), c_m has a maximum at $\alpha = 0.5$. Further, using U_0 as a velocity scale to estimate the Ma provides us with the maximum achievable values of Ma for the cavity. The time-averaged void fraction fields are used to estimate the local Ma for foamy cavities and re-entrant jet cavities in figure 4.20(*a, b*). It is seen that the Mach number is consistently lower than 0.3. The estimated Mach number of re-entrant flow front (Ma_{rej}, based on $\overline{u}_{rej}$) is shown in figure 4.20(*c*). It increases with Fr, yet remains lower than 0.1. This suggests that the effect of compressibility is negligible for the ventilated cavities under consideration. Although the void fractions are sufficiently low, the pressure in the cavities is sufficiently high to maintain the speed of sound as high as 25 ms^{-1}. This is in contrast with natural cavities, where the speed of sound (c_m) drops to a few ms^{-1} owing to low cavity pressures of a few kPa.

4.4. UNSTABLE CAVITY CLOSURES DURING SUPERCAVITY FORMATION

The stable ventilated cavities at different flow conditions show distinct and fixed cavity lengths. However, during the transition from one regime to another, the cavity length undergoes an abrupt increase in length (see figure 4.10(*a,b*)). During this sudden increase in length, cavities exhibit unique closure regions. We refer to these cavities as transitional/unstable cavities and the closure as *unsteady/transitional* closures. During the formation of supercavities starting from foamy cavities, they *pass through* these unstable cavity closure modes due to the monotonic increase in gas injection profile (see red profile in 4.3). It is imperative to understand the formation of supercavities and the unsteady closures to make a better estimation of ventilation demands and predict the transition from one closure to another, as shown later in subsection 4.4.3.

The formation of supercavities (TBCs and LCs) at a given Fr is studied with a prescribed C_{qs} profile. As the ventilation is increased to attain a final constant C_{qs} via the L-H ventilation strategy (see again figure 4.3), cavity formation begins. The formation of a twin branch cavity (TBC) at $Fr \approx 2.08$, 4.17 and long cavity (LC) at $Fr \approx 10.42$ are discussed separately.

4.4.1. FORMATION OF TWIN BRANCH CAVITIES (TBC)

At low Fr, for an increase of C_{qs} above 0.043, FC transitions to TBC, the only stable supercavity observed in this Fr range $(2.08 - 4.17)$. The formation process observed for $Fr = 2.08 - 2.66$ differs from $Fr = 3.4 - 4.17$ as illustrated in figure 4.21, 4.22 and 4.23:

Figures 4.21(*a-e*) and 4.22 show the transition process of FC to TBC based on optical visualisation and time-resolved X-ray measurements at $Fr = 2.08$ and $C_{qs} = 0.058$. This is representative of the observed formation dynamics for $Fr = (2.08 - 2.66)$. Note that final $C_{qs} = 0.058$ is achieved using the L-H ventilation strategy, see the ventilation (C_{qs}) profile shown in the inset of figure 4.22. As gas injection begins small dispersed bubbles accumulate near the wedge base as shown in figure 4.21, 4.22(*a, b*). With increasing C_{qs}, unsteady closure is formed and the cavity starts growing abruptly from *c-e*. This is accompanied by the cavity spanning the entire height of the wedge in the y-direction. Subsequently, the cavity is filled completely with air exhibiting high vapour

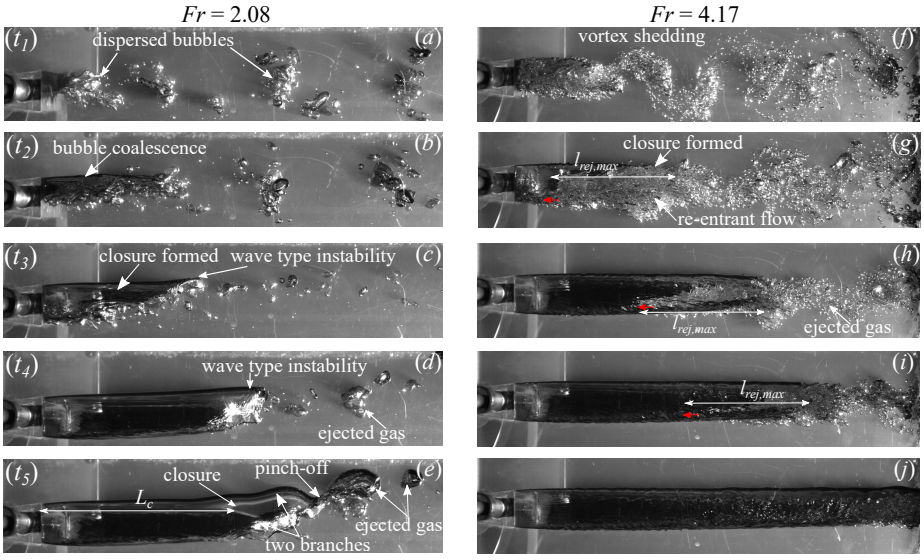

Figure 4.21: High-speed visualisation of Twin branch cavity (TBC) formation/development (gas entrainment and ejection) showing the difference in closure region for (*a-e*) $Fr = 2.08$, final $C_{qs} = 0.058$ and (*f-j*) $Fr = 4.17$, final $C_{qs} = 0.0514$. The unsteady closure is characterised by a wave-type instability for $Fr = 2.08$, while a constant length re-entrant flow ($l_{rej,max}/H \approx 3$) is seen at the unsteady closure for $Fr = 4.17$. The closure of fully developed TBC at $Fr = 4.17$ is not visualised as it spanned beyond the FOV.

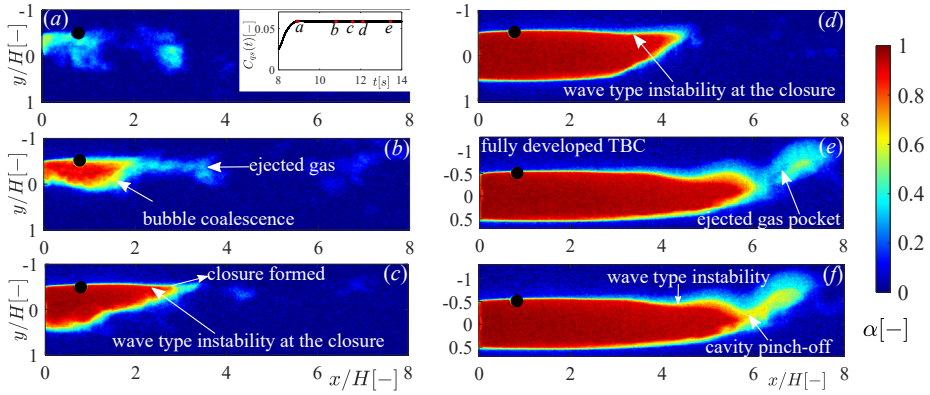

Figure 4.22: Twin branch cavity (TBC) formation/development (gas entrainment and ejection) for $Fr = 2.08$, $C_{qs} = 0.058$. The closure is characterised by wave-type instability. The inset shows the ventilation profile.

fraction ($\alpha \sim 1$) (see figure 4.22(*c*)). This process is shown in the supplementary movie S10. For $Fr = (2.08 - 2.66)$, the unsteady closure *cambers up*, without a re-entrant flow (see figure 4.22(*c,d*)). The closure of the unsteady cavities is marked by a wave-type instability, that pinches the cavity at the closure giving rise to gas ejection as shown in figure 4.22(*c, d*)). Finally, a stable twin-branch cavity with 3-D closure is formed at '*e*' shown in figure 4.22(*e, f*).

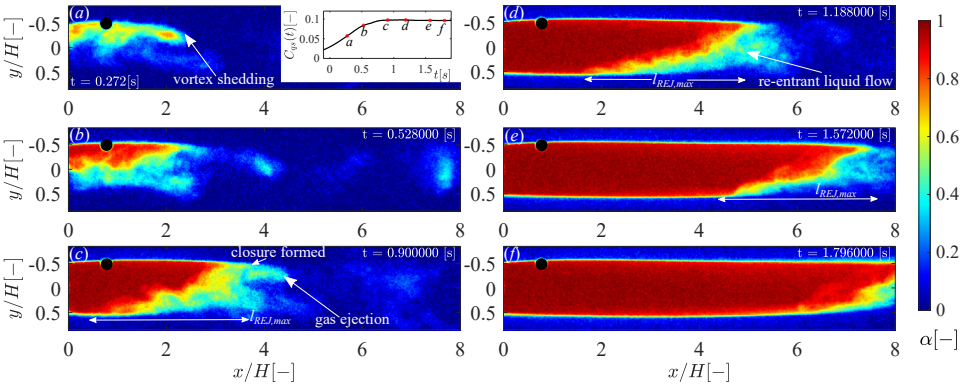

Figure 4.23: Twin branch cavity (TBC) formation/development(gas entrainment and ejection) for Fr = 4.17, C_{qs} = 0.096 showing fixed length re-entrant flow ($l_{rej,max}/H \approx 3$) near the closure receding away from the wedge base. The inset shows the ventilation profile.

At $Fr \approx 4.17$, a foamy cavity is observed as injection begins (see figure 4.21(*f*) and 4.23(*a*)) similar to the case of $Fr \approx 2.08$. As C_{qs} is increased (see ventilation profile in the inset of figure 4.23) FC transitions to a cavity with an unsteady closure. Once the closure is formed at 4.23(*c*), the cavity length increases abruptly from (*c*) to (*f*). The upper interface of the unsteady cavity formed during this transition does not camber up, but rather curves *downwards* as evident in figure 4.21(*g-j*) and 4.23(*b-e*). This is accompanied by a re-entrant flow at the cavity closure as visualised by a frothy mixture in high-speed visualisation. The ejected gas is seen as a vortex street as shown in figure 4.21(*f-h*). Figure 4.23 shows the X-ray time series of cavity formation at $Fr \sim 4.17$ but at a higher C_{qs} due to the unavailability of data at the identical C_{qs}. Note that despite the difference in C_{qs}, the dynamics of cavity formation are very similar. The re-entrant jet confined to the closure region of the cavity is visualised by low void fraction values ($\alpha \sim 0.5$) and shown in figure 4.23(*c-f*). Further, the length of this re-entrant jet is nearly constant ($l_{rej,max}/H \approx 3$). As the cavity length increases, this constant length re-entrant flow is seen to recede away from the wedge base (see red arrows in figure 4.21(*g-i*) and the re-entrant flow front in figure 4.23(*c-f*)). The gas is ejected via spanwise vortex shedding during the growth of the cavity to TBC as seen in figure 4.21(*f-i*) and 4.23(*b-e*). This is shown in the supplementary movie S11. It is worthwhile to note that the unstable cavities en route to the twin-branch cavity are nominally 2-D in contrast to fully formed TBC which exhibits a 3-D closure.

4.4.2. FORMATION OF LONG CAVITIES (LC)

The formation of the long cavity at Fr = 10.4, C_{qs} = 0.090 is shown by high-speed visualisation in figure 4.24 and X-ray image time-series in figure 4.25. Two transitions exist, FC to REJC and REJC to LC, see also regime map in figure 4.8. The ventilation profile is shown in the inset of figure 4.25. As gas injection begins, a foamy cavity is formed initially (see figures 4.24, 4.25(*a*)). As C_{qs} is increased, FC transitions to REJC upon the formation of cavity closure with a strong re-entrant flow shown in figure 4.24, 4.25(*b*). This results

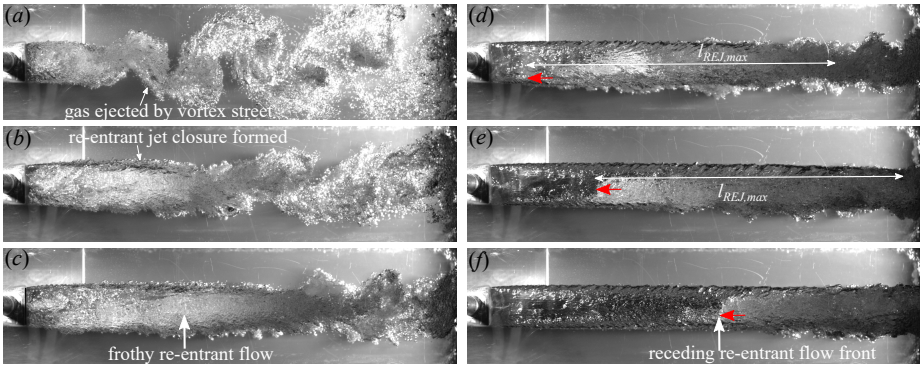

Figure 4.24: High-speed visualisation of LC cavity formation/development (gas entrainment, liquid re-entrainment, and gas ejection) for Fr = 10.42, C_{qs} = 0.090. The liquid re-entrant flow is visualised by a frothy mixture and has a maximum length ($l_{rej,max}/H$) of 8.5. The red arrow shows the REJ liquid front receding away from the wedge base.

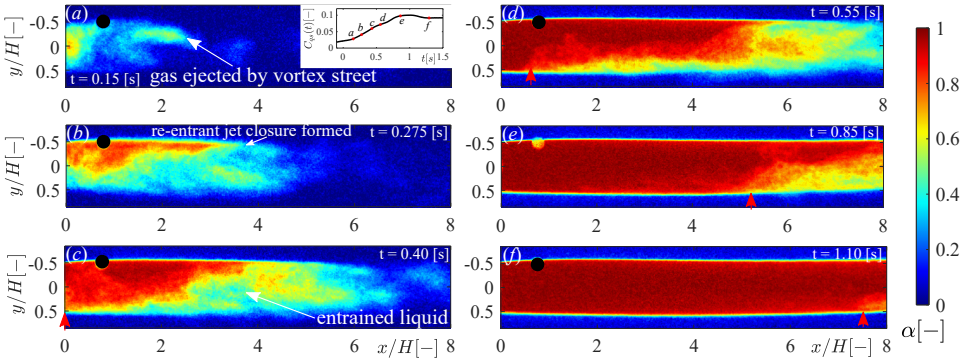

Figure 4.25: LC cavity formation/development (gas entrainment, liquid re-entrainment, and gas ejection) for Fr = 10.42, C_{qs} = 0.090. The black arrow shows the REJ front receding away from the wedge base. The inset shows the ventilation profile.

in the formation of a supercavity with a re-entrant jet that spans the entire cavity length and impinges on the wedge base (see figure 4.25(*b,c*)). The gas is ejected via re-entering liquid visualised by low void fraction region in X-ray snapshots, while spanwise vortices are visualised by Von Kármán vortices in high-speed optical snapshots. Figure 4.25(*d-f*) shows that with a further increase in C_{qs}, the re-entrant jet has assumed its maximum length similar to the $Fr \approx 4.17$ case. The transition of REJ cavity to LC begins and the re-entrant jet front cannot reach the wedge base. Instead, it recedes away from the wedge base as the cavity length grows. This is shown in figure 4.24 4.25-(*d-f*), where the re-entrant jet front is marked by a red arrow. This transition is more clearly shown in the supplementary movie S12. Due to the larger FOV, re-entrant flow is visualised better using high-speed images in figure 4.24(*d,e*). During the transition process, the length of the re-entrant jet remains constant ($l_{rej}/H \approx 8.5$) as its front recedes further away from the wedge base with the increase in cavity length (see red arrows in figure 4.25(*d-f*)) .

The existence of constant length re-entrant flow at the closure of unsteady cavities during the formation is observed for $Fr \geq 3.43$. The length of the re-entrant jet ($l_{rej,max}$), indicated by blue arrows in figure 4.26(*a-d*) can be used as a proxy for the strength of the re-entrant flow driven by a pressure gradient, akin to Barbaca et al., 2017. $l_{rej,max}$ is plotted for a range of Fr in figure 4.26(*f*). It is seen to scale linearly with Fr: $l_{REJ,max}/H \sim 0.85Fr - 0.73$, suggesting that the re-entrant jet is getting stronger with flow inertia (see figure 4.26(*f*)). This is in agreement with Barbaca et al. (2019) who showed a similar behaviour of re-entrant jet length in natural and ventilated cavity flows. The increase in re-entrant flow length is accompanied by a stronger curvature of the upper cavity interface resulting in a smaller radius of curvature (R) (see figure 4.26(*e*) and inset in *a*). For instance, $Fr = 2.08$ shows upward curvature, while as Fr increases, stronger downward curvature is exhibited by the upper cavity interface as shown in figure 4.26(*e*).

The combination of inertia and curvature results in a strong adverse pressure gradient at the cavity closure region which drives the re-entrant jet from the closure *inside* the cavity (Callenaere et al., 2001; Gawandalkar & Poelma, 2022). The pressure gradient (dp) across the cavity interface near its closure can be expressed with a 1-D Euler's equation (equation 4.4) in a streamline coordinate systems (Kundu et al., 2016). Here, n is a direction normal to the radius of curvature in a streamline-coordinate system, and R is the radius of curvature of the cavity. The pressure gradient scales directly with U_0 and inversely with R. Thus, a stronger pressure gradient and hence a longer re-entrant jet should exist for higher U_0 and smaller R, consistent with our experimental observations.

$$\frac{\partial p}{\partial n} \sim \rho \frac{U_0^2}{R} \tag{4.4}$$

Interestingly, such re-entrant jets are not reported in the study of Wu et al. (2021) dedicated to natural cavities in the same wedge geometry. The length of the re-entrant jet is suspected to play a significant role in determining the geometry of the stable REJ cavities: Stable REJ cavities are seen to span over 4-8 wedge height(s) (H). At $Fr = 5.79$, $l_{rej,max}$ is $4.2H$, which is the minimum length of the stable REJ cavity (see figure 4.10(*b*)). This then coincides with the critical Fr at which stable REJ cavities start to exist, shown by the black dotted line in figure 4.26(*f*). Furthermore, we propose that $l_{rej,max}$ dictates the gas ejection out of the cavity when REJ cavities transition to LCs. Consequently, if the ventilation input (C_{qs}) can overcome the gas leakage due to the re-entering flow, the REJ cavity transitions to LC. This will be addressed quantitatively in the following subsection 4.4.3.

4.4.3. GAS LEAKAGE OF UNSTEADY CLOSURES

The cavity formation dynamics, i.e. gas entrainment behind the wedge are dictated by the gas leakage via the unsteady cavity closure during its formation. The cavity length increases abruptly upon the formation of unsteady/transitional closure. Thus gas leakage quantification during cavity formation is important. The measured void fraction fields ($\alpha(x, y, t)$) along with ventilation input ($\dot{Q}_{in}(t)$) allow us to estimate gas leakage/ventilation demands ($\dot{Q}_{out}(t)$) using a simple gas mass balance via a control volume (CV) approach.

The formation of the cavity leading to the two different supercavity closure modes (TBC and LC) is examined. The time series of void fractions are recorded time-

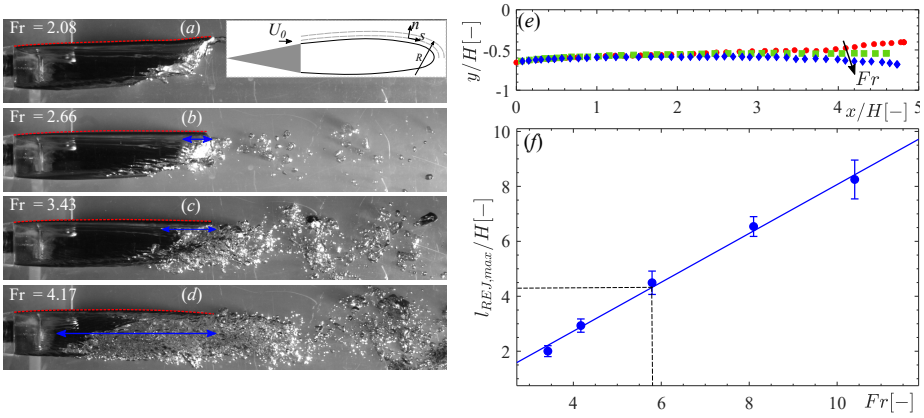

Figure 4.26: (*a*)-(*d*) Unstable cavity closure at a fixed cavity length seen at low Fr range during the transition from FC to TBC. The blue marking shows the length of the re-entrant flow, while the red dashed lines show the upper cavity interface. (*e*) The upper cavity interface as a function of Fr shows that the cavity interface curves downwards with an increase in Fr. (*f*) The maximum re-entrant flow length ($l_{rej,max}/H$) as a function of Fr. The solid blue line is a linear fit: 0.85Fr-0.73). The black dashed line shows the minimum length of the stable REJ cavity observed in this study at $Fr \approx 5.7$.

synchronised with the gas injection rate ($\dot{Q}_{in}$) while the cavity is being formed. Note that fully formed/developed, fixed length supercavity should satisfy $\dot{Q}_{g,in} \sim \dot{Q}_{g,out}$. If we consider a control volume around the cavity (see inset in figure 4.27), the mass balance of gas inside the cavity is given by equation 4.5, where ρ_c ($\approx \alpha\rho_g$) is the mass density, V_c is the cavity volume and $\dot{Q}$ is the gas volumetric flux. The subscript g is used to denote the gas phase, while in and out denote gas injection in and ejection out of the cavity respectively.

$$\frac{\partial \rho_{g,c} V_{g,c}}{\partial t} = \rho_g \dot{Q}_{g,in} - \rho_g \dot{Q}_{g,out} \tag{4.5}$$

The gas mass balance equation for a growing cavity can be written as equation 4.6, which is a rearranged form of equation 4.5. In equation 4.6, $\dot{Q}_{g,in}(t)$ is measured experimentally, while $\alpha V_c(t)$ is estimated from the X-ray based void fraction fields. Before differentiating $\alpha V_c(t)$, it is smoothed using a Savitzky-Golay filter of size 20 and order 5. Thus, the gas leakage w.r.t. gas injection (Q_f^*, subscript f corresponds to cavity formation) is quantified with equation 4.6 to estimate the rate of gas ejection during the supercavity formation.

$$Q_f^*(t) = \frac{\dot{Q}_{g,out}(t)}{\dot{Q}_{g,in}(t)} = 1 - \frac{1}{\dot{Q}_{g,in}(t)} \frac{\partial \alpha V_c(t)}{\partial t} \tag{4.6}$$

Figure 4.27 shows the gas leakage as a TBC is formed at $Fr \approx 3.43$ along with flow visualisation. Q_f^* is shown after the unsteady closure is formed, shown by 'A' in figure 4.27 until the cavity leaves the FOV, i.e. 'C' in figure 4.27. It appears that Q_f^* is constant at ~ 0.2 as the unsteady closure is formed and cavity length is growing to form TBC. The CV approach is valid only when the whole cavity is in FOV to estimate the rate of

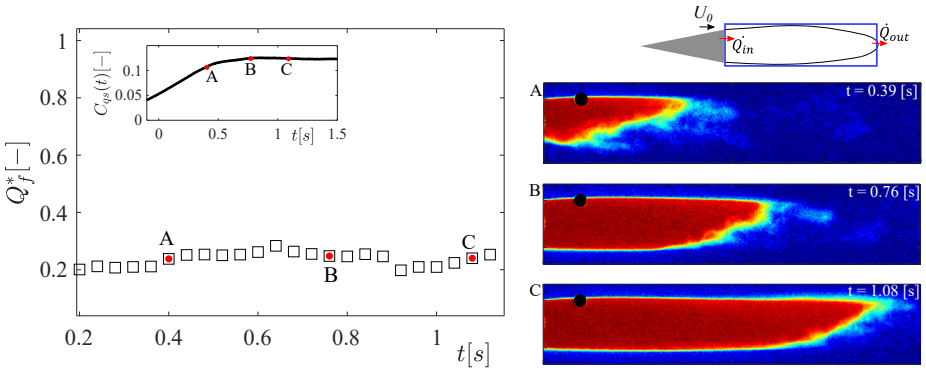

Figure 4.27: The temporal variation of $Q_f^* = \dot{Q}_{g,out}/\dot{Q}_{g,in}$ for $Fr = 3.43$, $C_{qs} = 0.12$ as TBC is formed from upon the formation of unsteady closure. The colorbar of jet colormap showing void fraction spans from 0 to 1. The injection profile is shown in the inset.

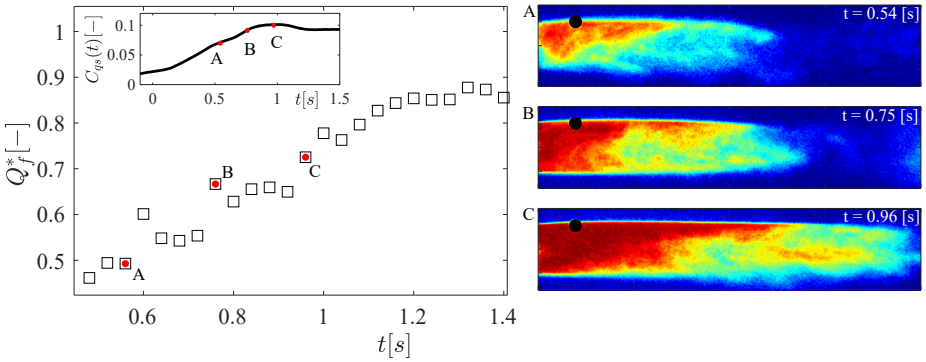

Figure 4.28: The temporal variation of $Q_f^* = \dot{Q}_{g,out}/\dot{Q}_{g,in}$ for $Fr = 10.41$, $C_{qs} = 0.090$ as LC cavity is formed from FC upon the formation of REJ closure. The colorbar of jet colormap showing void fraction spans from 0 to 1. The injection profile is shown in inset.

accumulation of gas in the CV. Figure 4.28, on the other hand, shows the gas leakage when a long cavity is being formed from a REJ cavity at $Fr \approx 10.4$. Q_f^* is shown after re-entrant jet closure is formed, such as shown by 'A' in figure 4.28, until the cavity leaves the FOV, i.e. 'C' in figure 4.28. It is seen that Q_f^* increases from $\sim$ 0.45-0.8 as the cavity length grows to form a LC. $Q_f^*(t)$ is significantly higher than $Q_f^* \sim 0.2$ for the TBC case. Note that Q_f^* at $t \gtrsim 1.2$ is nonphysical due to the cavity extending out of the CV.

Q_f^* for a range of Fr are shown in figure 4.29(*a,b*). The time is non-dimensionalised with the time the unsteady/transitional cavity takes to span out of the CV and is expressed as t^* since the CV analysis is valid *only* when the entire cavity lies in it. For the case of $Fr = 2.08$ the entire cavity lies in the FOV, and hence the time is non-dimensionalised differently; Time is non-dimensionalised with the time elapsed after the formation of unsteady closure (2-D) to just before the 3-D closure formation begins.

It is observed that during TBC formation Q_f^* is nearly constant in time in the range

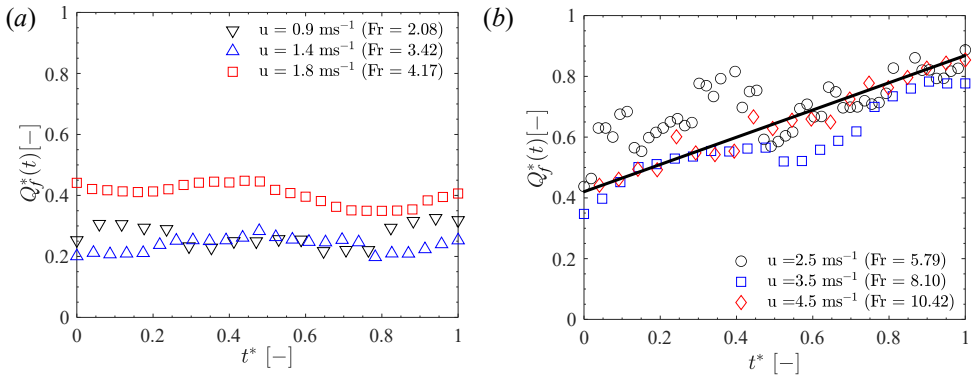

Figure 4.29: The temporal variation of gas leakage rate (Q_f^*) as the cavity grows abruptly to form (*a*) TBC, (*b*) LC upon the formation of their respective unsteady closures. The inset shows the schematic of the control volume.

4

of 0.2 for a range of Fr considered $\approx 2.08-3.42$ (see figure 4.29(*a*)). For $Fr \approx 4.17$, Q_f^* is slightly higher (~ 0.4). At higher $Fr \approx 5.79-10.42$, Q_f^* increases from 0.4 - 0.8 as the long cavity is being formed as shown in figure 4.29(*b*). Thus Q_f^* is significantly higher for high Fr cases. This trend in Q_f^* can be explained by the distinct closure modes unstable cavities assume during the formation of TBC and LC: During the formation of TBC, the unsteady cavity has a wave-type instability or mild re-entrant flow with vortex shedding as shown in figure 4.22 and 4.23 resulting in a smaller gas leakage rate. However, when the closure has a prominent re-entrant jet entering the cavity, a larger gas ejection occurs, i.e. $Q_f^* \sim (0.4-0.8)$. Further, the gas ejection is seen to increase as the cavity grows longer. Consequently, a prominent re-entrant jet closure contributes to a significantly larger gas leakage than wave-type instability or vortex shedding. This is consistent with the DIH measurements of Shao et al. (2022), who reported a large instantaneous gas ejection rate for cavities with re-entrant jet closure.

Moreover, it was observed that a constant length re-entrant flow exists at the closure of unsteady cavities, while supercavities are being formed for $Fr \geq 3.43$. For $Fr \geq 5.7$, REJ cavities transition to long cavities when the re-entrant flow reaches its maximum length ($l_{rej,max}$). Earlier, we hypothesised that gas ejection due to this re-entrant flow was responsible for this transition (REJC to LC). To verify this, a simple model is constructed. The gas ejection rate due to *periodic* re-entering liquid flow ($\dot{Q}_{out,rej}$) can be approximated as $V_{rej} f_{rej}$, where V_{rej} and f_{rej} are the volume and the frequency of the re-entering flow. V_{rej} can then be approximated as $l_{rej} HW/2$ due to the right-triangular shape of the averaged re-entering flow (see figure 4.11(*c*) and inset in figure 4.30(*a*)). The gas ejection can now be expressed as $C_{qs,out,rej}$ as per equation 4.7 and rearranged to obtain equation 4.8 using $\overline{u_{rej}}/U_0 \approx 0.3$. Finally, we arrive at equation 4.9 using empirical relations obtained experimentally for $l_{rej,max}(Fr)/H$, $St_{Hrej}(C_{qs,in})$ in figure 4.18(*d*) and 4.26(*e*), respectively. All the symbols have been explained previously.

$$C_{qs,out,rej} = \frac{\dot{Q}_{out,rej}}{U_0 WH} \tag{4.7}$$

$$C_{qs,out,rej} = l_{rej,max}\frac{f_{rej}}{2U_0} = 0.15\frac{l_{rej,max}}{H}St_{H,rej} \tag{4.8}$$

$$C_{qs,out,rej} = 0.15(0.86Fr - 0.73)(0.2 - 2.38C_{qs,in}) \tag{4.9}$$

The locus of $C_{qs,in}$ for which $C_{qs,in} > C_{qs,out,rej}$ is shown by the black dashed line in figure 4.30. $C_{qs,out,rej}$ matches well with $C_{qs,f}$ at higher Fr (> 4.17), suggesting that gas leakage due to re-entrant flow accounts for the majority of the gas ejection, preventing the ventilated cavity from growing longer to a LC. Thus, if $C_{qs,in} > C_{qs,out,rej}$, the cavity will experience net growth to a LC from a REJ cavity as it can overcome the gas leakage due to the re-entering liquid flow. Furthermore, at low Fr (< 4.17), the predicted leakage due to the re-entrant flow is less than the measured leakage ($C_{qs,f}$). This suggests that the re-entrant flow in such cavities is mild and does not account for the major gas leakage. Instead, wave-type instability and the spanwise vortex ejection cause the majority of the gas leakage, consistent with our experimental observations.

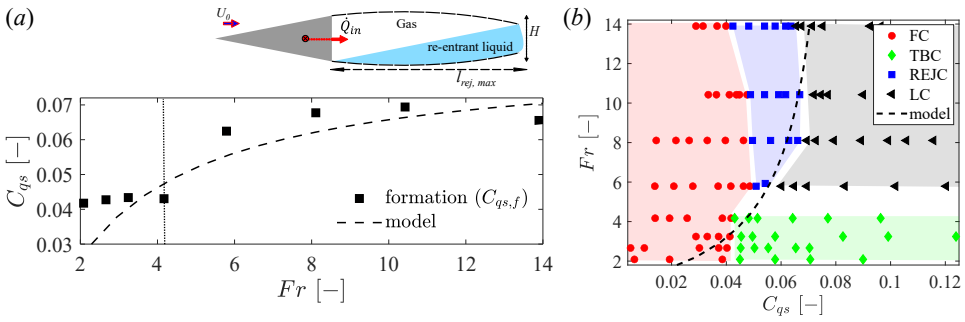

Figure 4.30: (*a*) $C_{qs,f}$ in comparison to model prediction as a function of Fr (the black vertical dotted line indicates the Fr limit where re-entrant flow dictates transition to a supercavity). The inset shows the schematic of the re-entrant flow. (*b*) Model prediction in the regime map of figure 4.8.

4.5. VENTILATION HYSTERESIS

In the previous section(s), ventilated cavities were established using a L-H ventilation strategy, i.e. by increasing the ventilation coefficient (C_{qs}) from zero to a given C_{qs}. In this section, behaviour of established ventilated cavities is reported by reducing C_{qs}, denoted as the H-L ventilation strategy. Figure 4.3 shows the gas injection profile of this H-L ventilation strategy. Figure 4.31 shows the cavity formation *history*: temporal variation of C_{qs}, σ_c along with flow visualisation for the low and the high Fr case. It is ensured that the cavity closure is completely formed, i.e. TBC at $Fr \approx 2.08$ and LC at $Fr \approx 10.41$ before reducing the ventilation.

4.5.1. CAVITY FORMATION AND MAINTENANCE

At $Fr = 2.08$, the ventilation (C_{qs}) is set to 0.1 to ensure that the TBC is completely formed (see green region in figure 4.8 and 'A' in figure 4.31(*a*)), followed by reducing C_{qs} to 0.019, as shown by 'B', 'C' in figure 4.31(*a*). At such a flow condition (Fr = 2.08, C_{qs} = 0.019), foamy cavities were observed in the L-H regime map shown in figure 4.8. However, TBCs

persist at lower C_{qs} with the H-L approach. Similarly, at higher Fr, i.e. (Fr = 10.4), C_{qs} is increased to 0.088 such that a long cavity is formed (see 'A', 'B' in figure 4.31(b)). Further reduction of C_{qs} to 0.062 sees the persistence of long cavity as shown by 'C', 'D' in figure 4.31(b). Note that for Fr = 10.4, REJ cavities were seen at such flow conditions using the L-H approach in the regime map of figure 4.8. It is also observed that upon formation of a supercavity (TBC and LC), the cavitation number (σ_c) remains unchanged, irrespective of the ventilation (C_{qs}) for a given Fr, as shown by the red markers in figure 4.31. This is consistent with the observations of Karn et al. (2016) and Arndt et al. (2009). It is worthwhile to note that the previous studies of Karn et al. (2016) observed

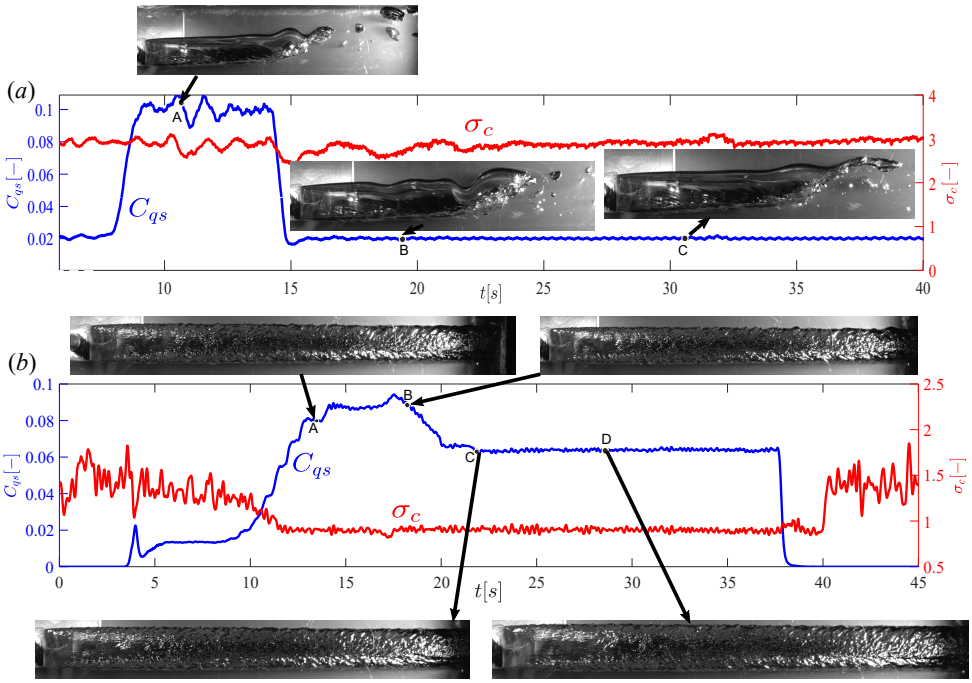

Figure 4.31: Time signals of C_{qs} and σ_c, showing ventilation hysteresis using H-L ventilation strategy for (a) Fr = 2.08 (TBC is formed at 'A' and can be maintained upon C_{qs} reduction at 'B' and 'C'), (b) Fr = 10.41 (LC is formed at 'A' and 'B', and can still be maintained upon C_{qs} reduction at 'C' and 'D'.

a change in cavity closure with the reduction in C_{qs}, without any effect on cavity length (L_c) and pressure (σ_c). In this study, a change in the closure is not observed for TBCs, however, long cavity closure is out of the optical FOV and needs further investigation.

A systematic variation of Fr and C_{qs} using H-L ventilation strategy results in the second regime map shown in figure 4.32(a). This regime map is different from that based on the L-H ventilation strategy shown in figure 4.8. As mentioned earlier, one of the main differences is the absence of REJ cavities observed at higher Fr for the L-H strategy. At lower Fr, it is seen that the transition boundary from FC to TBC, denoted by the interface between the green and red regions in figure 4.32(a) increases monotonically with Fr, as opposed to a constant C_{qs} = 0.043 in the regime map based on the L-H ventila-

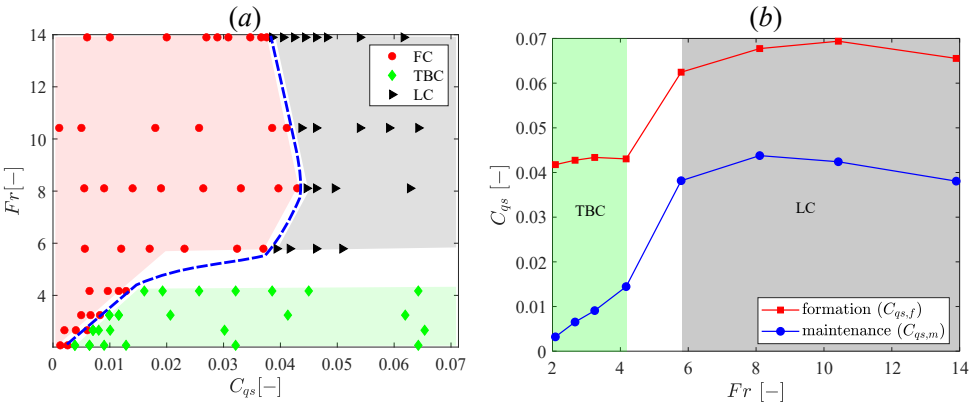

Figure 4.32: (*a*) Cavity regime map resulting from decreasing ventilation from a fully developed supercavity initial condition (H-L ventilation strategy). The blue dashed line shows the (approximate) C_{qs} limit where the supercavities are no longer maintained. (*b*) Ventilation coefficient required to form and maintain cavities at different Fr. The formation (red) line is the minimum C_{qs} required to establish a given cavity closure (TBC for $Fr \lesssim 5$, LC for $Fr \gtrsim 5$). The maintenance (blue) line is the minimum C_{qs} required to sustain a given closure, below which the cavity rapidly transitions to an FC.

tion strategy. At higher Fr, the transition boundary between FC to LC (denoted as the interface between the black and red regions in figure 4.32(*a*)) is similar to the FC to REJC transition in the 'L-H' regime map (blue dotted line in figure 4.8). For the H-L strategy, long cavities (LC) persist at comparable C_{qs} where REJ cavities were observed for the L-H strategy. Furthermore, LC transitions directly to FC upon C_{qs} reduction. For a given Fr and C_{qs}, the cavity closure and the geometry is seen to depend on the ventilation *history*. Consequently, supercavities (TBCs and LCs) can be maintained at a much lower ventilation coefficient (C_{qs}) when the cavity is formed with the 'H-L' ventilation strategy, denoted by $C_{qs,m}$. From the regime maps, it is clear that the ventilation required to *maintain* a supercavity ($C_{qs,m}$) is significantly less than the ventilation required to *form* a cavity ($C_{qs,f}$) as illustrated in figure 4.32(*b*). This is consistent with the observations in ventilated cavities generated behind a 2-D backward-facing step (Mäkiharju, Elbing, et al., 2013) and axisymmetric cavitators (Arndt et al., 2009).

The physical mechanism responsible for the ventilation hysteresis can be explained with the help of cavity formation dynamics, the cavity closure region, and the resulting gas ejection out of the cavity while the cavity is being formed. The low and high Fr cases exhibiting distinct cavity closures are discussed separately.

Low Fr ($\approx$ 2.08 - 4.17): At low Fr, when the gas injection begins in the wake of the wedge, dispersed bubbles are carried in the separated shear layers from where they are ejected out. The closure for the cavities (FC) is *not* formed, resulting in a minimal gas entrainment. As C_{qs} is increased to a critical C_{qs} = 0.043, the cavity closure is formed. For a constant C_{qs}, the ventilation required to form the closure scales only with flow inertia (U_0). Further, when the closure is formed, a smaller but constant gas ejection ($Q_f^* \sim 0.20 - 0.4$) occurs as shown in figure 4.29(*a*). Q_f^* <1 results in net gas entrainment behind the wedge resulting in an abrupt increase in cavity length to form a TBC. The

length (L_c/H) of a fully developed TBC scales directly with Fr. As the cavity achieves its maximum length and, the TBC closure is completely formed (see figure 4.22(*e, f*)), a cavity exists with $\dot{Q}_{g,out} \sim \dot{Q}_{g,in}$. Since L_c/H is fixed at a given Fr, a certain minimum gas flux, proportional to cavity length (L_c) is required to sustain the cavity volume ($\approx L_c W H$), when a TBC is fully developed. This is given by $C_{qs,m}$. To this end, $C_{qs,m}$ is *also* seen to increase monotonically with Fr for low Fr cases (figure 4.32(*b*)). C_{qs} required to fully form the TBC closure ($C_{qs,f}$) is higher than $C_{qs,m}$ due to the gas leakage of the unsteady closure leading up to the formation of a TBC supercavity.

High Fr ($\approx$ 5.8 - 14): At higher Fr, foamy cavities are seen at low C_{qs}. As the ventilation is increased monotonically using the L-H strategy, an unsteady supercavity with a closure marked by a strong re-entrant jet is formed. Thus, gas is ejected out ($Q_f^* \sim$ 0.45-0.8) due to the re-entraining liquid inside the cavity displacing the gas (see figure 4.29(*b*)). $Q_f^* < 1$ still results in the net entrainment of gas in the wake resulting in cavity length growing. However, the rate of growth of these cavities is significantly smaller than unsteady cavities leading up to TBC due to larger Q_f^*, consistent with our observations of cavity formation dynamics. When LC is being formed using the L-H strategy, it has to *pass through* this re-entrant jet closure overcoming the resulting gas leakage as shown by equation 4.9. Finally, when the closure of the long cavity is fully formed, the length of the LC is fixed by Fr similar to low Fr TBC cases with $\dot{Q}_{g,out} \sim Q_{g,in}$. Thus, a minimum amount of gas, proportional to L_c, is required to feed the cavity volume ($\sim L_c W H$) to sustain itself. This critical value ($C_{qs,m}$) is thus lesser than the ventilation required to form the closure of LC ($C_{qs,f}$) due to the gas leakage manifested by the unsteady closure with re-entering flow while the LC is formed. Our analysis shows that the unsteady closures and the resulting gas leakage leading up to the formation of supercavities are critical in explaining the hysteresis observed in supercavity formation. This in turn explains the difference in gas flux required to maintain and establish a supercavity.

4.6. SUMMARY AND CONCLUSION

Ventilated cavities/supercavities in the wake of a 2-D bluff body are studied with time-resolved X-ray densitometry over a wide range of flow velocity, i.e. Froude Number ($Fr \approx 2-13.9$) and Reynolds Number ($Re_H \approx 1.6\times10^4 - 1.2\times10^5$), and gas injection rate ($C_{qs} \approx$ 0.03 - 0.13). The ventilated cavities are created by systematically varying Fr and C_{qs}. This led to a regime map (Fr vs C_{qs}) where four different types of stable cavities are identified, each having a unique cavity closure.

Foamy cavity (FC) is an open cavity, i.e. the closure is not formed and is identified at low Fr and C_{qs}. The gas entrained in the near wake of the wedge is ejected out periodically by alternating Von Kármán vortices. Twin-branch cavities (TBC), re-entrant jet cavities (REJC), and long cavities (LC), on the other hand, have developed closures. TBCs are formed at low Fr and higher C_{qs} with a 3-D closure, i.e. it has a tail at mid-span with a mild re-entrant flow along with two branches along the walls. The gas is ejected primarily by a wave-like travelling instability that pinches the cavity at the branches. This instability is seen to travel with a speed that scales with the incoming velocity of the flow (U_0), suggesting it is driven by Kelvin-Helmholtz-type instability. However, a thorough linear stability analysis of the flow is deferred for future investigation. These cavities have

a fixed length for a given Fr that does not increase with increases in C_{qs} above $C_{qs,tr} \sim 0.043$.

At $Fr \geq 5.8$, the cavity closures exhibited are distinct: FCs exist at a low C_{qs}. REJ cavities are observed at an intermediate C_{qs}. These cavities have a strong re-entrant flow entering inside the cavity due to a large pressure gradient at the closure. Such stable cavities are seen to have multi-modal gas ejection brought about by (i) spanwise vortex shedding ($St_{H,v} \sim 0.27$), and (ii) a strong re-entrant jet ($St_{H,rej} \lesssim 0.1$). The jet velocity in the laboratory frame of reference is measured to be $\sim 0.3U_0$, for all Fr and C_{qs}. For a given Fr, the length of such stable REJ cavities increases monotonically with C_{qs}. Finally, at high Fr and C_{qs}, LCs exist which are characterised by travelling wave-type instabilities at the closure leading to gas pocket shedding. LC closure could not be measured quantitatively due to the limitation imposed by our test section and FOV. Nevertheless, LCs are suspected to have a 2-D closure from our qualitative visualisation, as also reported by Michel (1984). LCs deserve a thorough quantitative investigation with a longer test section and will be considered for future investigation. In summary, two types of cavity closures are seen: (i) wave-type instability, and (ii) re-entrant jet depending on Fr, C_{qs} and σ_c. Wave-type closure can be either 2-D or 3-D, i.e. at low Fr, wave-type closure is 3-D (TBC), while at high Fr it is 2-D (LC). REJ cavity closure is nominally 2-D and can exist as a *strong* ($Fr \geq 5.8$) or a *weak* re-entrant jet, depending on Fr. We hypothesise that the re-entrant flow at the cavity closure mitigates the cavity oscillation in the $x-y$ plane. Furthermore, compressibility effects in the ventilated cavities under consideration are found to be negligible, primarily due to high cavity pressures ($\gtrsim 70$ kPa) despite low void fractions in the cavity. Thus, incompressible solvers can be used to simulate such flows fairly well.

The cavity closure and the resulting gas ejection are seen to dictate the length of the cavity (L_c) and pressure inside the cavity; There is an abrupt increase in the cavity lengths with changing closure types. It is observed that the cavity length is not unique to a flow condition given by Fr and C_{qs}, i.e. different cavity closures can result in a similar L_c. For e.g., TBC and REJC at different Fr and C_{qs} can assume the same length. Thus, the pressure inside the cavity expressed as cavitation number (σ_c) is important to uniquely define the state of the cavity. The supercavity lengths, when plotted as a function of (σ_c), appear to follow a power law, except REJ cavities which appear much shorter/stunted. This is likely linked to the re-entering jet displacing larger amounts of gas, resulting in a larger gas ejection or low gas entrainment rate to form the cavity. The supercavities (TBCs and LCs) exhibit a maximum cavity length (L_c) for a given U_0 (Fr), meaning a finite volume of gas ($\sim WHL_c$) can be entrained in the wake of the bluff body to form a cavity. The excess injected gas is ejected out. It is observed that stable cavities after assuming maximum length (L_c), start to oscillate with a further increase in C_{qs} to eject the *excess* gas.

This observation led to the examination of the supercavity formation process. The supercavity formation at low and high Fr is seen to be distinct. A gas balance using a simple control volume (CV) is performed over *unsteady cavities* for a range of Fr. This is substantiated by the unsteady void fraction fields ($\alpha(x,y,t)$) measured in this study in combination with $\dot{Q}_{in}(t)$. It is observed that upon unsteady closure formation, the cavity length grows rather abruptly. The unsteady cavities at low Fr (≤ 4.17), have a constant

gas ejection rate ($\dot{Q}_{out}/\dot{Q}_{in}$) in the range of 0.2–0.4. The unsteady cavities at higher Fr have a higher $\dot{Q}_{out}/\dot{Q}_{in} \sim$ 0.45-0.8, which increases as the cavity approaches its final L_c. This is due to the different cavity closures the cavity assumes during its formation: At low Fr, the gas is ejected out via span-wise vortices or wave instability. However, at higher Fr, gas is ejected out via spanwise vortices *and* primarily via re-entrant flow. A prominent re-entrant flow at the closure results in significantly higher gas leakage than vortex or wave-type closure.

Re-entrant flow is seen at the closure of unsteady cavities as the supercavities are being formed for $Fr \geq 3.43$. Re-entrant flow at the unsteady closure is seen to get longer, hence stronger with increasing inertia. The length of the re-entrant flow scales linearly with Fr, leading to a larger gas ejection rate. A simple empirical model is constructed to verify that re-entrant flow accounts for the majority of the gas leakage at higher Fr. Further, REJ cavities transition to long cavities when the input ventilation can overcome the gas ejection caused by the re-entrant flow at its closure. Thus gas leakage due to re-entrant flow can prevent the cavities from growing, explaining the stunted length of stable REJ cavities reported in figure 4.10(*c*).

The unsteady cavity closure and the resulting gas leakage during the cavity formation provide us insights into observed ventilation hysteresis: REJ cavities transition to long cavities upon increasing ventilation, starting from foamy cavities. Hence, when an LC is being formed, a higher C_{qs} is required to overcome the gas leakage due to the re-entraining liquid. Additionally, when LC closure is fully formed, a finite volume of gas (cavity volume $\sim L_c W H$) is needed to sustain the formed cavity as the maximum cavity length is fixed by Fr, σ_c. Therefore, upon the establishment of fully developed cavities, followed by a decrease in C_{qs} results in LC being maintained at much lower C_{qs}. Similarly, TBCs can be maintained at much lesser ventilation ($C_{qs,m}$) than $C_{qs} \sim 0.043$ required to form the cavity. This cavity closure formation hysteresis explains why supercavities can be maintained/sustained at almost half the gas flux required to form/establish the supercavity reported by the previous studies of Arndt et al. (2009) and Mäkiharju, Elbing, et al. (2013).

Therefore, our experiments suggest that the ventilation strategy is paramount for the efficient formation of ventilated supercavities. This understanding of ventilated cavity closures can be used to design a control strategy to form a stable cavity of a given size with minimum gas injection. Furthermore, allows us to maintain the cavities at the minimum ventilation demands, making partial cavity drag reduction and aeration more efficient and sustainable. The rate of increase/decrease of gas ventilation in the ventilation strategy could play a significant role in closure formation. Hence, it is possible that a higher ramp rate can be used to achieve a ventilated cavity more efficiently, i.e. with less volume of gas. However, this is beyond the scope of the current investigation and can be investigated in the future. Furthermore, we recognise that Re_H is a more relevant parameter to characterise the ventilated cavities at higher Fr (≥ 5.7). Hence, the effect of Fr and Re_H can be segregated with different wedges and experiments across different scales.

SUPPLEMENTARY MOVIES

Supplementary movies are available here

5

CONCLUSIONS

Progress is the riddle of delays, serendipitously arranged.

– Rishloo

This chapter recapitulates conclusions that are drawn from the different chapters within this dissertation. Each chapter is based roughly on a publication, hence, these chapters are self-contained. Therefore, the most important conclusions are summarised here. Moreover, perspectives on future research are given in this chapter.

5.1. CONCLUSIONS

The aim of this study was twofold: Firstly, we study natural partial cavity shedding in an axisymmetric nozzle, with a focus on understanding the transition of shedding mechanism from bubbly shocks to re-entrant jets. Secondly, the dynamics of ventilated cavities are studied in the wake of 2-D bluff body. Although partial cavity (vapour-liquid) and ventilated cavity (air-liquid) flows are fundamentally different, they share numerous underlying physical phenomena. Additionally, due to the optical opaqueness of the flow and large separation in mass densities, similar flow diagnostic tools such as X-ray densitometry are used to study these flows. Hence, these flows are examined in tandem to generate acumen into each other.

5.1.1. CLOUD SHEDDING DYNAMICS IN VENTURI

In the first part of this dissertation, the partial cavitation dynamics were studied in an axisymmetric venturi for a range of Reynolds number ($Re_t \approx 1.86$–2.3×10^5) and cavitation number ($\sigma \sim 0.4$-1.1). The two shedding mechanisms, re-entrant jet and bubbly shocks were visualised and characterised in detail for a range of σ to elucidate their role in observed cloud shedding. With this, we addressed: *Why does the shedding mechanism change from re-entrant jet to condensation shock?*.

RE-ENTRANT JET

We employ tomographic imaging with the primary aim of visualising the near-wall *liquid* re-entrant flow during cavity growth. The axisymmetry of the venturi and the re-entrant flow is exploited to gain optical access to the re-entrant film. The fluorescent tracer particles along with optical filters are used to circumvent the issue of strong reflections and opacity arising from vapour cavity and frothy mixture. Moreover, a conditional phase-averaging methodology is introduced to study the temporal evolution of re-entrant flow in a shedding cycle. With this, the re-entrant jet below the vapour cavity was quantitatively visualised for the first time.

It appears that as the vapour cavity grows, the re-entrant flow is continuously fed below it, contrary to the previous understanding that it is periodically generated. Further, it is estimated that the maximum re-entrant flow thickness is about 1.2 mm for σ=0.95, i.e. 26% of the vapour cavity thickness. The velocity vector fields reveal that the re-entrant jet is a consequence of an impinging jet and a stagnation point formed at the cavity closure region. Moreover, it is driven by an adverse pressure gradient at the cavity closure region. The maximum velocity of the re-entrant flow below an attached cavity is found to be $0.5U_t$, where U_t is the venturi throat velocity.

As the cavity grows, the re-entrant flow is seen to evolve in time, i.e. it gets thicker in comparison to the vapour cavity. Further, the velocity of the re-entrant jet increases. The combination of these two effects allows the re-entrant flow to interact with the vapour cavity, resulting in its pinch-off near the throat. Further, the imploding cavitation cloud likely gives rise to a high-velocity travelling wave that appears to be superimposed on the existing re-entrant flow. However, this travelling wave is deemed inconsequential for the cavity detachment at such σ. The re-entrant jet causes the cavity pinching setting the final cloud shedding frequency at such $\sigma \sim 0.95$.

At a lower σ (~ 0.80), a sharp upstream travelling discontinuity attributed to a bubbly shock wave is observed in the axial velocity. This high-velocity discontinuity appears to be superimposed on the existing pressure gradient-driven, low-velocity re-entrant flow. Although the re-entrant jet coexists with bubbly shock fronts in a shedding cycle at low σ, it does not cause cavity detachment. Rather, the high-velocity discontinuity is seen to dictate the periodic cloud detachment. Bubbly shock waves in partial cavitation flow were characterised extensively in a follow-up study.

BUBBLY SHOCK FRONTS

Bubbly shock fronts are studied thoroughly with time-resolved X-ray densitometry, in combination with high-frequency pressure measurements: The densitometry circumvents the optical-opacity of the cavitating flow, enabling us to quantify the vapour phase ($\alpha(x, y, t)$), in contrast to the focus on the liquid phase in chapter 2. Multiple pressure transducers allow us to track the propagation of the pressure discontinuity (emanating from the cloud implosion) through the attached vapour cavity. The combination of the above two modalities is leveraged to visualise the interaction of the pressure wave with the attached vapour cavity at different σ ($\approx 0.46 - 0.90$). The static pressure and vapour fraction measured inside the cavity allow us to assess the effect of compressibility (the Mach number) in partial cavitation flows.

We visualise and characterise the pressure wave travelling *upstream* through the attached cavity at different σ by quantifying: vapour fraction (pre-front, α_1 and post-front,

α_2), pressure rise (Δp) across the shock front, the velocity of the shock propagation (u_{sw}) and its Mach number (Ma_{sw}). All the quantities are conditionally phase-averaged over multiple cycles using the methodology elaborated in chapter 2. It is seen that both the pressure pulse and propagation velocity of the pressure wave propagating through a low vapour fraction bubbly mixture are two orders of magnitude higher in comparison to when it propagates through the vaporous cavity. The upstream propagating pressure wave, after impinging on the cavity, starts condensing it, giving rise to a condensation shock front. The pressure rise across the condensation shock front (Δp) is of the order of magnitude $\sim$ 10 kPa. The vapour fraction of the cavity is in the range of (0.4-0.8). Further, the condensation shock front is seen to propagate at about $\sim 0.55U_t$, which is interestingly of the same order of magnitude as that of the re-entrant jet velocity, measured in chapter 2.

Our study unveils the interaction of the pressure wave (emanating from the cloud collapse) with the attached cavity at different σ. At low σ ($\sim$ 0.46), the pressure wavefront impinging on the cavity is supersonic since the bubbly mixture through which it propagates has a high vapour fraction ($\alpha_1 \sim 0.7$) and low mixture pressure (P_c). The combination of this makes the shock front supersonic ($Ma_{sw} > 1$), which completely condenses the vapour cavity, resulting in its fragmentation and destabilisation. The condensation shock enforces a strong periodicity in shedding, despite local instantaneous events in the shedding process. As σ increases, the pressure wave created by the cloud collapse is weaker. Thus, the pressure wave impinging on the cavity is subsonic ($Ma_{sw} < 1$). However, as it propagates upstream, it accelerates and becomes stronger, i.e. supersonic ($Ma_{sw} > 1$), resulting in the onset of cavity condensation. This is evident from the emergence of a sharp gradient in the vapour fraction as the bubbly shock wave propagates upstream. This is corroborated by an increase in shock front velocity ($u_{sw}(x)$) as it propagates upstream, leading to increased pressure rise (Δp) across the shock front. The observed acceleration is attributed to the converging walls of the venturi as seen by the shock front. Thus, the kinematics of bubbly shock waves have a significant influence on their dynamics which in turn influences the shedding dynamics. With a further increase in σ, pressure discontinuity from the cloud implosion gets even weaker and despite the acceleration of the shock front, the Mach number of the pressure wavefront seems to remain subsonic, i.e. $Ma_{sw} \lesssim 1$. Thus, more cycles exist where the condensation shock front is not favoured. At such σ, a strong re-entrant jet existing between the cavity and venturi wall causes cavity detachment. With an even further increase in σ (> 0.95), all the shedding cycles will be predominantly dictated by the re-entrant jet driven by an adverse pressure gradient as demonstrated in Chapter 2. Thus, the emergence of re-entrant jet-triggered cavity shedding coincides with bubbly shock being subsonic.

Thus, pressure and density/vapour fraction fields in such a bubbly flow have a significant influence on the interaction of the pressure waves with a vapour cavity. The combination of low pressure and high vapour fraction leads to the low speed of sound (a few ms^{-1}) in the vapour cavity. Hence, condensation shock propagating at merely $0.55U_t$ assumes the Mach number of greater than unity. Although both the shedding mechanisms can coexist in a shedding cycle, the effect of compressibility appears to set the cavity shedding mechanism, i.e. bubbly/condensation shock front for high Ma_{sw} while re-entrant jets for lower (subsonic) Ma_{sw}. Thus, compressibility plays a major

role in partial cavitation flows and cannot be neglected for numerical modelling. Moreover, the effect of a high-blockage flow geometry, such as the axisymmetric venturi, is to strengthen the shock front by accelerating it. This helps to explain the dominance of bubbly shock waves ($\sigma \sim 0.3$–0.80) over re-entrant jets ($\sigma \sim 0.95$–1) as a mechanism driving the periodic cloud shedding in an axisymmetric venturi. This understanding of partial cavitation can be used to mitigate its harmful effects. For instance, ventilation/aeration can increase the pressure inside the vapour cavities making them *less* compressible than cavities made of pure vapour. This can help prevent/arrest the periodic cloud-shedding and the resulting deleterious effects, such as wear, erosion and vibrations.

5.1.2. VENTILATED CAVITIES

In the second part of this dissertation, ventilated cavities in the wake of a 2-D bluff body were investigated using time-resolved X-ray densitometry over a wide range of flow velocity (Froude Number, $Fr \sim 2-13.9$ and Reynolds Number, $Re_H \sim 1.6\times10^4 - 1.2\times10^5$), and gas injection rate ($C_{qs} \sim 0.03-0.13$). The ventilated cavities were created by systematically varying Fr and C_{qs} with two different ventilation strategies, i.e. increasing ventilation ('L-H') and decreasing ventilation ('H-L'). This investigation aimed to address the question: *"Why can supercavities be maintained at almost half the gas flux required to form the supercavity?"*

With the 'L-H' ventilation strategy, a regime map (Fr vs C_{qs}) was developed, where four different types of stable cavities are identified, each having a unique cavity closure. Foamy cavities (FC) are identified at low Fr and C_{qs} *without* a developed closure region. Twin-branch cavity (TBC), Re-entrant jet cavity (REJC), and long cavities (LC), on the other hand, have developed closures. TBC is formed at low Fr (≤ 4.17) and higher C_{qs} with a 3-D closure, i.e. it has a tail at mid-span with a weak re-entrant flow along with two branches along the walls. The gas is ejected primarily by a wave-like travelling instability that pinches the cavity at the branches. For $Fr \geq 5.8$, the cavity closures exhibited are distinct: FC exists at a low C_{qs}, while REJ cavities are observed at an intermediate C_{qs}. These cavities have a strong re-entrant flow entering inside the cavity due to the large pressure gradient at the closure. Such stable cavities are seen to have multi-modal gas ejection brought about by spanwise vortex shedding and a strong re-entrant jet. These re-entrant jets share similarities with re-entrant jets in natural cavities discussed in Chapter 2. Finally, at high Fr and C_{qs}, LC with a 2-D closure exists. The closure is characterised by travelling wave-type instability leading to a gas pocket shedding. Interestingly, re-entrant flow at the cavity closure is suspended to mitigate the cavity oscillation in the $x-y$ plane. Furthermore, compressibility effects in the ventilated cavities under consideration are seen to be negligible in contrast to natural cavitation flows shown in chapter 3. This is primarily due to high cavity pressures ($\gtrsim 70$ kPa) despite low void fractions (~ 0.5) in the cavity, corroborating the conclusions presented in subsection 5.1.1.

The cavity closure and the resulting gas ejection rates are seen to dictate the length of the cavity (L_c) and pressure inside the cavity (P_c): there is an abrupt increase in the cavity lengths with changing closure types. It is observed that the cavity length is not unique to a flow condition given by Fr and C_{qs}. Thus, cavity pressure, expressed as cav-

itation number (σ_c) is important to uniquely define the state of the cavity. The supercavity lengths when plotted as a function of (σ_c) fall on a power law, except REJ cavities which appear much shorter. This is likely linked to the re-entering jet displacing larger amounts of gas, resulting in a low gas volume entrained to form the cavity. The supercavities (TBCs and LCs) exhibit a maximum cavity length (L_c) for a given U_0 (Fr), meaning a finite volume of gas ($\sim WHL_c$) can be entrained in the wake of the bluff body to form a cavity. The excess injected gas is ejected out.

The supercavity formation process is studied thoroughly for the first time. In particular, we focus on cavity closures formed during the transition process from one stable closure to another. It is observed that cavities transitioning from FC to TBC at low Fr (≤ 4.17) have much lower but constant gas ejection rates than at high Fr (≥ 5.7) when REJC transitions to LC. This is due to the different cavity closures the cavity assumes during the transition process: At low Fr, the gas is ejected out via spanwise vortices or wave instability. However, at higher Fr, gas is ejected via spanwise vortices *and* predominantly by the re-entrant flow. A prominent re-entrant flow at the closure is seen to result in significantly higher gas leakage than vortex or wave-type closure. Re-entrant flow is seen at the closure of transitional cavities as the supercavities are being formed for $Fr \geq 3.43$. The length of this re-entrant flow is seen to scale linearly with flow inertia. A simple empirical model is constructed to show that re-entrant flow accounts for the majority of the gas leakage at higher ranges of Fr. Further, re-entrant jet cavities transition to long cavities when input ventilation can overcome the gas ejection caused by the re-entrant flow. The transitional cavity closure and the resulting gas leakage during the cavity formation provide us insights into observed ventilation hysteresis. This also answers our question *why supercavities can be maintained/sustained at almost half the gas flux required to form/establish the supercavity.*

Finally, our data suggests that the ventilation strategy is paramount for forming and maintaining a ventilated cavity efficiently. This understanding of ventilated cavity closures can be used to devise a control strategy to form a stable cavity of a desired length with minimum gas injection. Further, it will allow to maintain cavities at the minimum ventilation demands, making partial cavity drag reduction and aeration more efficient and sustainable.

5.2. OUTLOOK ON FUTURE RESEARCH

Despite numerous interesting physics involving cavitating flows unveiled in this dissertation, limited time warranted pursuing the most significant and promising research directions. Nevertheless, some less-explored research directions and recommendations for future work are presented in this section.

The velocity of the re-entrant jet using tomographic imaging provides insights into the near-wall *liquid* flow, while X-ray densitometry in combination with pressure measurements probes the *vapour* phase. Due to the difficulty involved in setting up tomographic PIV experiments, re-entrant flow could be measured only for a few cases. It is advised to study the re-entrant jet at more cavitation numbers in the re-entrant jet-dominated regime ($\sigma \sim$ 0.95-0.99) to examine the variation of its velocity as a function of σ. The X-ray densitometry system employed in chapter 3 could not measure vapour fraction fields in the venturi at high σ (> 0.90). This is likely because: high σ typically

exhibit low vapour fraction values. The signal-to-noise ratio of the X-ray images can be improved with (i) a more sensitive scintillator plate and image intensifier, or (ii) enhancing spatial resolution by zooming in on the vapour cavities. This will allow quantification of compressibility effects in partial cavitation at higher ranges $\sigma \sim 0.90$-1. Here, we make a rough estimate of the speed of sound at σ=0.95; Although the vapour fractions could not be measured, cavity pressure (P_c) was measured to be about 15 kPa at σ = 0.95 in chapter 3. Further, with the monotonic decrease of α_1 with increasing σ, we can approximate the vapour fraction at σ=0.95 to be about 0.4. The speed of sound can now be approximated to be 10 ms^{-1}, which is of the order of throat velocity, U_t. In chapters 2 and 3, it was found that the velocity of the re-entrant jet front and the bubbly shock front is approximately $0.5U_t$. Thus, the Mach number of the condensation/re-entrant jet fronts is ≈ 0.5, suggesting it is subsonic.

It is found that static pressure distribution and density are key parameters governing partial cavitation. Steps can be taken to probe static pressure time-synchronised with vapour fraction measurement at multiple axial locations in the venturi to study the cavity shedding at $\sigma \sim 0.80$-0.9, where the shedding mechanism switches intermittently. In particular, it would be interesting to study static pressure distribution in the cavity during cycle-to-cycle variation observed in shedding at $\sigma \sim 0.80$-0.9. We observed *frozen/stationary* condensation shock fronts in some cycles at low $\sigma \sim 0.47$. It was suspected that the vapour production rate and the resulting higher pressure in the cavity were responsible for this behaviour. This hypothesis can be tested with static pressure measurements time-synchronised with density measurements. It is advised to consider different venturi geometries with varied degrees of an adverse pressure gradient to study the dynamics and kinematics of condensation shock waves and re-entrant jets for a range of σ.

It was attempted to study the cloud collapses in the divergent part of the venturi using PIV using fluorescent tracer particles and optical filter as described in Gawandalkar and Poelma (2022). As can be seen in figure 5.1, particle images have a sufficient signal-to-noise ratio, except in the region of the vapour cloud. With the measured velocities and turbulent stresses, the effect of cloud collapses on turbulent structures can be studied in detail. For instance, Brandao et al. (2019) proposed that the presence of the vapour phase in combination with compressibility effects severely modifies the vortex stretching process. This could be pursued for the fundamental understating of turbulence in cavitating flows.

Cavitation inception refers to the onset of a cavitation bubble which is a building block of a vapour cavity. The inception is a complex phenomenon exhibiting hysteresis and desinence with respect to the exact flow condition at which it occurs (Alamé & Mahesh, 2024). Inception studies require strict control over the water quality. The current cavitation loop being small can provide this condition allowing inception studies. The flow is optically transparent moments before the inception, hence PIV can be leveraged to obtain velocity and thus pressure fields using appropriate boundary conditions. Bernoulli's equation can be used to generate the boundary condition for pressure reconstruction near the core (axis) of the venturi. The presence of various impurities such as microbubbles, salt and particles can be investigated for cavitation susceptibility with wide relevance in process industries.

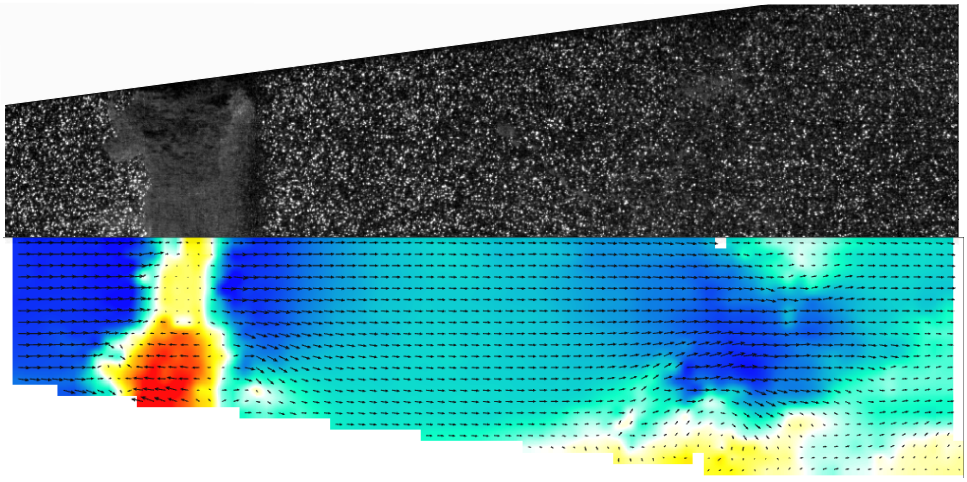

Figure 5.1: A sample PIV particle image and velocity field showing cloud shedding in an axisymmetric venturi at σ=0.97 acquired in the study leading up to Gawandalkar and Poelma, 2022. The colour map of velocity spans from -10ms^{-1} to 12ms^{-1}. The blurred structure in the particle image stems from the convecting cavitation vapour cloud.

Preliminary Magnetic Imaging (MRI) measurements were performed for cavitating flows to quantify the vapour fraction and velocity fields (see figure 5.2) in the follow-up study to John et al., 2020. The time-averaged velocity measurements although noisy showed decent agreement with CFD data (Brunhart et al., 2020) at similar σ. Unlike X-ray densitometry, the noise level in the vapour fractions (a function of signal intensity in figure 5.2) was significantly high. This was suspected due to the high turbulence level, multiphase effects, cloud collapse etc. However, the sensitivity of MR images to the above-mentioned factors needs further investigation. Although challenging, MRI as a diagnostic tool for studying liquid-vapour unsteady flows can be improved. The vapour/void fraction data from the X-ray densitometry obtained in this dissertation can be used as benchmark data for developing MRI sequences for quantifying vapour fractions in highly unsteady multiphase flows.

Stable ventilated cavities in the wake of the wedge have been studied thoroughly with the exception of long cavities. Long cavities extended beyond the FOV owing to a smaller observation window. New experiments can be performed with a larger observation window ($\sim 18H$) to observe and study the closure of these long cavities to examine the similarity of long cavities closure to twin branch cavity closure. It is recognised that at $Fr \geq 5.17$, Re_H is a more relevant parameter to express the effect of inertia in the dynamics of ventilated cavities. Hence, it is recommended to vary the wedge geometry (H), to segregate the effects of Re_H and Fr. This can also be done by performing similar experiments across different scales.

Several ventilation strategies can be tested to arrive at the most efficient way of establishing and maintaining a ventilated cavity, i.e. different ventilation profiles can be examined. Although not reported in this dissertation, the rate of increase in gas injection rate seems like a worthy parameter for further investigation. For instance, rapid C_{qs}

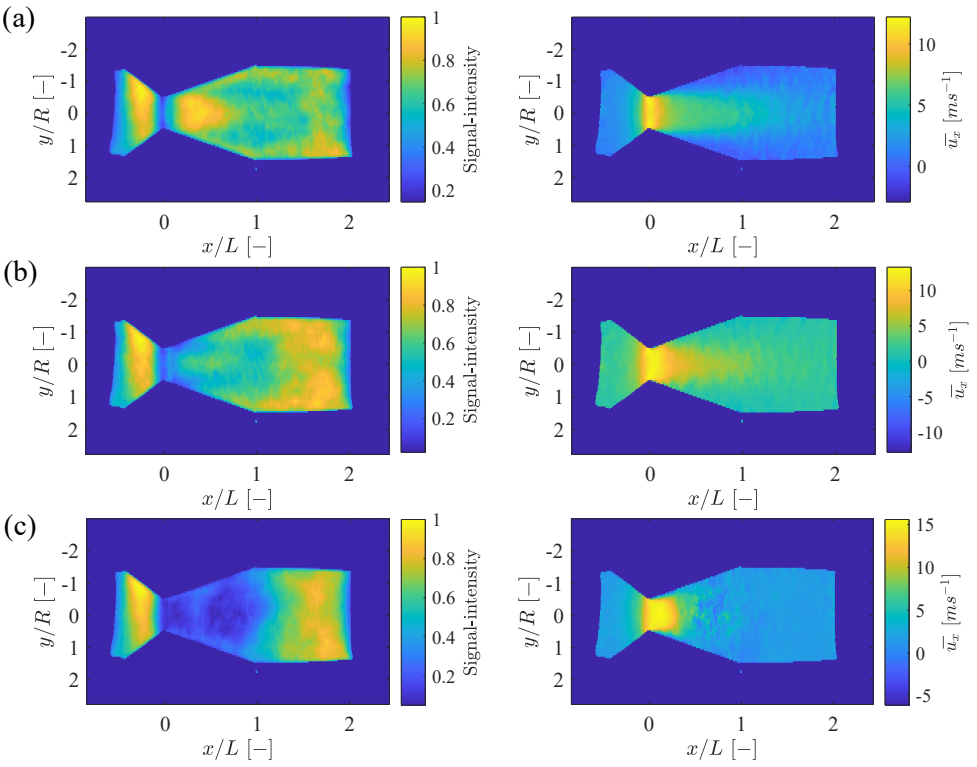

Figure 5.2: Signal intensity and time averaged velocity fields ($\overline{u_x}$) from the preliminary MRI measurements for (a) σ= 1.14 (non-cavitating), (b) σ= 0.98, and (c) σ= 0.79. The data was obtained in a follow-up study to John et al., 2020.

increases can result in faster formation of closure. Hence, the ventilated cavity can be formed at much lower net gas volume. This can be used to devise control strategies to maintain ventilated cavities of the desired length efficiently.

Digital inline holography (DIH) experiments can be undertaken near the cavity closure region to quantify the instantaneous gas leakage as a function of different flow conditions and closures (Shao et al., 2022). DIH, time-synchronised with X-ray densitometry will provide more insights into the gas ejection dynamics. Furthermore, ventilated cavities in the presence of pitching motion can be studied to examine the effect of acceleration, gust, and waves on the stability of ventilated cavities.

Finally, proper orthogonal decomposition (POD) analysis can be performed on the X-ray images of re-entrant jet-type cavities and twin Branch cavities to further study the flow structures associated with the identified gas ejection mechanisms. The preliminary POD analysis shows the flow structures corresponding to the internal boundary layer through which the gas is ejected via spanwise vortices (appearing dark red in mode 1 shown in figure 5.3). It is recommended to study this further with planar PIV in the clear part of supercavities akin to Wu, Liu, et al. (2019).

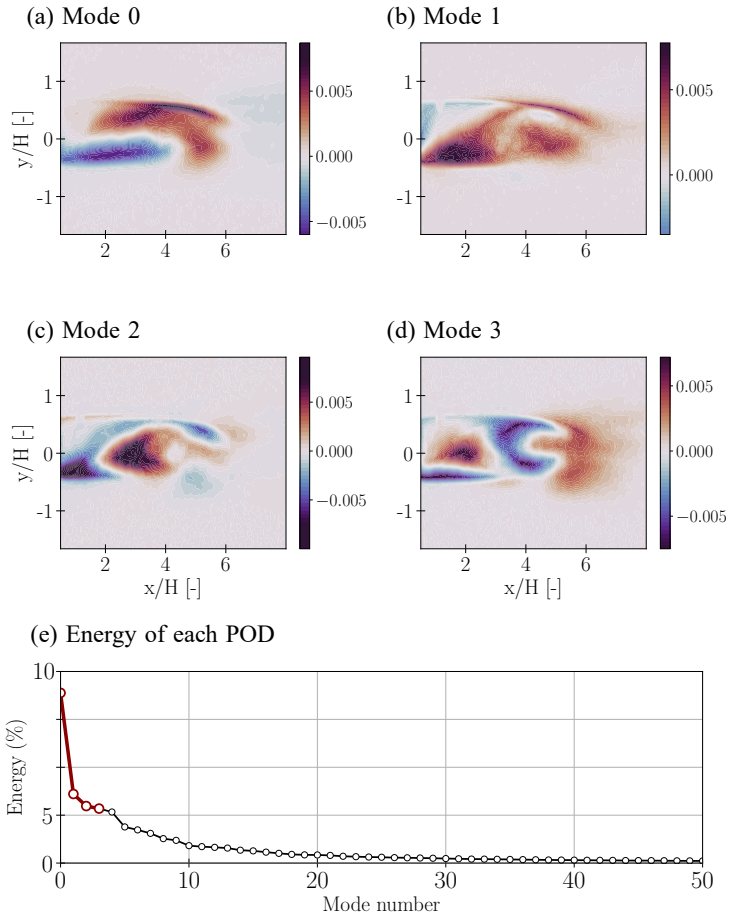

Figure 5.3: (a-d) POD modes and its energy content (e) at Fr = 5.79, C_{qs} = 0.054 for a case of stable re-entrant flow cavity (REJC). This is an ongoing work in collaboration with Ali Rahimi Khojasteh at TU Delft.

BIBLIOGRAPHY

Adhikari, U., Goliaei, A., & Berkowitz, M. L. (2016). Nanobubbles, cavitation, shock waves and traumatic brain injury. *Physical Chemistry Chemical Physics*, *18*(48), 32638–32652.

Alamé, K., & Mahesh, K. (2024). Effect of gas content on cavitation nuclei. *Journal of Fluid Mechanics*, *982*, 1–30.

Aliseda, A., & Heindel, T. J. (2021). X-Ray Flow Visualization in Multiphase Flows. *Annual Review of Fluid Mechanics*, *53*, 543–567.

Allen, J. R. (1985). *Sedimentary Structures—Their Character and Physical Basis* (Vol. 43). Elsevier Scientific Publishing Company.

Arndt, R., Hambleton, W., Kawakami, E., & Amromin, E. (2009). Creation and maintenance of cavities under horizontal surfaces in steady and gust flows. *Journal of Fluids Engineering, Transactions of the ASME*, *131*(11), 1113011–11130110.

Arndt, R. E., Song, C., Kjeldsen, M., He, J., & Keller, A. (2000). Instability of Partial Cavitation: A Numerical/Experimental Approach. *University of Minnesota Supercomputing Institute Research Report UMSI*, *183*, (pp. 140–155).

Asnaghi, A. (2015). *Developing Computational Methods for Detailed Assessment of Cavitation on Marine Propellers* [Doctoral dissertation, Chalmers University of Technology].

Barbaca, L., Pearce, B. W., & Brandner, P. A. (2017). Experimental study of ventilated cavity flow over a 3-D wall-mounted fence. *International Journal of Multiphase Flow*, *97*, 10–22.

Barbaca, L., Pearce, B. W., Ganesh, H., & Ceccio, S. L. (2019). On the unsteady behaviour of cavity flow over a two-dimensional wall-mounted fence, 483–525.

Barre, S., Rolland, J., Boitel, G., Goncalves, E., & Patella, R. F. (2009). Experiments and modeling of cavitating flows in venturi: attached sheet cavitation. *European Journal of Mechanics, B/Fluids*, *28*(3), 444–464.

Bhatt, A., Ganesh, H., & Ceccio, S. L. (2021). Cavitating flow behind a backward facing step. *International Journal of Multiphase Flow*, *139*, 103584.

Bhatt, A., Ganesh, H., & Ceccio, S. L. (2023). Partial cavity shedding on a hydrofoil resulting from re-entrant flow and bubbly shock waves. *Journal of Fluid Mechanics*, 1–36.

Bhatt, M., & Mahesh, K. (2020). Numerical investigation of partial cavitation regimes over a wedge using large eddy simulation. *International Journal of Multiphase Flow*, *122*, 103155.

Blake, J. R., & Gibson, D. C. (1987). Cavitation Bubbles Near Boundaries. *Annual Review of Fluid Mechanics*, *19*, 99–123.

Brandao, F. L., Bhatt, M., & Mahesh, K. (2019). Numerical study of cavitation regimes in flow over a circular cylinder. *Journal of Fluid Mechanics*, *885*(A19).

Brennen, C. E. (1995). *Cavitation and Bubble Dynamics*. Oxford University Press.

Brunhart, M., Soteriou, C., Gavaises, M., Karathanassis, I., Koukouvinis, P., Jahangir, S., & Poelma, C. (2020). Investigation of cavitation and vapor shedding mechanisms in a Venturi nozzle Maxwell. *Physics of Fluids*, *32*(8).

Budich, B., Schmidt, S. J., & Adams, N. A. (2018). Numerical simulation and analysis of condensation shocks in cavitating flow. *Journal of Fluid Mechanics*, *838*, 759–813.

Callenaere, M., Franc, J. P., Michel, J. M., & Riondet, M. (2001). The cavitation instability induced by the development of a re-entrant jet. *Journal of Fluid Mechanics*, *444*, 223–256.

Canchi, S., Kelly, K., Hong, Y., King, M. A., & Subhash, G. (2017). Controlled single bubble cavitation collapse results in jet-induced injury in brain tissue. *Journal of the Mechanical Behavior of Biomedical Materials*, *74*(February), 261–273.

Ceccio, S. L. (2010). Friction drag reduction of external flows with bubble and gas injection. *Annual Review of Fluid Mechanics*, *42*, 183–203.

Chanson, M. H. (2010). Predicting the filling of ventilated cavities behind spillway aerators Predicting the filling of ventilated cavities behind spillway. *Journal of Hydraulic Research*, *33:3*(January 2010), 361–372.

Coutier-Delgosha, O., Stutz, B., Vabre, A., & Legoupil, S. (2007). Analysis of cavitating flow structure by experimental and numerical investigations. *Journal of Fluid Mechanics*, *578*(2007), 171–222.

Coutier-Delgosha, O., Devillers, J. F., Pichon, T., Vabre, A., Woo, R., & Legoupil, S. (2006). Internal structure and dynamics of sheet cavitation. *Physics of Fluids*, *18*(1).

Cox, R. N., & Clayden, A. (1955). Air entrainment at the rear of a steady cavity. *Proceedings of the Symposium on Cavitation in Hydrodynamics. HMSO*.

Dash, A., Jahangir, S., & Poelma, C. (2018). Direct comparison of shadowgraphy and x-ray imaging for void fraction determination. *Measurement Science and Technology*, *29*(125303).

Davenport, J., Hughes, R. N., Shorten, M., & Larsen, P. S. (2011). Drag reduction by air release promotes fast ascent in jumping emperor penguins-a novel hypothesis. *Marine Ecology Progress Series*, *430*(2005), 171–182.

De Lange, D. F., & De Bruin, G. J. (1997). Sheet cavitation and cloud cavitation, re-entrant jet and three-dimensionality. *Flow, Turbulence and Combustion*, *58*(1-3), 91–114.

Deen, B. N. G., Westerweel, J., & Delnoij, E. (2002). Two-Phase PIV in Bubbly Flows : Status and Trends. *Chemical engineering and Technology*, *25*, 97–101.

Drazin, P. (2002). *Introduction to Hydrodynamic Stability*. Cambridge University Press.

Dular, M., Bachert, R., Stoffel, B., & Širok, B. (2005). Experimental evaluation of numerical simulation of cavitating flow around hydrofoil. *European Journal of Mechanics, B/Fluids*, *24*(4), 522–538.

Elsinga, G. E., Scarano, F., Wieneke, B., & Van Oudheusden, B. W. (2006). Tomographic particle image velocimetry. *Experiments in Fluids*, *41*(6), 933–947.

Epshteyn, L. (1961). Determination of the amount of gas needed to maintain a cavity behind a body moving at low Fr number. *Tr. TsAGI*, *824*, :45–56.

Fitzgerald, J. A., & Garimella, S. V. (1997). Visualization of the flow field in a confined and submerged impinging jet. *American Society of Mechanical Engineers, Heat Transfer Division, (Publication) HTD*, *346*, 93–96.

Foeth, E. J., Van Doorne, C. W., Van Terwisga, T., & Wieneke, B. (2006). Time resolved PIV and flow visualization of 3D sheet cavitation. *Experiments in Fluids*, *40*(4), 503–513.

Franc, J. P. (2001). Partial Cavity Instabilities and Re-Entrant Jet. *International Symposium on Cavitation*, (Tsujimoto).

Franc, J. P., & Michel, J. M. (2005). *Fundamentals of Cavitation* (Vol. 2).

Furness & Hutton. (1975). Experimental and Theoretical Studies of Two-Dimensional Fixed-Type Cavities. *Journal of Fluids Engineering, Transactions of the ASME*, *97*(4), 515–521.

Ganesh, H., Makiharju, S. A., & Ceccio, S. L. (2016). Bubbly shock propagation as a mechanism for sheet-to-cloud transition of partial cavities. *Journal of Fluid Mechanics*, *802*, 37–78.

Gawandalkar, U., & Poelma, C. (2022). The structure of near-wall re-entrant flow and its influence on cloud cavitation instability. *Experiments in Fluids*, *63*(5), 1–19.

Ghahramani, E., Arabnejad, M. H., & Bensow, R. E. (2019). A comparative study between numerical methods in simulation of cavitating bubbles. *International Journal of Multiphase Flow*, *111*, 339–359.

Giannadakis, E., Gavaises, M., & Arcoumanis, C. (2008). Modelling of cavitation in diesel injector nozzles. *Journal of Fluid Mechanics*, *616*, 153–193.

Gnanaskandan, A., & Mahesh, K. (2016a). Large Eddy Simulation of the transition from sheet to cloud cavitation over a wedge. *International Journal of Multiphase Flow*, *83*(March), 86–102.

Gnanaskandan, A., & Mahesh, K. (2016b). Numerical investigation of near-wake characteristics of cavitating flow over a circular cylinder. *Journal of Fluid Mechanics*, *790*, 453–491.

Gopalan, S., & Katz, J. (2000). Flow structure and modeling issues in the closure region of attached cavitation. *Physics of Fluids*, *12*(4), 895–911.

Graham, S. M., Carlisle, R., Choi, J. J., Stevenson, M., Shah, A. R., Myers, R. S., Fisher, K., Peregrino, M. B., Seymour, L., & Coussios, C. C. (2014). Inertial cavitation to noninvasively trigger and monitor intratumoral release of drug from intravenously delivered liposomes. *Journal of Controlled Release*, *178*(1), 101–107.

Hochberg, U., Herrera, J. C., Cochard, H., & Badel, E. (2016). Research paper Short-time xylem relaxation results in reliable quantification of embolism in grapevine petioles and sheds new light on their hydraulic strategy. *Tree Physiology*, 748–755.

Jahangir, S., Hogendoorn, W., & Poelma, C. (2018). Dynamics of partial cavitation in an axisymmetric converging-diverging nozzle. *International Journal of Multiphase Flow*, *106*, 34–45.

Jahangir, S., Wagner, E. C., Mudde, R. F., & Poelma, C. (2019). Void fraction measurements in partial cavitation regimes by X-ray computed tomography. *International Journal of Multiphase Flow*, *120*(103085).

John, K., Jahangir, S., Gawandalkar, U., Hogendoorn, W., Poelma, C., Grundmann, S., & Bruschewski, M. (2020). Magnetic resonance velocimetry in high-speed turbu-

lent flows: sources of measurement errors and a new approach for higher accuracy. *Experiments in Fluids*, *61*(2), 1–17.

Johnson, V. E., Chahine, G. L., Lindenmuth, W. T., Conn, A. F., Frederick, G. S., & Giacchino, G. J. (1982). The development of STRuctured cavitating jets for deep-hole bits. *Proceedings - SPE Annual Technical Conference and Exhibition*, *1982-Septe*.

Jyoti, K. K., & Pandit, A. B. (2004). Ozone and cavitation for water disinfection. *Biochemical Engineering Journal*, *18*, 9–19.

Karathanassis, I. K., Heidari-Koochi, M., Zhang, Q., Hwang, J., Koukouvinis, P., Wang, J., & Gavaises, M. (2021). X-ray phase contrast and absorption imaging for the quantification of transient cavitation in high-speed nozzle flows. *Physics of Fluids*, *33*(3).

Karn, A., Arndt, R. E., & Hong, J. (2016). An experimental investigation into supercavity closure mechanisms. *Journal of Fluid Mechanics*, *789*, 259–284.

Kawakami, E., & Arndt, R. E. (2011). Investigation of the behavior of ventilated supercavities. *Journal of Fluids Engineering, Transactions of the ASME*, *133*(9), 1–11.

Kawanami, Y., Kato, H., Yamaguchi, H., Tanimura, M., & Tagaya, Y. (1997). Mechanism and control of cloud cavitation. *Journal of Fluids Engineering, Transactions of the ASME*, *119*(4), 788–794.

Kawchuk, G. N., Fryer, J., Jaremko, J. L., & Zeng, H. (2015). Real-Time Visualization of Joint Cavitation. *PLoS ONE*, *10*(4), 1–11.

Kim, H., Westerweel, J., & Elsinga, G. E. (2013). Comparison of Tomo-PIV and 3D-PTV for microfluidic flows. *Measurement Science and Technology*, *24*(2), 024007.

Kinzel, M. P., & Maughmer, M. D. (2010). Numerical Investigation on the Aerodynamics of Oscillating Airfoils with Deployable Gurney Flaps. *48*(7).

Knapp, R. T. (1958). Recent investigations of the mechanics of cavitation and cavitation damage. *Wear*, *1*(5), 455.

Kubota, A., Kato, H., Yamaguchi, H., & Architecture, N. (1989). Unsteady Structure Measurement of Cloud Cavitation on a Foil Section Using Conditional Sampling Technique. *Journal of Fluids Engineering, Transactions of the ASME*, *111*.

Kuiper, G. (1997). Cavitation research and ship propeller design. *Applied Scientific Research (The Hague)*, *58*(1-4), 33–50.

Kundu, P. K., Cohen, I. M., & Dowling, D. R. (2016). *Fluid Mechanics*. Elsevier.

Laberteaux, K., & Ceccio, S. (2001a). Partial cavity flows. Part 1. Cavities forming on models without spanwise variation. *Journal of Fluid Mechanics*, *431*, 1–41.

Laberteaux, K. R., & Ceccio, S. L. (2001b). Partial cavity flows. Part 2. Cavities forming on test objects with spanwise variation. *Journal of Fluid Mechanics*, *431*, 43–63.

Le, Q. (1993). Partial Cavities: Global Behavior and Mean Pressure Distribution. *Journal of Fluids Engineering, Transactions of the ASME*, *115*(June 1993), 243–248.

Lee, S.-J., & Arndt, R. E. A. (2013). Investigation of the Behavior of Ventilated Supercavities in a Periodic Gust Flow. *Journal of Fluids Engineering*, *135*(August), 1–13.

Leroux, J. B., Astolfi, J. A., & Billard, J. Y. (2004). An experimental study of unsteady partial cavitation. *Journal of Fluids Engineering, Transactions of the ASME*, *126*(1), 94–101.

Liu, H., Xiao, Z., & Shen, L. (2023). Simulation-based study of low-Reynolds-number flow around a ventilated cavity. *Journal of Fluid Mechanics*, *966*.

Logvinovich, G. (1969). *Hydrodynamics of free-boundary flows*. Israel Program for Scientific Translations Jerusalem 1972.

Lush, P. A., & Skipp, S. R. (1986). High speed cine observations of cavitating flow in a duct. *International Journal of Heat and Fluid Flow*, *7*(4), 283–290.

Madabhushi, A., & Mahesh, K. (2023). A compressible multi-scale model to simulate cavitating flows. *Journal of Fluid Mechanics*, *961*, 1–32.

Mahesh, K. (2022). Numerical treatment of compressible turbulent flows. In *Numerical methods in turbulence simulation* (pp. 469–499). Elsevier Inc.

Mäkiharju, S. A., Elbing, B. R., Wiggins, A., Schinasi, S., Vanden-Broeck, J. M., Perlin, M., Dowling, D. R., & Ceccio, S. L. (2013). On the scaling of air entrainment from a ventilated partial cavity. *Journal of Fluid Mechanics*, *732*, 47–76.

Mäkiharju, S. A., Gabillet, C., Paik, B. G., Chang, N. A., Perlin, M., & Ceccio, S. L. (2013). Time-resolved two-dimensional X-ray densitometry of a two-phase flow downstream of a ventilated cavity. *Experiments in Fluids*, *54*(7).

Mäkiharju, S. A., Ganesh, H., & Ceccio, S. L. (2017a). The dynamics of partial cavity formation , shedding and the influence of dissolved and injected non-condensable gas, 420–458.

Mäkiharju, S. A., Ganesh, H., & Ceccio, S. L. (2017b). The dynamics of partial cavity formation, shedding and the influence of dissolved and injected non-condensable gas. *Journal of Fluid Mechanics*, *829*, 420–458.

Mäkiharju, S. A., Perlin, M., & Ceccio, S. L. (2013). On the energy economics of air lubrication drag reduction. *International Journal of Naval Architecture and Ocean Engineering*, (2012), 412–422.

Michel, J. M. (1984). Some features of water flows with ventilated cavities. *Journal of Fluids Engineering, Transactions of the ASME*, *106*(3), 319–326.

Mitroglou, N., Lorenzi, M., Santini, M., & Gavaises, M. (2016). Application of X-ray microcomputed tomography on high-speed cavitating diesel fuel flows. *Experiments in Fluids*, *57*(11), 1–14.

Mittapalli, G. V. S. S. (2015). Analysis of Pressures on Nagarjuna Sagar Spillway. *EC Agriculture*, *1.1*(June), 23–34.

Münch, B., Trtik, P., Marone, F., & Stampanoni, M. (2009). Stripe and ring artifact removal with combined wavelet-Fourier filtering. *EMPA Activities*, *17*(2009-2010 EMPA ACTIVITIES), 34–35.

Nakashima, K., Ebi, Y., Shibasaki-kitakawa, N., Soyama, H., & Yonemoto, T. (2016). Hydrodynamic Cavitation Reactor for E ffi cient Pretreatment of Lignocellulosic Biomass. *Industrial and Engineering Chemistry Research*, *55*, 1866–1871.

Nikolaidou, L., Laskari, A., Poelma, C., & Terwisga, T. V. (2022). Effect of incoming boundary layer characteristics on an air layer within a liquid turbulent boundary layer. *12th International Symposium on Turbulence and Shear Flow Phenomena, TSFP 2022, Osaka, Virtual, Japan.*

Pelz, P. F., Keil, T., & Gro, T. F. (2017). The transition from sheet to cloud cavitation. *Journal of Fluid Mechanics*, *817*, 439–454.

Pfister, M., Sc, D., Lucas, J., Hager, W. H., & Asce, F. (2011). Chute Aerators : Preaerated Approach Flow. *Journal of Hydraulic Engineering*, *137*(March 2015), 1452–1461.

Pham, T. M., Larrarte, F., & Fruman, D. H. (1999). Investigation of unsteady sheet cavitation and cloud cavitation mechanisms. *Journal of Fluids Engineering, Transactions of the ASME*, *121*(2), 289–296.

Poelma, C. (2020). Measurement in opaque flows: a review of measurement techniques for dispersed multiphase flows. *Acta Mechanica*, *231*(6), 2089–2111.

Pokharel, N., Ghimire, A., Thapa, B., & Thapa, B. S. (2022). Wear in centrifugal pumps with causes , effects and remedies : A Review. *Earth and Environmental Science*.

Prosperetti, A. (2015). The speed of sound in a gas – vapour bubbly liquid. *Interface Focus*, *5(5)*.

Qin, S., Wu, Y., Wu, D., & Hong, J. (2019). Experimental investigation of ventilated partial cavitation. *International Journal of Multiphase Flow*, *113*, 153–164.

Reisman, G. E., Wang, Y. C., & Brennen, C. E. (1998). Observations of shock waves in cloud cavitation. *Journal of Fluid Mechanics*, *355*, 255–283.

Reuther, N., & Kähler, C. J. (2018). Evaluation of large-scale turbulent/non-turbulent interface detection methods for wall-bounded flows. *Experiments in Fluids*, *59*(7), 1–17.

Rigby, G. D., Evans, G. M., & Jameson, G. J. (1997). Bubble breakup from ventilated cavities in multiphase reactors. *Chemical Engineering Science*, *52*(21-22), 3677–3684.

Saito, Y., Takami, R., & Nakamori, I. (2007). Numerical analysis of unsteady behavior of cloud cavitation around a NACA0015 foil. *Computational Mechanics*, *40*(85), 85–96.

Sakoda, M., Yakushiji, R., Maeda, M., & Yamaguchi, H. (2001). Mechanism of cloud cavitation generation on a 2-D hydrofoil. *Fourth International Symposium on Cavitation*, (1996), 1–8.

Semenenko, V. (2001). *Artificial Supercavitation. Physics and Calculation* (tech. rep.). National Academy of Sciences - Institute of Hydromechanics. Kyiv, Ukraine.

Shamsborhan, H., Coutier-Delgosha, O., Caignaert, G., & Abdel Nour, F. (2010). Experimental determination of the speed of sound in cavitating flows. *Experiments in Fluids*, *49*(6), 1359–1373.

Shao, S., Li, J., Yoon, K., & Hong, J. (2022). Probing into gas leakage characteristics of ventilated supercavity through bubbly wake measurement. *Ocean Engineering*, *245*(November 2021), 110457.

Silberman, E., & Song, C. S. (1961). Instability of Ventilated Cavities. *Journal of Ship Research*, 13–33.

Skidmore, G. (2016). *The mitigation of pulsation in ventilated super cavities* (Publication No. May) [Doctoral dissertation, The Pennsylvania State University].

Spurk, J. H. (2002). On the gas loss from ventilated supercavities. *Acta Mechanica*, *155*(3-4), 125–135.

Stanley, C., Barber, T., & Rosengarten, G. (2014). Re-entrant jet mechanism for periodic cavitation shedding in a cylindrical orifice. *International Journal of Heat and Fluid Flow*, *50*, 169–176.

Stutz, B., & Legoupil, S. (2003). X-ray measurements within unsteady cavitation. *Experiments in Fluids*, *35*, 130–138.

Stutz, B., & Reboud, J. L. (1997). Two-phase flow structure of sheet cavitation. *Physics of Fluids*, *9*(12), 3678–3686.

Terentiev, A., Kirschner, I., & Uhlman, J. (2011). *The Hydrodynamics of Cavitating Flows* (Vol. 1).

Tomov, P., Khelladi, S., Ravelet, F., Sarraf, C., Bakir, F., & Vertenoeuil, P. (2016). Experimental study of aerated cavitation in a horizontal venturi nozzle. *Experimental Thermal and Fluid Science*, *70*, 85–95.

Trummler, T., Schmidt, S. J., & Adams, N. A. (2020). Investigation of condensation shocks and re-entrant jet dynamics in a cavitating nozzle flow by Large-Eddy Simulation. *International Journal of Multiphase Flow*, *125*.

Tyree, M. T., & Sperry, J. S. (1989). Cavitation and Embolism. *Water*, 19–38.

Van Terwisga, T., Van Wijngaarden, E., Bosschers, J., & Kuiper, G. (2007). Achievements and challenges in cavitation research on ship propellers. *International Shipbuilding Progress*, *54*(2-3), 165–187.

van Aarle, W., Palenstijn, W. J., Cant, J., Janssens, E., Bleichrodt, F., Dabravolski, A., De Beenhouwer, J., Joost Batenburg, K., & Sijbers, J. (2016). Fast and flexible X-ray tomography using the ASTRA toolbox. *Optics Express*, *24*(22), 25129.

Versluis, M. (2013). High-speed imaging in fluids. *Experiments in Fluids*, *54*(2).

Versluis, M., Schmitz, B., Von der Heydt, A., & Lohse, D. (2000). How snapping shrimp snap: Through cavitating bubbles. *Science*, *289*(5487), 2114–2117.

Westerweel, J. (1997). Fundamentals of digital particle image velocimetry. *Measurement Science and Technology*, *8*(12), 1379–1392.

Westerweel, J., & Scarano, F. (2005). Universal outlier detection for PIV data. *Experiments in Fluids*, *39*(6), 1096–1100.

Whipple, K. X., Hancock, G. S., & Anderson, R. S. (2000). River incision into bedrock : Mechanics and relative efficacy of plucking , abrasion , and cavitation. *GSA Bulletin*, *112*(3), 490–503.

Wieneke, B. (2008). Volume self-calibration for 3D particle image velocimetry, 549–556.

Wosnik, M., & Arndt, R. E. (2013). Measurements in high void-fraction bubbly wakes created by ventilated supercavitation. *Journal of Fluids Engineering, Transactions of the ASME*, *135*(1), 1–9.

Wu, J., Deijlen, L., Bhatt, A., Ganesh, H., & Ceccio, S. L. (2021). Cavitation dynamics and vortex shedding in the wake of a bluff body. *Journal of Fluid Mechanics*, *917*, 1–32.

Wu, J., Ganesh, H., & Ceccio, S. (2019). Multimodal partial cavity shedding on a two-dimensional hydrofoil and its relation to the presence of bubbly shocks. *Experiments in Fluids*, *60*(4), 1–17.

Wu, Y., Liu, Y., Shao, S., & Hong, J. (2019). On the internal flow of a ventilated supercavity. *Journal of Fluid Mechanics*, *862*, 1135–1165.

Xu, Z., Ludomirsky, A., Eun, L. Y., Hall, T. L., Tran, B. C., Fowlkes, J. B., & Cain, C. A. (2003). Controlled ultrasound tissue erosion. *Proceedings of the IEEE Ultrasonics Symposium*, *1*(6), 732–735.

Yoon, K., Qin, S., Shao, S., & Hong, J. (2020). Internal flows of ventilated partial cavitation. *Experiments in Fluids*, *61*(4), 1–15.

Young, Y. L., Harwood, C. M., Montero, F. M., Ward, J. C., & Ceccio, S. L. (2017). Ventilation of Lifting Bodies: Review of the Physics and Discussion of Scaling Effects. *Applied Mechanics Reviews*, *69*(1).

Zhang, G., Khlifa, I., & Coutier-Delgosha, O. (2020). A comparative study of quasi-stable sheet cavities at different stages based on fast synchrotron x-ray imaging. *Physics of Fluids*, *32*(12).

Zhang, G., Khlifa, I., Fezzaa, K., Ge, M., & Coutier-Delgosha, O. (2020). Experimental investigation of internal two-phase flow structures and dynamics of quasi-stable sheet cavitation by fast synchrotron x-ray imaging. *Physics of Fluids*, *32*(11).

Zhang, G., Zhang, D., Ge, M., Petkovšek, M., & Coutier-Delgosha, O. (2022). Experimental investigation of three distinct mechanisms for the transition from sheet to cloud cavitation. *International Journal of Heat and Mass Transfer*, *197*, 123372.

Zverkhovskyi, O. (2014). *Ship drag reduction by air cavities* [Doctoral dissertation, Technische Universiteit Delft].

ACKNOWLEDGEMENTS

This dissertation is the culmination of more than four years of research, experiences, and immense learning. As I reflect upon this time, I realise that this journey was made easier by the direct and indirect involvement of many people. Hence, I would like to express my gratitude to all of them.

I would like to thank Christian for providing me with an opportunity to work on this project. It was a real pleasure to work with you, as I learned plenty from you, both in technical and non-technical aspects. I appreciate the confidence and freedom you gave me to pursue research directions in this dissertation. Your timely critical feedback, resourcefulness, acumen, and eye for detail were very beneficial for this thesis. Furthermore, your amiable, witty, yet sharp nature made our Monday-morning meetings both easier and productive. I hope we have many opportunities to collaborate in the future. I would also like to thank Jerry for his prompt approval of the initial draft of this dissertation.

Starting my PhD during the pandemic had its own challenges. I would like to thank the Laboratory for Aero and Hydrodynamics for efficient management and facilitating experimental work amidst all the restrictions. Many thanks to Edwin, Jasper, Jan, and GertJan for helping to realise the experiments. Your willingness to assist and ability to troubleshoot *any* practical problems played a significant role in the successful completion of this dissertation. Furthermore, thanks to Wout and Frits Hilvers (TNO-Ypenburg) for assisting with the experimental campaign in the bunkers of TNO. Amidst all the interruptions (loud ones), we managed to produce quality experimental data. It was truly a memorable experience. I would also like to thank Caroline for administrative support and many cheerful conversations.

I thank Harish and Steve for hosting me at the University of Michigan in Ann Arbor. I appreciate your openness, resourcefulness, and the freedom you provided me to pursue the research at your lab. My time at Ann Arbor was eventful yet productive. Thanks to Harish for constantly reminding me about the 'big picture'. Furthermore, I am grateful to Nick for helping to realise experiments in a short time and numerous technical deliberations–it indeed took courage to watch the big-wedge melt in front of our eyes. I would also like to extend my gratitude to Usha for her encouragement, kindness, treats, and various stimulating conversations in Michigan.

I had the pleasure of knowing and befriending numerous people with diverse backgrounds over the last few years–thank you for many shared experiences. Thanks to Tariq, Yavuz, and Guillermo for the fun bouldering sessions and cheerful conversations about music, sports, science, and more. Thanks to Ankur for helping me during the early stages of my PhD; I have enjoyed our friendship and detours after work. I would also like to thank Ellert for sharing the enthusiasm for prog and several jovial conversations about music concerts. Sarvesh, Shrinivas, Sharadhi, Vadiraj–we had some fun weekends watching and discussing Formula 1 and cricket, thank you for being accessible and mak-

ing me feel at home. Many thanks to Biswa for good times and company in exploring various concert venues in the Netherlands, listening to some of the finest prog metal. I also thank Aniket and Sherin for many meaningful conversations about shared experiences and navigating life. Numerous people I bouldered and had beers with at Delfts Bleau, thank you for cheerful times. Furthermore, I would like to thank my sisters, Sohani and Stuti, for impromptu calls and endless 'catching up'. I am grateful for your affection and for keeping me in the loop; you made me feel at home, even if only momentarily. Much appreciation and gratitude to Lyke, for her friendship, affection, and everything. We have definitely made plenty of memories to smile back at.

I would like to extend my gratitude to my colleagues: Mathieu, Willian, Sudarshan, Amitosh, Saad, Bidhan, Teng, Junaid, Bob, Koen, Parviz, Mike, Luuk, Haoyu, Wouter, Lina, Rens, Mariana, Nicola, Sowmya, Ali, Vilena, Robin, Tea, Jan-Willem, Ning, Zhou, Manuel, Arnoud, Gosse, Swaraj, Sören, Wim-Paul, Ruud, Gijs, Willem, Daniel, Mark, Gerrit, John, Emma, Angeliki and others with whom I enjoyed much-needed respites in the form of coffees, lunches, chats, drinks and most importantly, cakes. It was a pleasure to know you and have your company for the last few years. Numerous, riveting discussions at the coffee table will be missed; especially F1 *take–overs* and benign complaints about poor Dutch weather. Shout out to Jesse and Lyke for bringing the fresh *news* to the table from the *letters*. Special thanks to Abinash, Rafael, Abhirath, Esra, and Dirk for lively office environment during the last year of my PhD. We spoke about *nothing* yet everything; multiple original ideas were born here, including the arcane *Ab* number and microwaved tea. I will cherish all the joyful memories made in the lab.

Lastly, I would like to thank my family in India for their unconditional love and support, especially my Maa. Your love, strength, and unwavering belief in me have been my guiding light. I wish you could see this dissertation come to fruition. This work is a tribute to your memory, a reflection of the values you instilled in me, and a testament to your enduring presence in my life. Special thanks to my father and brother for their affection and support. I am deeply grateful for everything you have done to help me achieve this milestone. Many thanks to my sister-in-law and my aunts for your care and constant encouragement. You made it easier for me to walk this path.

Udhav Gawandalkar
Delft, August 2024.

CURRICULUM VITÆ

Udhav Ulhas GAWANDALKAR

11-12-1993	Born in Mapusa, Goa-India.

EDUCATION

1999–2009	Primary and Secondary School New Goa High School, Mapusa, Goa-India
2009–2011	Higher Secondary School Dnyanprassarak Mandal's College and Research Centre, Mapusa, Goa-India
2011–2015	Undergraduate (Bachelor of Technology) in Mechanical Engineering National Institute of Technology (NIT), Surathkal, Karnataka-India
2017–2019	Master of Science (cum laude) in Mechanical Engineering Delft University of Technology, The Netherlands
2019–2024	PhD Delft University of Technology, The Netherlands *Thesis:* On the Dynamics of Natural and Ventilated Cavitation Flows *Promotor:* Prof. dr. ir. C. Poelma & Prof. dr. ir. J. Westerweel

EXPERIENCE

2022–2023	Visiting Researcher University of Michigan, Ann Arbor, MI, USA
2018	Graduate Intern TNO, Leeghwaterstraat, Delft, The Netherlands
2016-2017	Research Assistant Indian Institute of Science, Bangalore, India
2015-2016	Assistant Manager Hero Moto Corp Limited, Gurgaon, India

LIST OF PUBLICATIONS

JOURNAL ARTICLES

- **Gawandalkar, U.U.**, Lucido, N.A., Jain, P., Poelma, C., Ceccio, S.L., Ganesh, H. *Examination of ventilated cavities in the wake of a two-dimensional bluff body using X-ray densitometry*, under review at the Journal of Fluid Mechanics, arXiv preprint (2024).
- **Gawandalkar, U.U.**, Poelma, C. *The characteristics of bubbly shock waves in a cavitating axisymmetric venturi via time-resolved X-ray densitometry*, Journal of Fluid Mechanics, **988** (A34), 1-33 (2024).
- **Gawandalkar, U.U.**, Poelma, C., *The structure of near-wall re-entrant flow and its influence on cloud cavitation instability*, Experiments in Fluids **63**(5), 1-19 (2022).
- John, K., Jahangir, S., **Gawandalkar, U. U.**, Hogendoorn, W., Poelma, C., Grundmann, S., Bruschewski, M., *Magnetic resonance velocimetry in high-speed turbulent lows: sources of measurement errors and a new approach for higher accuracy*, Experiments in Fluids **61**, 27 (2020).

CONFERENCE CONTRIBUTIONS

- **Gawandalkar, U. U.**, Lucido, N.A., Jain, P., Ganesh, H., Poelma, C., Ceccio, S.L. *X-ray measurements of ventilated cavities in the wake of a 2-D bluff body and an axisymmetric cavitator.* 35th Symposium on Naval Hydrodynamics (SNH), Nantes, France (2024).
- **Gawandalkar, U. U.**, Jahangir, S., Hogendoorn, W., Poelma, C. *V0011: Jets vs Shocks: dynamics of partial cavitation.* Gallery of Fluid Motion, 76th Annual Meeting of the Division of Fluid Dynamics, APS, Washington, DC, USA (2023).
- Jain, P., Lucido, N., **Gawandalkar, U. U.**, Poelma, C., Ceccio, S.L., Ganesh, H. *Examination of cavity type, closure mechanism, and gas entrainment rates of 2-D ventilated cavities behind a bluff body.* 76th Annual Meeting of the Division of Fluid Dynamics, APS, Washington, DC, USA (2023).
- **Gawandalkar, U. U.**, Lucido, N.A., Jain, P., Ganesh, H., Poelma, C., Ceccio, S.L.*X-ray densitometry of ventilated cavities in the wake of a bluff body.* 20th International Symposium on Flow Visualization ISFV-20, Delft, The Netherlands (2023).
- **Gawandalkar, U. U.**, Westerweel, J., Elsinga, G.E. *Turbulent pipe flow subjected to a mild straining.* 20th International Symposium on Applications of Laser and Imaging Techniques to Fluid Mechanics, Lisbon, Portugal (2022).
- **Gawandalkar, U.U.**, Poelma, C. *The characteristics of bubbly shock waves in a cavitating venturi via time-resolved X-ray densitometry.* 75th Annual Meeting of the Division of Fluid Dynamics, APS, Indianapolis, Indiana, USA (2022).

- **Gawandalkar, U.U.**, Poelma, C. *Tomographic PIV measurement of a re-entrant jet in a cavitating venturi.* 14th International Symposium on Particle Image Velocimetry, Chicago, USA (ISPIV 2021).

- **Gawandalkar, U.U.**, Poelma, C. *Dynamics of re-entrant Jet in a Cavitating Venturi.* 11th International Symposium on Cavitation, Daejon, Korea (CAV2021).

OTHER CONTRIBUTIONS

- Mahalingam, A., **Gawandalkar, U.U.**, Kini, G., Buradi, A., Araki, T., Ikeda, N., Nicolaides, A., Laird, J.R., Saba, L., Suri, J.S., *Numerical analysis of the effect of turbulence transition on the hemodynamic parameters in human coronary arteries,* Cardiovascular Diagnosis and Therapy **6**(3), 208-220 (2016).

- Omrani, P.S., Greidanus, A.J., Vercauteren, F., van't Westende, J., Henkes, R., **Gawandalkar, U.U.** *Effect of salinity and thermal ageing on the performance of foamers for gas well deliquification.* SPE Workshop: Production Optimization in Gas and Oil Assets, 2018, The Hague, The Netherlands.

PATENT

- Basu, S., Kumar, P., Chaudhari, G.D., **Gawandalkar, U. U.** *Laser based system for studying adsorption kinetics of adsorbent and adsorbate pair,* Indian Patent, WO2019116147A1 (2019).

DATASETS

- **Gawandalkar U.U.**, Lucido, N.A., Jain, P., Poelma, C., Ceccio, S.L., Ganesh, H. Data underlying the examination of ventilated cavities in the wake of two-dimensional bluff body using time-resolved X-ray densitometry, 4TU.ResearchData (2024).

- **Gawandalkar U.U.**, Poelma C. Data underlying the characteristics of bubbly shock waves in a cavitating axisymmetric venturi using time-resolved X-ray densitometry, 4TU.ResearchData (2024).

- **Gawandalkar U.U.**, Poelma C. Data underlying the quantification of re-entrant jet in a cavitating axisymmetric venturi using time-resolved tomographic velocimetry, 4TU.ResearchData (2024).


TU Delft